IDENTIFICATION AND SIMULATION OF EXTREME PRECIPITATION USING A COMPUTATIONALLY INEXPENSIVE METHODOLOGY

Christopher James Lennard

Dissertation submitted to the Faculty of Science,
University of Cape Town
for the Degree Doctor of Philosophy

Abstract

An examination of characteristics extreme precipitation in the greater Cape Town region is undertaken. Thereafter, an investigation into the characteristics of these changes is made using two approaches. The first is an empirical methodology to explore the historical attributes of extreme events and the second a numerical method. These are used to demonstrate an approach to produce high resolution forecasts of extreme precipitation if computational resources are scarce. Initially, changes in the characteristics of extreme precipitation in the greater Cape Town region is documented. Then self organizing maps are used to identify archetypal synoptic circulations that are associated with extreme precipitation over the region. Thereafter, days whose synoptic state matched those of the synoptic archetypes are simulated at a resolution of one kilometer to capture regional topographic modification of extreme precipitation. Following this, the simulated precipitation is validated against observed data and the model performance is assessed. These approaches were tested over Cape Town, South Africa which has complex topography where extreme rainfall is not well predicted. As this methodology is computationally relatively inexpensive, it has applicability to regions of the world where these resources are limited, more especially Africa where the state of climate science is poor.

An analysis of historical station data from three locations in the greater Cape Town region showed mixed trends in extreme rainfall where extreme rainfall was taken as that in the 90th percentile. One station, located in the lee of topography, showed a statistically significant increase in the intensity of extreme rainfall and another, at a relatively topography-free location, a significant decrease. The third station showed no significant trend. Decadal changes in monthly precipitation show a shift in the start and end of the extreme rainfall season to starting later in winter and continuing into the early spring. The station with the significant increase in extreme rainfall intensity also showed an increase in 99th percentile rainfall intensity.

Synoptic states associated with extreme rainfall in the greater Cape Town region were then examined. These were identified as mid-latitude cyclones with centers at relatively low latitudes. They were characterized by strong pressure gradients at the surface and in the upper air high as well as high regional humidities. Precipitation characteristics of the frontal systems ranged from precipitation that fell over a number of days in relatively low daily amounts to very heavy precipitation that fell in one day. Over the twenty-three year test period examined, there are changes

evident in synoptic circulation characteristics which indicate a decrease of synoptic states associated with winter rainfall, but an increase in those associated with extreme precipitation.

Very high resolution simulations produced topographically modified weather such as split flows in wind fields and lowest temperatures at highest altitudes. Enhanced precipitation fields were simulated over and downstream of topography. Validation of the precipitation fields against station data revealed a large over-estimation of precipitation using two-way nested simulations and were unusable. However, one-way nested precipitation simulations were similar to observed data. Two-way nesting created very enhanced topography fields which amplified circulation characteristics and set up a positive feedback at the lateral boundaries.

Station data for the region are spatially and temporally sparse, constrained to mostly lower elevations and only at the daily time scale. Weather radar data provided spatially and temporally continuous data that could be used as a proxy for rainfall across the region and showed the one-way nested simulations captured the spatial, temporal and volumetric characteristics of the extreme precipitation.

This approach successfully identified days associated with extreme precipitation and simulated these at very high resolution. The development and regional refinement of the methodology could make accurate, qualitative forecasts of extreme precipitation available to regions where the capacity for these is currently not available.

I declare that this is my own, unaided work, and that it has not been submitted previously as a dissertation or thesis for any other degree at any other University.

University of Cape Town, 2007

Nkosi sikelel' iAfrika
Maluphakanyisw' uphondo lwayo,
Yizwa imithandazo yethu,
Nkosi sikelela, thina lusapho lwayo.

God bless Africa
May her glory be lifted high,
Hear our petitions,
God bless us, Your children

Preface

Extreme precipitation events have been observed in many areas of the world to have become more frequent and more intense. Extreme precipitation and subsequent flooding can have devastating effects on a region's population, environment and economy and attempts to mitigate these impacts require an improved understanding of factors which influence regionally specific extreme precipitation. These factors include relationships between synoptic scale circulations and the localized expression of extreme precipitation, changes in the historical occurrence and intensity of extreme precipitation as well as their associated synoptic circulations and the effect that topography has on extreme rainfall fields.

Extreme precipitation in the greater Cape Town region was investigated to establish changes in frequency and intensity over time. These changes were examined using two approaches. The first, an empirical approach, explored atmospheric attributes to identify key circulations associated with extreme precipitation as well as historical changes in these. This also provided a means to identify days whose synoptic states were associated with extreme precipitation. The second approach tested the ability to produce high resolution simulations (one kilometer) that captured topographic enhancement of extreme precipitation using a regional climate model. The performance of the model was assessed through validation against observed data which included weather radar data.

These approaches were expressed in a potential extreme rainfall forecast methodology that identifies circulations associated with extreme storm environments and simulates associated days at high resolutions. The methodology is computationally relatively inexpensive and therefore accessible to nations that do not have a large computational capacity, especially African nations. It was tested for Cape Town, South Africa, where conventional forecasts do not capture the regional detail of extreme precipitation.

To this end, the following hypotheses were tested:

(i) There is a quantifiable change in the characteristics of extreme rainfall over the greater Cape Town region.

(ii) Synoptic states can be categorized such that circulation states associated with localized extreme precipitation can be identified.

(iii) Radar-derived precipitation data can be reliably used as proxy data for actual precipitation.

(iv) A regional climate model, run at very high resolution, can reasonably simulate the spatial and temporal characteristics of extreme precipitation.

Consequently, the broad research objectives were as follows:

(i) Quantification of changes in extreme precipitation characteristics over the study region.

(ii) Characterization of atmospheric states associated with extreme precipitation over the study region using Self Organizing Maps.

(iii) Verification of the the accuracy of radar-derived precipitation data for the region.

(iv) Numerical simulation of identified extreme rainfall events at very high resolutions over the region using a regional climate model.

(v) Verification of the simulated precipitation data with observed and radar-derived precipitation data and the interpretation of the results.

This dissertation is divided into seven chapters. **Chapter One** introduces extreme precipitation, observations of its changing characteristics in recent times, the regional impacts and current forecast skill levels of these events over in Africa and more specifically, Cape Town. An assessment of the characteristics of extreme rainfall in the Cape Town region is conducted here. **Chapter Two** presents an overview of the techniques used to identify extreme storms, the numerical simulation process and the use of radar in precipitation validation. Further technical descriptions of each technique are given in relevant chapters. **Chapter Three** presents the empirical technique used to identify synoptic states associated with extreme precipitation and the results from this. An additional an analysis of the occurrence of extreme precipitation in the region is performed. **Chapter Four** presents observed data obtained from weather stations in the region and notes the usefulness and short-comings of these data. **Chapter Five** assesses the quality of radar data over the region and discusses the reliability thereof as proxy data for rainfall here. **Chapter Six** presents the regional climate model and it's configuration for the high resolution simulations. Simulated temperature and wind fields are presented and discussed here. **Chapter Seven** presents the simulated precipitation fields and discusses these results. **Chapter Eight** summarizes key findings, notes some important caveats and discusses the usefulness of the methodology in the context of environments that only have access to limited computational resources.

I would like to thank a number of people and organizations who provided input to this thesis at various stages and who supported me along the way:

- The National Research Foundation and the Climate Systems Analysis Group for funding that made this work possible.
- Colleagues at the Climate Systems Analysis Group for bringing clarity to an often muddied understanding, especially Chris Jack and Ruwani Walawege.
- Karel de Waal of the South African Weather Service for invaluable assistance in understanding and interpreting weather radar data.
- Prof. Bruce Hewitson, my supervisor, and also Prof. Bill Gutowski for key academic and methodological insights.
- My friends for their encouragement when the end looked very far away.

Finally:

- My parents-in-law for the Herculean task of proof reading this work and their insightful criticisms.
- My parents, for providing the opportunity and means to pursue my dreams.
- My wife, the fulfillment of a dream, with whom I look forward to building many more.
- God, without Whom the question “Why?” would remain unanswered.

Contents

Chapter One

Introduction

1.1 Introduction

Heavy precipitation often results in flooding that is disruptive to a region's population, environment, economy and infrastructure. Red Cross estimates indicate that flooding affected more than 1.5 billion people between 1970 and 1995. Of that total more than 318 000 people were killed and 81 million became homeless (Pielke and Downton, 2000). During 1991 and 1995, flood-related damage was estimated to have accounted for 40 % of all economic damage attributable to natural disasters (IFRCRCS, 1997). Kundzewicz et al. (2006) reported the material losses of many recent individual flood events to have exceeded USD 1 billion with up to US$ 30 billion worth of damage being incurred during the summer 1998 floods in China. They further reported that during 2002, material damage on the European continent as a result of flooding was higher than in any other year. In August alone of that year, flood damage figures from risk insurance firm Munich Re totaled over €15 billion along the Danube and Labe/Elbe rivers and tributaries.

Sub-Saharan Africa is the only region of the world that has become poorer in the last generation (Ravallion and Chen, 2004) and the region is poorly equipped to cope with the effects of extreme events. Washington et al. (2004) identified, with the exception of only a few centers, a general lack of capacity for climate science in Africa. Washington et al. (2006) documented the state of climate observations in Africa as being worse than in any other continent and that this state is deteriorating. They also identified a severe lack of expertise in the area of climate science. Therefore the region is especially vulnerable to the effects of extreme events, including extreme rainfall, however the scientific research capacity here is small.

Although South Africa has a relatively advanced capacity for climate science, flooding caused by extreme rainfall often results in fatalities, damage to or loss of property and millions of rands (ZAR) worth of damage annually. Flooding may occur locally or over widespread regions depending on

the type of weather system(s). Typical flood-causing systems are tropical, sub-tropical and/or mid-latitude systems such as tropical and extra-tropical cyclones, cut-off lows and sub-tropical convective activity (van Heerden and Taljaard, 1998; Tyson and Preston-Whyte, 2000). For example, in 1981 an intense cut-off low system resulted in the deaths of more than 100 people and damage worth over ZAR10 million (not adjusted for inflation) in the arid Karoo region (Estie, 1981; Taljaard, 1985). During February 2000, the passage of two tropical cyclones in close succession resulted in the deaths of hundreds of people in the northern parts of the country, caused damage worth more than ZAR3 billion (approximately USD500 million) and farmers lost more than 50 % of their export product (du Plessis, 2002). In August 2006, a series of severe mid-latitude cyclones caused more than ZAR500 million of damage along the south coast of the country and the deaths of nine people (Fraser, 2006). The synoptic systems need not act in isolation - in February 1996 widespread flooding throughout almost the entire summer rainfall region was caused by the interaction between tropical lows, two strong mid-latitude cyclones and two ridging anticyclones (Edwards, 1997; Crimp and Mason, 1999). Thus flooding caused by extreme precipitation is a phenomenon that results in the loss of life and billions of Rands worth of damage in South Africa.

Changes in the characteristics of extreme precipitation (frequency, intensity and duration of events) have been observed globally as well as over South Africa in the last 50 -100 years. It is also very likely that these changes will continue into the future as a result of increased greenhouse gas forcing. In order to contextualize the potential and likely impact of extreme precipitation, a brief discussion of the observed changes in extreme precipitation characteristics, as well as those projected changes for the 21st century is presented below. The discussion is initially global then becomes more specific to South Africa and South-Western Cape.

It should also be noted at this point that the definition of heavy/intense/extreme precipitation is quite subjective due to the locality of climate at different locations and the nature of the research undertaken. An extreme event may be regarded as a rare, one in five or ten year event or it may also be regarded as an event that lies in the tails of the greater distribution. In 2002, the Intergovernmental Panel on Climate Change (IPCC) defined an extreme event as '...an event that is rare within its statistical reference distribution at a particular place... as rare as or rarer than the 10th or 90th percentile.' (IPCC, 2001, pg. 88). This definition is used in this study therefore extreme precipitation whose volumes fall into the 90th percentile of the distribution.

1.2 Observed and projected changes in the characteristics of extreme precipitation

Groisman et al. (2005) provide an overview of studies which documented changes in extreme and heavy precipitation at a global and regional scale. This section repeats much of the information provided in this paper but also lists additional studies to provide a context for the growing need to identify systems associated with extreme precipitation and correctly forecast them, especially in South Africa. It should be noted that in the studies referred to below, not all use the IPCC definition of extreme precipitation above.

Iwashima, T., and R. Yamamoto (1993) were the first to document changes in the characteristics of heavy precipitation. Using long-term station station data, they examined the number of extreme precipitation events at meteorological stations in Japan and found an increasing tendency in the number of extreme precipitation events. Additionally they found that more stations recorded their highest precipitation events in recent decades. Using data from 1910 to 1995 across the contiguous United States, Karl and Knight (1998) demonstrated an increase in the frequency of extreme precipitation events as well as the amount of rainfall associated with these. Groisman et al. (1999) used a model that was fitted to daily precipitation data from eight countries (Australia, Canada, China, Mexico, Norway, Poland, the United States and the former USSR) and found a disproportionate (usually positive) change in precipitation intensity whenever the mean precipitation changed. This disproportionate change was also theoretically demonstrated by Katz (1999).

Easterling et al. (2000) summarized the work of many studies to determine the change in the probability of heavy precipitation using daily data for many regions of the earth. They identified regions that experienced statistically significant changes in heavy and very heavy precipitation compared to the change in annual or seasonal precipitation and showed an increasing probability of intense precipitation events for many extratropical regions. Groisman et al. (2005) extended this work and provided more information for the Americas (Fig. 1). Notable for the purposes of this study are the significantly positive changes at the three southern African stations.

Frich et al. (2002) investigated a global dataset of derived extreme climate indicators and found those derived from wet spells and the number of heavy rainfall events (based on daily precipitation

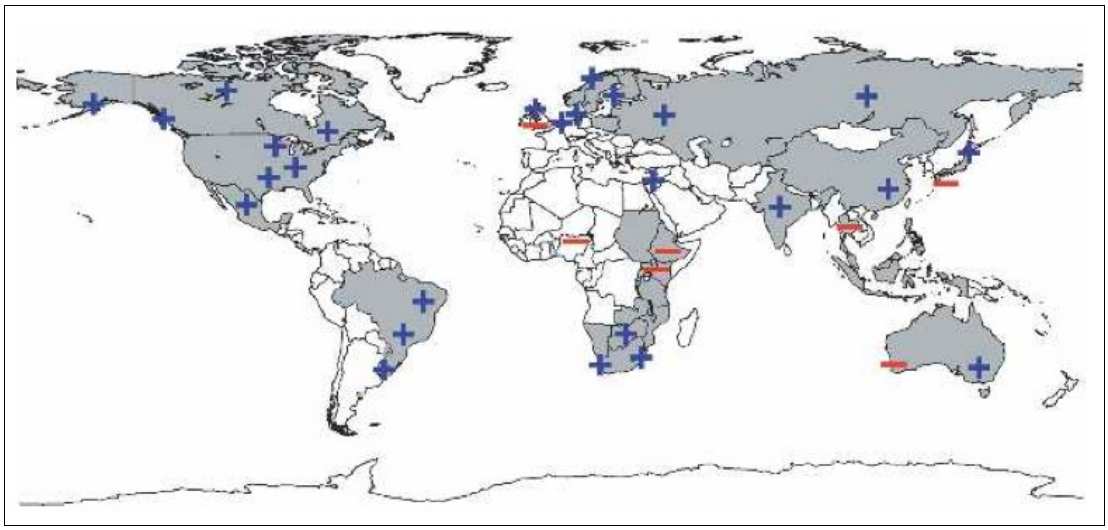

Fig. 1.1 Regions where disproportionate changes in heavy and very heavy precipitation during the past decades were documented compared to the change in the annual and/or seasonal precipitation. Plus and minus signs indicate regions where significant changes in heavy precipitation have occurred during past decades. Shaded regions indicate statistically significant changes. From Groisman et al. (2005).

data) displayed significant increases in the extreme amounts. This type of increase has been observed over many regions of the earth, e.g. the United Kingdom (Osborn et al. (2000) and Osborn and Hulme (2002)), Europe (Klein-Tank and Koennen (2003)), Nigeria (Tarhule and Woo, (1998)), Australia (Suppiah and Hennessy (1998)), China (Zhai et al. (1999)), the USA (Groisman et al. (2001)), Canada (Zhang et al. (2001)) and India (Roy and Balling (2004)). These studies also indicated that at a regional scale, statistically significant changes in the rainy season have generally been accompanied by relative changes in heavy precipitation that are of the same sign of and stronger than changes in the mean.

More recently, Groisman et al. (2005) empirically assessed the observed changes of intense precipitation in the twentieth century. They found that in the mid-latitudes there was a widespread increase in the frequency of very heavy precipitation over the last 50 – 100 years. Their results for South Africa were in agreement with Mason et al. (1999) who found significant increases in the intensity of extreme rainfall events between 1931–1990 over about 70% of the country. Additionally, they reported the intensity of the 10-year high rainfall events had increased by over 10% over large areas of the country with the greatest percentage increases in the intensity of high rainfall events being for the most extreme. Easterling et al. (2000) showed a statistically significant positive trend in extreme precipitation over the South-Western region of South Africa. In examining daily climate data over southern and western Africa, New et al. (2006) found evidence of statistically significant positive trends in extreme precipitation in regionally averaged daily rainfall

intensity. They also found that although there was an indication of decreasing total precipitation, this was accompanied by increased average rainfall intensity which was concentrated on extreme precipitation days. Thus there is evidence that the characteristics of extreme precipitation both globally and over South Africa has changed over the last 50-100 years to have become more frequent and intense in most extra-tropical regions. Many studies have documented the cause of this as an overall increase in intensity of extra-tropical cyclones in the southern hemisphere through a poleward shift of baroclinicity (e.g. Lambert, 1995; Kushner et al., 2001; Lin and Simmonds, 2002; Fyfe, 2003; Gillet et al. 2006). It is also likely that the characteristics of extreme precipitation over the region will continue to change in intensity, frequency and duration as a result of global warming.

In addition to the evidence of the observed change in the extreme precipitation characteristics, there is also a growing body of literature that indicates that as the global temperature increases as a result of the increase in greenhouse gas concentrations in the atmosphere, further changes in the characteristics of heavy precipitation are likely. Groisman et al. (2005) also analyzed output from three GCM simulations that had transiently increasing greenhouse gases during the twenty-first century and indicated an increased probability of heavy precipitation events for many extratropical regions, including South Africa. An increasing number of model projections have demonstrated this globally as well as regionally, e.g., Zwiers and Kharin, (1998); Meehl et al., (2000); Cubash et al, (2001); Allen and Ingram, (2002); Semenov and Bengtsson, (2002); Giorgi et al., (2004); Kim (2005), Tebaldi et al., (2006). Over the southern African region, Mason and Joubert (1997) showed the frequency and intensity of extreme daily and prolonged (five-day) rainfall events increased under doubled-CO_2 conditions over the southern African region, even in areas where decreases in mean annual rainfall were simulated. Largest increases in the severity of flood events were exhibited over the winter rainfall region, which includes the western Cape.

In the IPCC's Fourth Assessment Report, observed long term changes in extreme weather and climate were presented in the summary for policy makers (IPCC, 2007). These changes have been observed in precipitation fields as an increased frequency of heavy precipitation events over most land areas. The report further states that it is “very likely” (a likelihood of an occurrence of 90 %) that extreme events will become more frequent in the future with increased greenhouse gas concentrations.

Thus, observed changes in the characteristics of extreme precipitation indicate that these have become more frequent and more intense. Projections into the twenty first century indicate that this historic trend is very likely to continue into the future. Given this apparent inevitability, and the poor state of climate science in Africa, it is vitally important to increase the understanding of factors that influence regionally specific extreme precipitation. These factors include relationships between synoptic scale circulations and local extreme precipitation, changes in the historical characteristics of extreme precipitation and their associated synoptic circulations, the effect that topography has on extreme rainfall fields and validation techniques in data sparse environments. Additionally, accurate, qualitative forecasts are needed where these are poor or provide limited regional detail of extreme precipitation.

1. 3 Extreme precipitation in the South-Western Cape

In the greater Cape Town region of the South-Western Cape, extreme precipitation often leads to flooding that affects thousands of people annually. Approximately 23 % of the population in this region live in informal shelters (loosely constructed tin and wood shacks) in an area called the Cape Flats (Boraine, 2004). For these populations severe flooding causes devastating loss through the destruction of dwellings and loss of goods. An example of the effect that flooding has in these settlements is presented below as further motivation for a qualitative forecast across the region. The characteristics of rainfall and extreme rainfall in the South-Western Cape are first described after which the impact that flooding had on the region's population and economy during severe storms experienced in the winter of 2001.

The South-Western region of South Africa experiences a Mediterranean climate with warm, dry summers and colder, wet winters. Most of the rainfall here occurs between May and September when the South Atlantic anticyclone moves north-westwards, which facilitates a northward shift of eastward tracking mid-latitude (extra-tropical) cyclones to influence the regions weather. As the fronts propagate eastwards, the topography of the region modifies downstream weather at the mesoscale through the action of the Cape Peninsula as well as the Hottentots Hollands mountain range (Fig. 1.2). When the extra-tropical cyclones are particularly intense they are associated with gale force winds and very heavy rainfall. The unique topography of the Cape Peninsula also serves to enhance precipitation in it's lee. It is under these circumstances that the Cape Flats region, in the lee of the Cape Peninsula, is severely effected by extreme flooding and high winds.

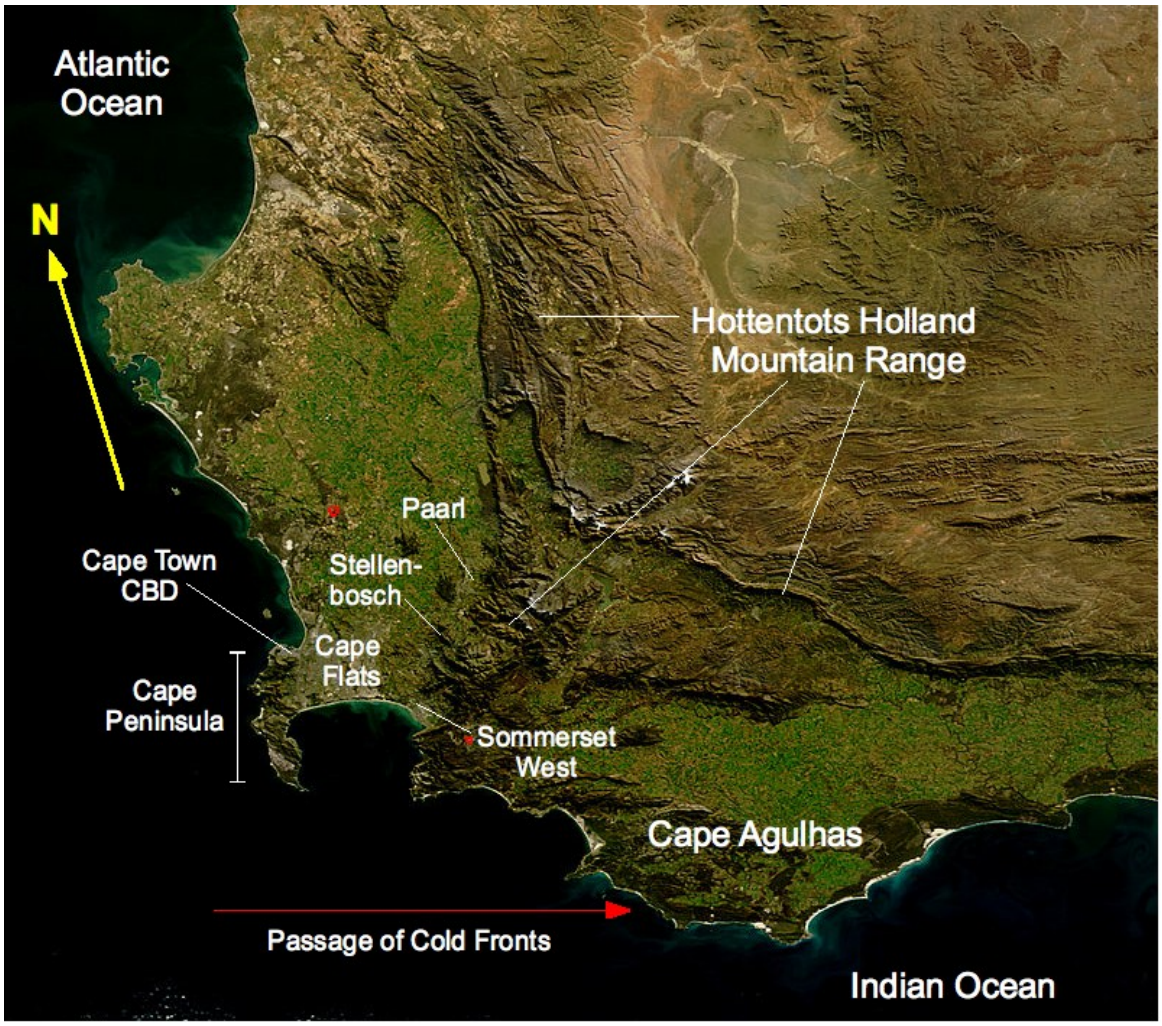

Fig. 1.2 Satellite image of the western most region of the Western Cape. Snow can be see over the high lying regions of the Hottentots Holland mountain range and the small areas in red outline show fire locations that day. The image was obtained from NASAs MODIS Rapid Response System website (http://rapidfire.sci.gsfc.nasa.gov). The locations of some towns where weather stations are situated are included. A more detailed map of the Cape Peninsula is presented in Chapter 4 which also shows the locations of other weather stations.

In the greater Cape Town area, extreme mid-latitude cyclones result in localized flooding that affects thousands of people each year, the majority of these being the very poor who live in flood prone informal settlements on a region called the Cape Flats. For example, during the winter of 2001, Cape Town was affected by several extreme mid-latitude cyclones that caused tremendous flood damage and displaced many thousands of people. In July and August of that year, the Cape Town International Airport recorded well-above-average rainfall figures of 198 mm in July and 97 mm in August. These were almost 220 % and 126% their respective monthly climatologies of 82 mm and 77 mm. During July, six mid-latitude cyclones passed over the region in six days and and

deposited 80% of the recorded monthly rainfall. The Cape Town City Council estimated 31 000 people to have been affected by the storms, including 8 000 homesteads. A total of 5 529 people were displaced and had to be housed and fed in care centers that were set up in various communities. The situation deteriorated to such an extent that a large portion of the City of Cape Town was declared a disaster area by the President of South Africa. The total financial cost of these storms, including humanitarian aid (feeding, bedding and other immediate needs) and provision of basic household necessities (to re-establish homesteads) was estimated at more than USD2 000 000.

1.4 Trends in extreme precipitation in the Cape Town region.

The studies listed above, e.g. New et al. (2006), Groisman et al. (2005) and Easterling et al. (2000), show that historically there has been an increase in the frequency and intensity of extreme rainfall in many regions of the world, including the Western Cape region of South Africa. However, the nature of these studies does not facilitate the inspection of the localized expression of extreme precipitation in a region. They, of necessity, have used one station to represent an entire region, which in the case of the south-western Cape is at Cape Town International Airport. However, the weather, and thus expression of extreme precipitation in Cape Town is highly modified by the topography of the region and should not bet expected to be homogeneous across the region. It is therefore necessary that data from all weather stations in the region be considered in assessing the characteristics of extreme precipitation at the scale of a city metropole.

Precipitation data from stations in the greater Cape Town region for which there were adequate data were used to examine characteristics of precipitation and extreme precipitation in the region. Unfortunately only three stations had an adequately long data record. However, these are situated in topographically distinct locations which allowed for an analysis of rainfall in the immediate lee of the peninsula (Simonstown), the Cape Flats (Cape Town International Airport) and at the foot of the Hottentots Holland mountain range (Paarl). Data were available from 1950-2006 for the Airport and Paarl and 1963-2006 for Simonstown. Various metrics of the 90th percentile rainfall were examined. These included annual, monthly of and decadal trends in extreme monthly rainfall.

A large degree of heterogeneity was shown in the trends of extreme rainfall between the three stations. Annual trends, both in terms annual frequency of extreme rainfall events and intensity of

rainfall varied. At the Airport (CTIA), the number of extreme rain days per year shows a decrease from 11 days per year to 7.5 days per year (Fig. 1.4) over a 57 year time period. At Paarl there was also a decrease in the number of extreme rain days per year but this was smaller than at the Airport. The Simonstown station show an increase from 9 days of extreme rainfall per year to 11 days. These trends, however, were not significant at the 95 percent level. The change in extreme rainfall days per year are echoed in the amount of extreme rainfall received by each station per year. The Airport and Paarl show a decrease whereas Simonstown shows an increase. From the the slope of the regression lines, the Airport receives 101 mm less extreme rainfall today than it did in 1950 whereas Simonstown receives 98 mm more as extreme rainfall today than it did in 1963. Paarl displays very little change in extreme precipitation volumes, the difference between 1950 and 2006 being less than 1 mm. The trends at the Airport and Simonstown are significant at the 95 percent level ($p=0.043$ and $p=0.041$). Thus the Airport currently experiences significantly less annual 90^{th} percentile precipitation volumes than at the start of the data record whilst Simonstown receives significantly more.

In order to assess changes in extreme precipitation at an interannual resolution, 90^{th} percentile data were extracted for each month of the time series. The resulting data were used to produce monthly trends at a decadal scale at each station in terms of the number of extreme rain days and extreme rainfall volumes per month per decade. The change in the number of days per month per decade that experienced extreme rainfall were very small, of the order of 0.1 days per decade. Thus, there does not seem to be any change in the frequency of the occurrence of extreme rainfall at these three stations. However, changes in the amounts of monthly extreme rainfall these stations receive are evident. The Airport shows a decrease in extreme rainfall amounts per decade from April – August ranging between 2-5 mm per month per decade (Fig. 1.5). Considered together, these months account for a 19 mm decrease in extreme rainfall per decade which over 5 decades is almost 100 mm less extreme rainfall, as seen above. On the other hand, the Simonstown station show increases of extreme rainfall days and intensity for April, May and July and small decreases in June and August. The July data at this station display the highest absolute number of the three stations in terms of change in extreme rainfall volume per decade. The Paarl station recorded a large negative change in rainfall intensity during April and May and smaller increases during July and August.

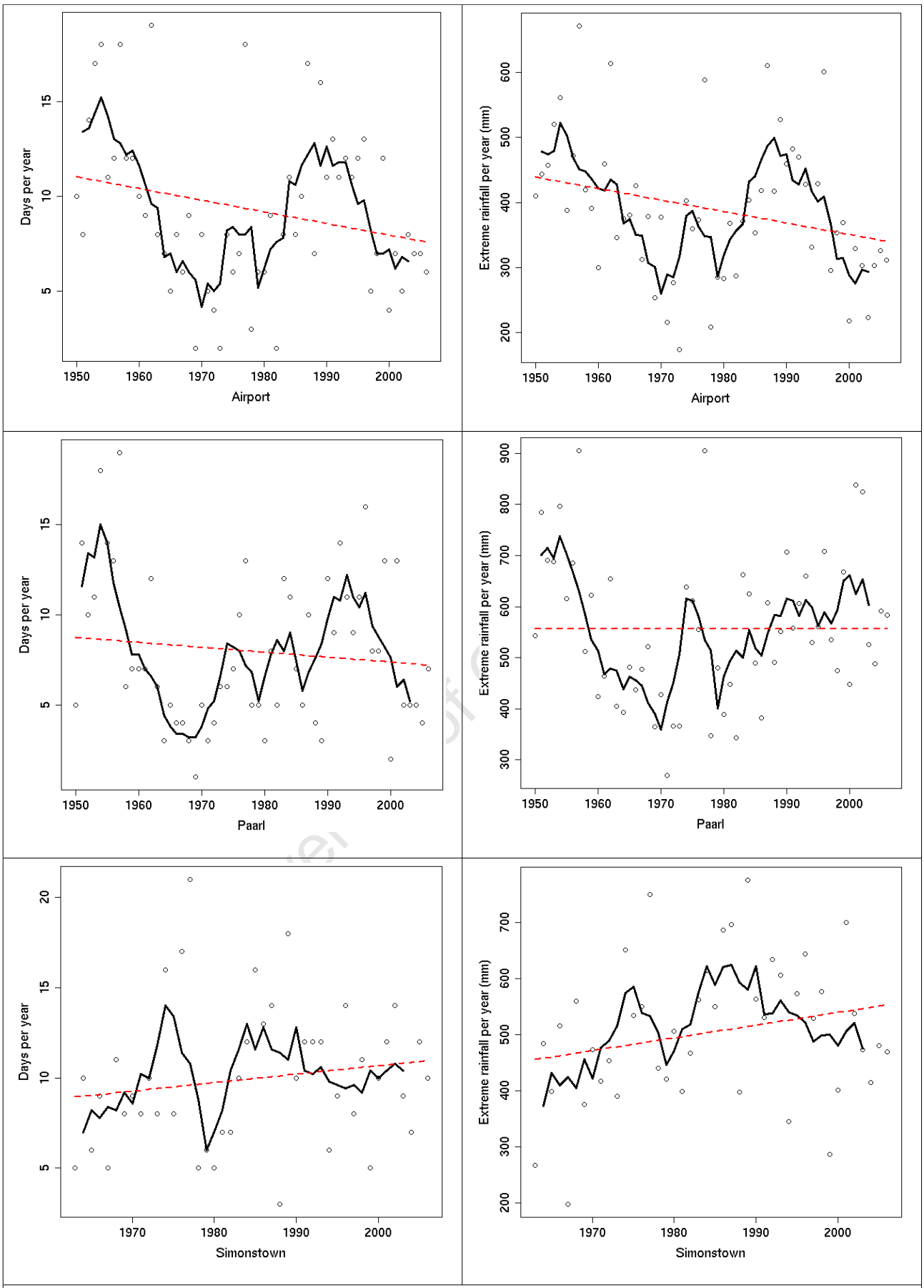

Fig. 1.4. Changes in annual extreme precipitation events and annual extreme precipitation amounts. Annual values are points, the solid line is a 5-year running mean and the red dashed line is a regression line.

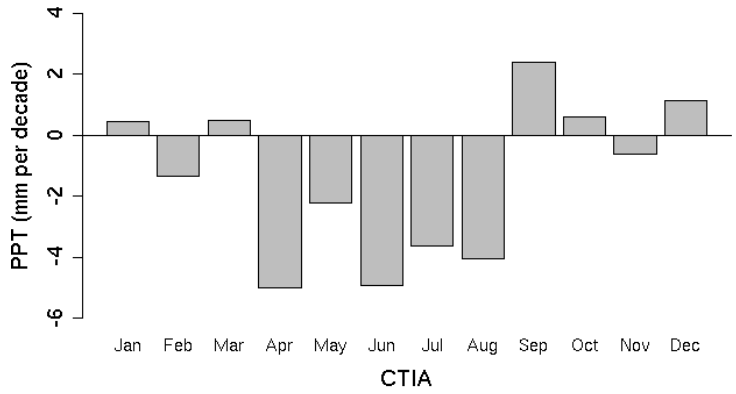

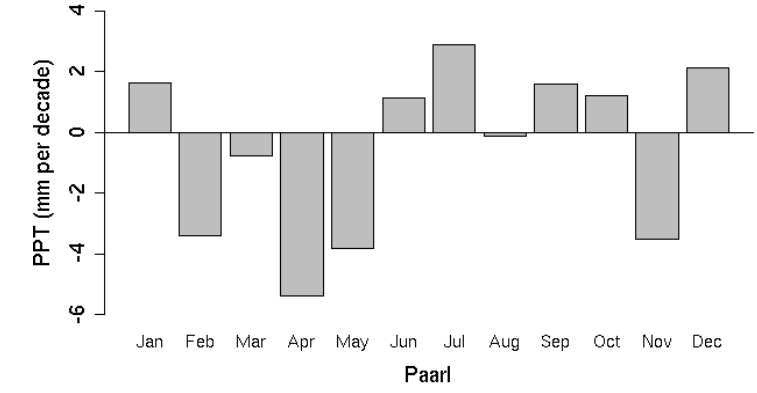

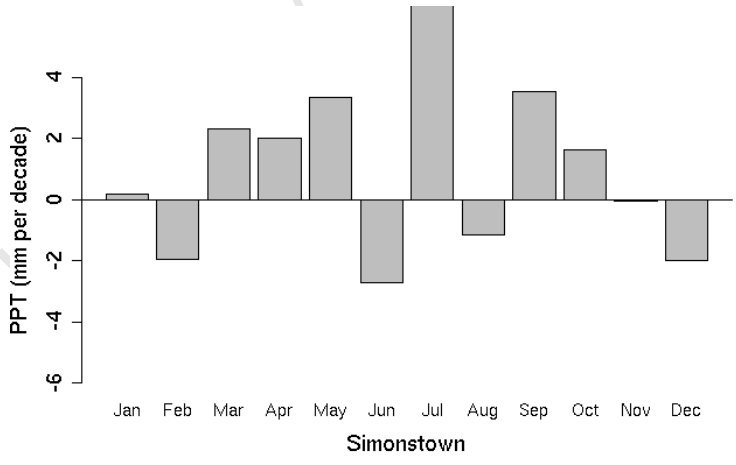

Fig. 1.5. Changes in decadal monthly rainfall volumes of 90th percentile rainfall amounts at the three stations.

A change in the seasonal characteristics of extreme rainfall is evident in all three stations. April shows a large decrease in the amount of extreme rainfall it receives per decade, only Simonstown having a small positive change. In September, all three stations show an increase in the amount of extreme precipitation they receive. All three stations do not indicate a change in the number of days

displaying extreme precipitation for either April or September. This indicates a shift in the seasonality of extreme rainfall in the region to having higher intensity events later in the traditional winter months and also persisting into the early spring.

In order to examine changes in the characteristics of the most severe of extreme rainfall, this decadal analysis was also performed on 99th percentile data. No changes in the frequency of these events were evident at any of the stations. However, intensity changes were present. The Airport show a decrease in the intensity of events of 2 mm per month per decade in April and May and an increase of similar magnitude during June and July (Fig. 1.6). Unlike the 90th percentile rainfall, the changes here are not homogeneous across months with the months that climatologically receive the most rainfall (June and July) showing an increase in the rainfall received through the most severe of extreme events. Paarl shows a large increase in the amount of very extreme rainfall it receives during June and August and to a lesser extent April and September. There are large decreases evident in May and July. The increases in April and August are opposite to the 90th percentile changes for these months indicating an increase in the amount of precipitation received as very severe rainfall despite there being less overall extreme rainfall. The opposite is evident for July which shows an increase in 90th percentile rainfall but a decrease in very severe extreme precipitation. The Simonstown station shows large increases in May and July (3 and 5 m per month per decade) and a large decrease of 3.5 mm per month per decade in August. The signs of the decadal changes match those of the corresponding 90th percentile data, however, the August decrease is the only notable decrease in the winter months. Thus Simonstown shows an increase in the amount precipitation received from both 90th percentile and 99th percentile rainfall. The intraseasonal shift in 99th percentile rainfall is not as evident in the 90th percentile rainfall amounts. April shows increases at Paarl and Simonstown but not at the Airport, however, September still shows an increase at all stations. Precipitation occurring as very extreme rainfall has increased in the late winter-early spring season at all three stations.

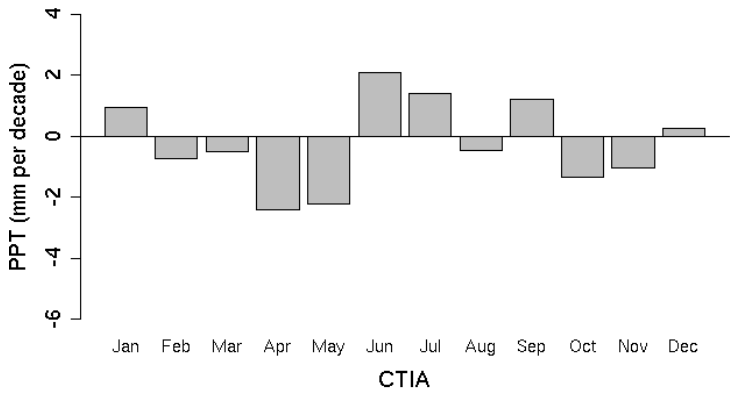

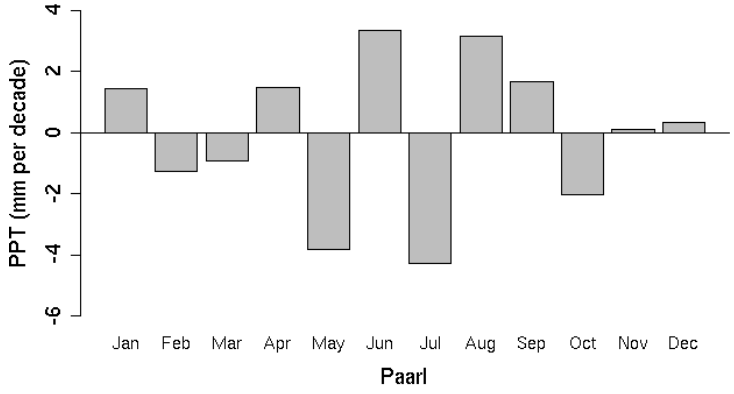

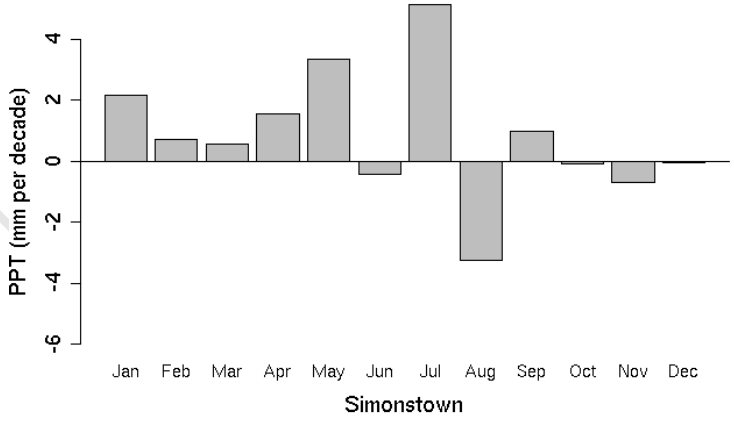

Fig. 1.6. Changes in decadal monthly rainfall volumes of 99th percentile rainfall amounts at the three stations.

In summary, station data from these three stations showed mixed trends in extreme rainfall. The Simonstown station, located in the lee of topography, showed a significant increase in the intensity of extreme rainfall as well as 99th percentile. The Airport, a relatively topography-free location,

showed a significant decrease in the intensity of extreme rainfall. No significant trend was evident at Paarl. No station showed significant trends in the number of extreme rainfall days. Decadal changes in monthly precipitation shows a shift in the start and end of the extreme rainfall season to starting later in winter and continuing into the early spring. This was evident at all three stations.

In the light of these long-term changes, it is necessary for a forecast of extreme precipitation to capture the spatially heterogeneous nature of the precipitation in the region which means it has to be run at very high resolution. However, the forecast of severe precipitation in South Africa, let alone the Cape Town region, is often not well captured (Banitz, 2001) and Du Plessis (2002) found little evidence of a formal flood forecasting, warning and response system in the country. Landman et al. (2005) tested the predictability of extreme seasonal precipitation over South Africa and achieved low skill levels temporally in the winter and spring seasons and spatially over the South-Western Cape. Over this region an accurate forecast of extreme precipitation does not seem to be readily in evidence.

The effect extreme storms have on the local population forms an important motivation for this study. Due to primarily the human, but also the environmental and economic impact these severe storms have on the region, an improved understanding of the processes associated with extreme precipitation is necessary. This would facilitate an improved preparedness of local populations and disaster management resources, as well as benefit other sectors such as aviation, ground transportation, electrical networks, construction, environmental management etc.

1.4 Thesis objectives

In order to advance the understanding of extreme precipitation in the greater Cape Town region, this research adopted three stages. The first investigated the linkage between synoptic scale circulations and regionalized extreme precipitation using an empirical technique that identified archetypal synoptic states in climatological data associated with extreme rainfall in the region. This also provided a means to identify days whose synoptic states were associated with extreme precipitation which facilitated the second stage which was an assessment of the changes in the frequency and intensity of extreme precipitation in the region. This assessment used gridded as well as weather stations in the greater Cape Town region. The third stage utilized a regional climate model run at a

resolution of one kilometer to investigate the spatial and temporal characteristics of extreme rainfall at the very localized scale and the topographic modification of the precipitation field. The simulated precipitation data were validated against observed and radar-derived precipitation data.

These approaches facilitate the description of the changing characteristics of extreme precipitation in a very localized context and offers a potential methodology, that is computationally relatively inexpensive, for the identification and high resolution simulation of severe storm environments. It is therefore accessible in an African context where the capacity for conventional high resolution forecasts is small as only days with synoptic states historically associated with extreme rainfall need be simulated at very high resolutions.

There are three distinct techniques employed to this end: (1) the identification of weather systems associated with extreme rainfall using an empirical technique, (2) the numerical simulation of extreme rainfall events at high resolution using a regional climate model and (3) a validation of the simulated extreme precipitation against observed and radar data. As a result of the devastating effects the series of storms in July and August 2001 had over the Cape Town region, it would be expected that such extreme precipitation would be identified by the empirical technique. Thus days in these months were used as case studies for the SOM and regional model.

In the Methodology chapter that follows, a brief overview and description of each technique is presented, together with a motivation for the use of that technique. Complimentary to the Methodology chapter is a technical description of each technique in the respective chapter that presents the results. It was deemed more appropriate to place the technical description here as it is informative to decisions taken in the configuration of each methodology.

Chapter Two

Methods

2.1 Introduction

A methodology is presented that uses three distinct techniques to identify extreme precipitation environments, simulate these at high resolution and assess the simulated results. In the first, an empirical technique was used to identify synoptic environments associated with extreme precipitation, after which individual days were allocated to the respective synoptic states. In the second, days identified by the empirical technique as being associated with extreme precipitation were simulated at very high resolution using a regional climate model. The third technique was one of validation in which the simulated precipitation was tested against observed and radar-derived precipitation data to assess spatial and temporal accuracy of the simulated fields. This chapter provides an overview of these three techniques and also serves as a motivation for their usage. As the techniques are distinct, a more detailed technical description of each is contained at the beginning of each respective results chapter.

2.2 Investigating extreme precipitation in the Cape Town region

Precipitation data from stations in the greater Cape Town region for which there was adequate data were used to examine characteristics of precipitation and extreme precipitation in the region. Unfortunately only three stations had an adequately long data record but were placed in topographically distinct locations which allowed for an analysis of rainfall in the immediate lee of the peninsula (Simonstown), the Cape Flats (Cape Town International Airport) and at the foot of the Hottentots Hollands range (Paarl). A suite of statistical analyses were performed using the R statistical package which examined characteristics in the rainfall records and included the full rainfall record, 90^{th}, 95^{th} and 99^{th} percentile rainfall and various metrics of these.

2.3 Identification of extreme rainfall circulations using self organizing maps

The spatial characteristics of synoptic states associated with extreme precipitation can be classified to facilitate the examination of these systems and provide an assessment of their frequency distribution. A large number of classification methodologies, which involve grouping or clustering, are available and can be correlation- or eigenvector-based (Yarnal, 1993). Correlation-based methods are used mainly for map pattern classification, which is usually based on patterns formed by one variable, such as surface pressure. The eigenvector approach can also be used for this and additionally for synoptic type classification. This approach is used in this study.

Within the eigenvector approach is the principal component analysis (PCA), a technique which is used often in studies involving precipitation regionalization (Ehrendorfer, 1987; Andres et al., 2000) and classification (Harrison, 1984). This method clusters data into groups that have minimal differences within the group and maximum differences between groups. There is thus an imposition of artificial boundaries on data, which are essentially a continuum, resulting in a generalization of synoptic types. As extreme events are often not restricted to a single synoptic type, this method is disadvantageous in this context. An alternative method, which treats the data as a continuum, is that of empirical downscaling through the use of artificial neural nets (Hewitson and Crane, 1992; Hewitson and Crane, 1994). Reusch et al. (2005) investigated the relative performance of artificial neural networks (ANNs) and PCA in extracting patterns from synthetic climatological data and concluded that the ANN based approach was more robust and was able to isolate pre-defined patterns with correct attribution of variance.

Artificial neural networks are networks of highly interconnected neural computing elements that can respond to input stimuli and learn to adapt to the environment (Patterson, 1996). An ANN is comprised of a large number of neurons (cells or nodes) which are the simple processing elements. Each of these nodes are connected to the other nodes and have corresponding weights which act to increase or decrease the input signal to the next node. An ANN is characterized by its architecture (pattern of connections), its training or learning algorithm (method determining the weights on each connection) and its activation function (Fausett, 1994). The application of ANNs spans a variety of fields requiring pattern recognition (e.g. Fausett, 1994; Patterson, 1996; Tarassenko, 1998) and recently have even been used to predict the box-office success of motion pictures (Sharda and Delen, 2006). Figure 1 shows the topology of simple ANN which demonstrates the flow and

training of data from the input layer, through the processing (hidden) layer to the output layer.

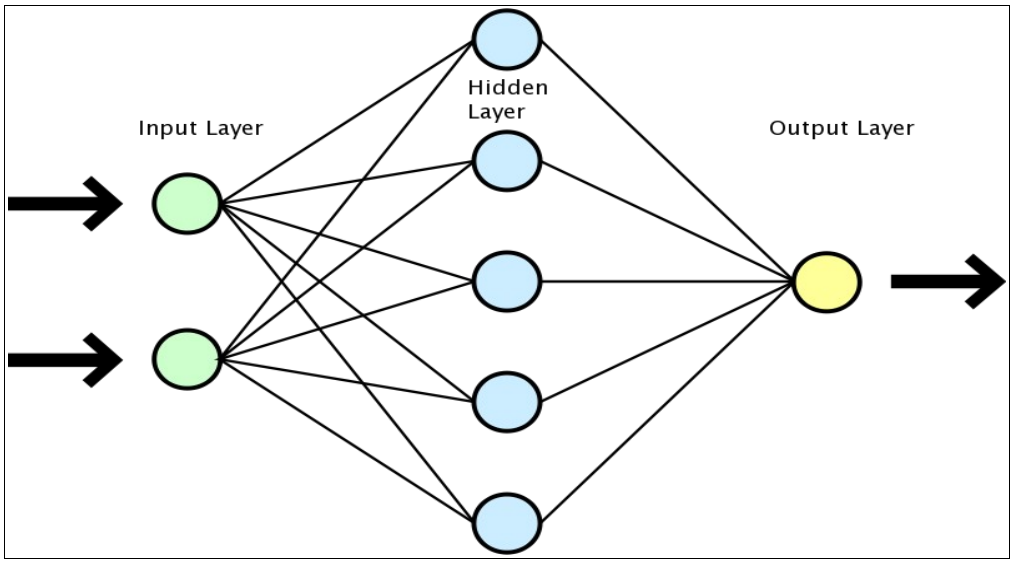

Fig. 2.1 A simple ANN topology with training nodes in one hidden layer. There may be multiple hidden layers and multiple connections between nodes as well as multiple output nodes in the output layer.

The ability of ANNs to handle large volumes of data, process these quickly and detect patterns in (often noisy) data is an important benefit to the field of climatology. Since the introduction of ANNs to climatology (Hewitson and Crane, 1994), they have been used in a number of research projects (Badran and Thiria, 1991; Hewitson and Crane, 1992; Bankert, 1994; Navone and Ceccatto, 1994; Marzban and Stumpf, 1996; Gardner and Dorling, 1998). Amongst the many methods that exist in using ANN technology is that of self-organizing maps (SOMs).

Self organizing maps were initially developed by Kohonen (Kohonen, 1995) and provide a technique that identifies dominant modes within a dataset such that the distribution of these modes within the data space represents the observed distribution. A number of disciplines make use of SOMs for data analysis e.g. cardiology (Joutsiniemi et al., 1995), audiology (Palakal et al., 1995) and organic chemistry (Chen & Gasteiger, 1997). In a climatological context, the SOM represents these modes visually as an array of atmospheric states (synoptic archetypes) that span the data space and are clustered according to spatial patterns. The examination of variance within each mode is also possible.

Although their use in the field of climatology is still developing, a number of studies have already

been undertaken: Hewitson and Crane (1994, 2002, 2005); Eckert et al. (1996) used SOMS to classify meteorological forecasts; Main (1997) used SOMs to categorize observed and GCM-derived sea level pressure data; Cavazos (1999, 2000) used SOMs for climate classification and Ambroise et al. (2000) for cloud classification. Hope et al. (2006) used SOMS to show historic shifts in the synoptic systems that influence southwest Western Australia and Hope (2006) projected future changes over the same region. Other climatological studies which used SOMs include Hudson (1998), Gutowski (2001) and Tennant (2002). An example of a SOM, taken from Hope et al. (2006), is shown in Fig. 2.2 which presents 20 archetypal sea-level pressure circulations for southwest Western Australia between the years 1948-2003.

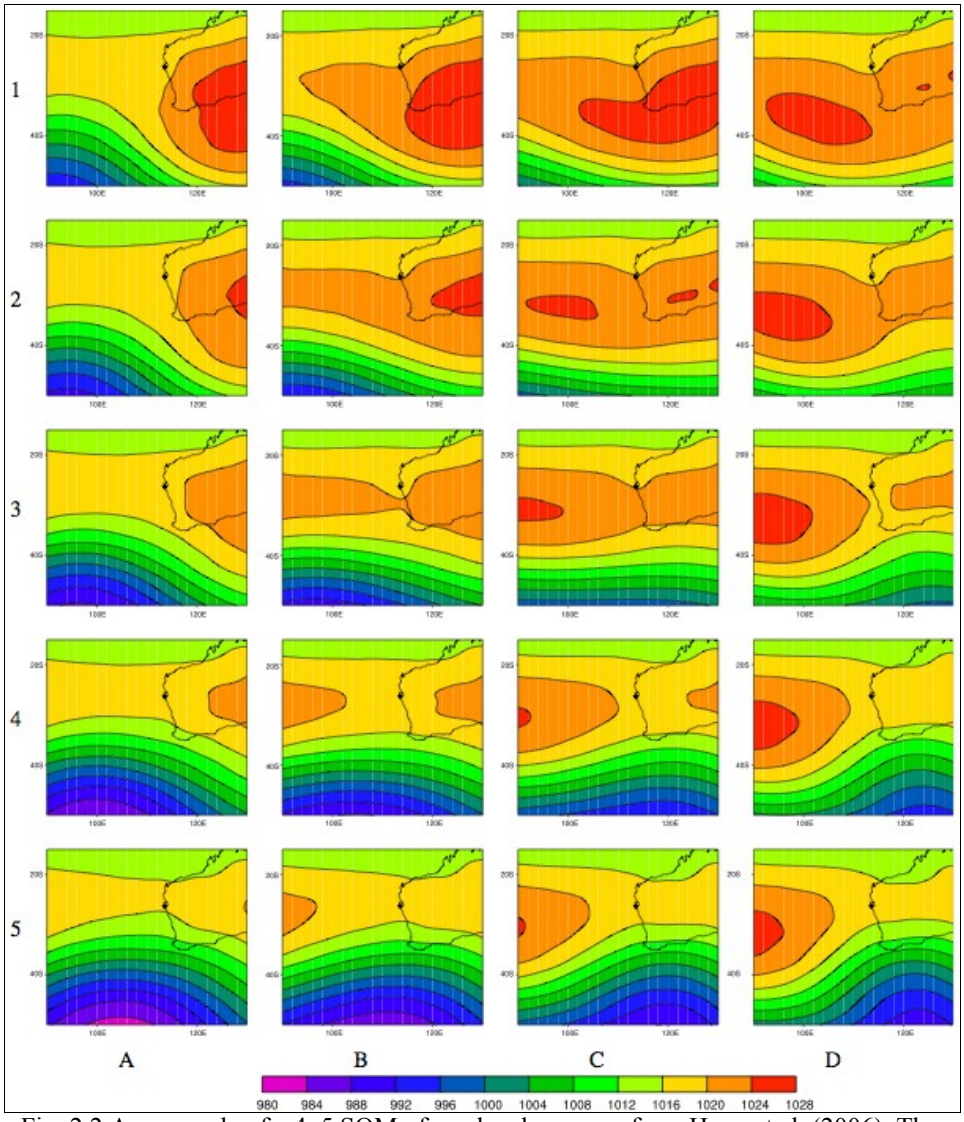

Fig. 2.2 An example of a 4x5 SOM of sea-level pressure from Hope et al. (2006). The SOM generated 20 archetypal synoptic circulations of SLP between 1948 and 2003 over southwest Western Australia where the reds indicate high pressure and the blues lower pressure. The SOM was compiled using twice daily NCEP/NCAR reanalysis SLP data.

The aims of using the SOM were threefold. First, the SOM technique was used to identify archetypal synoptic states that were associated with extreme precipitation over the greater Cape Town region and to examine the spatial and temporal characteristics of these states. Secondly, the SOM provided a means to identify days whose synoptic states were associated with extreme precipitation which facilitated an assessment of the changes in the frequency of extreme precipitation and the associated synoptic circulations in the region.

The SOM-based assessment of changes in the characteristics of extreme precipitation used gridded data of 50 km. This is therefore not able to capture changes at the very local station scale, which will reflect topographic weather modification. Thus, precipitation data from stations in the greater Cape Town region for which there were adequate data were used to examine characteristics of precipitation and extreme precipitation in the region. Unfortunately only three stations had an adequately long data record but were situated in topographically distinct locations which allowed for an analysis of rainfall in the immediate lee of the peninsula (Simonstown), the Cape Flats (Cape Town International Airport) and at the foot of the Hottentots Hollands range (Paarl). Characteristics examined included the full rainfall record, 90th, 95th and 99th percentile rainfall and various metrics of these.

Thirdly information obtained from the SOM was used to identify days which experienced extreme precipitation that caused widespread flooding in the Cape Town region. These days were simulated at high resolution using a regional climate model (RCM). The section following describes the development of RCM's and motivates for their suitability in this study.

2.4 General Circulation Models and Regional Climate Modeling

Early Atmospheric General Circulation Models (AGCMs) were designed for short-term weather prediction. In the 1950s and 1960s, as integrations over longer periods became necessary, numerical prediction schemes were formulated and the term General Circulation Model (GCM) was introduced. The first AGCM, developed by Phillips (1956), was a quasi-geostrophic two-layer hemispheric model which could capture zonal flow and mid-latitude eddies. Smagorinsky (1963) contributed to the advancement of GCMs in his development of a two-layer model that solved

primitive equations for a 60 day period in the region between the equator and 64^{o} latitude which included planetary waves and kinematics of a sphere. As AGCMs developed in a climate change context, the term GCM could be understood as general circulation *climate* model (Henderson-Sellers and McGuffie, 1987). Since this time models have grown substantially through improvements in computational facilities and capabilities (Pixoto and Oort, 1992).

The modern GCM solves a series of equations having prescribed initial boundary conditions, physical constants and parameterized sub-grid scale processes. Parameterization implies the minimum scale at which a process can be resolved and includes features such as clouds, for example, which are very important to the energy budget of the model, but are sub-grid scale and therefore difficult to represent realistically. Clouds, along with the hydrological balance over the land surface and the surface oceanic heat flux have been identified as the primary uncertainties in GCMs (IPCC, 1996).

GCMs have been used over the last decade for projections of a possible future climate and are the only quantitative tools available for this (Trenberth, 1996). A climate model is used in future climate studies to ascertain whether or not the perturbation of certain model parameters has a significant effect on the climate (Henderson-Sellers and McGuffie, 1987).

More recently, there has been a rapid increase in coupled ocean-atmosphere general circulation models (AOGCMs). Representation of the ocean in coupled models is in one of the following forms: a swamp ocean with no heat storage or ocean currents, a slab mixed-layer ocean with no ocean currents but some heat storage, or a dynamical ocean GCM where there is heat storage, upwelling and ocean currents. The last of these three is computationally intensive, yet potentially the most powerful tool for studying the global climate (Meehl, 1992). The development of more accurate coupled models has been a primary focus for some time, since it is generally accepted that these models will provide better scientific understanding of climate and climate change (IPCC, 1996).

The IPCC Second Assessment Report (SAR) published in 1996 describes in detail the use of climate models as the main tool available for developing projections of climate change into the future. The AOGCMs provide good descriptions of climate on scales larger than the horizontal resolution. However, regional climate is often affected by forcings and circulations that occur at the sub-AOGCM horizontal grid scale (e.g. Giorgi and Mearns 1991). Thus, AOGCMs are not able to

provide a detailed description of current climate (or detailed projections of likely climate change) on spatial scales smaller than the horizontal resolution, nor explicitly capture the fine scale structure that characterizes climatic variables in many regions of the world.

In order to capture these finer scale features, GCMs would have needed to be run at much higher resolutions. This, however, is impractical as computational cost becomes too high. The computational cost of an atmospheric model is a function of the number of cells in the domain and the time step which behaves as a function n^3, where n is a grid dimension. Thus a doubling of resolution results in an eight-fold increase in computational cost. In order to provide regional structure, it was proposed by Dickinson et al. (1989) and Giorgi (1990) that limited area models (LAMs) be nested in GCMs to 'downscale' from the course GCM resolution to a finer, regional resolution (Fig. 2.2). Large-scale meteorological fields from GCM simulations are used to provide initial and time-dependent meteorological lateral boundary conditions for high resolution LAM simulations.

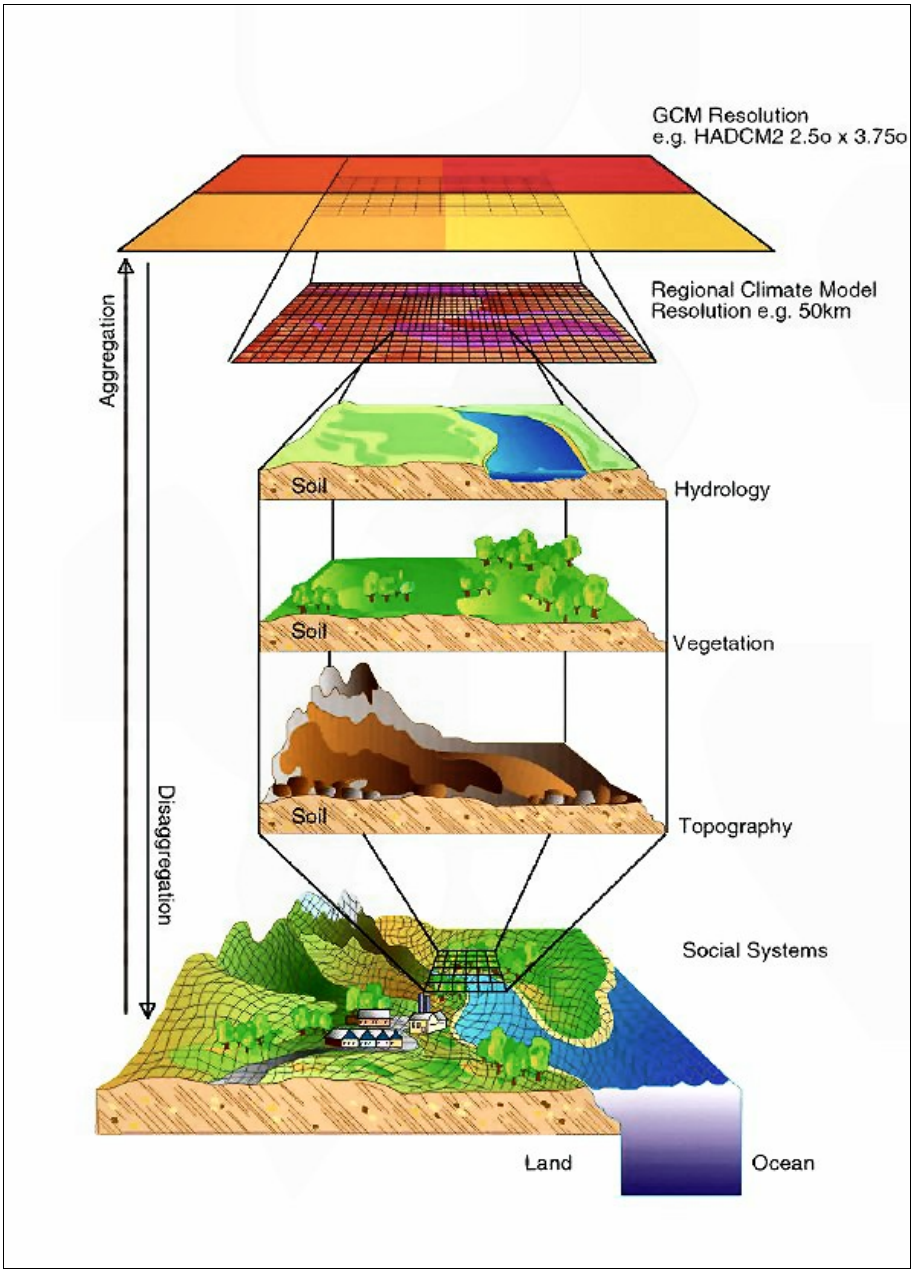

Fig. 2.3 Schematic representation of the downscaling principle. Here data from a GCM of 2.5 x 3.75 degree resolution is downscaled to a resolution of 50 km. The process takes into account hydrology, vegetation responses, topography, land/sea processes and social systems at the higher resolution. Image courtesy of the UK Met. Office (http://www.metoffice.gov.uk).

There are a number of LAMs, or regional climate models (RCMs), that have been used in a variety of different meteorological applications. These range from paleoclimate studies to modeling of present day climate characteristics and possible future climate states. Regional climate models have been used as research tools to advance the understanding of regional-scale processes and help develop parameterizations of these processes for use in large scale weather forecast and climate prediction models. Regional models are already being used for real time simulations at high

resolutions by various institutions for operational forecasts of regional weather[1,2] (Horel and Gibson, 1994, Mass and Kuo, 1998), forest fires (Smallcomb 2001) and air pollution (Fast et al. 1995; Sistla et al. 2001).

A partial list of the application of RCMs, modified from Jones et al. (2002), is given below:

1. Operational numerical weather prediction and analysis, forcing a RCM with a global model prediction (e.g. White et al., 1999)
2. Seasonal prediction (e.g. Cocke and LaRow, 2000)
3. Reconstruction of recent regional climate (e.g. Machenhauer et al., 1996; Christensen et al., 1997, 1998; Noguer, 1998) as well as paleoclimate (Hostetler et al., 1994, 2000)
4. Climate change projects (e.g. McGregor and Walsh, 1994; Giorgi et al., 1998; Jones et al., 1997; Machenhauer et al., 1998; Laprise et al., 1998; Durman et al., 2001) and the detection of historical anthropogenic climate change on a regional scale (Zwiers and Zhang, 2003).
5. Air quality simulations (e.g. Stauffer et al., 1993; Jacobs et al., 1995; von Storch et al., 2002)
6. Impact of changing physiographic factors on regional climate (e.g. Pielke et al., 1999).
7. Land surface studies (e.g. Wen et al., 2000)
8. High resolution regional climate modeling (e.g. Christensen et al., 1998; Hisashi et al., 1999)
9. Modeling of atmospheric processes (e.g. Doyle 1995; Lynch et al., 1997; Gachon et al., 2003; Wang, 2001; Zhang et al., 2003).
10. Simulation of severe storms and flooding (e.g. Spencer and Strensrud, 1988; Li et al., 2003)
11. Modeling climate on a global scale (e.g. Dudhia and Bresch, 2002)

As many centers work with RCMs, the interaction between these allows for quality control of regional data as well as a sharing of resources, methods, regional physics optimizations, data and experiments. In this way, RCMs have improved the understanding of mesoscale weather systems and phenomena providing high temporal and spatial resolution modeling for operational and experimental purposes (Mass and Kuo, 1998).

1 http://weather.mhpcc.edu/
2 http://meso.geos.ntnu.edu.tw/~jfj/mm5

Additionally, projects detailing the research of participating international groups that use different RCMs have been and are still being conducted (Project to Intercompare Regional Climate Simulations (Takle et al., 1997; Christensen et al., 1997). These studies focus on particular applications such as short-term forecasting (White et al., 1999), precipitation (Colle et al., 1999a) and transport and diffusion (Hanna and Yang, 2001) and generally use horizontal grid sizes of larger than 10 km. However, with the doubling of computing performance every 18 months to 2 years (see e.g. MacDonald et al., 2000), an order of magnitude of reduction in grid size is achievable every 20 years. If these trends continue, within a few years numerical weather prediction models will be able to run routinely with 10 km grid sizes (Dudhia and Bresch, 2002), matching current research studies that run at these resolutions.

Many studies have used very high resolution simulations (< 5 km) to ascertain if any improvement is gained over coarser resolution results, especially over topographically complex areas. Mass et al. (2002) considered the improved accuracy in weather forecasts between using a 12 km and 4 km grid resolution and concluded that improvements were regionally specific having dependencies on the regions topography. An improvement in forecast skill was gained at the finest resolution only in regions with prominent topography. Bernadet et al. (2000) found that simulations at 2 km were needed to capture convection explicitly in their examination of four convective events, including two supercells. Colle and Mass (2000a) simulated the Pacific Northwest flooding event of 1996 and found a significant improvement in precipitation forecast skill as the grid resolution was decreased from 36 to 4 km. Furthermore, in going from 4 km to 1.33 km, rainfall was enhanced along windward slopes of orography and the immediate lee of these.

Other studies examined very fine scale weather phenomena. Colle and Mass (1998) examined the role of the Washington Cascades Mountains on lee storm-strength windflows and demonstrated the relative importance of gap flow and mountain wave accelerations using a 1 km grid. Gohm et al. (2004) simulated a south foehn windstorm observed across the Brenner Pass in the Wipp Valley near the Austrian–Italian border in 1999 at an extremely high resolution of 0.267 km. The model captured characteristic features of the fully developed foehn such as regions of flow descent, across-valley asymmetries of foehn strength and hydraulic jump-like features. Brown et al. (1999) simulated the leading edge of a cold front in which rainfall is generally concentrated at a maximum resolution of 2 km. In this region, the narrow cold-frontal rainband, precipitation is often organized into precipitation cores with gap regions in between (Hobbs, 1978; Hobbs and Biswas, 1979; James

and Browning, 1979; Locatelli et al. 1995 and Browning and Roberts, 1996). The simulation successfully identified precipitation cores and gap regions as well as the gravity waves associated with them. In simulating Pacific cold front, Chien et al. (2001) found that only at very high resolutions (1.67 km) were they able to produce an observed narrow frontal structure and an associated convective rainband. In an intercomparison study, Zhong and Fast (2003) describe results from three RCMs using a horizontal grid spacing of less than 1 km. These and other studies suggest that moving to very high resolution (grid spacing less than 5 km) results in an improved definition of meso- and microscale phenomena across a range of synoptic states, particularly in topographically complex areas.

Due to the lack of computational resources at most institutions in South Africa, very few, if any high resolution studies (< 5 km) have been performed and documented for the greater Cape Town region. As an attempt to address only one aspect of this knowledge gap,namely extreme rainfall, very high resolution simulations were performed over the greater Cape Town region for several extreme rainfall days. This would facilitate an examination of the spatial nature of extreme rainfall in the area as a result of topographic modification by the peninsula. The regional climate model used was the fifth-generation Pennsylvania State University – National Center for Atmospheric Research Mesoscale Model (PSU-NCAR MM5). This is a finite-difference primitive equation regional climate model used for numerical weather prediction, research and mesoscale modeling applications. It is non-hydrostatic and has multiple nesting capabilities that facilitate simulations at very high resolutions. The MM5 was used to simulate temperature and precipitation fields which were then examined against observed data obtained from weather stations. Precipitation data was additionally validated against weather radar data, which provided spatially continuous precipitation data complimentary to the point source station data.

2.5 Volumetric derivation of precipitation

Point source station data cannot provide contiguous information over a large area as each station is representative only of the area immediately surrounding it (Huffman et al., 1997). To overcome this problem, weather radar data is used to derive precipitation characteristics (Marshall et al., 1947; Marshall and Palmer, 1948). These data potentially span the spatial continuum of a region at multiple vertical levels and provide much enhanced temporal and spatial information of a rainfall-

generating weather system.

A radar (***ra***dio ***d***etecting ***a***nd ***r***anging) emits a pulse of energy which strikes an object e.g. a water droplet, which reflects some of the incident energy back to the radar unit. In the context of weather radar, the reflected data are used to measure characteristics of the precipitation by analyzing the strength of the returned pulse (signal attenuation), the time the pulse took to travel to the droplet and back again, and phase shift of the pulse. Objects that reflect much of the incident energy have a high reflectivity e.g. hail, large droplets in a thunderstorm, whereas softer precipitation has a lower reflectivity.

Weather radar is used by many institutions to monitor current weather conditions e.g. the National Oceanic and Atmospheric Administration's (NOAA) Radar Operations Center (ROC)[3] in the United States (Serafin and Wilson, 2000). Weather radar is also often used in conjunction with a regional climate model. Davidson et al. (1998) used radar data and an observational network in examining extreme mesoscale precipitation in Japan and the modeling thereof. Pradier et al. (2002) used Doppler radar to observe a frontal precipitation band in both convective and stratiform regions of the precipitation line, and together with high-resolution numerical simulations demonstrated the retardation of the frontal system by orography. In the United Arab Emirates, radar data were used to gain understanding into the large scale organization, spatial distribution and size, frequency, intensity and history of storms in the region (Breed et al., 2003). As a result of the understanding gained through this process, a RCM was employed to develop high resolution forecast fields for use in a cloud model. Rogers et al. (2002) also demonstrated a technique that used radar data to initialize a RCM resulting in an improved model description of the mesoscale environment during the pre-forecast time period, enabling an improved forecast of precipitation. Although these studies used ground based radar data, satellite based radar data have also been used (e.g. Cecil et al., 2002; Cecil and Zisper, 2002; Toracinat et al., 2002).

In this study, radar data were first tested against observed station data to establish it as a suitable proxy for rainfall in the region. The radar data were then used to describe the characteristics of precipitation over the region for the the selected time periods as well as validate the simulation of precipitation by the regional climate model.

3 http://www.roc.noaa.gov/

2.6 Summary

The characteristics of extreme rainfall in very localized contexts of the region is examined to ascertain changes, if any, in these characteristics over time. Thereafter, three distinct methodologies were employed for the identification, simulation and verification of extreme precipitation over the greater Cape Town region. First, self organizing maps were used to produce a series of characteristic circulation modes in which were identified certain modes associated with extreme precipitation. Secondly, days associated with these extreme modes were identified and a regional climate model was used to simulate them at very high resolution to capture the heterogeneous nature of extreme precipitation in region. Thirdly, the simulated precipitation fields were validated against radar-derived precipitation data.

Chapter Three

Identification of Extreme Precipitation Environments Using Self Organizing Maps

3.1 Introduction

The weather in a local region is conditional on the nature of the synoptic state of the atmosphere. Some synoptic events may dominate the response of regional precipitation, while in other cases the synoptic events may be secondary to smaller-scale rainfall producing processes such as thunderstorms. However, the synoptics establish the environment for the regional weather. Self organizing maps were used to investigate the relation between synoptic scale circulation and the local scale responses in the region. These were also used to investigate changes in the characteristics of synoptic circulations associated with extreme precipitation in the region. Additionally, days with synoptic circulations associated with extreme precipitation could be identified.

Relating synoptic scale characteristics to local scale responses requires the reduction of a large number of variables into a smaller set of data that still represent the original data. For example, precipitation is a function of many variables, e.g. pressure, temperature, humidity. Interactions between these variables have to be preserved in relating synoptic sale characteristics to the local scale precipitation response. This was accomplished with a self organizing map (SOM), which uses multivariate atmospheric data over a specified time series to produce generalized weather circulations. These are easily visualized as an array of archetypal synoptic states that span the continuum of events. The method allows the user to define the degree of generalization required by defining the dimension of the SOM, without losing the ability to visualize the results. In so doing, daily synoptic atmospheric data are categorized into a number of archetypal synoptic (circulation) modes. With this information it was possible to examine extreme precipitation associated with each mode of circulation.

3.2 The SOM Methodology

The SOM technique is used for clustering, visualization and abstraction of data. The process uses a non-linear projection of the probability density function of high-dimensional input data onto a two-dimensional array of nodes while spanning the full continuum of data space. The SOM identifies nodes within a given data space such that the nodal distribution represents the observed distribution, providing a means for data to be generalized into a number of arch-types. The application of SOMs to atmospheric circulation reduces the degrees of freedom in the data by forming archetypal circulations and facilitates identification of dominant modes of circulation within the data set as well as the visualization of this array of atmospheric states. Following is a brief description of the SOM procedure and how it was used in this study. A more detailed description of the SOM technique is available in Kohonen (1997).

The SOM architecture is comprised of an output layer of nodes in a single or multi-dimensional lattice, which can be arranged in a rectangular or hexagonal topology. The rectangular lattice is used in this study as it facilitates easier visual display and analysis (although the choice of lattice has little effect on the end product (Openshaw, 1994)). The SOM software used in this study was SOM_PAK version 3.1[1] which processes data in four distinct stages.

The first stage in the SOM routine is to define a random distribution of nodes within the data space during which the reference vectors of the map are initialized with either random or linear values. In the latter, reference vectors undergo an orderly initialization along a two-dimensional subspace spanned by the two principal eigenvectors of the input data vectors. The former allocates random numbers to the reference vectors equally across the data space. Both initializations are equally effective, although more care needs to be taken with input data preparation when using the latter. A random initialization was chosen for the SOMs in this study. The size of the map is chosen subjectively according to the degree of generalization desired and has a strong bearing on the range of synoptic situations represented. A fewer number of nodes in the SOM array would result in a more generalized circulation archetypes, while a greater number of nodes would represent a wider range of circulations.

1 Software and documentation available online at http://www.cis.hut.fi/research/som_lvq_pak.shtml

The second stage of the SOM is the map training process, which takes place in two phases. The first phase develops the broad-base mapping of the SOM and the second phase develops the finer aspects of the array. Both phases consist of an iterative training process in which the weights on a node are adjusted toward the training vectors such that they span the variance structure of the data space. During this process, the node whose weight matches the input vector most closely (having the minimum error between node vector and data vector) is chosen as the 'winning' node for the particular vector.

The nodes surrounding the winning node also benefit from the learning process by adjusting their weights such that each vector converges to the input pattern. These form an update neighbourhood, at whose center the winning node lies. The radius of influence of the wining node on surrounding nodes decreases to unity. A proper ordering of the map is achieved if the radius is initially set to a higher value, as a value set too low at this stage may cause various kinds of error on the map (Kohonen, 1997; Clothiaux and Bachmann, 1994). The learning rate, which determines how much weighting a node vector experiences around each input data sample and iteration, is specified and decreases to zero.

The number of training iterations is chosen such that final convergence (the fine adjustments) can be achieved by the end of the training. The initial training phase orders the map and the second phase captures the final convergence of the map. The vectors adjust during the iterations such that they span the whole data space, unlike other clustering techniques.

The result of the training is a two-dimensional map of nodes whose weight vectors span the data space continuum as represented by the input data. Each node represents a position that is the approximate mean of the nearby data samples, the 'archetypal' points in the data space. Nodes most dissimilar from each other are placed furthest from each other. Individual data elements, such as sea level pressure, may then be associated with the best matching node in the map.

The third stage of the process evaluates the quantization of error to attain the best SOM. For each input vector, the winning node is selected through an assessment of the Euclidean distance to the node vectors. The shortest distance between nodes is calculated (quantization error) and the input vector is allocated to that node. The best SOM is attained when the averaged minimum Euclidean

distance is obtained (the smallest average quantization error). Detection of error in the SOM can be monitored easily through the use of Sammon maps (Sammon, 1969). Sammon maps use a non-linear mapping technique that allows the mapping of high dimensional data space to a lower dimensional data space whilst maintaining the structure of the data. It does so by creating a two-dimensional image of the reference vectors where distance between the node image vectors approximate the Euclidean distances in data space. It is not desirable to have folds in the Sammon map as this makes physical interpretation of the SOM more complex.

The final stage in the process is data visualization. As each individual data element is associated with the best matching node in the map, the individual quantization error can be used for calculating frequency data for the node (error maps) as well as other statistical information. Additionally, the frequency of archetypal states can be extracted from the original dataset for analysis.

3.3 Training data

Training data for the SOM were daily mean atmospheric fields constructed from six-hourly NCEP/NCAR reanalysis data. This is a gridded (2.5 x 2.5^{o}), global observed data set assimilated from a number of sources including land stations, ships, rawisonde, pibal, aircraft and satellite (see Kalnay et al., 1996). For the Southern African region, data quality prior to 1979 has been shown to be problematic (Kistler et al., 2001; Tennant, 2004) thus the range of the data has been restricted to post-1979, when the advent of satellite data facilitated a significant improvement of the reanalysis data for the Southern Hemisphere. Data from 01 April to 30 September (winter) were used for the years 1979-2001 to train the SOM. The domain over which the data were extracted was chosen to capture synoptic circulation from the tropics to the deep mid-latitudes, the interactions between these regions as well as the evolution and translation of mid-latitude cyclones. This resulted in a domain that stretched from 10^{o}S to 60^{o}S and 20^{o}W to 45^{o}E which consisted of 21 x 27 grid cells (Fig. 3.1).

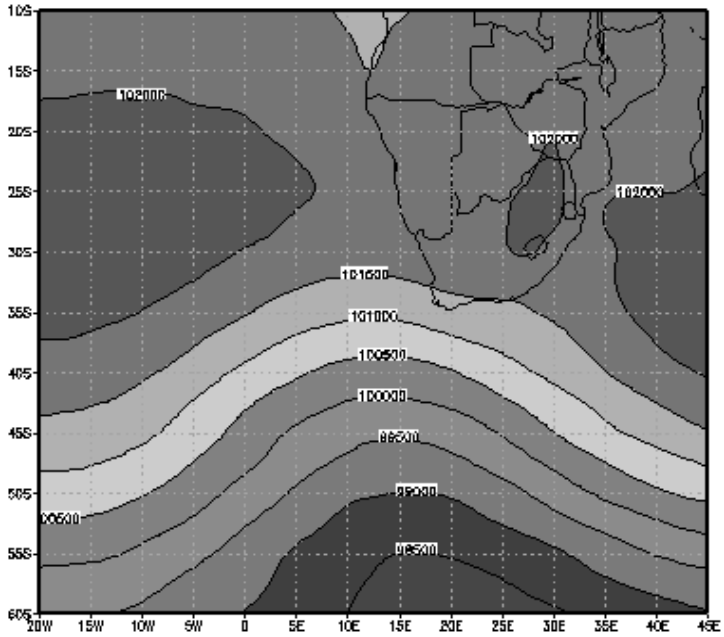

Fig. 3.1. Domain from which NCEP data were used to train the SOM. Shown in this domain is sea level pressure which displays a low pressure trough, the South Atlantic and south Indian High pressure systems and an inland high pressure.

The choice of predictor variables has been shown to be critical in capturing climate change signals (Hewitson and Crane, 1996). Cavazos and Hewitson (2005) examined 29 atmospheric predictors of daily precipitation in 15 locations that encompassed diverse climate regimes and evaluated the best combination of predictors that were able to capture different sources of variation. They showed that mid-tropospheric circulation was the most relevant predictor of daily rainfall followed by humidity fields. The most relevant surface predictor identified was sea level pressure, which is also a principal variable in assessing surface weather characteristics at the local scale. Thus 500 hPa geopotential heights, surface relative humidity and sea level pressure data were used to train the SOM. The inclusion of relative humidity at 500 hPa did not alter the results of the SOM significantly therefore for ease of analysis this field was excluded from the training process. The individual data fields were first standardized using the means and standard deviations of the 27 x 21 cell time series, thus preserving the local gradients in each field. The three variables used at their respective levels in the 27 x 21 grid window created a 1701-element vector which described the daily atmospheric state.

3.4 Identification of extreme precipitation days

Extreme precipitation was defined as precipitation whose volumes fell into the 90th percentile of the distribution. In identifying synoptic states associated with extreme precipitation, two SOMS were generated. An initial SOM used all daily winter precipitation data (April to September) from 1979-2001 to identify circulation archetypes throughout the winter months. This also provided a trained SOM onto whose archetypal modes data from only extreme precipitation days in the period could be mapped. Thereafter, a second SOM was trained using only data from days that experienced extreme precipitation in the greater Cape Town region. This served to disaggregate into further synoptic archetypal states those identified in the initial SOM.

The Computing Centre for Water Research (CCWR) in South Africa has recorded daily precipitation station data from approximately 7000 stations across South Africa since 1950. Hewitson and Crane (2005) interpolated these station data onto a 0.5 degree grid over South Africa using a conditional interpolation technique. Although the stations in the study region have missing data through the 23 year time period in space and time, the interpolation technique used by Hewitson and Crane (2005) is able to account for both temporally and spatially missing data. Therefore this gridded data set was used as the basis for the extraction of the 90th percentile precipitation data. A domain over the study region was chosen such that it was represented by four grid points of the interpolated data (Fig. 3.2). Daily values were examined for each grid cell and the 90th percentile determined for each. If one or more cells recorded a 90th percentile value on any particular day, that day was extracted. This process yielded 488 extreme precipitation days of a total of 3156 days for which precipitation was recorded. Using these dates, corresponding daily NCEP/NCAR Reanalysis data were extracted and used to train the second SOM. In addition to an analysis of the results from the SOMs, an analysis was performed on the interpolated CCWR data to assess trends in extreme precipitation days over time.

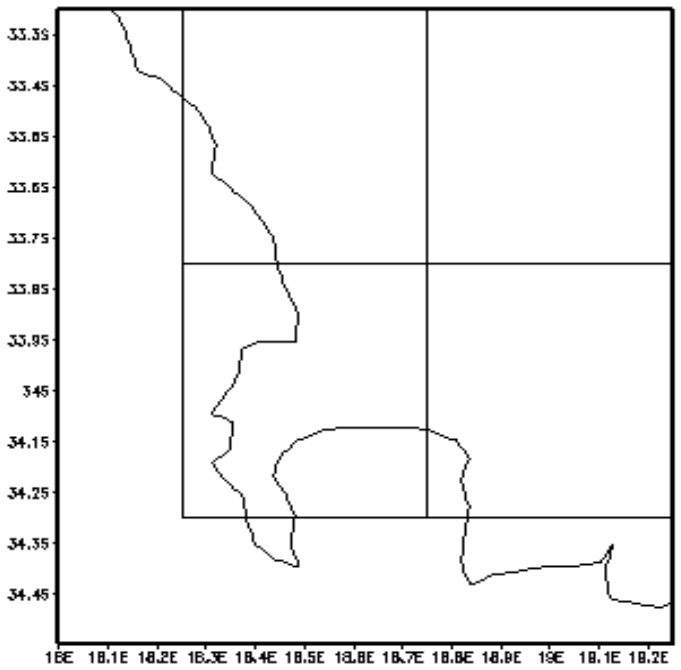

Fig. 3.2. Four grids in the interpolated CCWR data from which 90th-percentile precipitation data were extracted.

3.5 SOM parameters

The size of the SOM array was selected subjectively. As with Hope et al., (2006), an initial rectangular 5x7 array for the first SOM was selected following the work of Hewitson and Crane (2002). To test the adequacy of this SOM size, the synoptic types in the resulting SOM were assessed to determine if they represented the expected range of winter synoptic circulations. These included low pressure troughs to the south of the domain, high pressure circulations over the interior of the South Africa, including the South Atlantic and South Indian anticyclones, and also the appropriate translation of troughs and highs across the region. For more information on South African synoptic circulations see Tyson and Preston-Whyte, (2000). With the 5x7 array, all expected synoptic types were well represented but it was decided that the the spectrum could be represented with fewer nodes. A smaller 4x5 array was selected for the initial SOM which still captured all the expected circulation types and gave maximum variance in the data space. Although somewhat arbitrary, the choice of array size is guided by the the need for a coarser of finer archetypes in the application. Smaller arrays did not adequately capture the range of expected synoptic types.

The radius of influence was set to three for the first iteration, allowing for a wide influence across nodes, and to one for the second iteration, which constrained influence to nodes in the immediate vicinity of one another. The learning rate was set to 0.1 for the first phase and 0.01 for the second. The number of training iterations was set at 5 000 for the first training phase, developing the broad-base mapping of the SOM and to 100 000 for the second to develop the finer aspects of the array. This produced a SOM trained on all winter data from 1979-2001. Data from days that experienced extreme precipitation were then passed through the trained map to identify nodes to which they mapped and thus identify synoptic states associated with extreme precipitation.

The second SOM, using only the 90th percentile data as training data, used a 3x4 data map. Data maps with larger dimensions were tested but did not yield significantly different circulation archetypes. The radius of influence of both training phases was set to one to constrain influence to the node's immediate vicinity on account of the map size. The learning rate again was set to 0.1 for the first phase and 0.01 for the second and the number of training iterations set to 5 000 and 100 000 respectively. Visualization of the SOM results was done using the GrADS (Grid Analysis and Display System)[2] software.

3.6 Results

3.6.1 SOM using all winter data

The 20 nodes in the first SOM represented 20 distinct circulation archetypes across the data space continuum. The Sammon map (Fig. 3.3) provided a 2-dimensional representation of the inter-nodal distances across the N-dimensional data space. Referencing of node co-ordinates start at the bottom left hand corner and move from left to right, then up to the next line and from left to right again. The bottom left hand corner node is node one, bottom right corner node five, the node immediately above node one is node six, the top left corner node 16 and the top right corner node 20.

2 http://grads.iges.org/grads

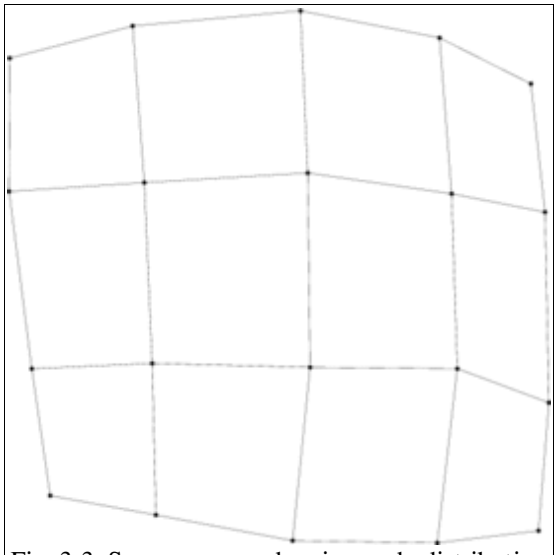

Fig. 3.3. Sammon map showing node distribution in data space.

The nodes were not equidistant from each other and their relative distance from one another was in terms of data space dimensionality. The frequency of synoptic states associated with each archetype could thus be determined and contoured across the 2-dimensional surface as a frequency map (Fig. 3.4). Data mapped homogeneously across nodes, each node having approximately 5 % of 4232 winter days map to it. The homogeneous nature of the distribution meant it was not possible to identify dominant circulation type(s).

5	4	5	5	5
5	5	5	6	5
5	5	5	6	5
5	4	5	5	5

Fig. 3.4. Frequency map for all winter data.

Each day used in creating the SOM mapped to a single node, thus circulation archetypes could be

produced where the most dissimilar circulations were placed furthest from each other in the SOM. The sea level pressure archetypes represented typical winter circulations over South Africa (Fig. 3.5). A persistent high pressure was located over the interior of the country across all nodes. Nodes in the center of the map were characterized by an unbroken band of high pressure across of South Africa which represented the descending limb of the Hadley Cell. This subtropical anticyclone is associated with upper air convergence, subsidence and surface divergence causing fine, dry weather over the interior of the country characteristic of winter in this region. Nodes indicating this circulation or the development thereof or a ridging South Atlantic High pressure system would generally not be associated with precipitation. Archetypes of these types were located at nodes 1 to 4, 6 to 9, 12, 13, 17 and 18.

In the top row and right hand column, the passage of low pressure troughs situated at relative lower latitudes could be seen to disturb the sub-tropical high pressure band and break it into the South Atlantic and South Indian high pressure systems. The low pressure troughs indicate the passage of mid-latitude cyclones which are regions of strong baroclinicity and result in precipitation in the Western Cape. Synoptic states represented by all of the nodes in the right hand column as well as nodes 15, 16, 19 and 20 would likely be associated with this frontal precipitation.

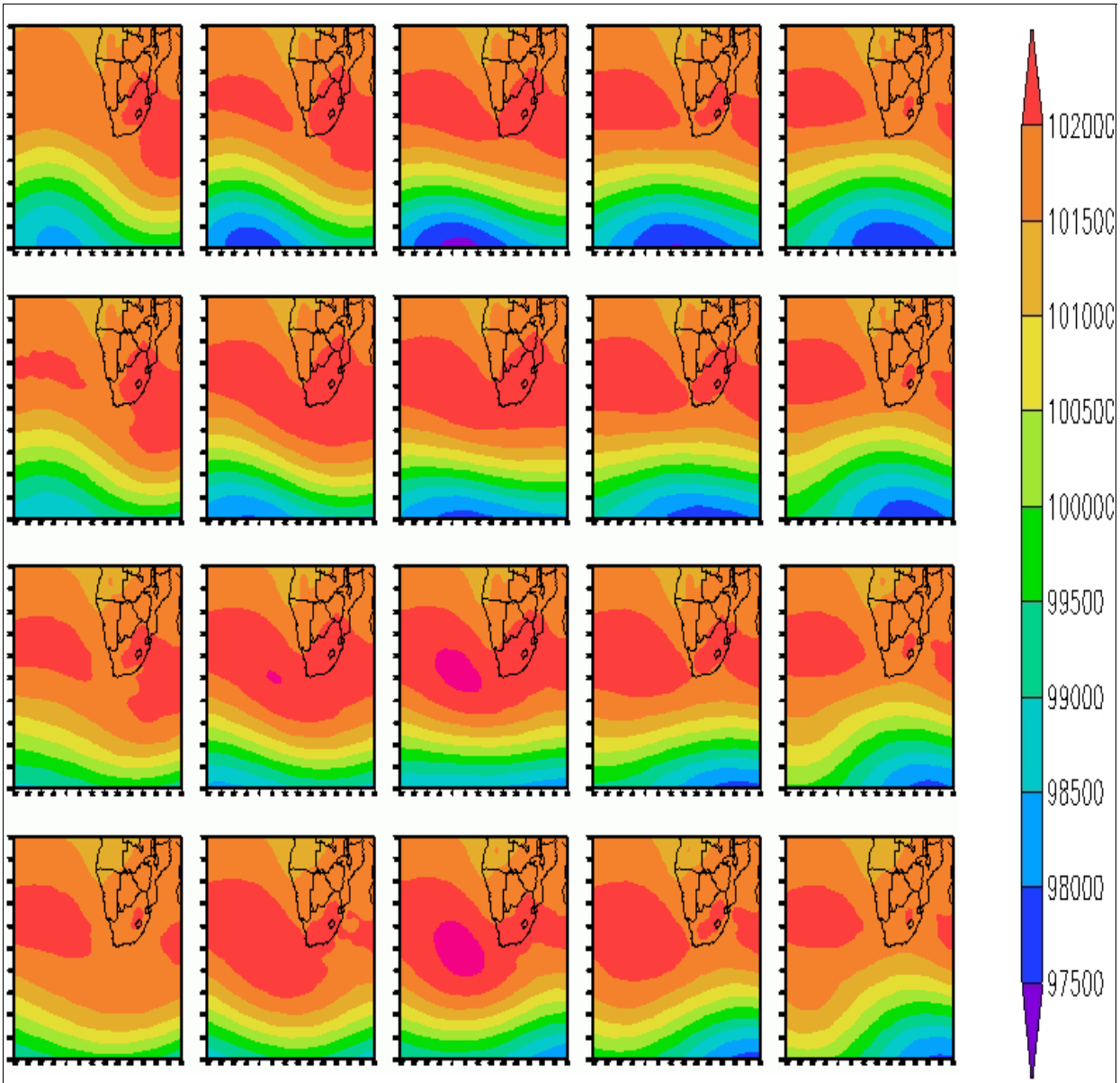

Fig. 3.5. Archetypes of sea level pressure from all winter data (scale in hPa).

In the 500 hPa geopotential heights map, winter synoptic circulations were again evident. Generally unperturbed conditions were seen near the center and bottom left of the SOM with a high pressure dominant over the interior of the country (Fig. 3.6). The passage of low pressure troughs was again most evident in the top row and right hand column.

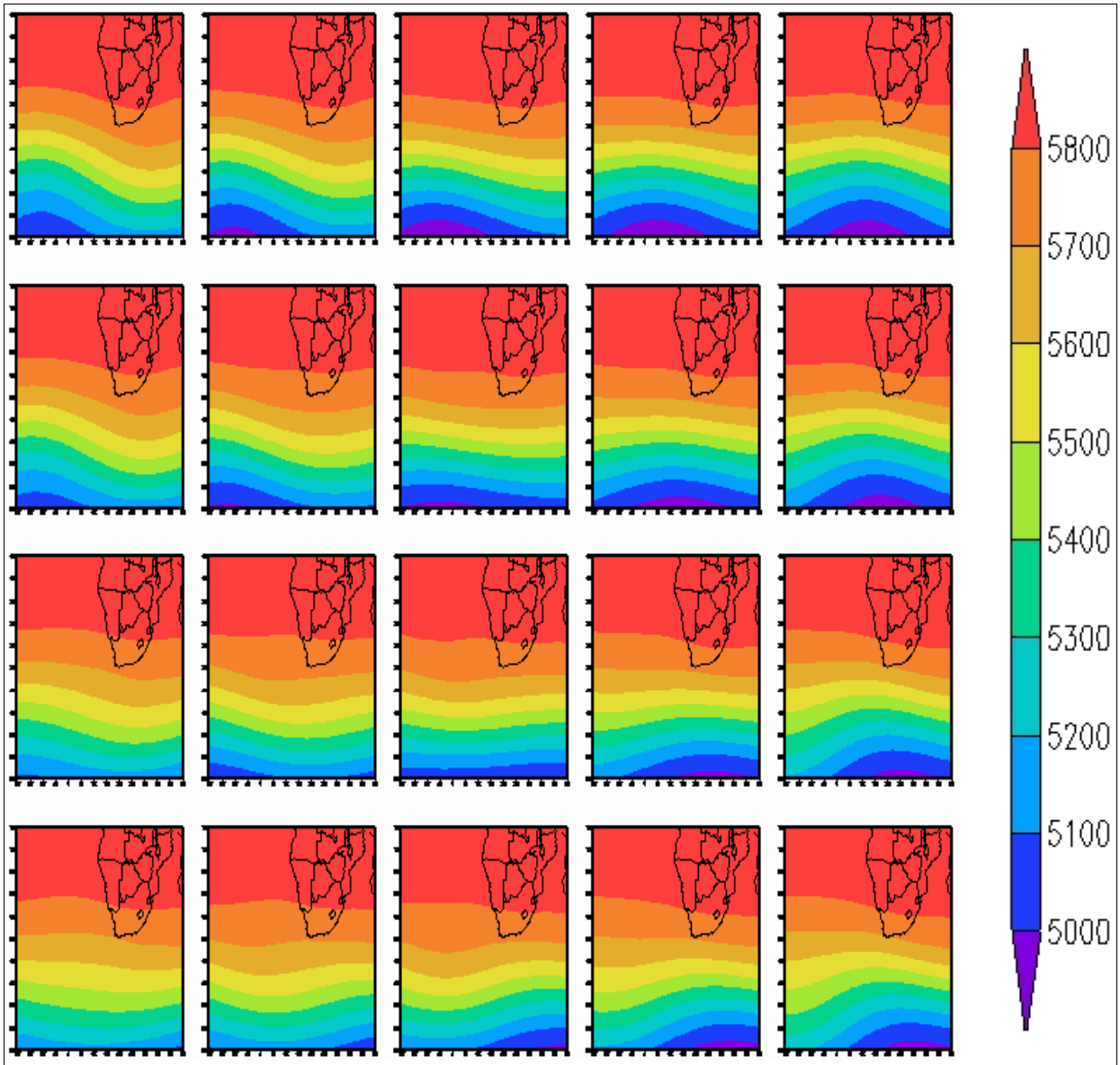

Fig. 3.6. Archetypes of 500 hPa geopotential heights from all winter data (scale in gpm).

The surface relative humidity map showed driest conditions over the interior of the country across all nodes, as a result of subsidence associated with the descending limb of the Hadley Cell (Fig. 3.7). Highest values occurred at high latitudes and were associated with the passage of mid-latitude cyclones. Nodes in the top row and right hand column showed a tongue of moisture that stretched from the higher latitudes up the west coast of the sub-continent over the cold, northward flowing Benguela current. This tongue of moisture was situated close to Cape Town especially in nodes 10, 15, 19 and 20, indicating circulations with enhanced moisture concentrations.

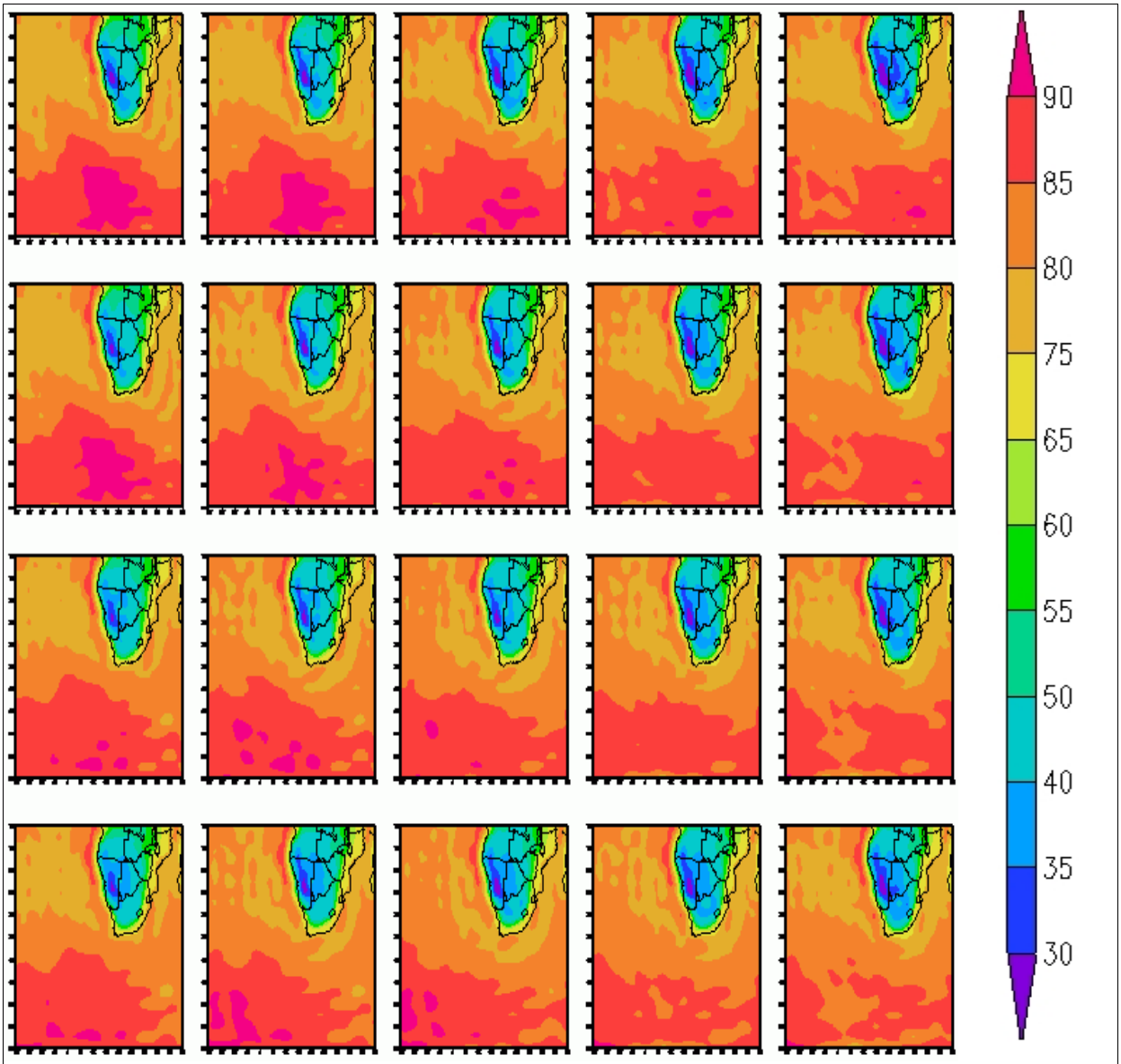

Fig. 3.7. Archetypes of surface relative humidity distribution from all winter data (scale in %)

The initial SOM produced a trained map that displayed a continuum of winter conditions experienced over South Africa, including the dominant subtropical high pressure over the interior and the passage of mid-latitude cyclones to the south of the country. In order to identify which of these nodes extreme rainfall days mapped to, the extreme data were passed through the trained SOM and each day mapped to a single node of the trained map. The frequency map produced indicated that most of the extreme data mapped to nodes on the right hand side of the SOM, and to a lesser extent nodes one and 16 (Fig. 3.8), these nodes accounting for 72 % of the days.

9	1	3	4	15
2	1	1	2	15
3	1	1	2	11
10	1	3	3	12

Fig. 3.8. Mapping of extreme rainfall days to the map trained with all winter days.

With the exception of node one, the archetypal circulation associated with these nodes are of a low pressure trough passing the South-Western Cape. Node one may indicate cut-off /tear-off low features and associated thunderstorm activities. The circulation indicates a trough having moved through the region recently with the south Atlantic high having not ridged in yet. Unfortunately, the detection of cut-off lows from low resolution NCEP data is difficult and falls somewhat beyond the ambit of this study. However, this is the focus of a current study at the Climate systems Analysis Group. For the other nodes associated with extreme rainfall, sea level pressure and 500 hPa geopotential heights both indicate the eastward movement of the low pressure trough moving down the right hand column. These nodes are also associated with higher relative humidity values near the Cape Town region. Amongst dates mapping to these nodes were days in July and August 2001 identified in Chapter One. The 2nd, 3rd, 4th, 17th, 18th and 19th July mapped to nodes 15 or 19 and the 23rd and 29th August both mapped to node ten.

The SOM identified synoptic circulations associated with extreme precipitation from a dataset that included all winter days over 23 years. In order to further disaggregate the synoptic conditions of days which experienced extreme precipitation, a second SOM was trained using circulation data of only days associated with extreme precipitation.

3.6.2 SOM using extreme precipitation data

It should be noted here that days extracted as having experienced extreme precipitation were defined as having one grid cell in the interpolated CCWR data set domain with precipitation in the 90th percentile (see Fig. 3.1). Thus grid cells over the greater Cape Town region would not necessarily contain 90th percentile precipitation data in every day extracted.

The 12 nodes in the extreme precipitation SOM represented 12 distinct circulation archetypes across the data space continuum. The Sammon map representing nodal distribution is shown in Figure 3.9 and frequency map in Figure 3.10. Each day used in creating the SOM mapped to a single node and almost 60 % (278 days) mapped to nodes which were situated near the corners of the SOM space.

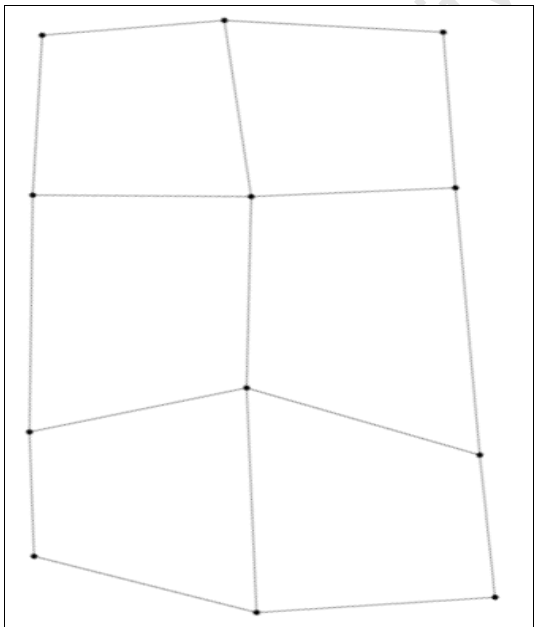

Fig. 3.9. Two-dimensional representation of the distances between the SOM nodes

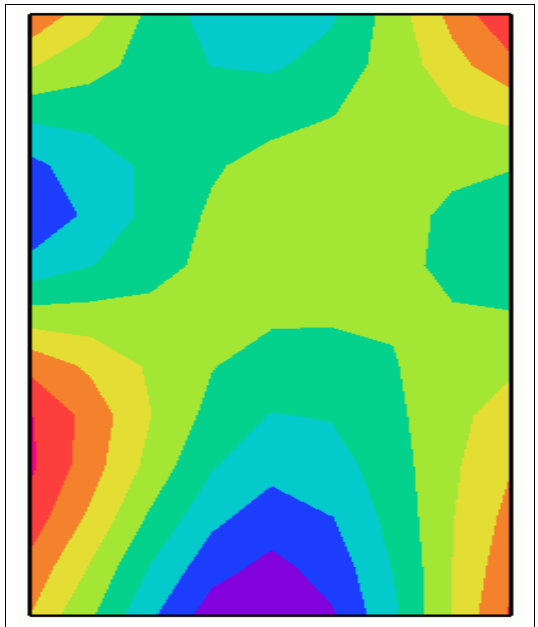

Fig. 3.10. Mapping frequency of each node (%). Reds are a high and blue low frequencies.

The 14 days in July and August 2001 that were identified from the CCWR data as having experienced extreme precipitation mapped to nodes one through five. To get an indication of precipitation distribution across these five nodes, daily station precipitation data at Cape Point, Slangkop and Cape Town International Airport were averaged for these dates and allocated to the appropriate node. The highest precipitation values were recorded on July 2nd, 3rd and 4th with an average of 24 mm per day at these stations (Fig. 3.11). Over the 17th, 18th and 19th July a daily average of 15 mm per day was recorded. The Airport station recorded a total of 184 mm during these six days of a total of 198 mm for the whole month, thus 93 % of rainfall recorded in July 2001 could be classified as extreme precipitation. Of the five days which recorded extreme precipitation in August, four mapped to node five and one to node four. Less precipitation fell as extreme precipitation during August over the greater Cape Town region, an average of 35 mm across the three selected stations and at the Airport station only 32 mm from a monthly total of 97 mm.

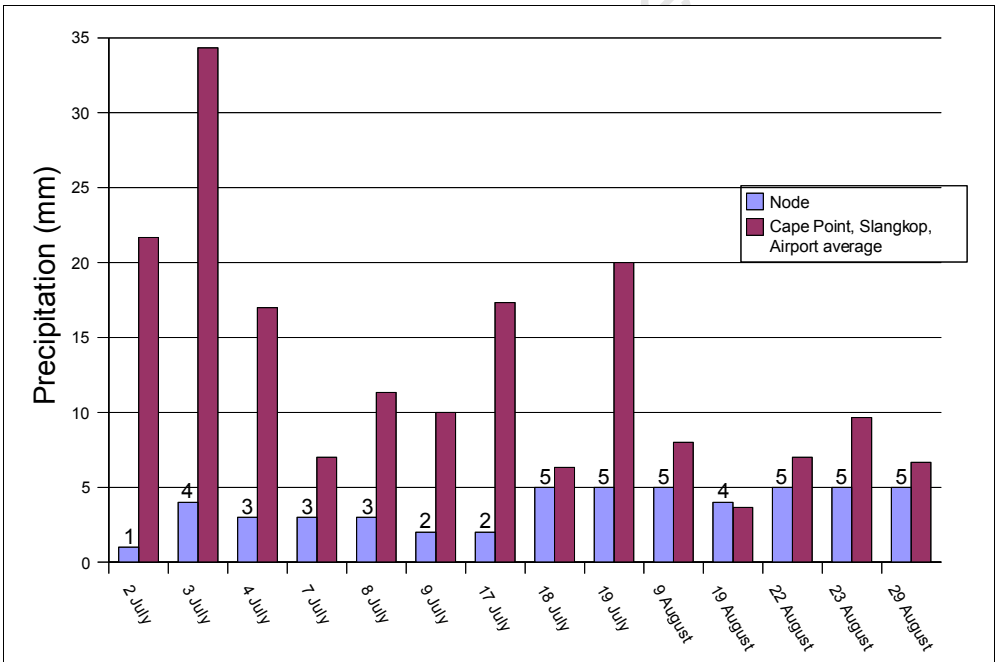

Fig 3.11. Nodes to which extreme precipitation days mapped to and corresponding daily precipitation amounts. The label above the blue bar is the node number.

Node five had the most days map to it and it was associated with the highest amount of rainfall in the region over the 14 days (Fig. 3.12). Node four had the second highest amount of precipitation associated with it although only two days mapped to it.

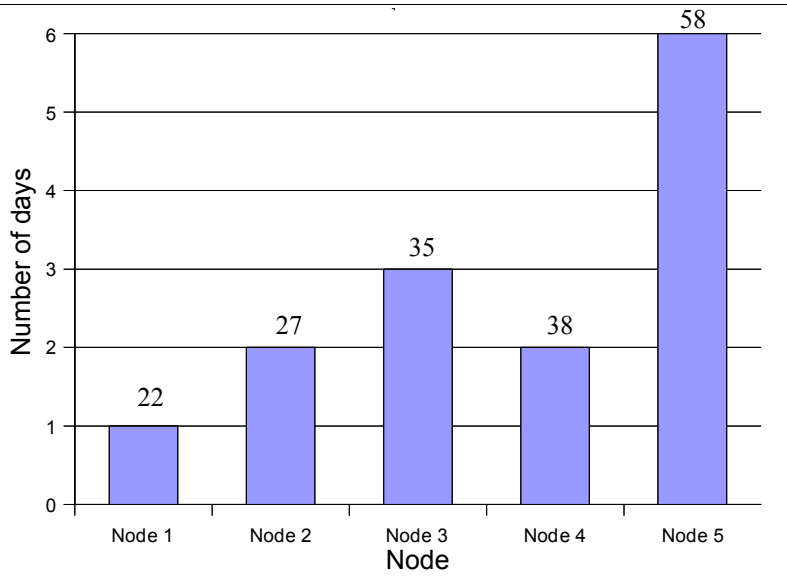

Fig. 3.12. Nodal mapping of days in July and August 2001 which experienced extreme precipitation. The total averaged precipitation (in mm) associated with each node are labeled respectively.

The nodal loading for July showed that three days mapped to node three, two days to nodes two and five and one day each to nodes one and four (Fig. 3.13). The three days that mapped to node three accounted for the highest amount of precipitation associated with a single node. Nodes four and one had only one day each map to them but these days experienced the highest single-day rainfall amounts, node four having the second highest amount of total rainfall associated with it. Nodes two and five had two days map to each and together had 53 mm of rain associated with them.

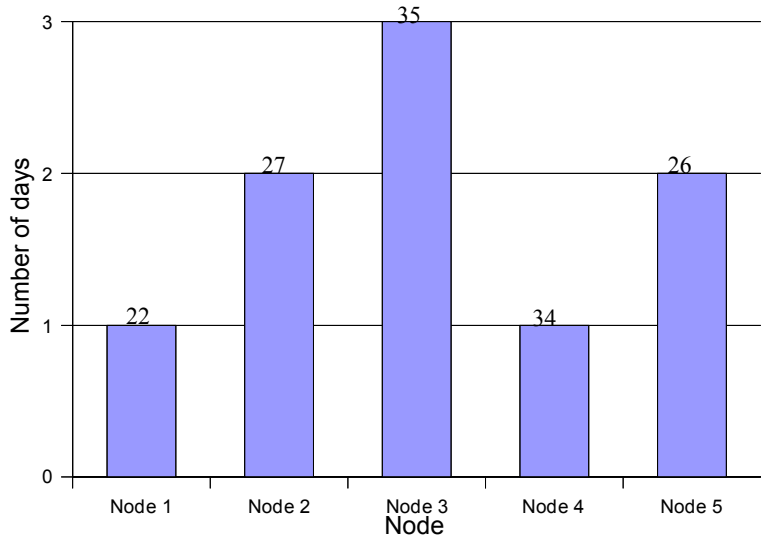

Fig. 3.13. Nodal mapping of days in July which experienced extreme precipitation. The total amount of precipitation (in mm) recorded for the day(s) at each node are labeled respectively.

Of the five nodes to which the July data mapped, high amounts of precipitation were associated with nodes to which only one day mapped (e.g. node four) as well as nodes which had multiple days map to them (e.g. node three). Considering the well-above-average rainfall for July 2001, the synoptic states associated with these nodes could be regarded as having a high potential of being associated with extreme precipitation. Thus a discussion of the circulation archetypes associated with extreme precipitation is presented below. Special attention was paid to nodes one through five as a result of their association with the extreme precipitation experienced in July 2001. Pressure fields are presented first followed by the relative humidity field.

3.6.3. Synoptic archetypes associated with extreme precipitation days

A continuum of sea level pressure circulations associated with extreme precipitation days was established by the SOM. All the nodes were associated with the passage of a low pressure trough (Fig. 3.14). There was no evidence of archetypal circulations which included the unbroken band of high pressure over the interior of the country as seen in the SOM using all winter data. Days with synoptic states that had low pressure troughs at higher latitudes mapped to nodes in the upper two rows. In the top row, nodes had days mapped to them that represented synoptic states following the passage of a low pressure trough from which a closed circulation budded off, as represented in node

12. Pressures were generally higher in these nodes. Days which indicated the passage of a low pressure trough at lower latitudes mapped to nodes in the lower two rows, the bottom row having these systems at lowest latitudes. A much stronger pressure gradient between the southern edge of the domain and South Africa was apparent in these nodes.

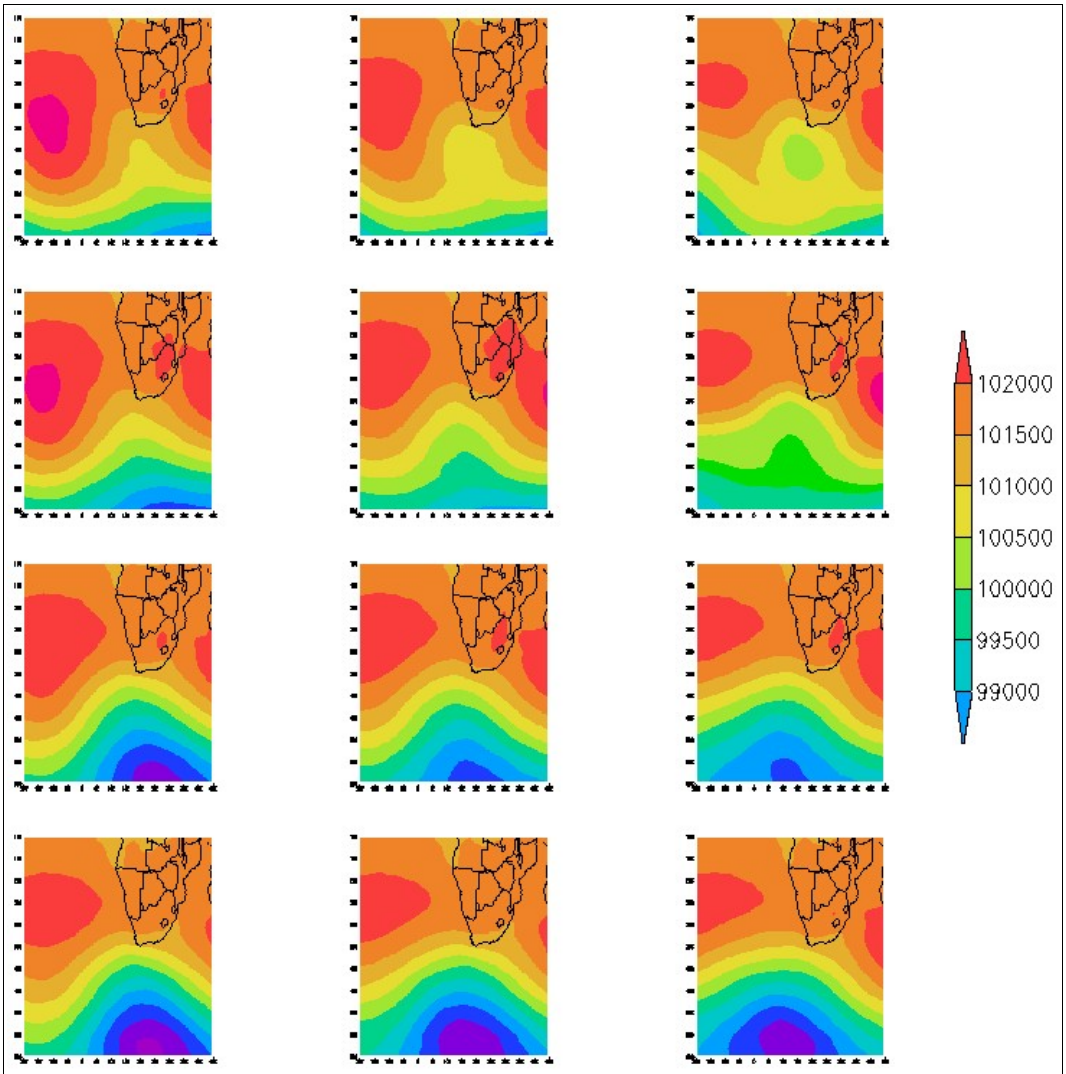

Fig. 3.14. Archetypal sea level pressure circulations associated with extreme rainfall in the South-Western Cape.

Circulations at the 500 hPa geopotential level mirrored those of the sea level pressure map (Fig. 3.15). In the upper two rows the low pressure troughs were at higher latitudes than in the lower two rows. The pressure gradients of these troughs at higher latitudes were again much steeper than in archetypes represented in the upper two rows.

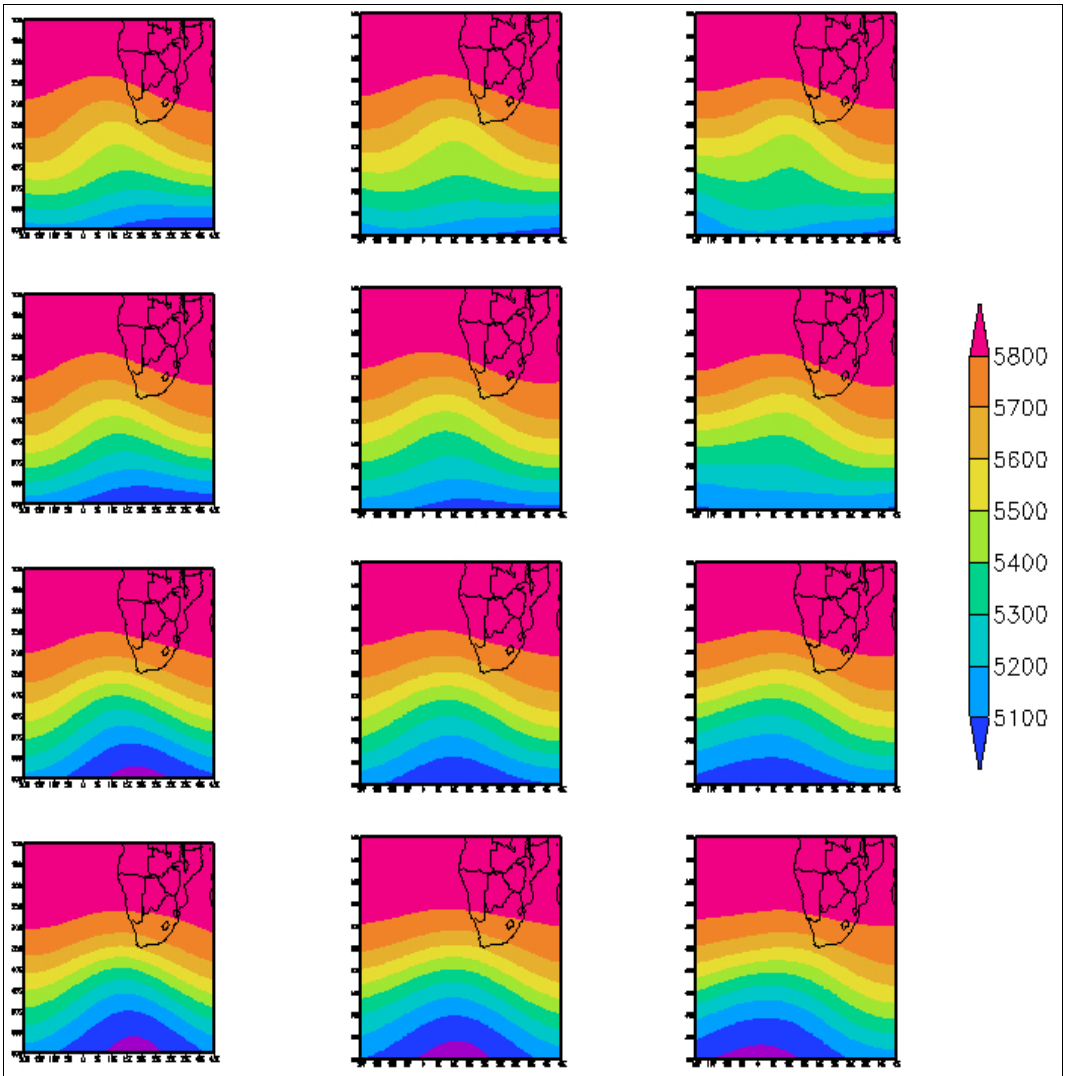

Fig. 3.15. Archetypal 500Hpa level circulations associated with extreme rainfall in the South-Western Cape.

Lowest relative humidity values were situated over the interior of the country across all nodes (Fig. 3.16), as was seen in the initial SOM using all winter data. Maxima were associated with the centers of low pressure troughs. The band of higher values that stretched from the high latitudes up the west coast was also present, with very high values seen over the west coast in nodes two and three.

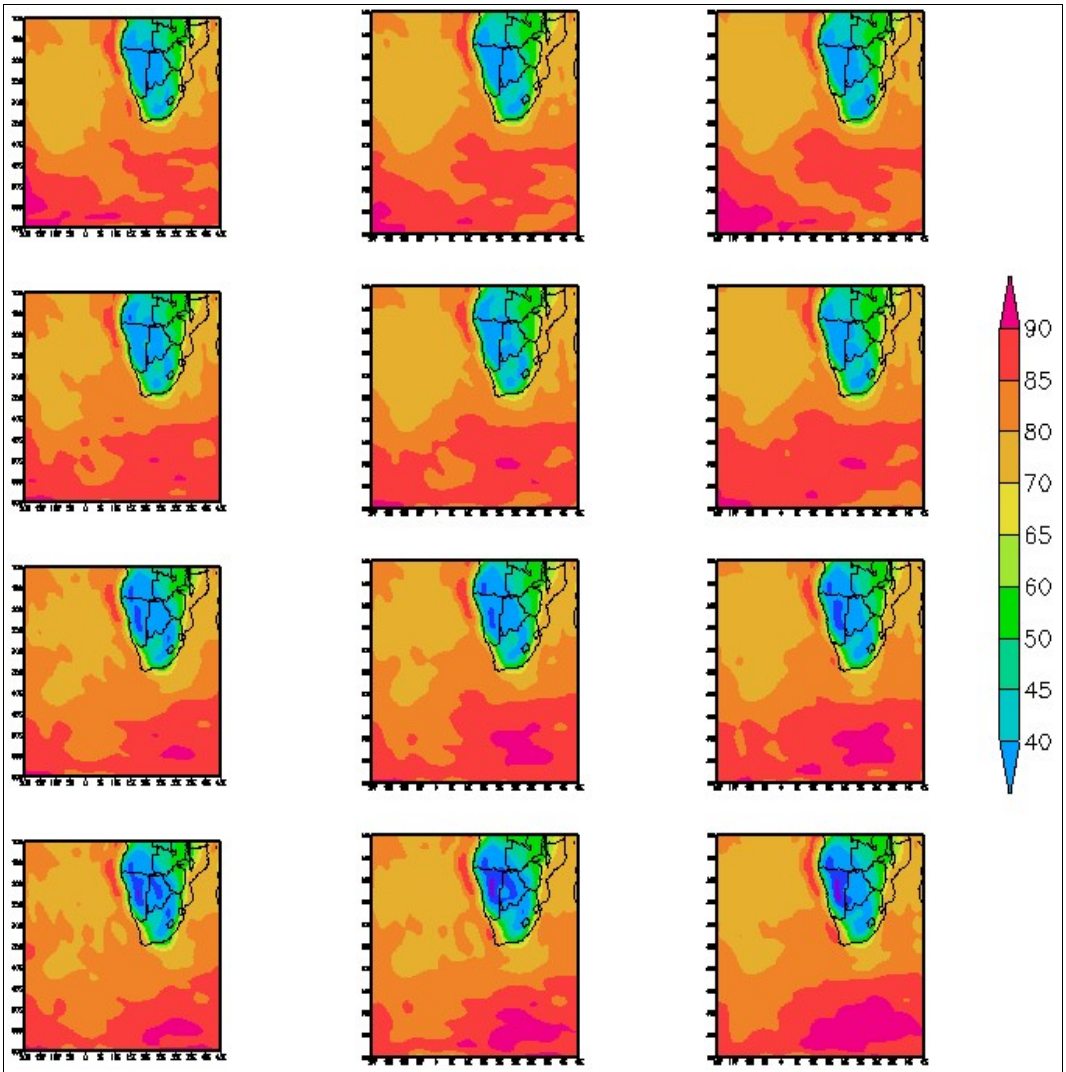

Fig. 3.16. Archetypal relative humidity circulations aassociated with extreme rainfall in the South-Western Cape.

As mentioned above, all days in July and August 2001 which experienced extreme rainfall mapped to nodes one through five. Synoptic states associated with these nodes are presented in detail in Figure 3.17 a-e. The sea level pressures along the bottom row of nodes (nodes one to three) displayed low pressure troughs with centers at lower latitudes than nodes four and five. This was also apparent in the 500 hPa circulation and indicated stronger pressure gradients under these particular synoptic forcings.

Node 1	Node 2
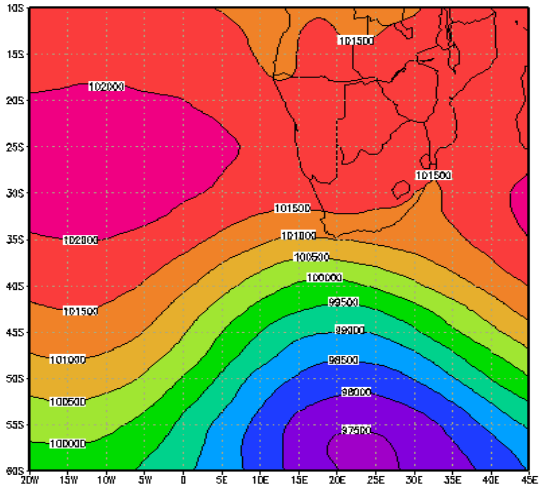	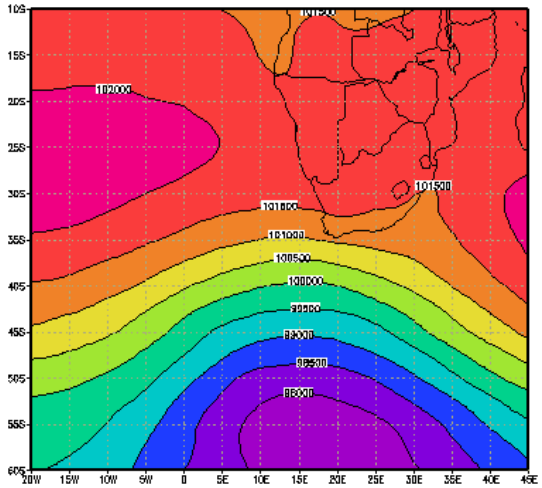
Sea level pressure	Sea level pressure
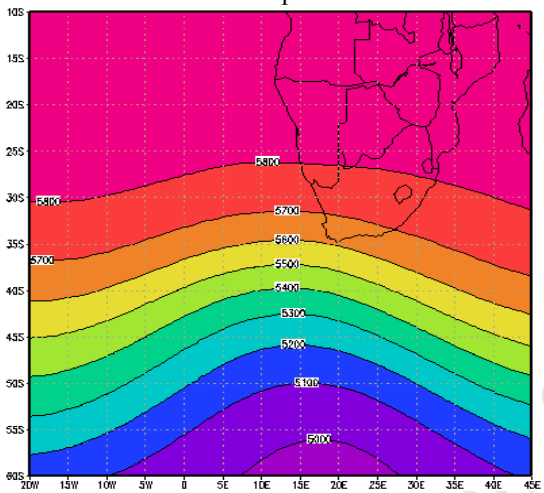	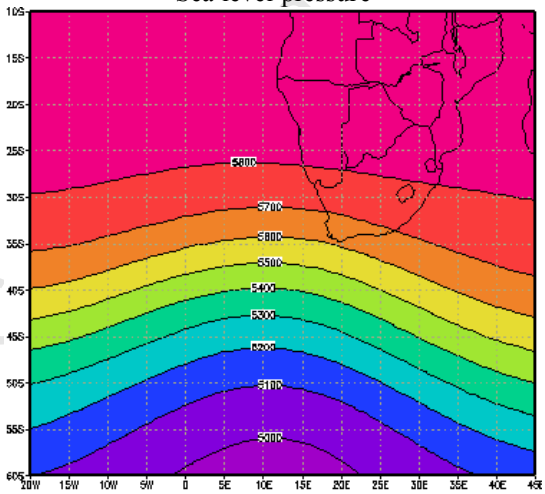
500 hPa Geopotential Height	500 hPa Geopotential Height
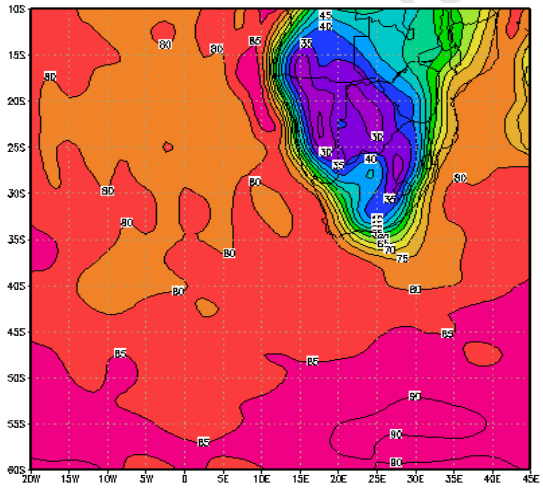	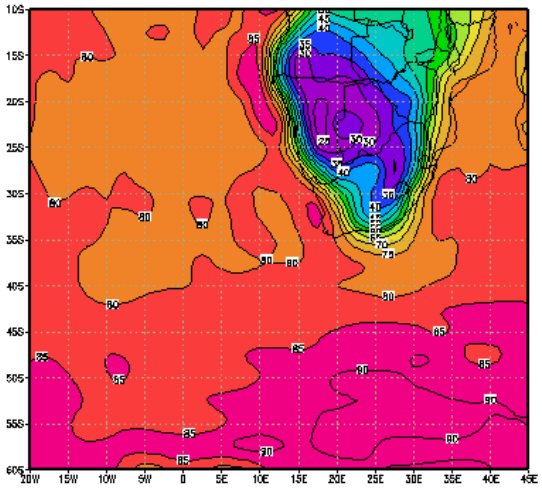
Surface Relative Humidity	Surface Relative Humidity
Fig. 3.17a. Archetypal circulations associated with extreme precipitation which mapped to node one.	Fig. 3.17b. Archetypal circulations associated with extreme precipitation which mapped to node two.

Node 3	Node 4
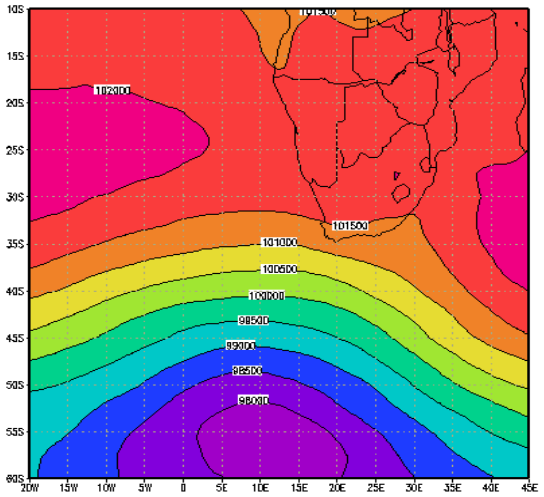 Sea level pressure	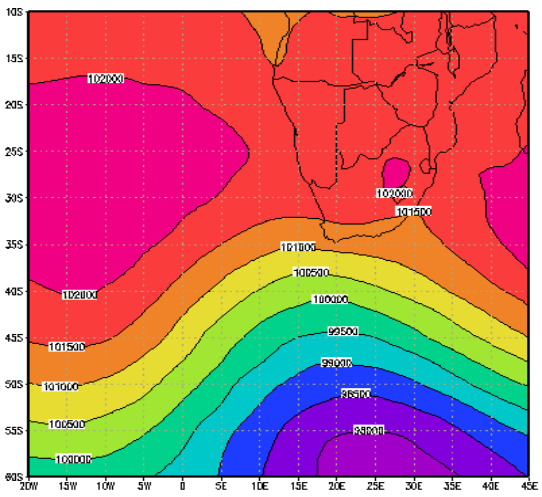 Sea level pressure
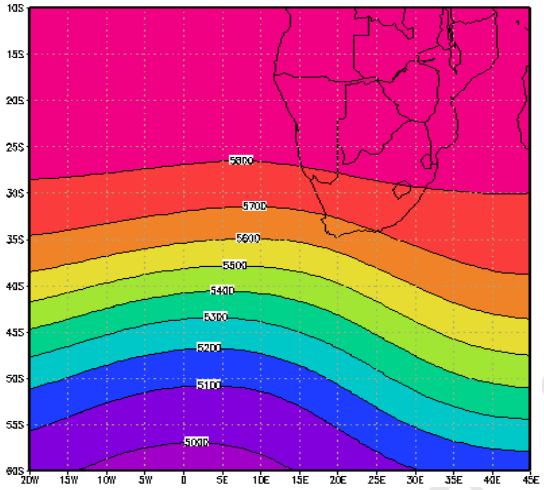 500 hPa Geopotential Height	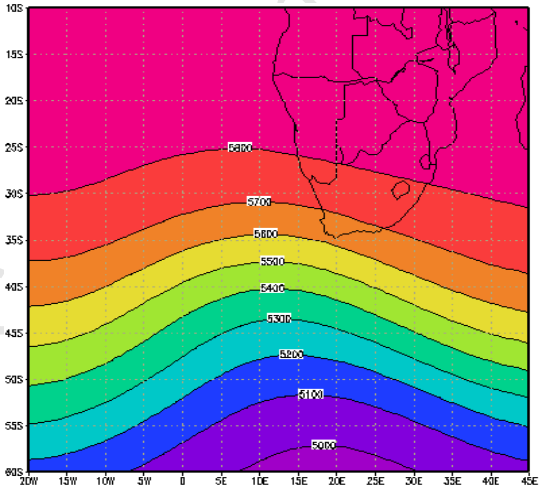 500 hPa Geopotential Height
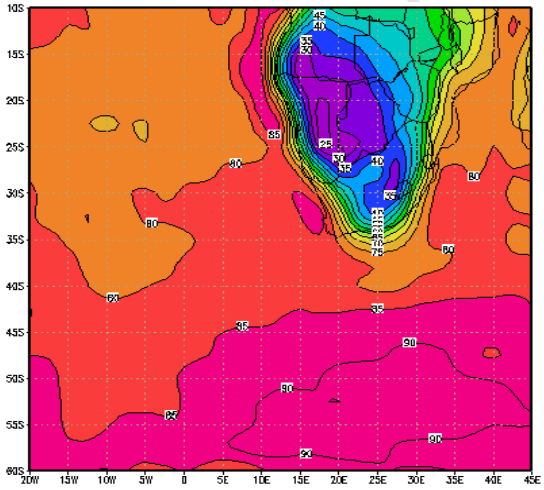 Surface Relative Humidity	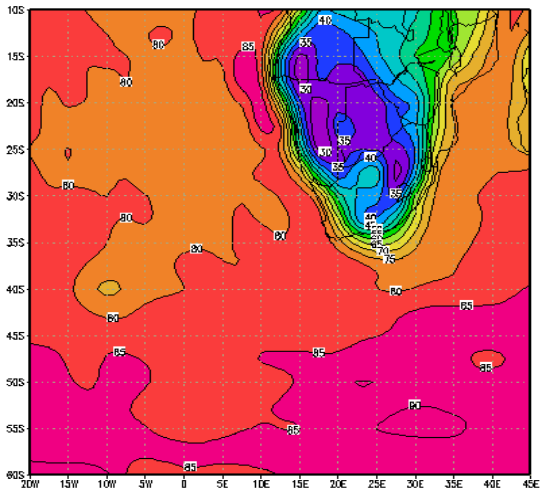 Surface Relative Humidity
Fig. 3.17c. Archetypal circulations associated with extreme precipitation which mapped to node three.	Fig. 3.17d. Archetypal circulations associated with extreme precipitation which mapped to node four.

Node 5

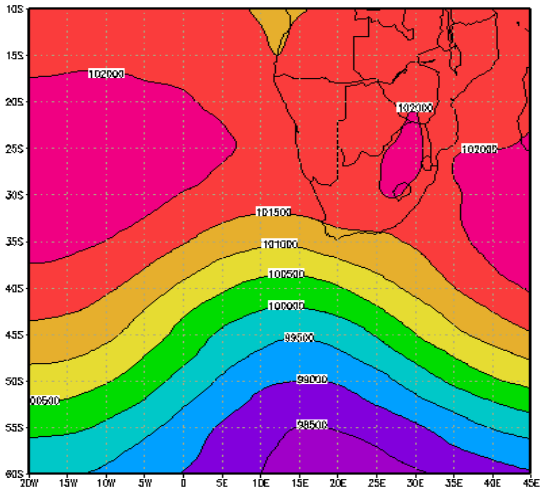

Sea level pressure

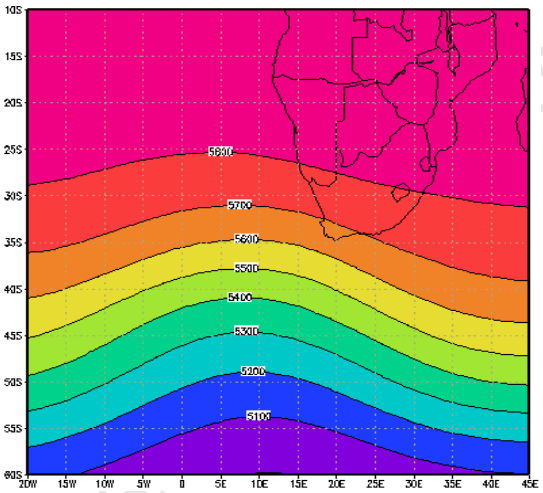

500 hPa Geopotential Height

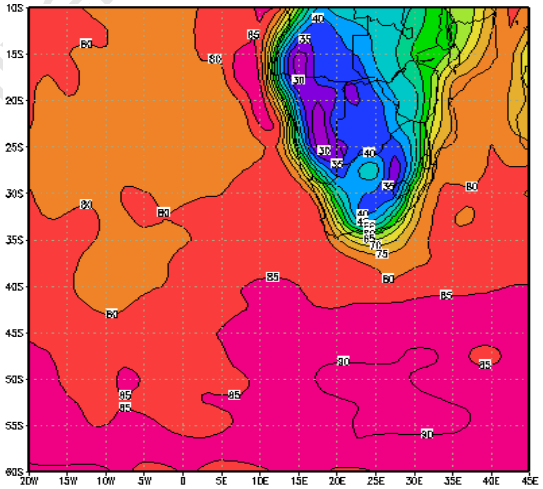

Surface Relative Humidity

Fig. 3.17e. Archetypal circulations associated with extreme precipitation which mapped to node five.

The south Atlantic high pressure ridge extended further southward in nodes one and five and were shallower on the right hand side of the SOM space. The 500 hPa circulation of the South Atlantic High pressure was similar to the surface pressure characteristics with a shallower wave evident on the right hand side of the SOM. At the surface, an intrusion of a tongue of low pressure up the east coast of the country disrupted the formation of a high pressure circulation (nodes one, two and three). This intrusion represented the passage of coastal lows which generally precede mid-latitude cyclones. This intrusion was not as apparent in node four and absent in node five, where the inland anticyclonic circulation was present. In node five, the South Indian high pressure system was situated very close to the east coast of southern Africa and the spatial extent of the inland high pressure was at a maximum.

Surface relative humidity values of 80 % were evident over the west coast interior in all nodes. The inland extent of the band decreased in nodes four and five compared with nodes in the bottom row. A small region of maximum relative humidity values (> 85 %) was situated off the west coast near Cape Town in nodes two and three.

Synoptics states represented by nodes two and three were associated with extreme precipitation that fell over a number of days in relatively low daily amounts and not as a single event with a high precipitation volume. In July 2001, these nodes had five days map to them which recorded 43 % of the extreme precipitation experienced in this month. Distinctive circulations associated with these nodes were a low pressure trough at lower latitudes, a shallower high pressure ridge over the south Atlantic and a region of high relative humidity off the west coast close to Cape Town. The remaining nodes had four days map to them for this period, one each to nodes one and four and two days to node five.

Nodes one and four had only one day each map to them throughout July but these experienced very high volumes of precipitation (22 mm and 34 mm respectively). Circulation characteristics of these nodes again included a deep low pressure trough at lower latitudes, however, a distinctive high pressure ridge to the west of the trough was evident. Node one was associated with the passage of a coastal low and node four with a small region of anticyclonic circulation over the interior of the country. Values with relative humidities of 80 % did not extend very far inland over the west coast and were restricted largely to the coastal region for both nodes.

Node five was characterized by a low pressure trough at higher latitudes and relative humidities of 80 % that were restricted to the coastal region of the west coast. The distinctive feature of this node was the position of the the South Indian High pressure system close to the east coast of South Africa and an anticyclonic circulation over the interior. Should this circulation be stationary for any length of time, it could potentially retard or block the eastward passage of low pressure troughs. This would cause cold fronts to have a longer residence time over the region and result in increased precipitation. This feature resembles blocking highs that affect South African circulation which generally have centers situated near 55^0E, and a lifespan of a few days (Tyson and Preston- Whyte, 2000). An inspection of the synoptic conditions of days that mapped to this node confirmed that many days did display blocking high characteristics. Additionally, the circulation state persisted over two days for over half the number of times the node was mapped to.

3.7 Trends in circulations associated with extreme precipitation

Two data sets are used to assess trends in the occurrence of extreme storms over the 23 year study period, the extreme data set extracted from the interpolated CCWR data and data produced by the SOM. An initial assessment was made to assess trends of extreme precipitation days over the 23 year time period using extracted 90^{th} percentile CCWR data. Thereafter, data from both SOMs are used to assess trends in extreme precipitation days as well as synoptic types associated with these days. Results from the interpolated CCWR data are presented first after which are the results obtained from the SOM.

The extracted 90^{th} percentile data consisted of 488 days over the 23 year time span whose distribution of extreme precipitation days per year varied. An increase in the number of days that experienced extreme precipitation was evident from the early 1980's and peaked at 30 days for the winter of 1987 (Fig. 3.18). Throughout the early and mid 1990's, the number of extreme days per year varied between 28 and 19. From 1997 -2000, the number of extreme days per year dropped but did not reach the lowest records of 1979 and 1982. In 2001 the number of extreme precipitation days increased again to 24.

A multiple regression analysis showed a positive trend through the years (slope of 0.3) although

this was not statistically significant at the 5 % level ($p < 0.28$). Nine years fell within the 95th percentile confidence limits. There was also a very weak positive correlation of the number of days which experienced extreme storms with time of 0.23 ($p < 0.05$).

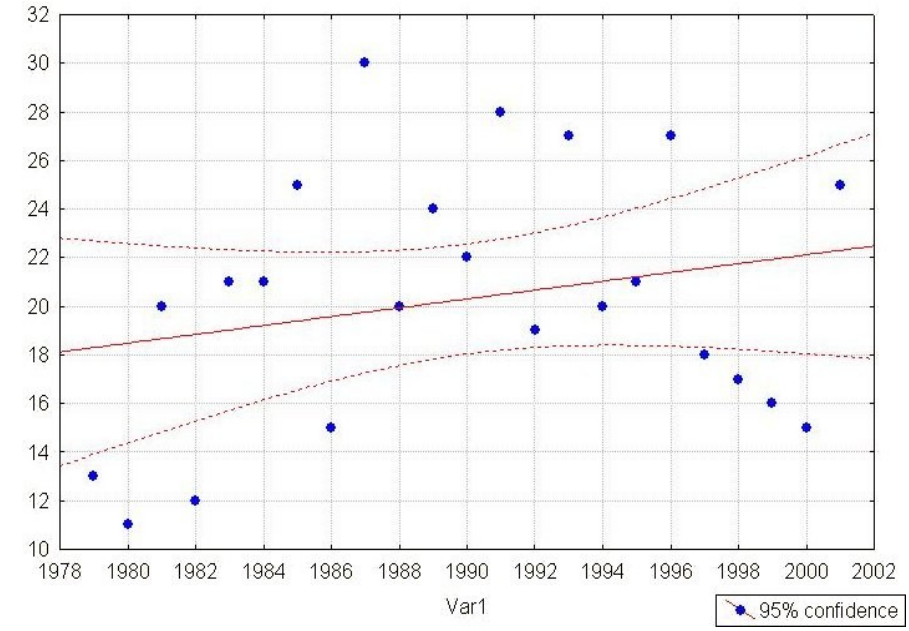

Fig. 3.18. A regression analysis of the number of days in each year experiencing extreme precipitation over the 23 year time period using a logarithmic regression.

This additional investigation of these extreme data (additional to the investigation in the Introduction which used station data) revealed no significant trends in the occurrence of extreme precipitation days in the winter seasons of the 23 year period for the region. It should be borne in mind that the data used here are gridded data with a 50 km resolution. At this resolution there is a smoothing out of any topographic weather modification by orographic features so no information is available for an assessment of trends which might reflect the topographic influence. This further highlights the importance of station-based trend analyses in topographically complex regions.

Although not providing information at the station scale, the SOM data could be used to examine trends in synoptic states that were associated with extreme precipitation days in the region. In order to do this, the 1979-2001 period was divided into a 12 year period (1979-1990) and an 11 year period (1991-2001). Data for these respective sub-periods were passed through the trained SOMS and their frequency maps differenced such that data from the former period was subtracted from the latter. This simple technique produced anomaly maps which provided information on changes in nodal loading throughout the 23 year time period and also changes in the frequency of occurrence

of days experiencing extreme precipitation.

The initial SOM, which used all winter data, displayed frequency anomalies that were both positive and negative across the SOM space (Fig. 3.19). Regions with negative anomalies represented nodes to which more days mapped in the former period than the latter, indicating a decrease in these types of circulation with time. Similarly, regions with positive anomalies indicated an increase of associated circulations with time. Synoptic states that are associated with precipitation in the South-Western Cape displayed both positive and negative anomalies; positive at nodes 5, 10 and 20 and negative at nodes 15, 16 and 19. The combined positive frequency anomaly across these respective nodes was 1.2 % and for nodes which displayed a negative frequency anomaly 1.8 %. Thus, across nodes associated with winter rainfall there was an overall negative difference throughout the 23 year study period, indicating a slight decrease of circulations associated with winter rainfall.

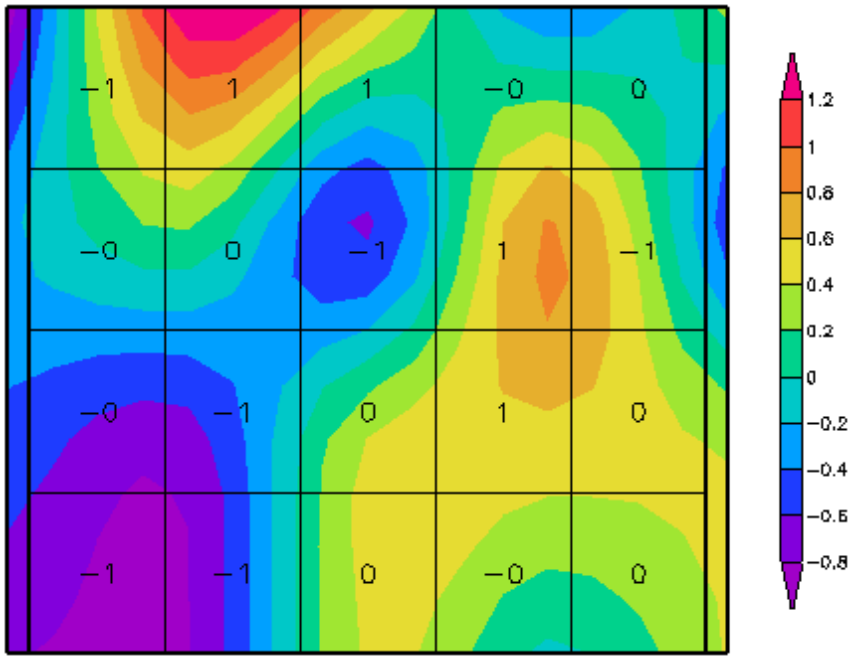

Fig. 3.19. Percentage difference in the frequency of synoptic types between the periods 1979-1990 and 1991-2001.

Nodes representing synoptic states generally not associated with precipitation also displayed positive and negative frequencies. Nodes in the lower left of the SOM (nodes 1, 2, 6 and 7) and node 13 showed a decrease in the frequency of these types of circulations. Together, these nodes accounted for 19 % of the initial SOM mapping and displayed a negative anomaly of 2.8 %. However, nodes 3, 4, 8, 9, 12, 14, 17 and 18, which accounted for 41 % of the initial SOM

mapping, displayed positive frequency anomalies. The combined positive frequency anomaly across these nodes was 4.5 %, indicating that there was an increase in the number of winter days associated with generally non-precipitating circulations. The trend at node 17 was statistically significant at the 95 percent level (p=0.02). This was the only statistically significant trend evident.

The majority of days which experienced extreme precipitation during winter mapped to nodes 1, 5, 10, 15, 16 and 20 of the initial SOM (see Fig. 3.8). The frequency anomaly map showed an increased mapping of days to all these nodes except node five (Fig. 3.20). The percentage frequency increase of days that experienced extreme precipitation and mapped to these nodes was 16.6 %, including node five's negative value. This indicated an increased frequency of synoptic conditions associated with extreme precipitation over the 23 year study. Days which mapped to these nodes included the days in August and July 2001 (listed above) which mapped to nodes 10, 15 and 19. Further analysis indicated statistically significant changes at the 95 percent level only at nodes 18 and 19. The change in node 18(19) was from 2(5) events in the period 1979-1990 to 14(15) in the period 1991-2001. These two nodes only represented 36 days of the time series but the majority of these are in the latter time period. These circulations may be associated with convective activity through the intrusion of the sub-tropical low into the region.

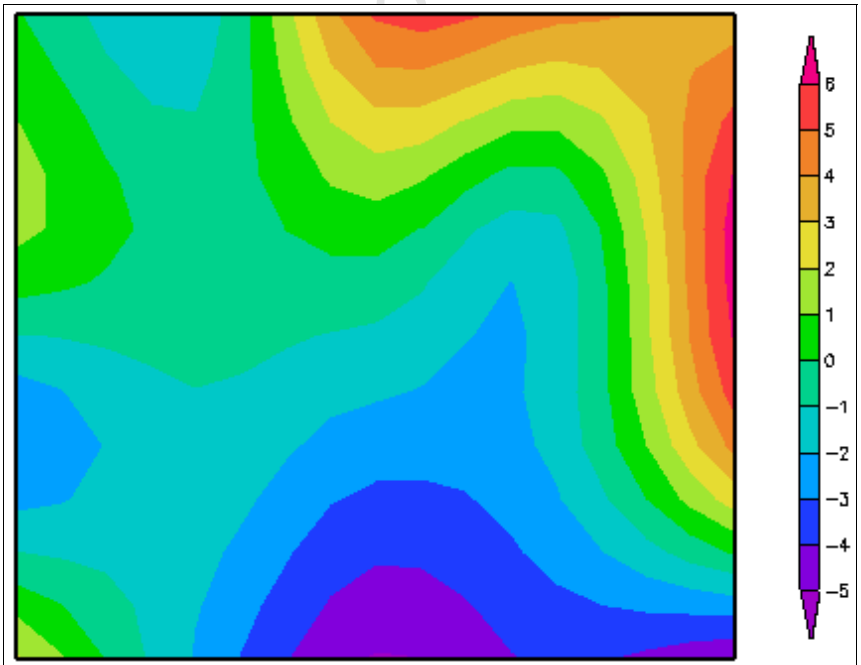

Fig. 3.20. Percentage difference in the frequency of synoptic types associated with extreme precipitation amongst all winter archetypes between the periods 1979-1990 and 1991-2001.

The second SOM, trained using only data from days that experienced extreme precipitation, had the majority of days map to nodes at the perimeter of the SOM (see Fig. 3.10). A similar analysis was performed on this data. Immediately evident was a very large negative trend in the top left of the SOM (nodes seven and ten) and a very large positive trend in the bottom left (node one) (Fig. 3.21). Synoptic states associated with nodes seven and ten displayed a strong ridging South Indian anticyclone and relatively weaker low pressure trough and had 16 % of the training data map to them. Node one was associated with a deep low pressure trough at the surface as well as at the 500 hPa level, the passage of a coastal low around the south and east coast of South Africa as well as a distinct high pressure ridge to the west of the trough at the surface. This node had 9 % of the training data map to it. The nodes associated with extreme precipitation in July and August 2001 mapped to nodes one to five.

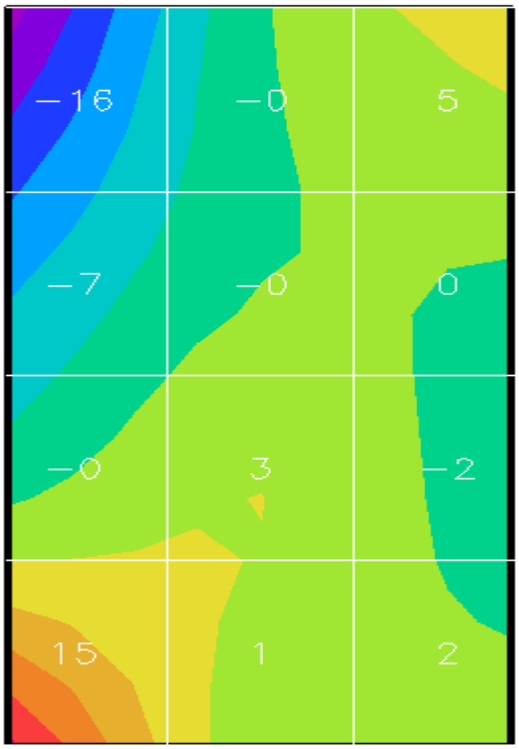

Fig. 3.21. Percentage difference in the frequency of synoptic types associated with extreme precipitation between the periods 1979-1990 and 1991-2001.

With the exception of node four, whose trend was weakly negative, all the remaining nodes displayed positive trends. More rigorous statistical testing revealed that the trends in Fig 3.21 in nodes 1, 3 and 10 (p=0.0002, 0.009 and 0.002) (Fig. 3.22).

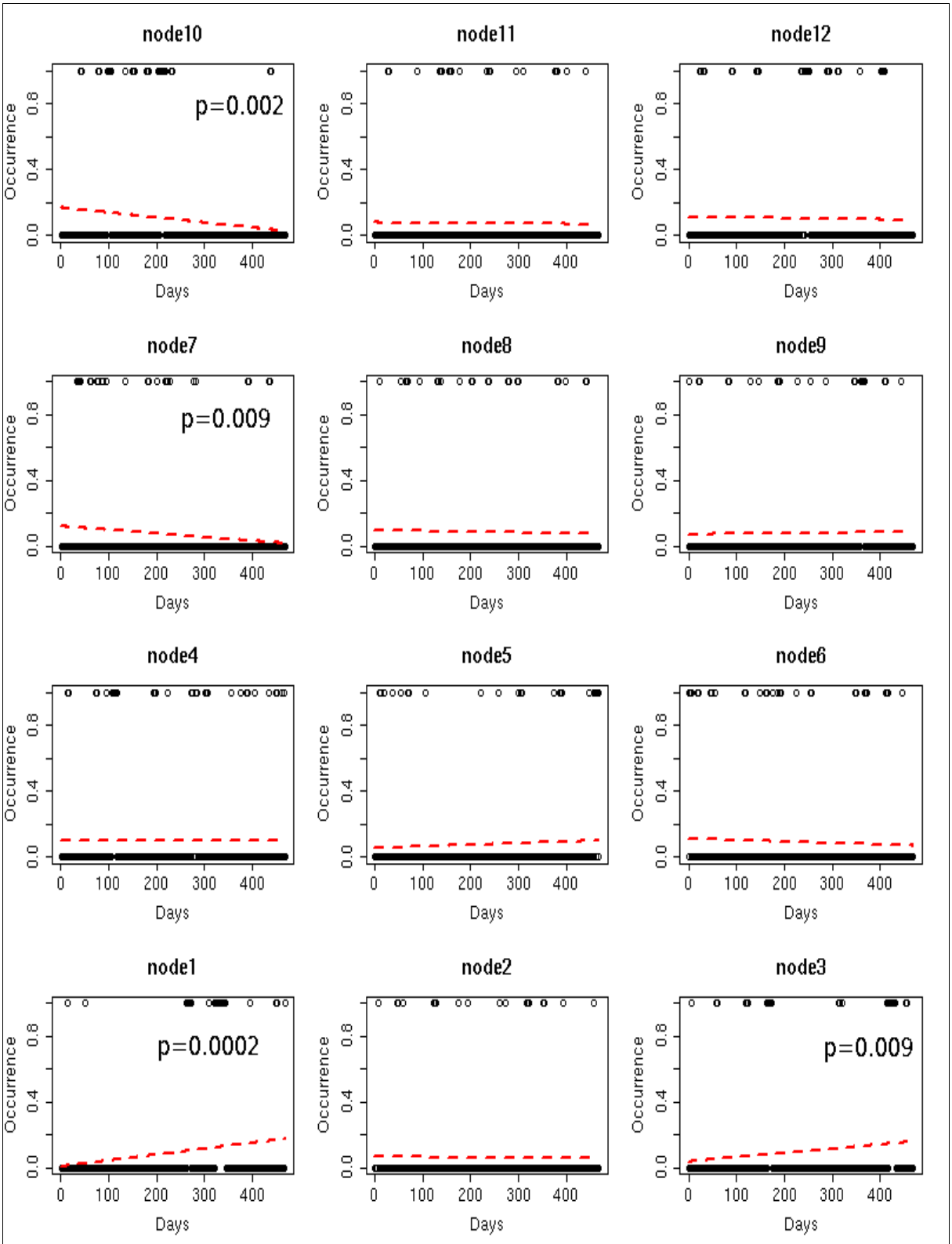

Fig. 3.32. Trends in extreme precipitation circulations (significant changes labeled).

From the extreme precipitation data, it was evident that synoptic states associated with strong high pressure ridges and weaker low pressure troughs displayed a negative trend and those associated with deep low pressure troughs a positive trend. Thus the frequency of synoptic states associated with extreme precipitation has increased over the 23 year study period.

3.8 Summary

The initial SOM identified 20 synoptic archetypes characteristic of winter circulation over South Africa. Synoptic conditions for days which experienced extreme precipitation in the greater Cape Town region were also successfully identified as the passage of low pressure troughs in the mid-latitudes. Almost three-quarters of days which experienced extreme precipitation mapped to nodes with these synoptic archetypes.

The second SOM, trained only with data from days that experience extreme precipitation in the 23 year period, identified synoptic states which were associated with the extreme events. These states were all characterized by low pressure troughs whose centers were at relatively lower latitudes as well as higher relative humidity values over the west coast (80 % and above). Additional characteristics, such as a deep high pressure ridge behind the trough, a strong South-Indian high pressure circulation or elevated relative humidity values were distinctive to certain regions of the SOM and were associated with higher or lower relative daily precipitation volumes.

When considering days in July and August 2001 with extreme rainfall, days with different rainfall characteristics mapped mapped to various nodes. For example, node five had the most days map to it and was associated with the most rainfall in the region. Other nodes had fewer days map to them but these days experienced exceptionally high rainfall amounts e.g. nodes one and four had only one and two days respectively map to them but these days experienced highest daily rainfall amounts. Thus, no one particular circulation archetype could be identified as being associated with extreme precipitation in the region based on July and August 2001 extreme rainfall days. However, all the extreme precipitation days in these two months were associated with a cluster of nodes near the bottom of the SOM (nodes one to five) indicating a high probability of extreme precipitation for days displaying these synoptic states.

The first SOM indicated a positive trend in synoptic states generally not associated with precipitation as well as a weak negative trend in synoptic states generally associated with precipitation. However, the frequency of synoptic states associated with extreme precipitation displayed a positive trend in both SOMS. It should be noted, however, that these trends are statistically not significant and require a more rigorous analysis. Despite this, the fact that the circulation modes show a shift towards more frequent extreme precipitation in the region reflects the findings of a number of works listed in the Introduction (e.g. Mason et al., 1999, Easterling et al., 2000 and New et al., 2006). However, the analysis of the CCWR data revealed no significant trend in the occurrence of extreme precipitation days over the 23 year period. This highlights the difficulty in detecting climate change in rainfall values alone, especially extreme rainfall. In such analyses, consideration should also be given to large scale circulation patterns of the region.

Chapter Four

Observational Data - Station Observations

4.1 Introduction

The South African Weather Service operates a network of weather stations across South Africa that provide measurements of daily precipitation and temperature. Eight such stations are situated at various locations in the greater Cape Town region and report daily precipitation amounts. Of these, four also record maximum and minimum temperatures. Data from these stations are used for validation purposes for the techniques employed in this study.

The SOM identified days that the greater Cape Town region experienced extreme precipitation. Precipitation data from the local weather stations were used to investigate extreme precipitation over the July-August 2007 period and if days that experienced extreme precipitation were identified by the SOM, which used a more homogeneous gridded product as training data. The validation of the SOM results is necessary to justify the selection of days which were to be simulated at high resolution.

Additionally, the station data were also used to determine the adequacy of radar-derived precipitation in the region (Chapter 5) as well as validation of simulated temperature and rainfall fields in Chapters 6 and 7 respectively. Thus station data formed the basis of the verification of the SOM results and model output and were also used to establish the robustness of radar-derived precipitation data.

In this chapter, station data of days which were identified by the SOM (and selected for high resolution simulation) are analyzed and discussed. However, before this is done, a very brief overview of winter weather systems that affect the region is presented to contextualize rainfall in the Cape region as well as the nature of the topographic modification of the weather by the Cape Peninsula. The chapter concludes with a discussion of the usefulness and limits of the station data.

4.2 Winter weather in Cape Town

Cape Town is a winter rainfall region that receives it's rain primarily through the passage of mid-latitude cyclones in the westerly wave. Weather associated with the passage of a front may be categorized into pre-frontal, frontal and post-frontal stages (Tyson and Preston-Whyte, 2000). Pre-frontal conditions typically consist of north-westerly winds and subsidence induced clear skies. A coastal low (a shallow, coastally trapped closed cyclonic circulation that forms on the west coast and propagates eastwards around the coast of the country) may also form with characteristic warm 'berg winds' at it's leading edge and cooler fog conditions at the trailing edge. Frontal conditions are generally associated with widespread rainfall, strong northerly to north-westerly winds and a drop in temperature. Post-frontal winds usually have a strong southerly component and advect cold, polar air into the region. Light, post-frontal rainfall may occur as squalls as the remnant of the front moves through the region. These stages are generalizations and the progression described above may vary and exhibit different weather characteristics, e.g. if two fronts are in close proximity there may be no southerly flow and pre-frontal rain may be experienced before the second front arrives, coastal lows may not form with an approaching front.

The synoptic scale circulations interact with the Cape Peninsula and results in topographically modified mesoscale circulations over the greater Cape Town region. The Cape Peninsula runs for 50 km in a north-south direction from Table Bay to Cape Point and is 3 km and 11 km wide at its narrowest and widest points respectively. It can be divided into three parts: a northern section from the face of Table Mountain to Constantia Nek featuring its highest points; a central section between Constantia Nek and the Noordhoek Valley; and a southern section south of Noordhoek Valley, which is of generally lower elevation (Fig. 4.1). It is bordered by the Atlantic Ocean to the west and False Bay and the low-lying Cape Flats region to the east. The complex topography of the peninsula modifies circulation and can result in a wide variety of mesoscale phenomena such as split flow, orographically enhanced rainfall and rain shadows.

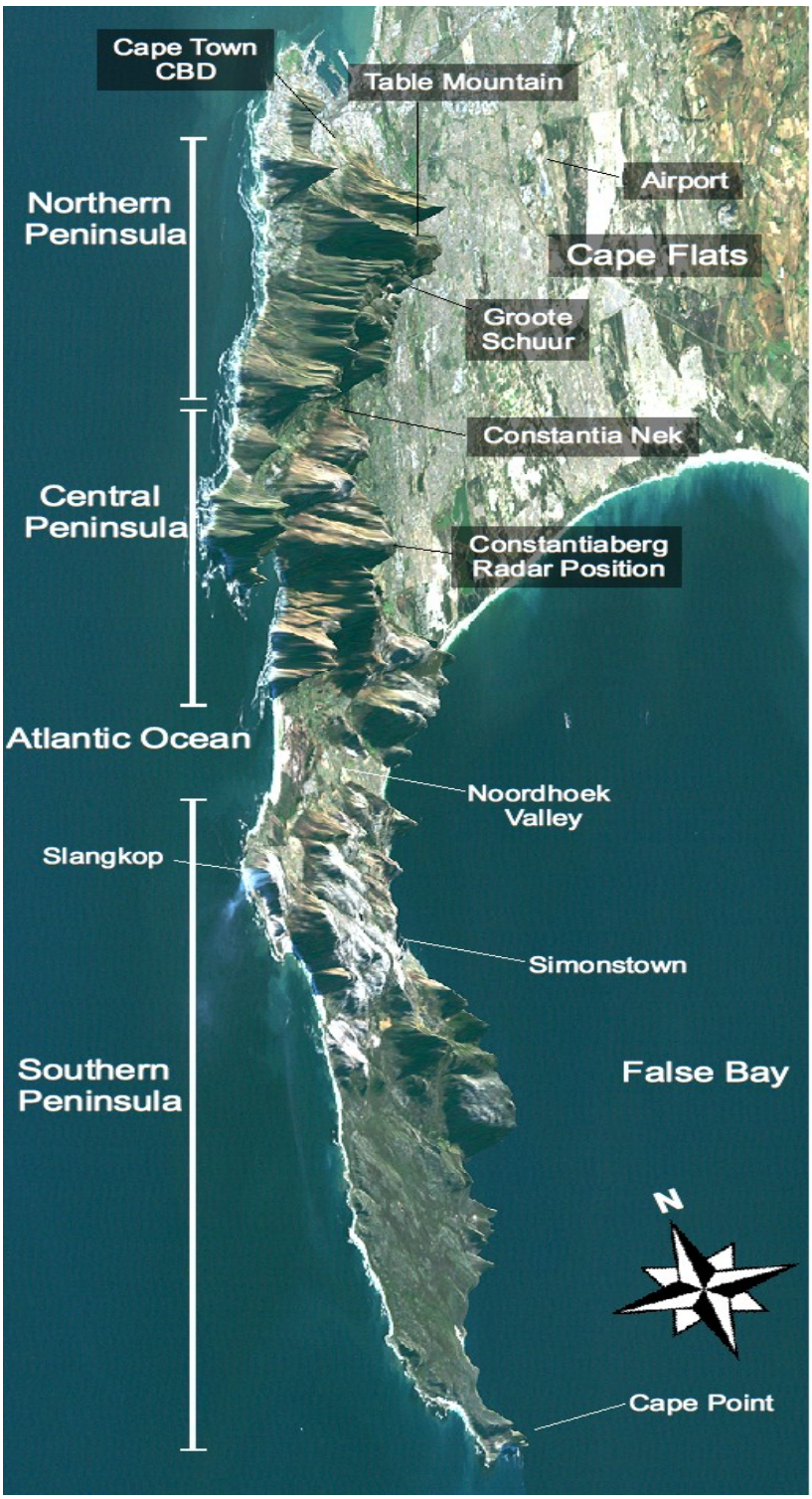

Fig. 4.1 Landsat/Shuttle Radar Topography Mission (SRTM) image of the Cape Peninsula. In this image the viewing angle is from the west and the topography of the peninsula is exaggerated which serves to demonstrate its weather modification role. Image courtesy of NASA/JPL/NIMA.

4.3 Case study selection

Cape Town receives most of its rainfall in the winter months of June, July and August. As mentioned in Chapter One, during July and August of 2001 flooding in the region affected approximately 31 000 people and many of the worst affected regions were declared disaster areas. The total cost of the flooding was estimated at being over USD2 000 000. As a result of the severity of these floods, days in these two months which recorded very heavy rainfall were identified in the station record. This was done as much for comparison with the results produced by the SOM using gridded data as for an investigation into the spatially heterogeneous nature of extreme rainfall in the region.

Six of the days in July which were identified by the SOM recorded very high precipitation amounts. These were the 2nd, 3rd, and 4th and the 17th,18th and 19th which realized 80 % of the total precipitation for the month at the Airport. These days experienced six mid-latitude cyclones and were selected to be simulated by the regional climate model. However, radar data, which would have been used for verification of the simulated precipitation data, were not available for July 2001. An additional period from the 22nd to 29th August 2001, in which the SOM identified two days that experience extreme storms, was also chosen for simulation. The August period also experienced a weak cold front, a coastal low, land-sea breezes and a well defined ridging high pressure system in addition to the two extreme storms. These synoptic states were useful as they could be used to validate the regional scale simulation of multiple weather regimes over the entire eight day period.

A summary of the weather conditions at Cape Town for these three periods is presented in Table 4.1. Synoptic charts of the three respective periods follow in Fig. 4.2a-c. These charts cover a southern African domain and the accompanying discussion section is for this entire region. The description of the weather for Cape Town in Table 4.1 is based on the synoptic state, the station data and the discussion section shown in the synoptic charts. The charts were obtained from the South African Weather Service.

Table 4.1. Description of synoptic weather state over Greater Cape Town over the study period

Date	***Weather summary***
2 July	A cold front approached Cape Town in early afternoon; moderate north-westerly winds at 28 kilometer per hour (kmh^{-1}); cloudy with intermittent rain.
3 July	A cold front approached Cape Town in late afternoon; gentle north-westerly winds at 18 kmh^{-1}; overcast with general rain in the study region.
4 July	A small front developed from the previous days front and made landfall in the late morning; light westerly winds at 9 kmh^{-1}; general rain across the region as showers.
17 July	A cold front passed over Cape Town in the early afternoon; near gale force north-north-westerly winds at 37 kmh^{-1}; general rain later in the afternoon.
18 July	A front made landfall near midday; near gale force north-westerly winds at 37 kmh^{-1}; general rain.
19 July	A cold front passed over Cape Town in the early afternoon; near gale force north-north westerly winds at 37 kmh^{-1}; general rain later in the afternoon.
22 August	A cold front approached Cape Town; near gale force north westerly winds at 37 kmh^{-1}; overcast with light rain in places.
23 August	A cold front made landfall; near gale force north westerly winds; cloudy with general rain over the region.
24 August	Post frontal conditions; moderate westerly to south westerly winds at 28 kmh^{-1}; overcast with some light; scattered showers.
25 August	Weak pre-frontal conditions; gentle westerly winds at 18 kmh^{-1}; overcast with light rain in places.
26 August	A weak front made landfall; moderate north westerly winds; overcast with general light rain over the region.
27 August	Weak post-frontal conditions; light westerly wind at 9 kmh^{-1}; sunny with no rain.
28 August	Pre-frontal conditions with formation of a coastal low ahead of the front; moderate north westerly winds; became cloudy with general rain in the evening.
29 August	A front made landfall with general heavy rainfall in the morning; gale force south-easterly winds once the front moved past the region caused clearing in the afternoon.

4.4 Weather station data

The SAWS maintain a rain gauge network across South Africa. These instruments provided readings accurate to 0.1 mm and are accumulated over 24 hours. Across the case study region, stations are located at Cape Point, Groote Schuur, Paarl, Simonstown, Slangkop, Somerset West, Stellenbosch and the SAWS weather office at Cape Town International Airport (Table 4.2). Average annual rainfall figures (1960 to 2007) were kindly provided by the SAWS.

Table 4.2. Location of weather stations operated by SAWS in the Cape Town region.

Station	***Latitude***	***Longitude***	***Elevation (m)***	***Average annual rainfall (mm)***
Cape Point*	34.35 deg. S	18.50 deg. E	140	30
Groote Schuur	33.97 deg. S	18.47 deg. E	40	98
Paarl*	33.75 deg. S	18.97 deg. E	108	71
Airport*	33.98 deg. S	18.60 deg. E	37	44
Simonstown	34.20 deg. S	18.45 deg. E	50	55
Slangkop*	34.15 deg. S	18.32 deg. E	8	41
Somerset West	34.05 deg. S	18.85 deg. E	244	49
Stellenbosch	33.93 deg. S	18.87 deg. E	116	59

* Also record maximum temperature

Historically, the Groote Schuur and Paarl stations above have recorded highest rainfall data as a result of strong orographic forcing as opposed to, for example, the Cape Flats Airport station which receives generally less rainfall. Stations closer to the coast (e.g. Slangkop and Simonstown) also receive generally less rainfall than those further inland. The Slangkop station, as a result of it's location experiences very high wind speeds during storms. However, no wind correction is made to correct the likely undercatch of rain here which may lead to a low bias in the station's record.

The unique precipitation characteristics at each station is evident in Figure 4.2. The two wetter stations recorded averaged daily extreme rainfall of 32 and 29 mm respectively with highest values of 110 and 87 mm. The Airport and Slangkop stations recorded much lower averages of 18 and 13 mm and maxima of 61 and 37 mm respectively.

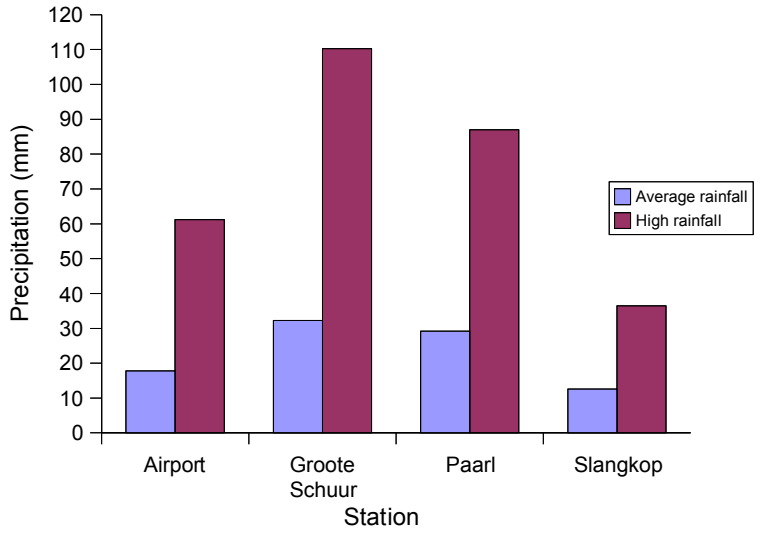

Fig. 4.2. Average and highest recorded rainfall figures of extreme rain days at selected stations from 1979 to 2000.

Despite the unique nature of each station, data recorded at these locations provided valuable insight into the spatial characteristics of rainfall in the region and provided a potential means of validating the more spatially continuous rainfall measurement that radar facilitated. Below, station data is presented as a first look at temperature and precipitation characteristics during the case study periods. Where no data were available for a particular station, these were treated as missing when performing any calculations. Thereafter the precipitation data is presented and used for the verification of the radar data.

4.4.1. Temperature

Temperature data, as daily maxima, were available for only four of the eight stations, namely Cape Point, the Airport, Paarl and Slangkop. Over the July periods, temperatures varied five degrees across all stations (Fig. 4.3). Slangkop and the Airport stations consistently recorded the warmest temperatures, averaging 16 and 15.9 °C across the six days respectively, as a result of their lower elevations and their locations compared to the other two stations (see Table 4.2). Although the Cape Point station was situated at the highest elevation of all the stations, the station at Paarl recorded the lowest maximum temperatures in five of the six days. This far inland the warming effect of the sea is much reduced compared to the location of Cape Point. Coldest average temperatures were recorded on the 3rd and 4th and were a further indicator of the intensity of the fronts that passed through the region on these days.

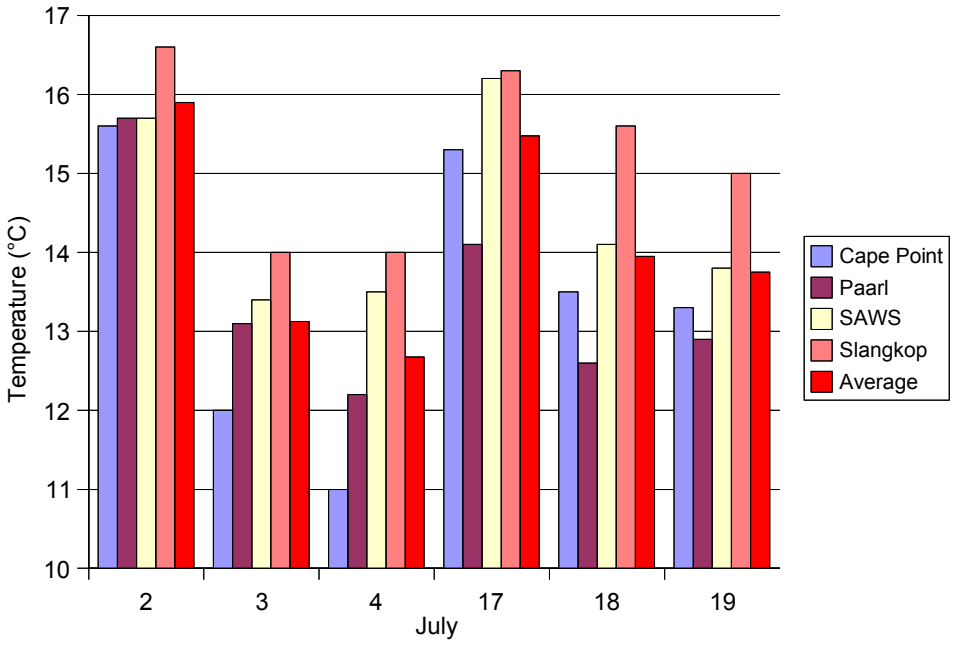

Fig. 4.3. Daily maximum temperatures for available stations over 2-4 and 17-19 July 2001

Temperature data available for the August time period reflected the passage and relative intensity of the three cold fronts as well as the clear, warmer conditions on the 27th (Fig. 4.4). The stronger fronts on the 22nd and 29th have correspondingly lowest average temperatures associated with them and the weaker front caused a lowering of temperatures by about one degree on the 25th and 26th. The fine conditions of the 27th are also evident on the 28th, indicating that the front arrived late in the evening of the 28th or early morning of the 29th. The passage of the front on the 29th and subsequent advection of cold air into the region through the southerly flow resulted in the coldest average temperature of the time period being recorded on this day.

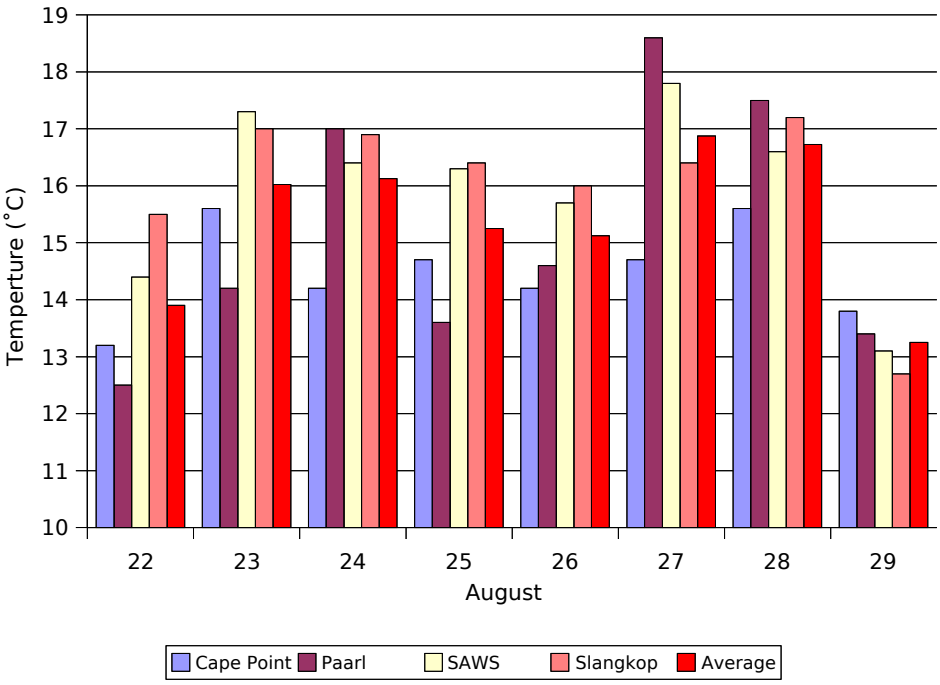

Fig. 4.4. Daily maximum temperatures for available stations from 22-30 August 2001

4.4.2 Precipitation

The passage of the six fronts in July is evident in the station data and in conjunction with the daily synoptic charts. The period of the 2nd to the 4th of July realized average daily precipitation of 33 mm per station and every station recorded a total of over 55 mm of rain in this three day period. For the period 17-19 July, stations recorded an average of 22 mm per day and all the stations recorded three day totals of 25 mm or over. The 3rd July recorded the highest amount of rainfall averaged over all stations at 42 mm followed by the 19th July with 30 mm (Fig. 4.5). Stations which recorded the highest daily totals as well as highest six day averages were Paarl (84 and 49 mm respectively) and Groote Schuur (57 and 40 mm). It should be noted the highest daily precipitation value for Paarl in the 1979-2000 dataset is 87 mm, thus the amount of rain that was recorded here on 3rd July was close to the record value of the 23 year data set. The lowest daily totals and six-day averages were recorded at Cape Point (4 and 13 mm respectively). In the low lying areas of the Cape Flats, the Airport recorded 148 mm in the six days, which was three quarters of the month's precipitation and 180 % the climatological average.

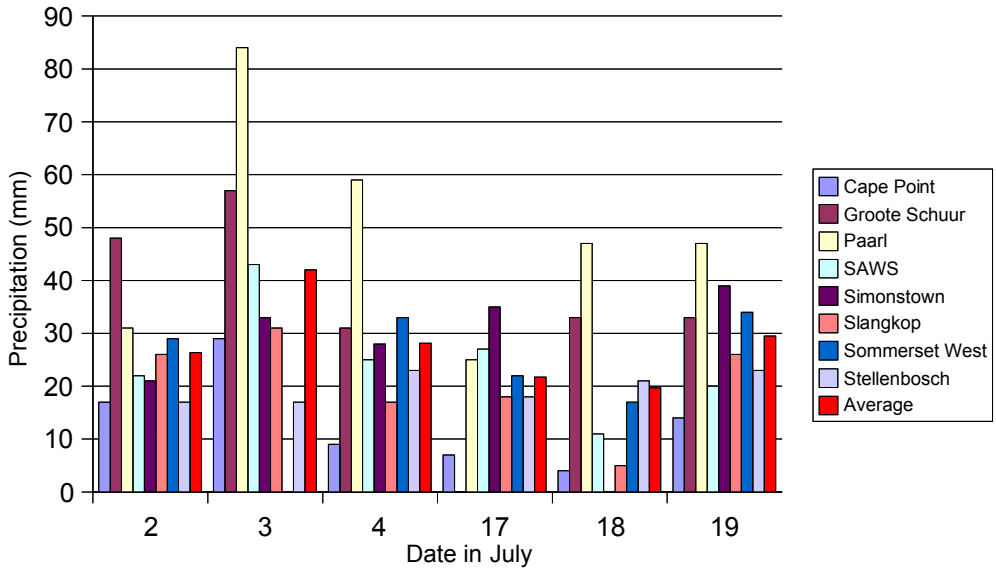

Fig. 4.5. Daily precipitation for selected stations for the dates 2, 3, 4 and 17, 18, 19 July 2001. The average column is data averaged over all stations for that day.

The July station data were compared with data of the extracted 90th percentile CCWR dataset. Percentiles of the extreme data into which the July 2001 data fell were calculated for four stations for which there were data in both datasets, namely, the Airport, Groote Schuur, Paarl and Slangkop. On the 3rd July, which recorded highest precipitation amounts, data from all these stations fell into the 97th percentile of of each stations extreme data with the exception of Groote Schuur which fell into the 89th percentile (Fig. 4.6). Rainfall averaged across the four stations for this day fell into the 96th percentile. For the three day period 2-4 July, the averaged rainfall at these stations fell into the 83rd percentile of the extreme data.

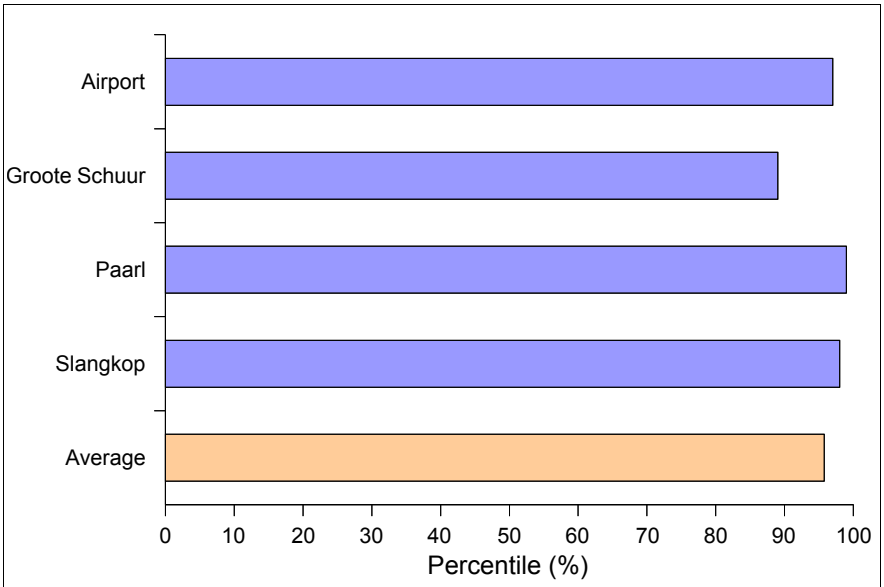

Fig. 4.6. Percentiles of extracted extreme precipitation into which precipitation that was recorded on the 3rd July fell.

On the 19th July, which recorded the second highest amount of rainfall in July, rainfall averaged across the four stations fell into the 80th percentile of the extreme storm dataset despite the (relatively) lower record for Groote Schuur (Fig. 4.7). On the 17th and 19th July, precipitation magnitudes recorded at the airport fell into the 83rd and 75th percentiles respectively and at Slangkop the 83rd percentile and 91st percentile. Precipitation magnitudes over this time period were also well above the average extreme precipitation magnitudes shown in Figure 4.2.

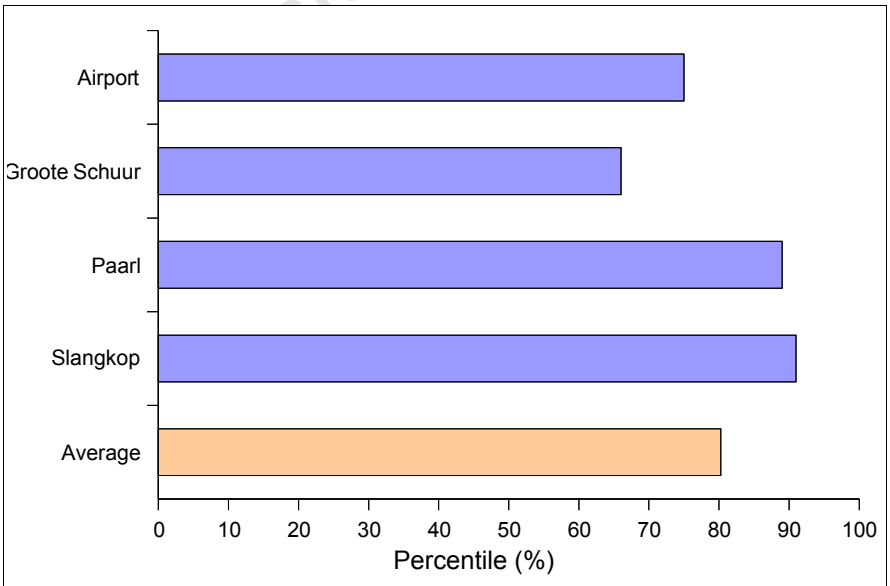

Fig. 4.7. Percentiles of extracted extreme precipitation into which precipitation that was recorded on the 19th July fell.

Percentiles across the four stations for 2nd - 4th and 17th - 19th July averaged in the 74th percentile of the extreme precipitation dataset. Thus the precipitation experienced during these periods fell into the 97th percentile of all precipitation recorded at these stations, indicating that the storms experienced in July 2001 were amongst the most severe of extreme storms in the region.

Although the precipitation volumes during August 2001 were lower than July, the rainfall experienced was well above the August climatology. Half of the total recorded precipitation for August occurred between the 22-29th and of this 82% occurred with the passage the two frontal systems on the 23rd and 28-29th (Fig. 4.8). A weaker front passed just south of the country on 26th and brought light rain to most stations. Across the eight days, precipitation maxima were recorded at Groote Schuur (228 mm) and Paarl (154 mm) with minima at the airport (37 mm) and Cape Point (28 mm).

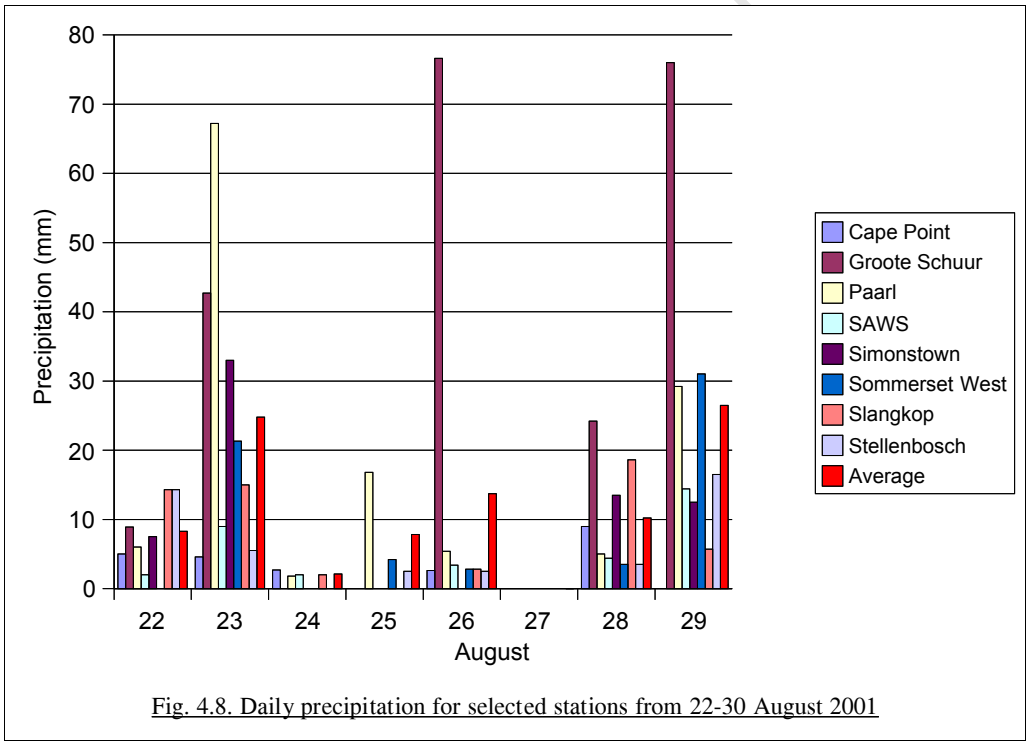

Fig. 4.8. Daily precipitation for selected stations from 22-30 August 2001

A comparison of rainfall magnitudes on the 23rd and 29th was made with the 90th percentile dataset. Data recorded at the Airport fell below the extreme rainfall average (18 mm) on both days. At Slangkop this was 2 mm above the average extreme figure of 13 mm on the 23rd but much lower than this on the 29th at 6 mm. However, Paarl and Groote Schuur recorded data at or above average extreme figures. On the 23rd, Paarl recorded rainfall in the 98th percentile of the extreme rainfall

dataset whereas on the 29th it recorded average extreme rainfall (29 mm). At Groote Schuur, rainfall on the 23rd fell into the 80th percentile and on the 29th into the 95th percentile. Rainfall across both stations for the 23rd and the 29th averaged 54 mm and fell into the 82nd percentile of these stations extreme rainfall records. The average across all four stations for these two days was 32 mm which was above the average extreme figure of 23 mm and fell into the 57th percentile of the extreme precipitation record. Although these storms were less severe that the July storms, they nevertheless fell into the 96th percentile of of all precipitation experienced at these stations.

Despite the spatially discontinuous nature of the precipitation station data, some characteristics of the extreme precipitation experienced in July and August (which were identified by the SOM) were evident. The region received above average extreme precipitation at these times, especially during July. The precipitation in July was more severe than August and more widespread. The severity of these storms was evident in the high precipitation volumes recorded as well as the high percentile placing of these days in the extreme data set.

However, station data represent some area of variable size surrounding the instrumentation (Huffman et al., 1997). Such spatially variable, point measurements are a poor representation of rainfall data at other locations under the same synoptic forcing. Additionally, the local network is unrepresentative of other locations e.g., the whole Cape Flats region is represented by only one station at the Airport and there are no stations at orographic peaks. Furthermore, the sparseness of the station network and daily nature of the data limited the ability to accurately measure the spatial and temporal passage of the fronts and the associated precipitation. It was not possible to ascertain the time of day a front made landfall or when in the day heavy precipitation occurred. There were also no station data for regions worst affected by heavy rainfall. The next chapter describes how radar data were used to provide information about spatial and temporal characteristics of precipitation in the region not discernible from the station data and also presents results of surface precipitation estimates.

4.5 Summary

Station data provided an initial, coarse examination of precipitation characteristics in the region and was used to assess storm severity. Precipitation across the region was spatially very heterogeneous

with maxima evident at the Groote Schuur and Paarl stations due to topographic modification of the rainfall. Rainfall was not recorded at all stations with each front, further demonstrating the spatial heterogeneity of precipitation distribution in the region.

The precipitation recorded in August in the two extreme precipitation days was in the 96th percentile of all precipitation and as extreme precipitation was above average. During July, the station data identified the precipitation as amongst the most severe experienced in the region in the 23 year time period. Precipitation recorded in this month fell into the 97th percentile of all rainfall data and in to the 74th percentile of the extreme rainfall data.

Despite the information available from the station data, the distribution of rainfall across the region as a spatial continuum and the timing of the events could not be accurately assessed due to the point source nature of the data and the daily temporal time scale. Radar data can be used to provide precipitation data that is spatially continuous over the region to complement the point source station data. In the next chapter, radar data is assessed to ascertain its suitability as a proxy for local precipitation characteristics over the region.

Chapter Five

Observational Data – Radar Observations

5.1 Introduction

The South African Weather Service (SAWS) operates a network of weather stations across the region of interest that records daily precipitation and temperature data. Unfortunately this network is not dense enough to accurately capture the topographically modified spatial and temporal characteristics of either variable. During extreme precipitation events, many of the regions worst affected by flooding have no rainfall measurements available. To overcome this problem, radar data is used. Radar data provides the equivalent of a very dense gauge network (a one square kilometer grid) that spans a region's spatial continuum and provides estimates of surface precipitation at this resolution. Additionally, the radar data are of a very high temporal resolution (less than five minutes).Thus the radar data adds observational information that is not discernible from station data alone.

The weather radar network operated by the SAWS consists of eleven weather radars[1], amongst which is a C-band (5.6cm) radar situated at the top of the Constantiaberg Peak (928 m above sea level) which has an effective range of about 150 km. The C-band radar are preferred in climates with predominantly stratiform precipitation such as Cape Town. Data from this radar are received locally at the SAWS office at the Cape Town International Airport and transmitted to the Meteorological Systems and Technology (METSYS) division of the SAWS. Radar data received by METSYS is processed using the Thunderstorm, Identification, Tracking and Nowcasting software (TITAN) developed by the NCAR Research Applications Programme (RAP).

TITAN has a storm tracking capability using data from weather radars operating in volume scan surveillance mode and provides information on the current and forecast location of existing storms and their size. A storm is defined as a continuous region exceeding given reflectivity and volume

1 http://metsys.weathersa.co.za/nwrn.htm

thresholds. In order to track the storms, an optimization method that matches storms at one radar volume time to those at a subsequent time is used. Based on past storm trends, TITAN also predicts future storm location and size. TITANs detection and forecast is based on 3-D Cartesian radar data (Dixon and Wiener, 1993) and uses automated forecast rules based primarily on results from Wilson and Mueller (1993). The automated thunderstorm forecast algorithm has been described in detail by Gould et al. (1993) and an initial evaluation of the automated thunderstorm forecasting rules was conducted by Henry (1995).

TITAN is able to detect convective and non-convective rainfall within mid-latitude cyclones and provides reflectivity and hence precipitation data for these systems. The radars operated by the SAWS do not have Doppler capability thus only precipitation data can be assessed. Data is published on the world wide web[2] by METSYS and also stored for research purposes. The weather radar data and the TITAN software were kindly provided by SAWS and were used to validate the high resolution simulation of precipitation by the MM5.

5.2 Radar data

Two radar products were used in the validation of the simulated precipitation fields. Radar reflectivity data were used to examine the timing and intensity of storms and derived precipitation data provided information on the daily spatial distribution of regional rainfall. Radar-derived precipitation data was tested against observed data to ascertain it's usability for the validation of model results. Only data for the 22nd to the 29th August was tested as no radar data were available for July 2001.

The location of the radar on Constantiaberg necessitated some caveats in the analysis and interpretation of the data. As the radar is situated at 928 m above sea level, reflectivity values were for this level and higher, therefore accumulated precipitation values are at this level and not at the surface. Thus in section 5.3.1, where accumulated precipitation was examined, corresponding radar-derived values and observed station data could not be precisely reconciled as rainfall distribution and magnitude between the radar-measured level and the surface may have altered slightly.

2 http://metsys.weathersa.co.za/index.html

5.3 Assessment of the spatial and temporal characteristics of precipitation through radar reflectivity

Radar reflectivity is proportional to the sixth power of the particle diameter (Rayleigh, 1871). In the radar beam, larger raindrops reflect more energy thus have higher reflectivity values than smaller droplets. Reflectivity (Z), measured in decibels (dBZ), can be negatively affected by various atmospheric and environmental conditions which need to be accounted for when processing and analyzing signal information. Returns from mountains and other non-meteorological targets (clutter), the attenuation of the radar signal when viewing weather echoes through areas of intense precipitation (especially with C-band radars), the 'bright band' (a layer of enhanced reflectivity caused by the melting of ice particles as they fall through the 0 $^{\circ}$C level) are effects that can result in erroneous interpretation of reflectivities. In the data obtained from SAWS, clutter is compensated for as part of the signal processing procedure by TITAN, so reflectivity values give a good indication of temporal and spatial characteristics of precipitation in the region. Over the Hottentots Holland, anomalously high reflectivity values are often recorded as a result of the bright band as well as clutter effects (clutter is enhanced when the ground is wet). These were masked out of the analysis to preserve clarity of the diagrams affected. Table 5.1, obtained from the SAWS website[3], provides a rough guideline to the interpretation of dBZ factors and associated rainfall characteristics.

Table 5.1. Generalized reflectivity - precipitation relationship.

dBZ	Rain rate (mmh $^{-1}$)	Comments
10	~0.2	Significant but mostly non-precipitating clouds
20	~1	Drizzle, very light rain
30	~3	Light rain
40	~10	Moderate rain, showers
50	~50	Heavy rain, thundershowers, some hail possible
60	~200	Extremely heavy rain, severe thunderstorm, hail likely

Radar reflectivities were used to assess the spatial and temporal characteristics of the storm of the 29th August (Fig. 5.1). Precipitation was evident from about 02h30 and the storm made landfall

3 http://www.weathersa.co.za/References/RadarInfo.jsp

across the Peninsula at about 03h00. The Peninsula retarded the progression of the front which eventually moved over the Cape Flats at about 05h00 as a band of light to moderate precipitation which also moved through the Noordhoek Valley. Between 05h00 and 06h00 the front cleared the Peninsula and the Cape Flats experienced generally light to moderate rainfall with heavy rain in places. A second, smaller band of precipitation was evident over the Peninsula at this time which passed over the Cape Flats at about 07h00 and brought general light rain. By 09h00 the heaviest rainfall had passed and the region experienced light rain or drizzle in places until the early afternoon. During these times the topographic effect on precipitation can be clearly seen in the south east lee of the Peninsula as the rainfall field is spatially larger over False Bay and reflectivities higher in this region. The small circle in the immediate vicinity of the radar with with very high reflectivity values, evident in the last three panels was an error in the reflectivity processing sequence by the radar and not rainfall (de Waal, pers. comm). This artefact was subsequently evident in the accumulated precipitation field as well. The front affected the region for about nine hours, the heaviest rainfall occurring in the early and mid-morning.

A similar analysis for the weaker storm on the 23rd showed that it made landfall at about 14h10. By 15h30 an initial band of precipitation had reached the Cape Flats, it's movement again retarded by the Peninsula, and a second band approached the coast. The second, more extensive band of precipitation made landfall at about 16h45 causing some moderate rainfall over the Peninsula between 17h00 and 19h00. The moderate rainfall tracked over the Cape Flats between 19h00 and 20h30 as the Peninsula cleared and the remnants of the storm passed through the region by 21h30. The front affected the region for about six hours, heaviest rainfall being experienced in the mid-afternoon and early evening.

Using only reflectivity data, it was possible to examine the spatio-temporal characteristics and intensities of the storms as they made landfall and moved across the Peninsula to the Cape Flats. Regions that experienced high rainfall rates could be identified as could the duration of the heavy rainfall. Radar reflectivity data thus provided useful information of the characteristics of the storms, which alone would have facilitated the testing the temporal accuracy of the four-hourly simulation data. However, in addition to the spatio-temporal information, radar reflectivity data can be also related to surface precipitation. In the following section, radar-derived precipitation data was examined against station data to ascertain if precipitation volumes could be accurately estimated and used in simulation verification.

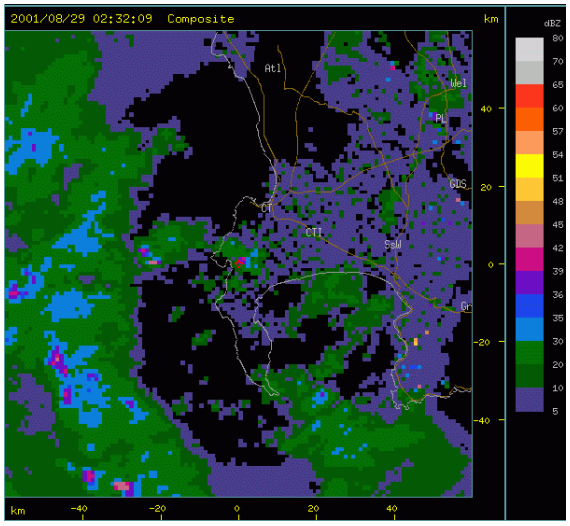

02h32

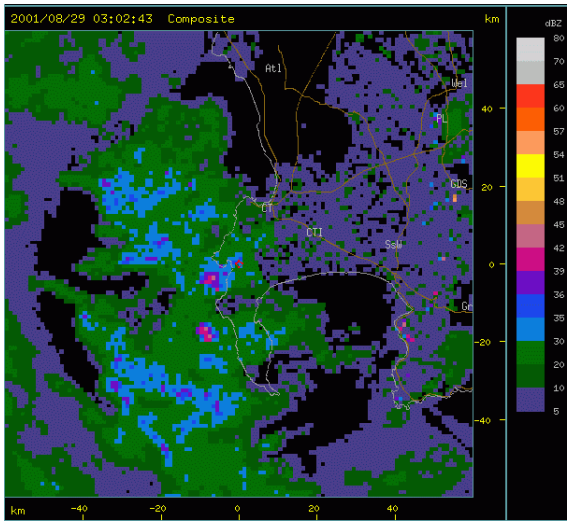

02h43

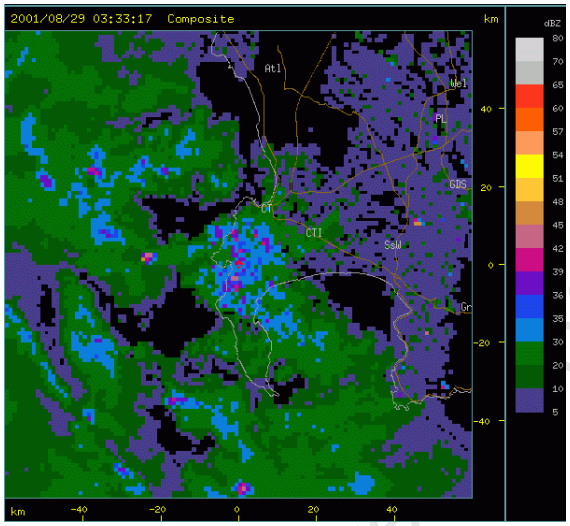

03h33

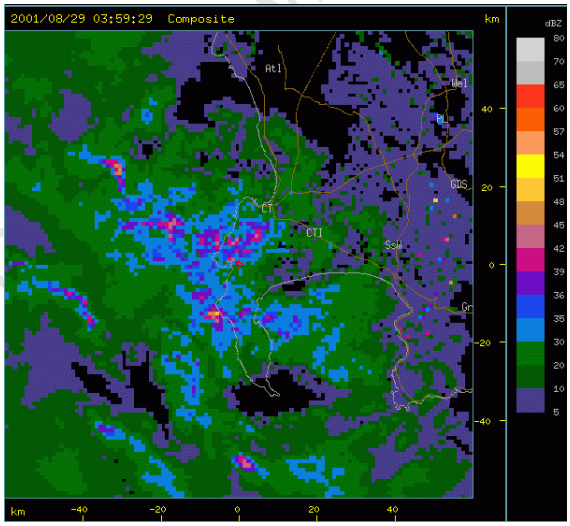

03h59

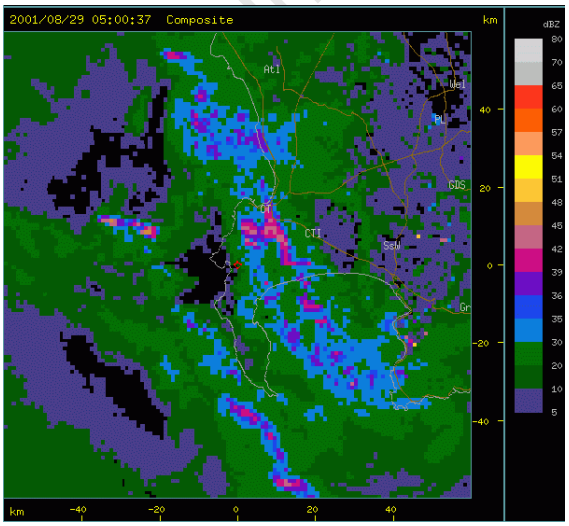

05h00

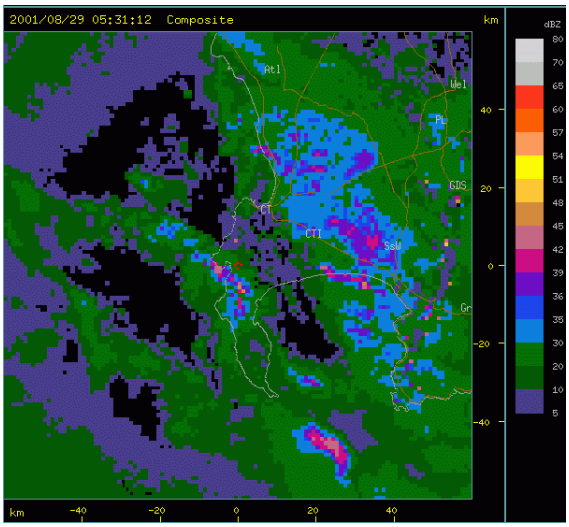

05h31

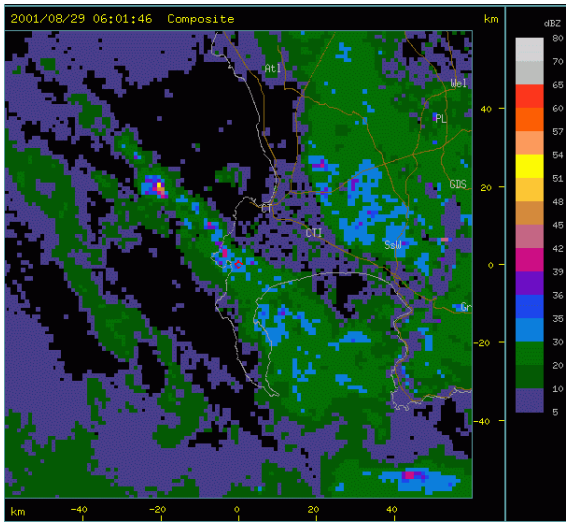

06h01

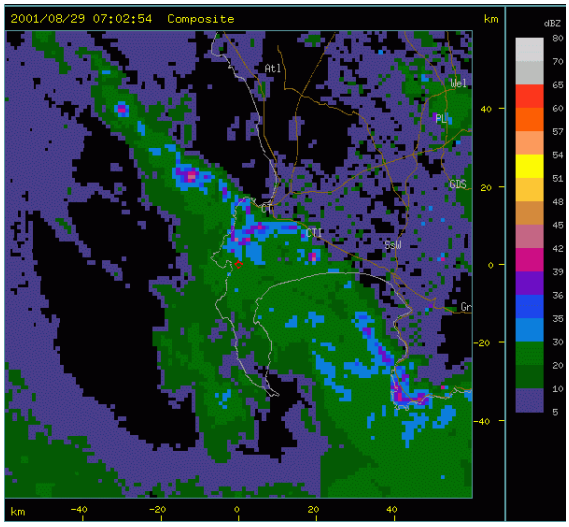

07h02

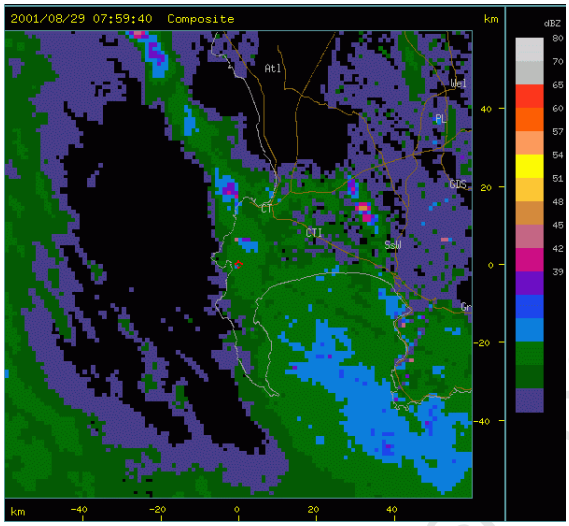

07h59

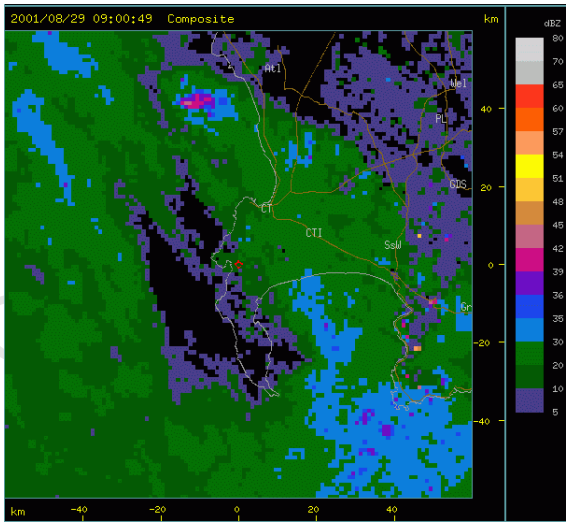

09h00

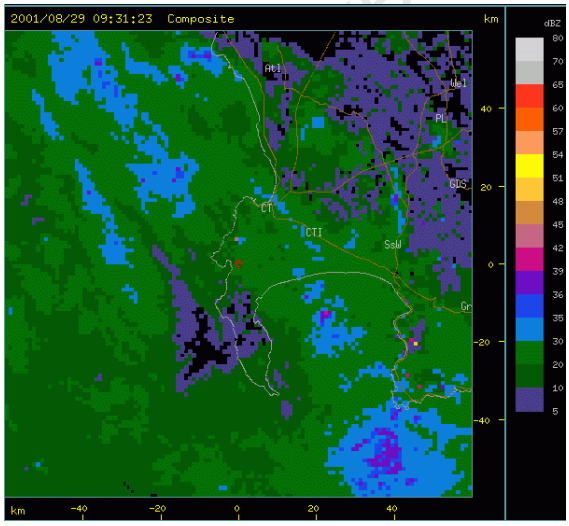

09h31

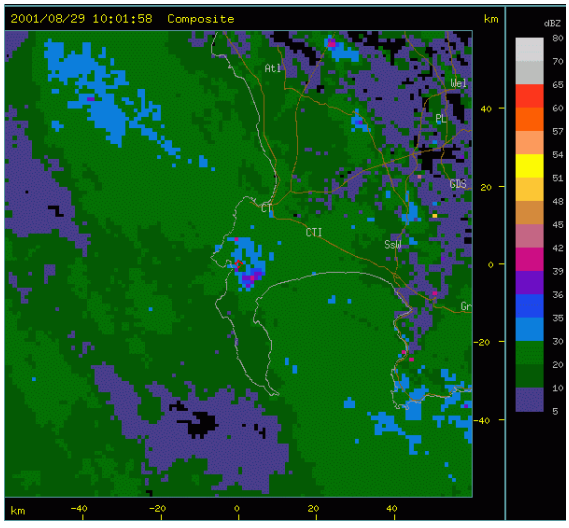

10h01

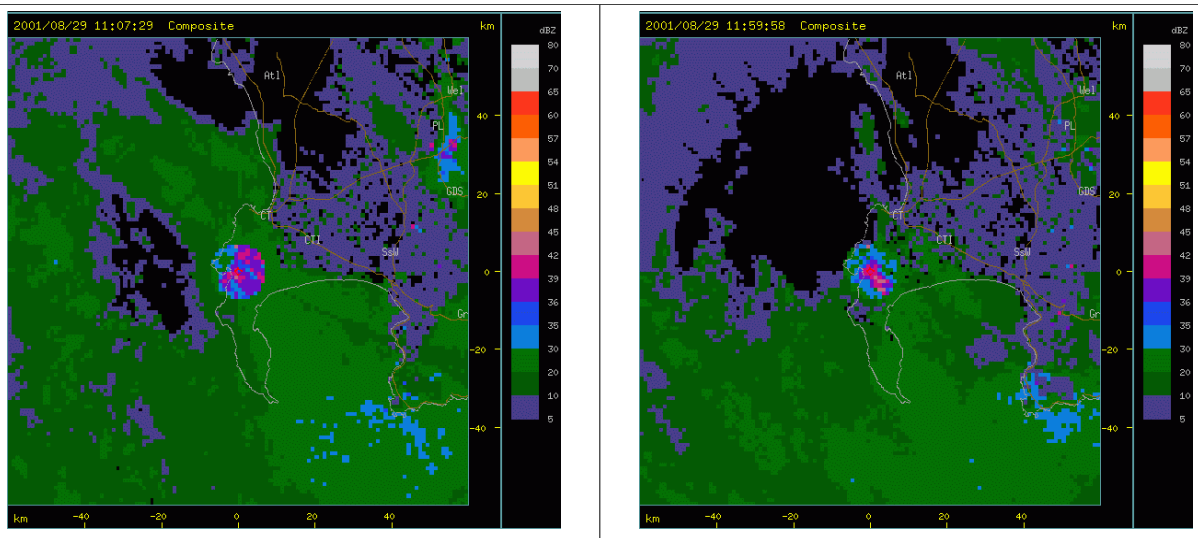

11h07 11h59

Figure 5.1. Radar reflectivities at selected times on the 29th august 2001 showing the spatio-temporal nature of the cold front and associated intensity in precipitation.

5.4 Relating reflectivity to precipitation

Two empirical approaches are used to relate radar reflectivity (Z) to rainfall rate (R), the power law regression and the probability matching method. The first is based on the physical relation between rain parameters (rain rate, density parameters) and reflectivity (Marshall and Palmer, 1948) while the second classifies the type of rain (e.g. drizzle, thunderstorm, convective) using objective criteria before deriving a Z-R relation (Calheiros and Zawadedski, 1987). Haddad and Rosenfelt (1997) mathematically justified each approach and suggested that if the original data was largely uncategorized, the first approach should be used.

As the precipitation data in this study is uncategorized, the power law regression method was used. The relationship between Z and R is represented as $Z = aR^b$, where a and b are empirically-derived constants that are related to the type of precipitation experienced in a region (Rinehart, 1991). The most common form of the Z-R relationship is for rain that assumes a Marshal-Palmer drop size distribution which sets $Z = 200R^{1.6}$. However, optimal Z-R relationships are specific with respect to precipitation type (e.g. convective versus stratiform), location (e.g. continental versus maritime) and the influence of orography. Thus many Z-R relationships have been reported in the literature (e.g., Stout and Mueller, 1968; Battan, 1973; Rosenfeld and Ulbrich, 2003; Steiner et al., 2004).

No empirical study has been performed to ascertain an optimal Z-R relationship for rainfall in the Cape Town region, only more convective, interior regions of South Africa have been investigated (van Heerden and Steyn, 1999). As it falls beyond the scope of this study to investigate this relation closely, the Z-R relationship selected here is based on stratiform, non-cellular values of *a* and *b* found in the literature (e.g. Batten, 1973; Austin, 1987) as well as discussions with Karel De Waal of METSYS, who is responsible for radar-derived products of the SAWS. The relationship was set such that $Z = 100R^{1.4}$.

5.4.1 Accumulated precipitation

Accumulated precipitation data was derived using software included with TITAN that calculates rainfall rates and then accumulates the rainfall over a specified time period. Using the above Z-R relation, daily derived precipitation values were compared against daily station data in the study region for the 23rd and 29th August. The average value of derived precipitation for nine pixels in a 3x3 matrix over each respective station was used for the comparison with the station data where the station was situated in the center of the matrix.

For all stations except Slangkop, precipitation on both days was underestimated, most significantly at the Groote Schuur and Paarl stations. Observed data, summed from all stations over both days, showed the radar to underestimate precipitation by by 44 %. However, when the Groote Schuur and Paarl stations were excluded from calculations, radar-derived precipitation estimations were only 14 % lower than observed data (Fig. 5.2). The exclusion of Groote Schuur and Paarl was deemed not likely to adversely affect the validation of radar-derived precipitation in this study as these stations are subject to complex topographic forcings which could not be captured given the location of the radar. The results below thus exclude these two stations.

Total recorded rainfall on the 23rd across stations was 81 mm with radar estimations of 75 mm, an underestimation of only 6 mm (7 %). On the 29th total recorded station rainfall was 67 mm and radar estimations 51 mm, an underestimation of 16 mm (24 %). The primary reason for the higher difference on the 29th was an underestimation at Stellenbosch of 9 mm, which is an historically wetter station. At the Airport, which is the only station in the Cape Flats (where the impact of flooding on the population is greatest), the underestimation was 1 mm on the 23rd and 4 mm on the

29th.

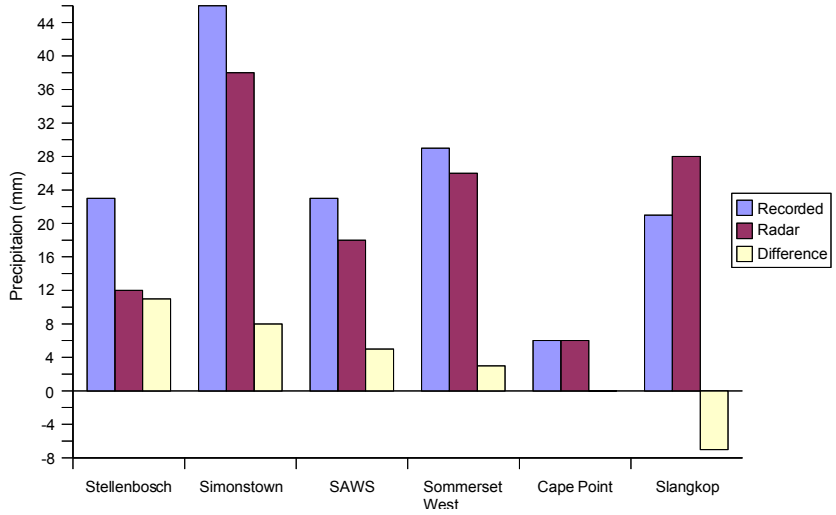

Fig. 5.2. Observed vs radar-derived precipitation values at selected stations for the 23rd and 29th August.

The distribution of the accumulated precipitation on the 23rd and 29th is shown in Fig. 5.3 and Fig. 5.4 respectively. The radar location is in the center of the image and the colour key is in millimeters of rainfall. The coastline is grey and major roads are brown in colour. Station data for the respective days are also shown on the map.

On the 23rd, the whole region experienced light rainfall of over 4 mm as indicated by the light and dark blue distribution. Embedded in this, two further significant precipitation distributions could be seen, a broader band that stretched from the northern and central Peninsula across False Bay to Cape Hangklip and a second, thinner band slightly north of the thicker band that stretched from

Milnerton across the northern regions of the Cape Flats to Somerset West. A band of lower rainfall values was located between these two (in which the Airport lies). Precipitation can be seen to be spatially heterogeneous across the region due to topographic modification. Highest precipitation amounts (> 20 mm) were confined largely to the northern and central Peninsula. On the Hottentots Holland mountains, bright band effects could be seen and very high values were masked out to preserve the clarity of the map.

On the 29th, two bands of heavier precipitation were embedded in a region of lighter precipitation. A thicker band extended from north west of the Peninsula, over the northern and central Peninsula to south of Cape Hangklip. Heaviest rainfall values were seen in this band. A thinner band was to the north of the thick band and extended over the northern parts of the Cape Flats. The spatial extent of rain in the 29th was greater than on the 23rd, as was the precipitation volume, which was also indicated in the observed data.

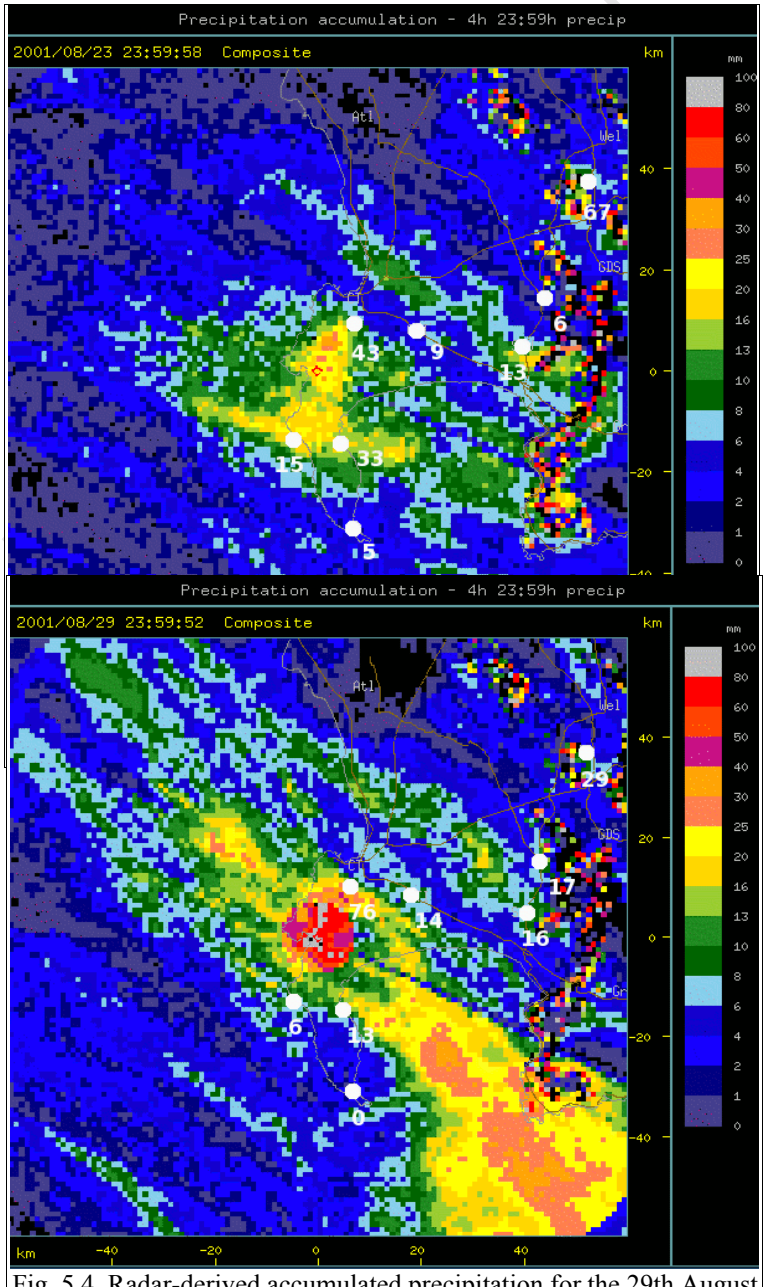

Fig. 5.4. Radar-derived accumulated precipitation for the 29th August with station data.

5.5 Summary

The radar data provided information on the spatial distribution, intensity of rainfall and timing of the storms over the entire region at an effective 1x1 km resolution. Radar data were initially validated against station data to check the reliability of radar-derived precipitation data over the region. Although it was not possible to perform any kind of statistical significance tests with such a small sample, the radar-derived precipitation generally underestimated precipitation, especially at stations that experienced historically high, topographically enhanced rainfall, such as Groote Schuur and Paarl. At other stations, however, although there was also a general underestimation of precipitation, this underestimation was small. The spatial daily derived rainfall field indicated that highest rainfall volumes fell over the northern and central Peninsula and in its lee. Two bands of rainfall with a north-west/south-east orientation were evident, a smaller band to the north of the Cape Flats and a larger band that extended from the Peninsula over False Bay.

As a result of the relatively small difference between station data and the derived precipitation product, the radar data could be used together with observed data to examine spatial and temporal characteristics of rainfall in the region. Radar reflectivity data were therefore used to test the temporal, spatial and intensity characteristics of the simulated precipitation fields and radar-derived precipitation data were used as proxy data where observed precipitation data were not available.

Chapter Six

High Resolution Simulations – Model Configuration and Initial Results

6.1 Introduction

Regional climate models (RCMs) have been used as research tools to advance the understanding of regional-scale weather processes for many years. As RCMs can be optimized for local regions through the experimentation with the model physics, they are able to simulate regionally specific weather phenomena. In the South-Western Cape, rainfall is received generally as stratiform precipitation associated with the progression of mid-latitude cyclones over the region. The modeling of stratiform precipitation at the synoptic scale has been reasonably successful given the synoptic-scale circulation is properly accounted for (e.g. Petroliagis et al., 1996; Jones et al., 1995; Lüthi et al., 1996; Christensen et al., 1998; Giorgi et al., 1998).

Some RCMs can perform simulations at very high resolutions (< 5 km) which capture meso- and micro-scale features of the circulation. A RCM was used here to simulate precipitation fields at a 1x1 km resolution of days identified by the SOM in Chapter 3 as having experienced extreme precipitation. Three periods were simulated, 2-4 July, 17-19 July and 22-30 August 2001 and the spatial and temporal weather characteristics of these days examined at the meso- and micro-scale. Although precipitation characteristics were of primary interest to this study, precipitation is a function of multiple variables. Therefore, in order to check the consistency of the modeled results, temperature and wind results were also examined. The temperature and precipitation fields were examined against observed data, which in the case of precipitation also included radar data.

The August simulation was performed primarily to test the model's ability to simulate precipitation for comparison with radar data. However, in addition to the extreme rainfall weather regime, three other regimes were experienced over the nine days, namely a coastal low, land and sea breezes and a ridging South Atlantic high pressure system. Thus this period provided additional information that the simulation would have to capture. The July simulations were dominated by frontal circulations and only observed station data could be used in validation of the July precipitation

data. Although there were no observed data for wind fields, the validity of the simulated data could be inferred from synoptic circulation patterns as well as localized circulations such as the land and sea breezes.

In this chapter a brief description of model is presented, including a discussion of nesting procedures used. The model configuration is presented as well as the parameterizations employed. The August period was modeled first to test simulated precipitation data against radar data as well as the model's ability to capture multiple weather regime circulation characteristics. Thereafter the two July periods were simulated primarily to examine simulated precipitation fields. To prevent this chapter from being too voluminous, only temperature and wind data are presented here, the precipitation results are presented separately in the next chapter.

6.2 The regional climate model

The regional model used is the fifth-generation Pennsylvania State University – National Center for Atmospheric Research Mesoscale Model (PSU/NCAR MM5). It is a finite-difference, primitive equation model used for numerical weather prediction, research and mesoscale modeling applications. It has grown into a widely used model with many physical parameterizations since its initial description by Anthes and Warner (1978).

The horizontal grid is an Arakawa-Lamb B-grid (Arakawa and Lamb, 1977) that staggers the horizontal wind components relative to scalar variables (temperature, moisture etc.) while the vertical grid is based on a terrain following sigma (σ) coordinate system (Dudhia, 1993; Grell et al., 1995). Dudhia (1993) introduced non-hydrostatic dynamics by removing the restriction of the hydrostatic approximation which extended its range of applicability to very small grid scales (1–5 km). For further details about this modeling system and its evolution refer to Anthes et al., (1987), Dudhia, (1989, 1993), Grell et al., (1994) and Warner et al., (1992). A short review detailing the scope of use of the model is given below:

1. Examination of the interaction of synoptic and mesoscale processes with topography (e.g. Chien and Mass, 1997; Chien et al., 1997; Colle et al., 1999b, Faccani et al., 2003; Roebber and Gyakum, 2003).
2. Simulation and study of extratropical, frontal cyclones (e.g. Chaing et al., 1997; Zhang et al.,

1999a,1999b).

3. Simulation and diagnosis of tropical cyclones (e.g. Liu et al., 1997,1999; Zhang et al. 2001,2002,2003).
4. Modeling of severe storms and flooding (e.g. Spencer and Stensrud, 1998; Colle and Mass, 2000a).
5. Simulation and study of convective processes (e.g. Warner and Hsu, 2000; Zhang et al., 2003).
6. High resolution modeling of wind flow (e.g. Colle and Mass, 2000b; Feng and Chen, 2001; Chen and Feng, 2001).
7. Coastal low simulation (Garreaud and Rutlland, 2003).
8. Studies of Antarctic and Arctic circulation (Guo et al., 2003, Wei et al., 2003).
9. Coupling of MM5 with other models such as an orographic precipitation model (Kuligowski and Barros, 1999), a sea-ice model (Wei et al., 2003) and hydrology model (Chen and Dudhia, 2001a,b).
10. Land surface studies (Xiu and Pleim, 2000).
11. Modeling global climate (Dudhia and Bresch, 2002).

The MM5 has a multiple nest capability which facilitates the examination of small, high resolution domains nested in larger, lower resolution domains and makes it particularly well suited for studies of mesoscale and microscale systems. Nesting entails the placement of a smaller domain of a finer grid resolution within a larger domain of coarser resolution. The finer domain is the nested domain and the coarser domain referred to as the mother domain. Two nesting techniques are used by the MM5. One-way nesting uses data from the coarser, mother domain as lateral boundary conditions to drive the finer nested domain with no feedback from the latter to the former. Two-way nesting incorporates a feedback from the nest to the mother domain in addition to using mother domain lateral boundary forcing of the nest. This nesting capacity is discussed in detail below as both schemes were tested in the simulation periods to identify any differences between nesting techniques.

6.3 Nesting techniques used by the MM5

Orographic features in a region establish the circulation of air masses from the synoptic to microscale. For a mesoscale model to reproduce this behavior, a topography at a resolution such that orographic features are not smoothed out is necessary. In addition, the simulation domain has

to be large enough to include all the terrain characteristics that are believed to participate in the circulation of air masses. However, modeling a large enough domain at a high enough resolution to account for orographic forcing, such as the Cape Peninsula, makes it computationally impractical.

The MM5 uses a nesting technique to solve this problem through increasing spatial resolution only in domains where small scale phenomena might occur and are relevant for the reproduction of all the forcing mechanisms in the study area. The process nests a domain with higher spatial resolution in a coarser, outer domain. The outer domain facilitates the introduction of larger scale forcings into the inner domain.

The MM5 can perform multiple nested runs with up to nine domains running simultaneously. Each nested domain has a mother domain in which it is completely embedded, and is initialized with progressively higher-resolution topographic and land-use data (terrain data). This study used four domains to move from the forcing data synoptic resolution of 100 km to 1 km in the finest nest (Fig. 6.1.a-d). Figure 6.1.d also shows place names that are referred to later in the text.

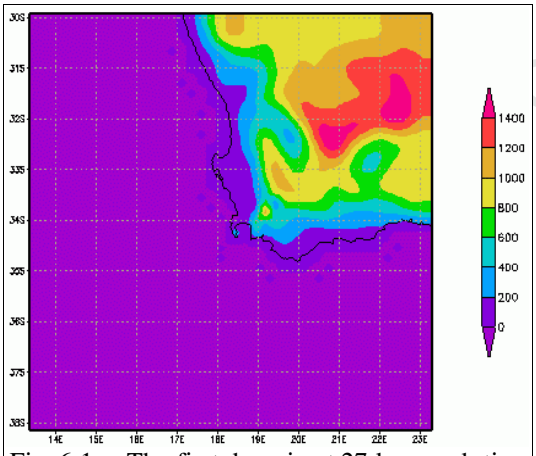

Fig. 6.1.a. The first domain at 27 km resolution with topography shown.

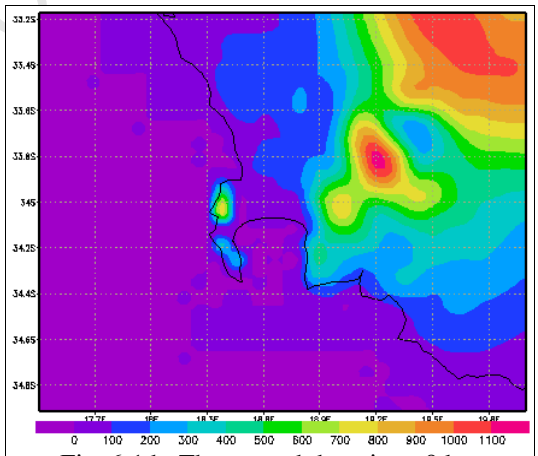

Fig. 6.1.b. The second domain at 9 km resolution with topography shown.

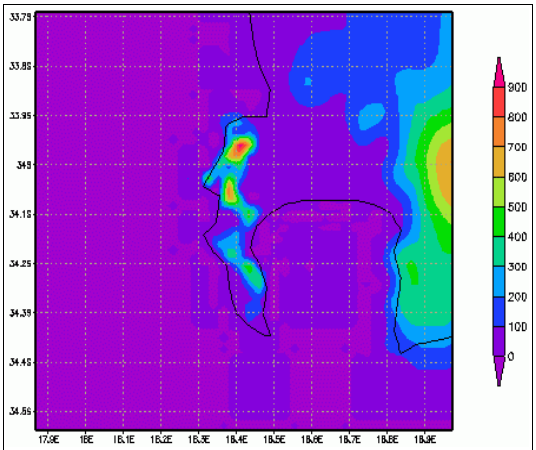

Fig. 6.1.c. The third domain at 3 km resolution with topography shown.

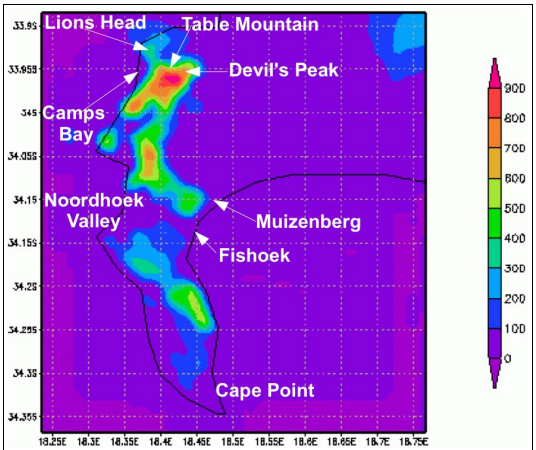

Fig. 6.1.d. The fourth domain at 1 km resolution with selected places shown.

Interaction between nests can be either one-or two-way. The one-way nesting method uses data generated by the mother domain as boundary forcing for nested domains with no feedback from the nested domain. This data is interpolated in space and time with enhanced resolution terrain data using the MM5 'Nestdown' procedure to supply the nest boundary forcing files. This procedure is repeated for each nest, resulting in a one-way flow of forcing information to each subsequent nest. For the two-way interaction, there is a flow of information from the mother domain to the nest as well as from the nest back to the mother domain. Input to the nest from the coarse domain comes via the boundaries while the feedback from the nest occurs over the nest interior as the values of the mother domain are replaced by combination of fine and coarse domain values. Two-way nesting requires domains to be run at the same time and the nesting ratio to be 3:1 whereas one-way nesting does not.

The nesting techniques adjusts terrain data for each domain through 'blending' data of the nested domain with that of the mother domain. Two methods are used to interpolate the mother domain's terrain fields to the nest domain grid points: an overlapping parabolic interpolation scheme for one-way nesting and a Cressman-type objective analysis for two-way nesting. Manning and Haagensen (1992) provide a description of these two methods. In the case of one-way nesting the interpolation is performed such that consistent terrain data are maintained along the nest boundaries and it is not necessary to have the same terrain values for interior grid points of overlapping domains. In the two-way nested mode, the terrain data of the interior nest grid points must have identical values at overlapping points so that the surface pressure field is consistent between the domains, so blending occurs over the entire nested region.

These different nesting processes result in different topographies for an identical domain. In Figure 6.2a,b, topography data of the third domain is presented for each nesting technique. Over the Cape Peninsula (where the fourth nest is situated), the topography of two-way nesting technique can be seen to be of a higher resolution than that of the one-way nesting as there is a blending of the inner values with that of the nested fourth domain.

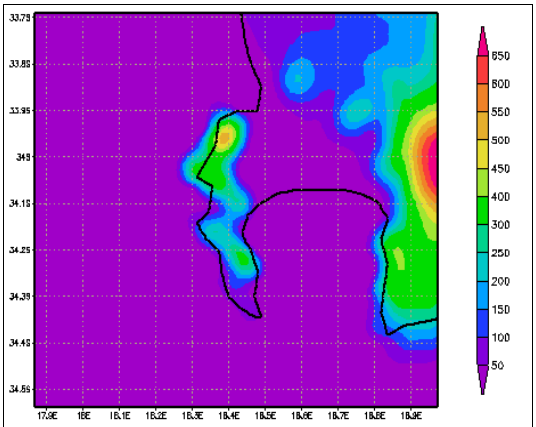

Fig. 6.2a. One-way nesting topography data of domain three of the four nest run.

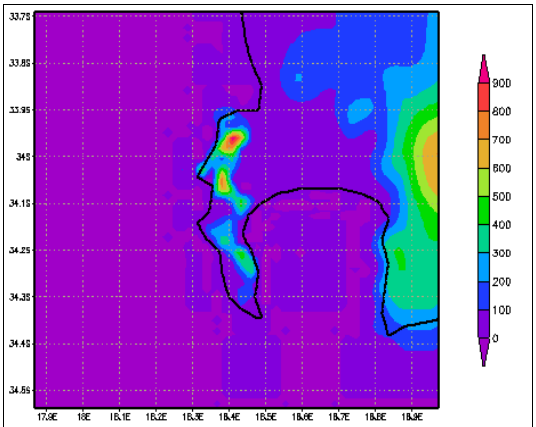

Fig. 6.2b. Two-way nesting topography data of domain three of the four nest run.

The topographical differences could be clearly seen when anomaly maps (which subtracted topography data produced by one-way nesting from that of two-way nesting) were produced for each domain (Fig. 6.3a-c). The blending process used in the two-way nesting technique enhanced the terrain resolution in the mother domain over the nest region such that higher lying regions as well as coastal boundaries were better defined. In the finest nest, domain four, the terrain data were identical.

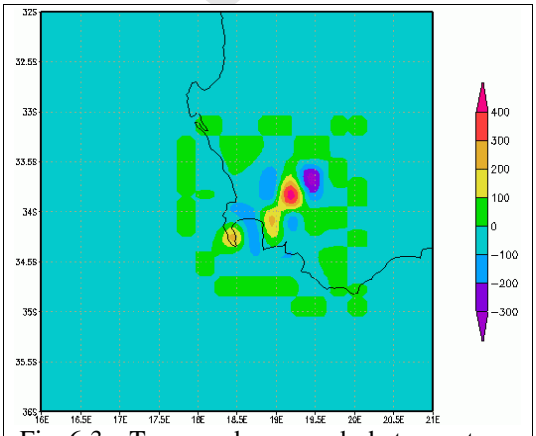

Fig. 6.3a. Topography anomaly between two- and one-way nesting procedures for domain one.

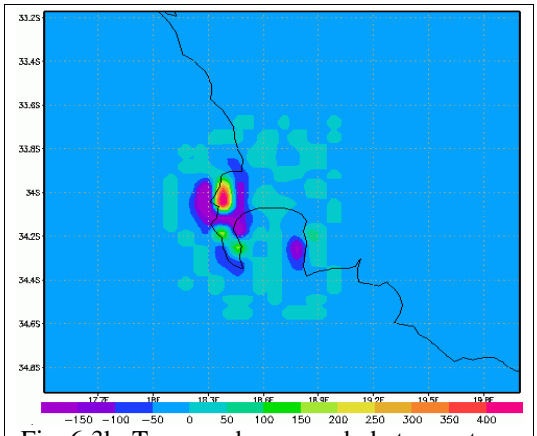

Fig. 6.3b. Topography anomaly between two- and one-way nesting procedures for domain two.

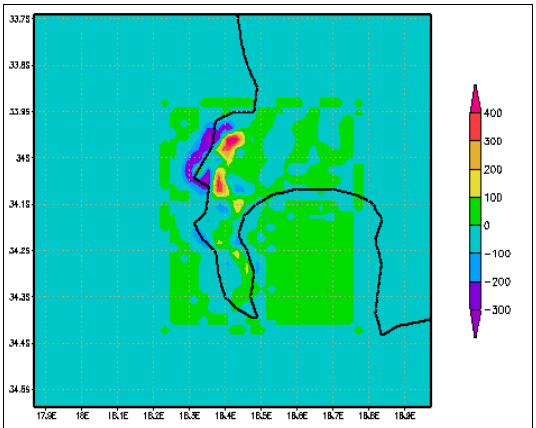

Fig. 6.3c. Topography anomaly between two- and one-way nesting procedures for nest area of domain three.

In summary, one-way nesting differs from two-way nesting in having (1) no feedback of data to the mother domain from the nest domain, (2) a coarser spatial resolution over the nested region in the mother domain, and (3) coarser temporal resolution at the boundaries. It is not necessary to maintain the 3:1 nesting ratio during one-way nesting this was done to maintain consistency in nest and grid sizes.

To examine the effect of nesting type on model results, two simulations were run for each time period, one using one-way nesting and the other two-way nesting. The model was configured identically for both techniques, the only difference being the nesting technique. The configuration of the simulations is described below after which results for temperature and wind fields are presented and discussed.

6.4 Simulation configuration

Four domains were used with resolutions of 27, 9, 3 and 1 km (Fig. 6.1a-d above). The domains were chosen to capture synoptic scale forcing in the largest domain, mesoscale interactions of approaching weather systems with the Cape Peninsula in the mid-sized domain, and high resolution, meso- and microscale characteristics in the two smallest domains.

United States Geological Survey (USGS) data were used for topography and land use and varied in resolution from 10 minutes for the outer domain to 30 seconds for the inner. Convective processes

were parameterized using the Grell scheme (Grell, 1993), although there was no convective parameterization used for the inner three domains as MM5 resolves these explicitly at these resolutions. An explicit moisture scheme that included prognostic equations for cloud water, rain water, ice, and supercooled water was used (Reisner, 1998). The planetary boundary layer was parameterized with the high resolution, multilayer Blackadar scheme (Blackadar, 1979; Zhang and Anthes, 1982), which included surface fluxes of heat, moisture and momentum. The radiation scheme facilitated longwave and shortwave radiation fluxes with the clear atmosphere, cloud, precipitation, and the ground (Dudhia, 1989). These parameterizations were based on information provided in Grell et al. (1995) as no sensitivity studies have been performed to establish optimal parameterizations over the region. Table 6.1 provides a summary of domain setup and parameterization information.

Table 6.1. Setup and parameterizations of the MM5 simulations.

	Domain 1	**Domain 2**	**Domain 3**	**Domain 4**
Grid size	27 km	9 km	3 km	1 km
Domain size	43 x 43	28 x 34	40 x 43	61 x 61
Terrain data (USGS)	10 min. (19 km)	9 min. (9.25 km)	2 min. (4 km)	30 sec. (0.925 km)
Convective processes	Grell	Explicitly resolved	Explicitly resolved	Explicitly resolved
Boundary layer processes	Blackadar	Blackadar	Blackadar	Blackadar
Explicit moisture scheme	Mixed-Phase	Mixed-Phase	Mixed-Phase	Mixed-Phase
Radiation scheme	Cloud Radiation Scheme	Cloud Radiation Scheme	Cloud Radiation Scheme	Cloud Radiation Scheme

The vertical co-ordinate system used 49 unevenly spaced full sigma levels with a relatively large concentration at the lowest levels in order to resolve planetary boundary layer structure and processes. The top of atmosphere was set at 10 hPa.

The initial time step (for the largest domain) was set at 80 seconds so as to satisfy the Courant-Friedrichs-Lewy (CFL) stability criterion (Courant et al., 1928). For each domain, the time step decreased following the 3:1 ratio the domain grid sizes follow resulting in a time step for the smallest domain of approximately three seconds.

The simulations were forced with 12-hourly MRF data from NCAR which had a resolution of 100 km and were given a spin up time of 2 days. Model output was written every four hours to facilitate the capture of synoptic flow at a high enough temporal resolution and so as not to mask out

significant mesoscale processes at higher spatial resolutions.

The simulations were run on a Compaq ES40 Alphaserver using four 667 MHz EV67 64-bit processors each with 1 Gb of RAM. The five day July one-way nesting simulations took 50 hours to run and the two-way nesting runs 54 hours. Run times for the August simulation were not accurately recorded. Once the simulations were completed, data were interpolated from sigma to pressure levels and converted into a format for analysis using the Grid Analysis and Display System (GrADS[1]).

The August results are presented first as this period facilitated an examination of four different synoptic regimes. Thereafter results from the two July runs are presented, these two periods having been dominated by a single regime. Only results from the two-way nested runs are presented graphically for temperature and wind data. One-way nesting results are presented through the use of anomaly maps, which subtracted one-way nesting data from two-way nesting data. Please note precipitation results are presented in the next chapter.

6.5 Temperature fields

6.5.1 August 21-29

Simulated surface temperature fields at the synoptic scale reflected the position of the weaker cold front on the 25th August as well as the stronger front on the 28-29th August (Fig. 6.4a,b). The advection of cold air behind the cold front on the 29th by a ridging south Atlantic high pressure system was also well represented (Fig. 6.5). The diurnal cycle accounted for the largest temperature variation, most noticeably over land areas. These characteristics were evident through all the nests.

1 http://grads.iges.org/grads/grads.html

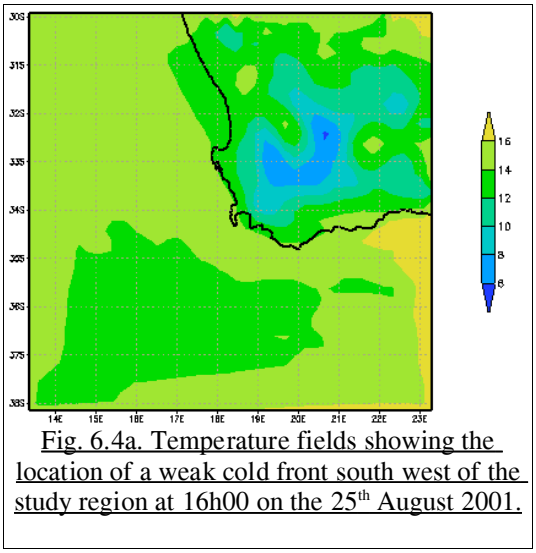

Fig. 6.4a. Temperature fields showing the location of a weak cold front south west of the study region at 16h00 on the 25th August 2001.

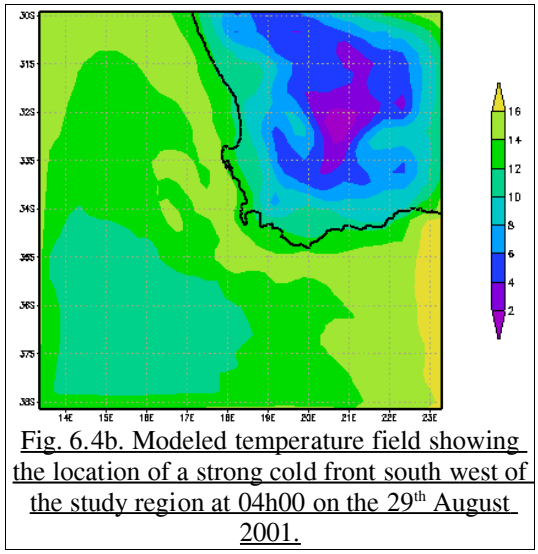

Fig. 6.4b. Modeled temperature field showing the location of a strong cold front south west of the study region at 04h00 on the 29th August 2001.

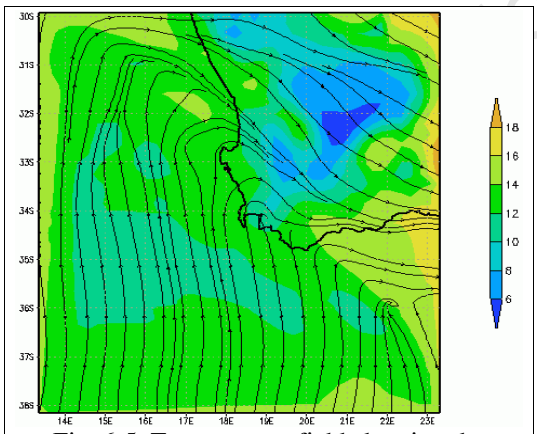

Fig. 6.5. Temperature field showing the advection of cold air into the region at 12h00 on the 29th August through southerly wind flow (streamlines).

Surface temperature anomalies between one- and two-way nesting results ranged between positive and negative 0.8 °C. These were not confined to areas of topography or only in the nest area and included marine areas which had generally negative anomalies (Fig. 6.6). In the upper air (500 hPa), the averaged anomaly was 0.15 °C with maxima evident only over a small region of topography in the nested area in the Hottentots Holland mountains (Fig. 6.7).

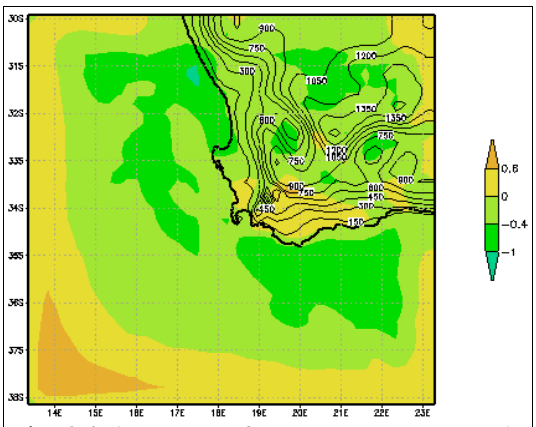

Fig. 6.6. Average surface temperature anomaly over the nine days between the two-way and one-way nesting simulations in the mother domain .

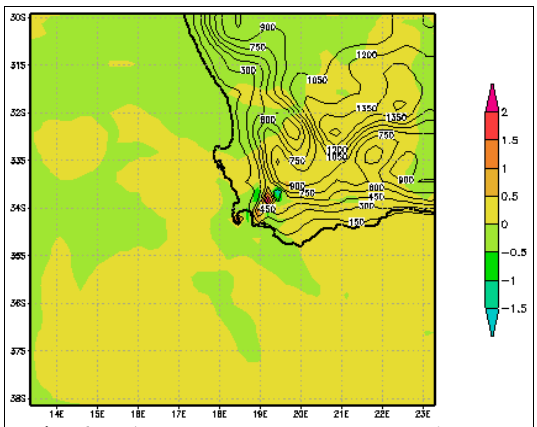

Fig. 6.7. Average temperature anomaly over the nine days between the two-way and one-way nesting simulations at the 500 hPa level.

The first nest (domain two) captured the influence of the higher resolution topography as the range of the nine-day averaged surface temperature anomaly increases to 1 °C (Fig. 6.8). The one-way nesting procedure produced slightly warmer temperatures than the two-way nesting procedure with highest anomalies apparent over the Cape Peninsula and the southern parts of the Hottentots Holland. As the topography used in the one-way nesting was of lower resolution than the two-way nesting, the lower altitudes contributed to higher surface temperatures. Additionally, it is likely that respective circulations resolved in parent nests, a function of the respective nesting technique topographies, also contribute to the temperature differences through boundary conditions passed to the inner nest as well as the resolved circulations. At this resolution, the warmer days of the 26th and 27th were also captured (Fig. 6.9), which were not evident in the first domain. Temperatures at the 500 hPa levels exhibited a small positive anomaly only over the highest lying regions of the Cape Peninsula, which were in the nested region of the mother domain. The rest of the mother domain showed very small anomalies at this level.

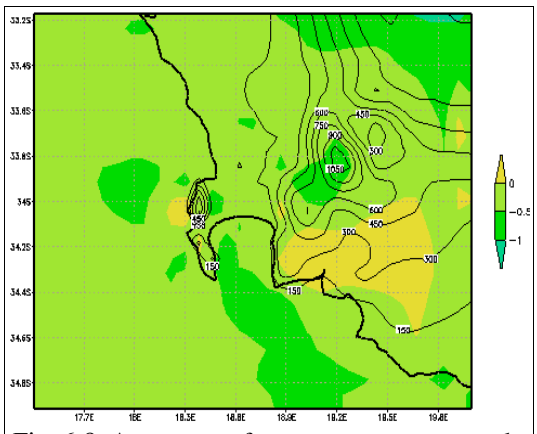

Fig. 6.8. Average surface temperature anomaly over the nine days between the two-way and one-way nesting for the second domain.

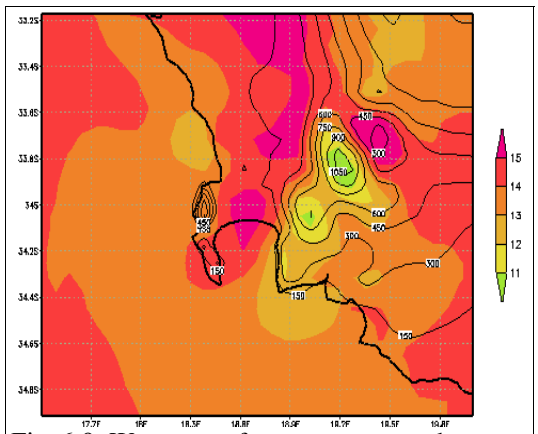

Fig. 6.9. Warmer surface temperatures between 12h00 and 16h00 of the 27th August.

In the third domain, consistently cooler temperatures over regions of high topography were produced in all time steps as were warmer temperatures over the Cape Flats and coastal regions (Fig. 6.10). At this resolution it was possible to introduce station data where these were available. The averaged daily model temperatures were generally lower than station data as the station data were daily maxima. When viewing modeled data for time step 12h00-16h00 each day, which is the time of day when temperatures were at a maximum, there was better agreement between observed and modeled data (Fig. 6.11).

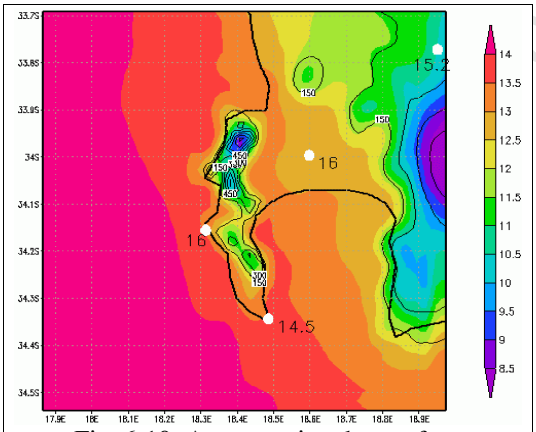

Fig. 6.10. Average nine day surface temperatures for the two-way nesting simulation of domain three with average nine day station data .

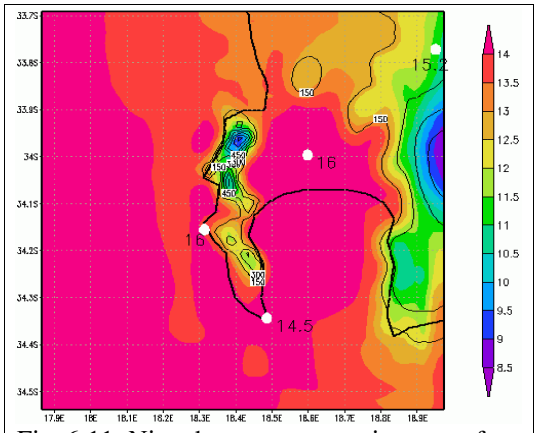

Fig. 6.11. Nine day average maximum surface temperatures for the two-way nesting simulation of domain three with average nine day station data .

The largest differences between the one- and two-way nesting procedures were confined to the Cape Peninsula, where one-way nesting produced a warmer nine-day average temperature as a result of the topography data with lower elevations (Fig. 6.12). The spatial distribution of the

temperature anomaly is similar to that of the topography anomaly seen in Fig. 6.3c above. In the upper air anomalies were small (0-0.2 °C).

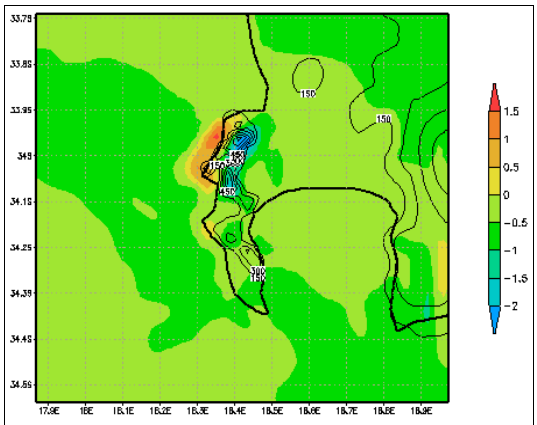

Fig. 6.12. Average surface temperature anomaly over the nine days between the two-way and one-way nesting simulations in the third domain.

In the finest domain, results from both techniques showed lowest temperatures over higher lying regions of the Peninsula with a relatively homogeneous temperature range over the Cape Flats and False Bay (Fig. 6.13). Modeled daily temperatures were again cooler than averaged observed maxima, but when the averaged 12h00 to 16h00 time step was used the observed and modeled data were similar (Fig. 6.14).

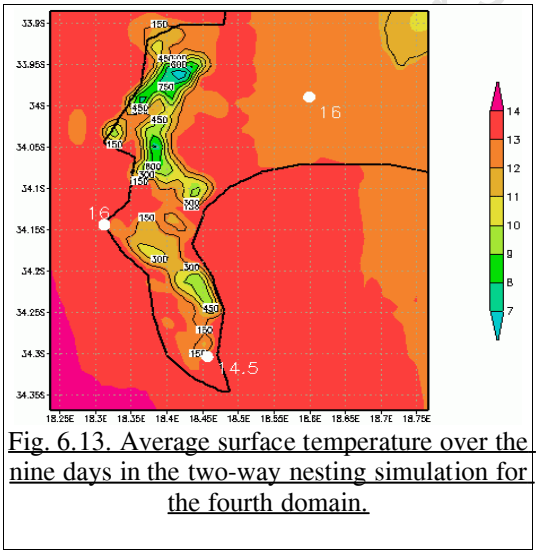

Fig. 6.13. Average surface temperature over the nine days in the two-way nesting simulation for the fourth domain.

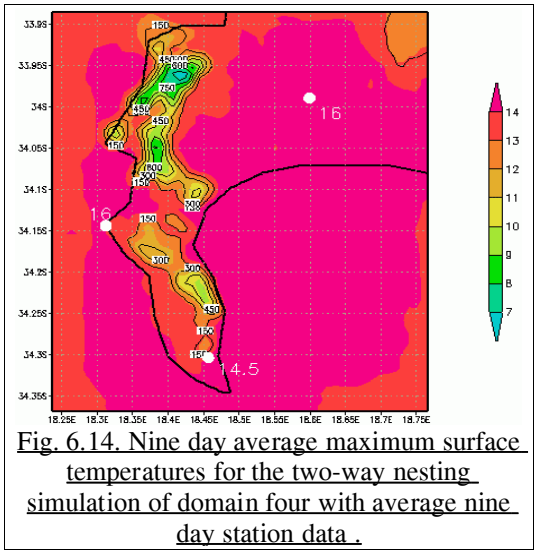

Fig. 6.14. Nine day average maximum surface temperatures for the two-way nesting simulation of domain four with average nine day station data .

Temperatures generated by the 2-way nesting procedure were generally lower over the Peninsula than those generated using the one-way nesting procedure (Fig. 6.15). The magnitude of the

averaged positive anomaly was very small compared to other domains at 0.1 °C, although at specific times this reached up to 2 °C over a region immediately east of the Peninsula. In this domain there was no difference between the topographies of the one- and two-way nested runs, so anomalies were due to the respective boundary forcings from the third domain of each run, as well as each respective nesting technique. Average temperature anomalies at the 500 hPa level were again low with highest anomalies over the Peninsula.

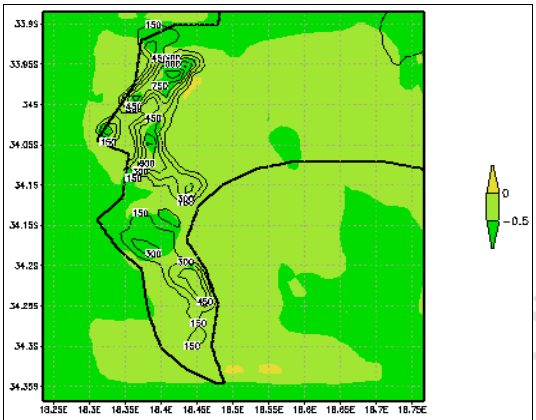

Fig. 6.15. Average surface temperature anomaly over the nine days between the two-way and one-way nesting simulations in the fourth domain.

6.5.2 July 2-4

The position of the cold fronts were evident in the synoptic scale temperature fields on the 2nd and the 4th of July. The front of the 4th had colder temperatures associated with it and was simulated to make landfall in the morning (Fig. 6.16). Coldest temperatures were simulated inland over the mountains at night and the greatest temperature variation was seen in the diurnal cycle. At a higher resolution, topographic modification of the temperature field became apparent with coldest temperatures simulated over the highest regions of the Peninsula and relatively warmer temperatures over the Cape Flats and the ocean (Fig. 6.17).

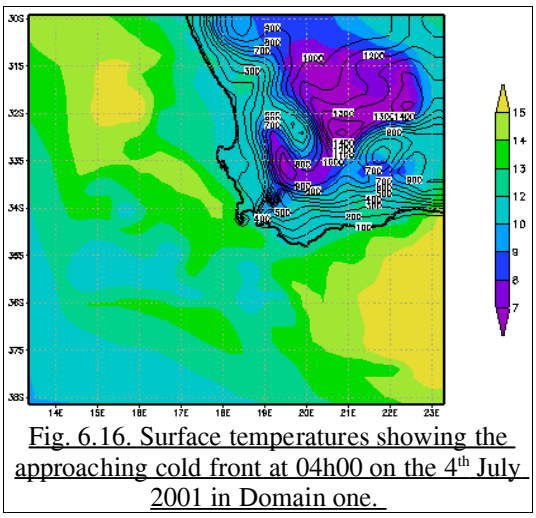

Fig. 6.16. Surface temperatures showing the approaching cold front at 04h00 on the 4th July 2001 in Domain one.

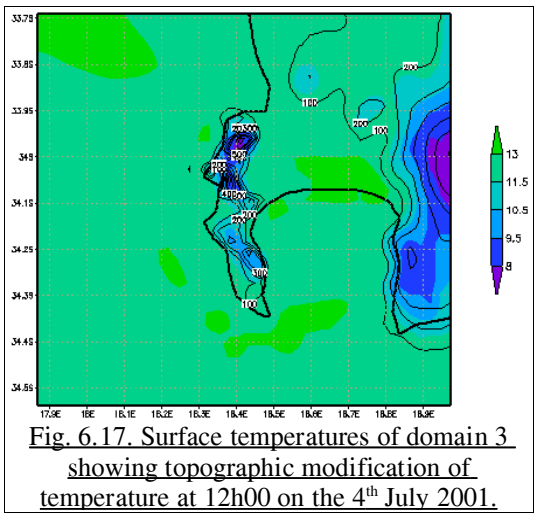

Fig. 6.17. Surface temperatures of domain 3 showing topographic modification of temperature at 12h00 on the 4th July 2001.

The highest daily maximum temperature was above 15 °C on the 2nd July in regions of the Cape Flats (Fig. 6.18). Where station data were available, simulated temperatures were lower at all stations, the highest difference being four degrees at Slangkop. On the 4th July, when the coldest temperature was recorded, the difference between recorded and simulated temperatures were smaller, e.g. simulated temperatures at the Airport and Cape Point were the same as the observed, at Paarl it was one degree below the observed and Slangkop two degrees. The highest simulated temperature on the 4th was in a small region of the Cape Flats which reached 13 °C (Fig. 6.19). On both days temperature minima were simulated over the highest regions of the Peninsula and the Hottentots Holland mountains.

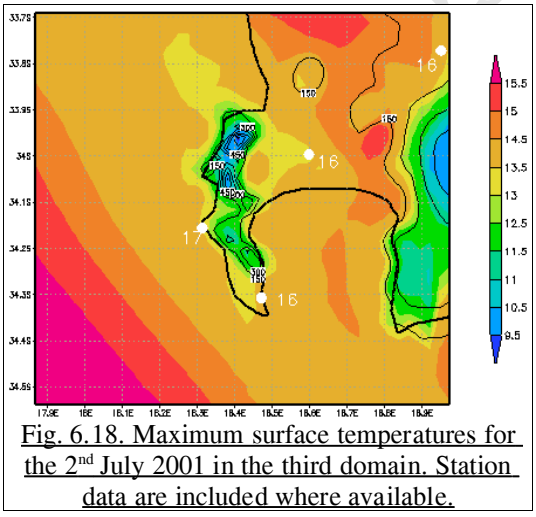

Fig. 6.18. Maximum surface temperatures for the 2nd July 2001 in the third domain. Station data are included where available.

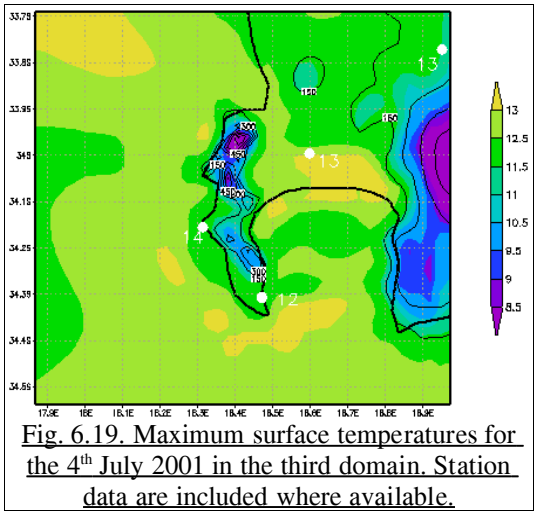

Fig. 6.19. Maximum surface temperatures for the 4th July 2001 in the third domain. Station data are included where available.

Averaged simulated maximum daily temperatures compared favourably with averaged observed maximum temperatures. In the third domain, the model simulated similar maxima at three of the

four stations (Fig. 6.20). Coldest temperatures were simulated over the highest regions of the Peninsula and warmest temperatures over the ocean and at the foot of the Hottentots Holland. In the fourth domain, simulated temperatures at Slangkop and the Airport were on average lower than observed by two and one degrees respectively but at Cape Point the averaged temperatures were the same (Fig. 6.21). Temperature minima were again situated over the highest regions of the Peninsula with maxima on the eastern edge of the domain.

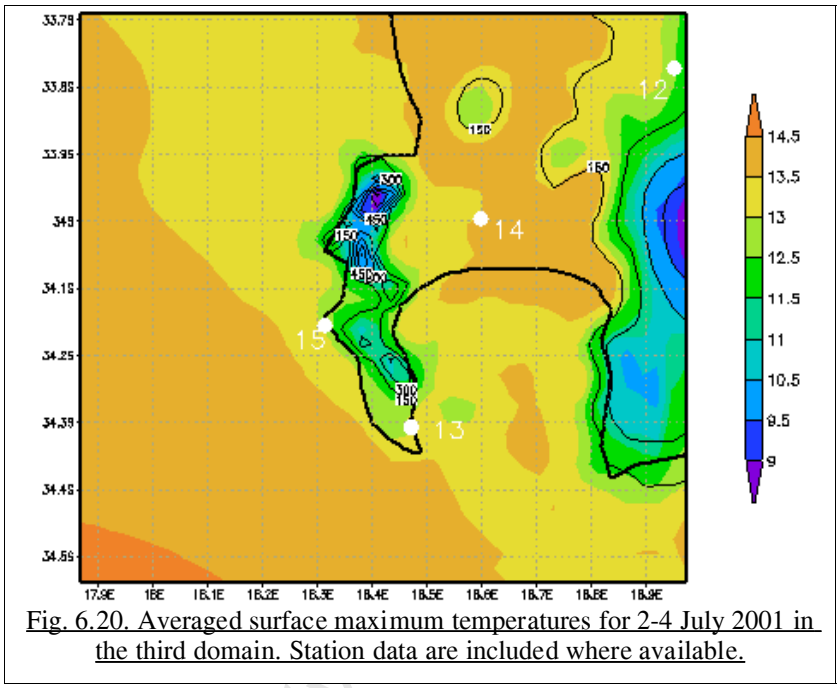

Fig. 6.20. Averaged surface maximum temperatures for 2-4 July 2001 in the third domain. Station data are included where available.

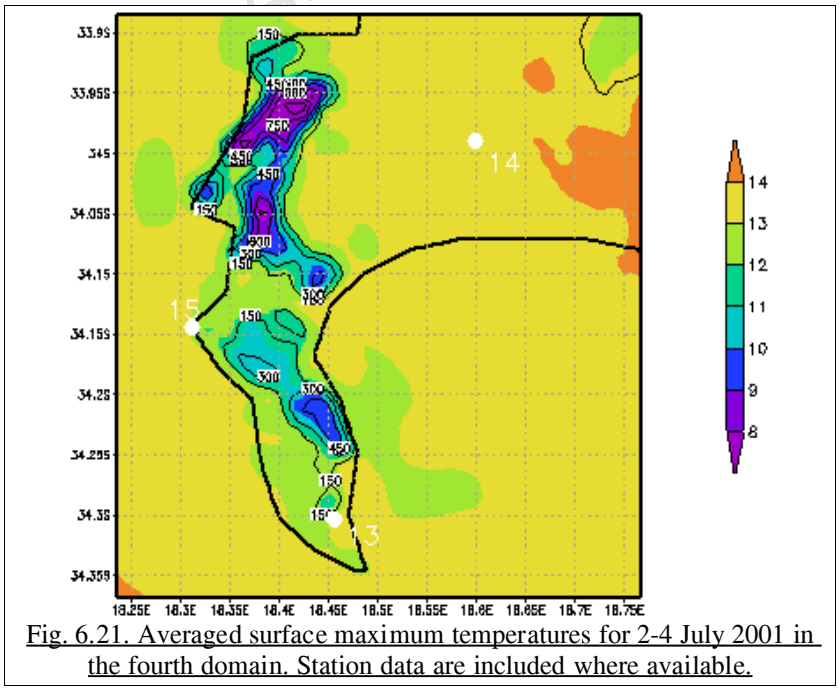

Fig. 6.21. Averaged surface maximum temperatures for 2-4 July 2001 in the fourth domain. Station data are included where available.

Anomalies between one- and two-way nesting indicated that two-way nesting produced generally warmer temperatures over the northern regions in the second domain (Fig. 6.22). Negative anomalies were evident over the highest regions of the Hottentots Holland mountains. Over the study region, nesting anomalies were between 0-1 °C with smaller anomalies over the southern Peninsula. In the fourth domain, high positive and negative anomalies were produced over the northern and central Peninsula (Fig. 6.23). High positive anomalies were located in the immediate lee of the Peninsula and high negative anomalies over the windward side. This indicated two-way nesting produced lower temperatures on the windward side of the Peninsula and higher temperatures in it's lee during the predominantly northerly flow. As the topographies were identical in this domain these anomalies were again a result of forcing data at the boundaries from the respective mother domains, which are a a function of circulation generated by the respective nesting techniques. The mountains are not identical in all grids in the lower resolution nests, thus affecting resolved circulation as well as boundary conditions passed to inner nests. This anomaly distribution was not apparent in the third domain which showed generally no or very low negative anomalies over the Peninsula. Over the rest of the fourth domain, an difference of between minus one and zero degrees was produced over False Bay and of zero to positive one degrees over the Cape Flats.

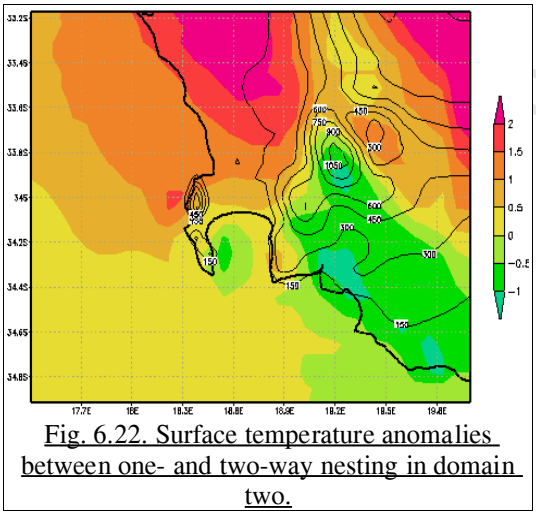

Fig. 6.22. Surface temperature anomalies between one- and two-way nesting in domain two.

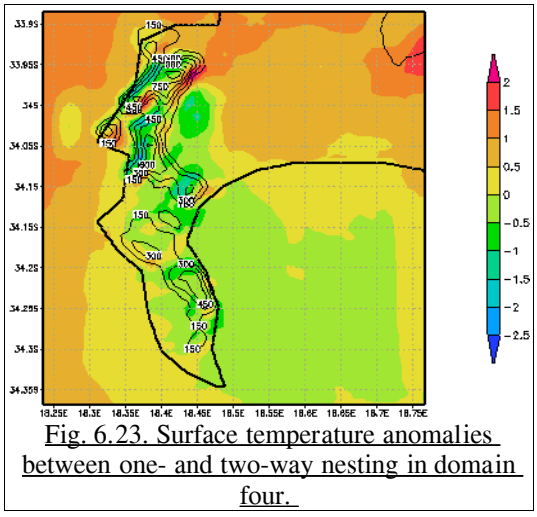

Fig. 6.23. Surface temperature anomalies between one- and two-way nesting in domain four.

6.5.3 July 17-19

The three fronts made landfall in close succession over this three day period. Warmest maximum temperatures were recorded and simulated on the 17th and coldest on the 19th (Figs. 6.24 and 6.25). The diurnal cycle again accounted for the largest temperature variation, most noticeably over land areas. Maximum temperatures on the 19th July were on average one degree warmer than those on the 4th July.

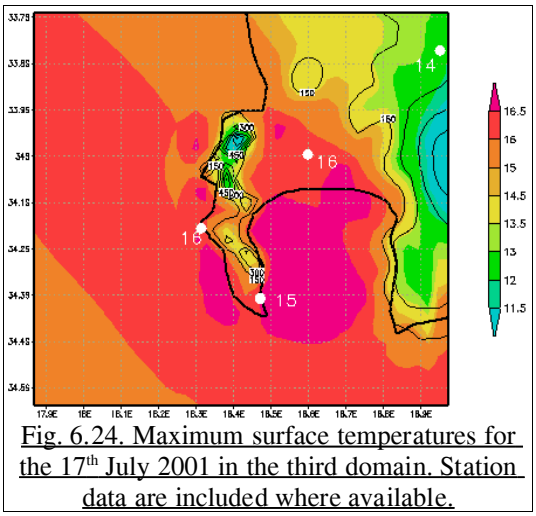

Fig. 6.24. Maximum surface temperatures for the 17th July 2001 in the third domain. Station data are included where available.

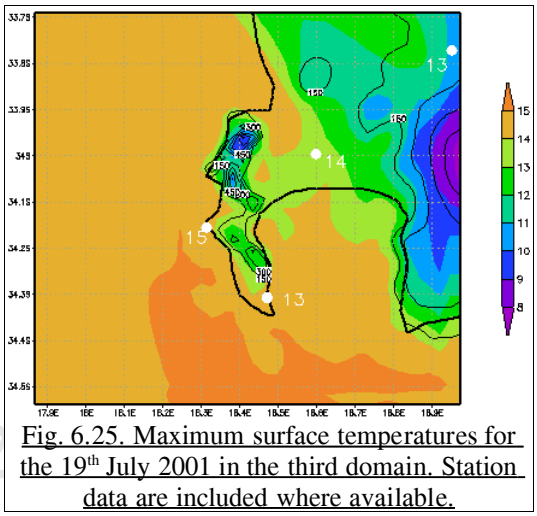

Fig. 6.25. Maximum surface temperatures for the 19th July 2001 in the third domain. Station data are included where available.

With increasing resolution, orographic forcing of temperatures could again be seen with coldest temperatures simulated over regions of high topography (Figs. 6.26 and 6.27). There was good agreement between simulated maximum temperatures and observed maximum temperatures at stations for which data were available in the fourth domain. The simulation produced cooler average and maximum temperatures than the August as no warmer weather regimes were experienced.

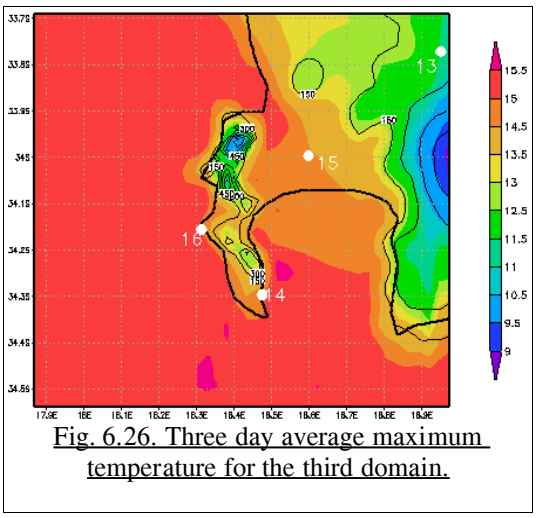

Fig. 6.26. Three day average maximum temperature for the third domain.

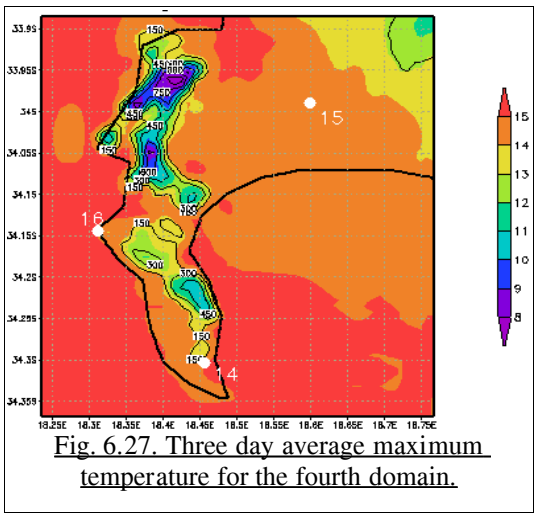

Fig. 6.27. Three day average maximum temperature for the fourth domain.

The magnitudes of the anomalies between nesting techniques in the second domain were again highest over regions of topography, where one-way nesting generally produced higher temperatures as a result of lower resolution topography data (Fig. 6.28). This was especially evident in the eastern part of the domain. Over the sea the difference was small, an indication of the controlling effect of an essentially constant sea surface temperature. In the fourth domain, topographic modification of the temperature field was most apparent over the northern Peninsula. The highest positive of 1 °C occurred in this domain occurred in the immediate lee of the Peninsula (Fig. 6.29). Highest negative anomalies were located on the windward (western) side of the Peninsula indicating warmer temperatures simulated here using the one-way nested technique.

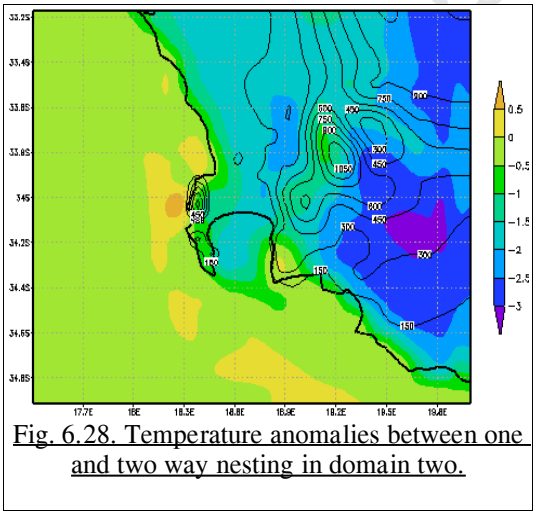

Fig. 6.28. Temperature anomalies between one and two way nesting in domain two.

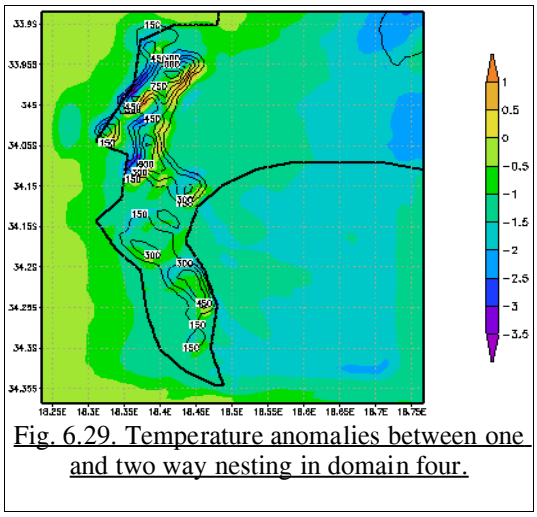

Fig. 6.29. Temperature anomalies between one and two way nesting in domain four.

6.5.4 Temperature field summary

Synoptic scale features such as the passage of cold fronts, cold air advection and warming of the region between fronts were captured in the low resolution simulated temperature fields. Moving from the coarse to fine domains, orographic forcings became more evident with greater spatial resolution of temperature in each successive nest. Spatially, temperature fields also became more distinct. There was good agreement between observed maximum temperatures and simulated maxima in the two way nesting results at higher resolutions. The 1 km and 3 km resolution nests both produced accurate, too warm or too cold temperatures at different time thus a longer time series would be need to ascertain which of these resolutions would be optimal in reproducing and accurate temperature field.

One-way nesting produced generally higher temperatures than two-way nesting as the topography was less well resolved here resulting in a less effective capture of the orographic modification of temperature. Highest anomalies between one- and two-way nesting were over nested regions which covered regions of topography. This through the simple lapse effect but also due to circulation differences as the mountainous regions are not identical in all grids, thus affecting resolved circulation as well as boundary conditions passed to inner nests. Averaged anomalies were highest during the homogeneous weather regimes in July. In the fourth domain of the August run the average anomaly range was 1 °C whereas in the July runs these reached over 5 °C. The July runs experienced only one dominant weather regime for each time period in the form of three cold fronts whereas the August run experienced multiple weather regimes. The single regime circulations resulted in amplified anomalies over specific regions whereas the heterogeneous nature of the circulation in August served to shrink the anomaly range. Temperature fields produced by the two-way nesting scheme compared more favourably with observed data.

6.6 Wind Fields

6.6.1 August 22-29

Surface wind fields in the first domain reflected the passage of the three cold fronts over the region during this period. In each case, northwesterly winds preceded the front and became westerly as the front passed the study region (Fig. 6.29). (In all figures, streamlines were coloured with magnitude

(ms^{-1}) according to the colour bar.) In the upper air, the passage of the westerly wave was reflected in the wind streams as a well developed wave in the case of the two stronger fronts of the 23rd and 29th (Fig. 6.30) but less so in the case of the weaker front of the 26th.

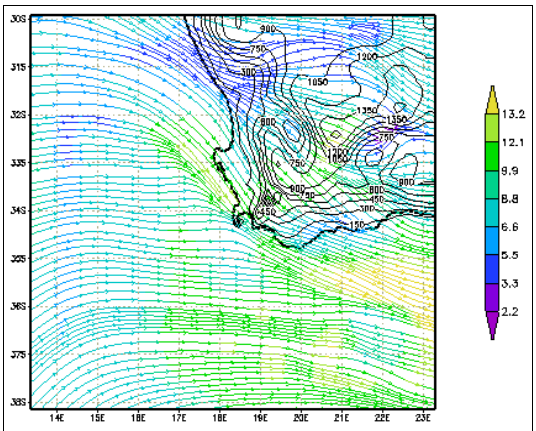

Fig. 6.29. Surface wind fields at 20h00 on the 23rd August showing the passage of a cold front over the Cape Peninsula.

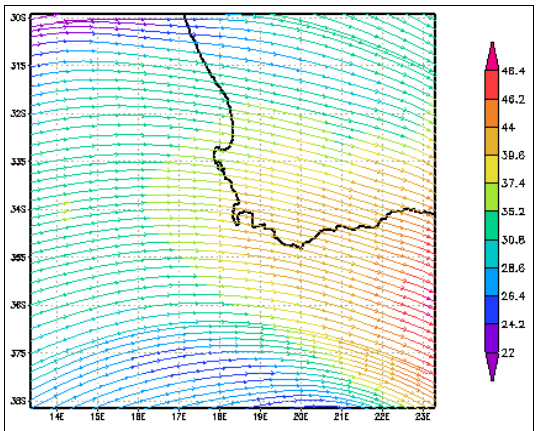

Fig. 6.30. 500 hPa wind fields at 20h00 on the 23rd August showing the upper air westerly wave associated with the surface cold front.

On the 27th August, the surface wind field showed a closed cyclonic circulation east of Cape Agulhas associated with the coastal low (Fig. 6.31). A well developed southerly meriodinal flow was simulated once the front of the 29th August had passed (Fig. 6.32) with comparable wind velocities and directions as recorded by ship and station data (see Fig. 4.2).

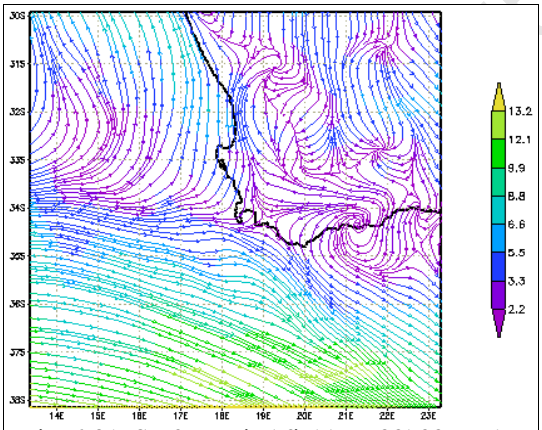

Fig. 6.31. Surface wind fields at 20h00 on the 27th August showing evidence of a coastal low on the south coast east of Cape Agulhas.

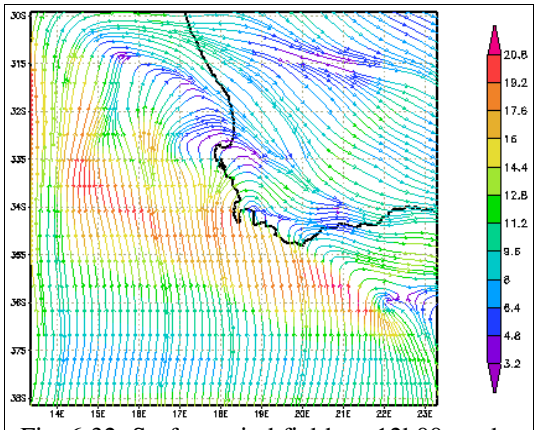

Fig. 6.32. Surface wind fields at 12h00 on the 29th August showing southerly meriodinal flow following the passage of a cold front.

Wind anomalies between one and two-way nesting, averaged over the nine days, were small in this domain in both flow magnitude and direction (Fig. 6.33). Anomalies were graphically represented as the resultant between wind vectors whose colour and length indicated the magnitude of the

anomaly. Over the nine days, anomalies showed a maxima of 2.4 ms^{-1} along the south coast of South Africa but were generally very small over the whole region.

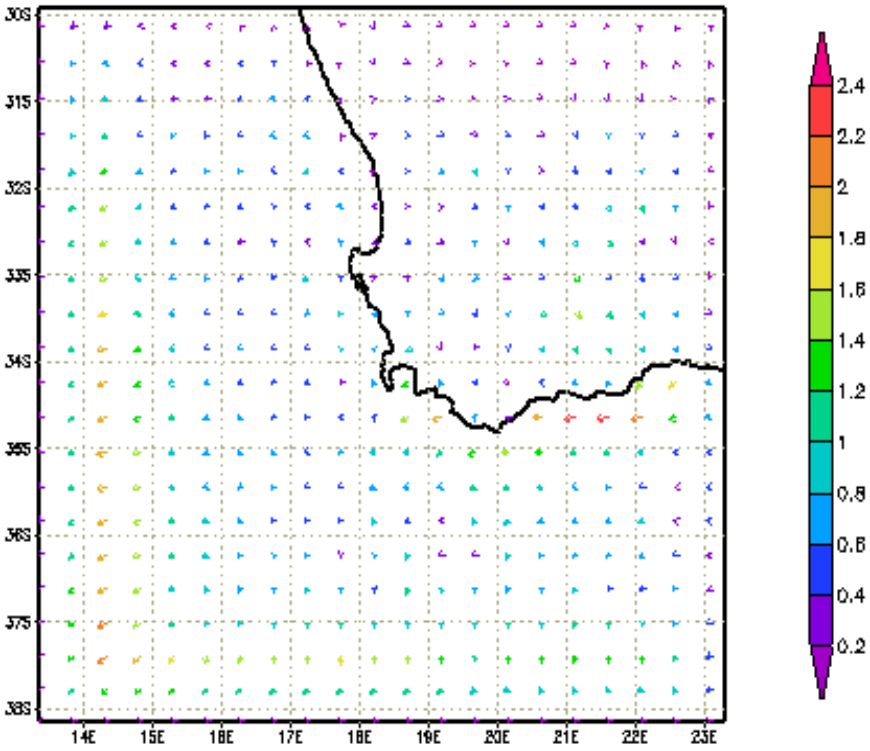

Fig. 6.33. Nine day averaged surface wind anomaly in the first domain between one- and two-way nesting simulations.

Wind fields in the second domain reflected the same large scale circulation patterns as noted for the first domain and also showed some finer mesoscale structure, especially in the two-way nested run. There was better evidence of the position of the cold front on the 23rd and 29th. On the 27th, land and sea breezes became evident in both nesting techniques. A land breeze was simulated over False Bay and the west coast at 00h00 on the 27th which persisted until 08h00 (Fig. 6.34). A sea breeze then developed between 12h00 and 20h00 (Fig. 6.35). This broke down as circulation from the approaching cold front began to dominate late on the 27th. Both the sunny conditions and weak synoptic forcing of this day would facilitate these circulations.

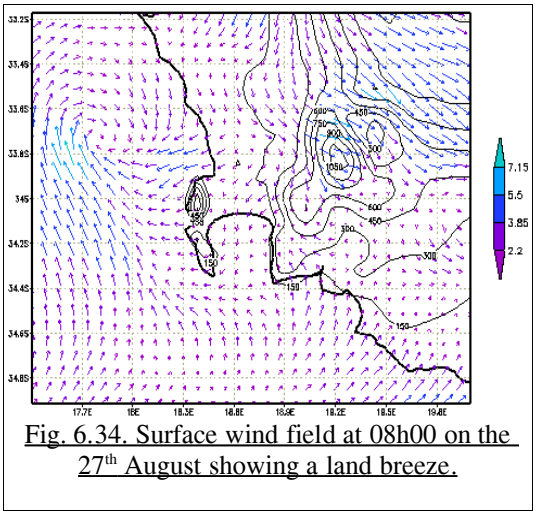

Fig. 6.34. Surface wind field at 08h00 on the 27th August showing a land breeze.

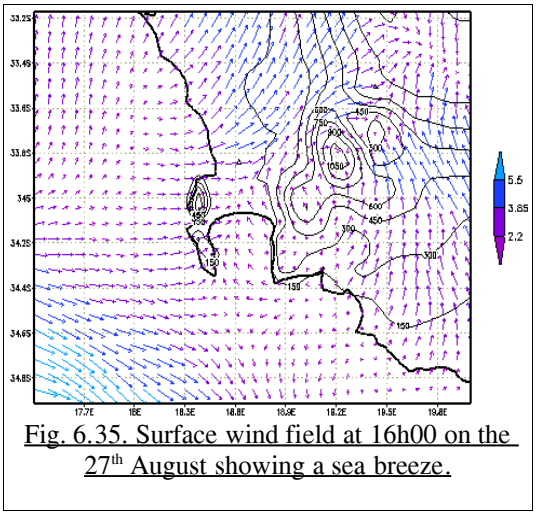

Fig. 6.35. Surface wind field at 16h00 on the 27th August showing a sea breeze.

The two-way nesting simulation produced a very localized cyclonic circulation over the eastern part of False Bay and the Cape Flats as southerly meriodinal flow interacted with the northerly flow of the preceding cold front on the 29th (Fig. 6.36). This feature was not produced in the one-way nesting simulation. Unfortunately, due to the lack of observational data, this circulation could not be verified.

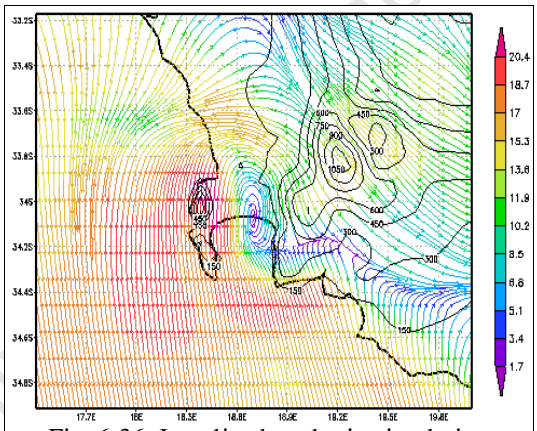

Fig. 6.36. Localized cyclonic circulation formed as southerly meridional flow and northerlies interacted.

Surface wind anomalies between nesting techniques were again small. The maximum anomaly of 2.28 ms^{-1} was less than that of first domain and was located in the lee of the northern Peninsula (Fig. 6.37). The north-westerly direction of the arrow indicated that two-way nesting produced stronger average flows during this period over in that particular region. In the upper air (500 hPa) anomalies were even smaller and ranged between 0.2 ms^{-1} and 1.2 ms^{-1}.

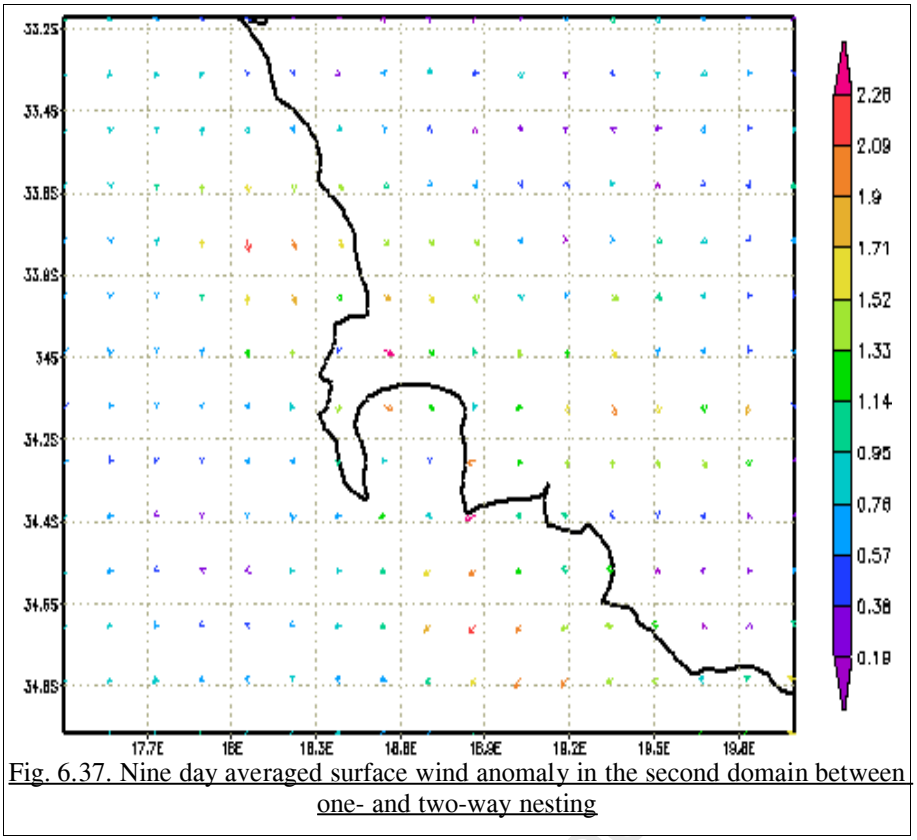

Fig. 6.37. Nine day averaged surface wind anomaly in the second domain between one- and two-way nesting

Wind fields in the third domain showed further influence of the orography on wind flow, especially at slower wind velocities. Evidence of this was seen at midnight on the 25th during a moderate west-north-westerly flow regime when the wind field was deflected south around the Peninsula and also west across the face of Table Mountain (Fig. 6.38). There was also evidence of wind being reflected upstream before it began to move to the south. This deflection was not evident in the one-way nested run, nor at higher wind velocities and was constrained to the surface (below the 950 hPa level). Winds regimes with a significant northerly component exhibited no significant convergence or divergence fields at the surface. However, during the south easterly flow on the 29th, surface divergence was evident over and in the lee of the higher regions of Peninsula with corresponding convergence further up stream (Fig. 6.39).

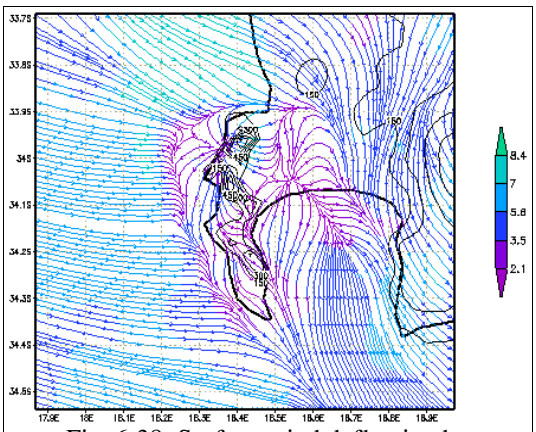

Fig. 6.38. Surface wind deflection by topography during a west-north-westerly wind flow on the 25th August.

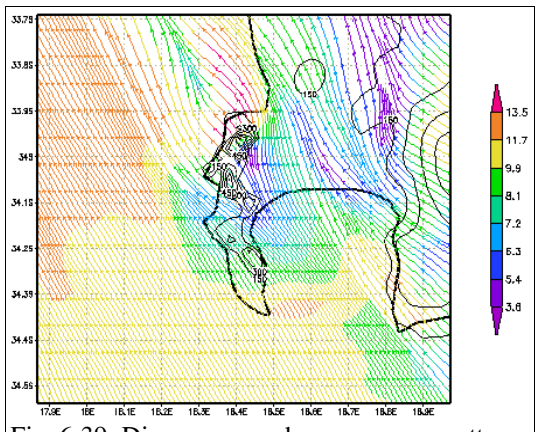

Fig. 6.39. Divergence and convergence patterns over the Peninsula during south-easterly wind flow

Although anomalies between the two nesting procedures were again generally small, higher maxima were produced in the lee of the Cape Peninsula by the two-way nested run (Fig. 6.40). In this area, two-way nesting produced consistently higher wind magnitudes during northerly flow regimes which accounted for the maxima being located here. At the 500 hPa level, anomalies were smaller and ranged between 0.1 - 1.3 ms^{-1}.

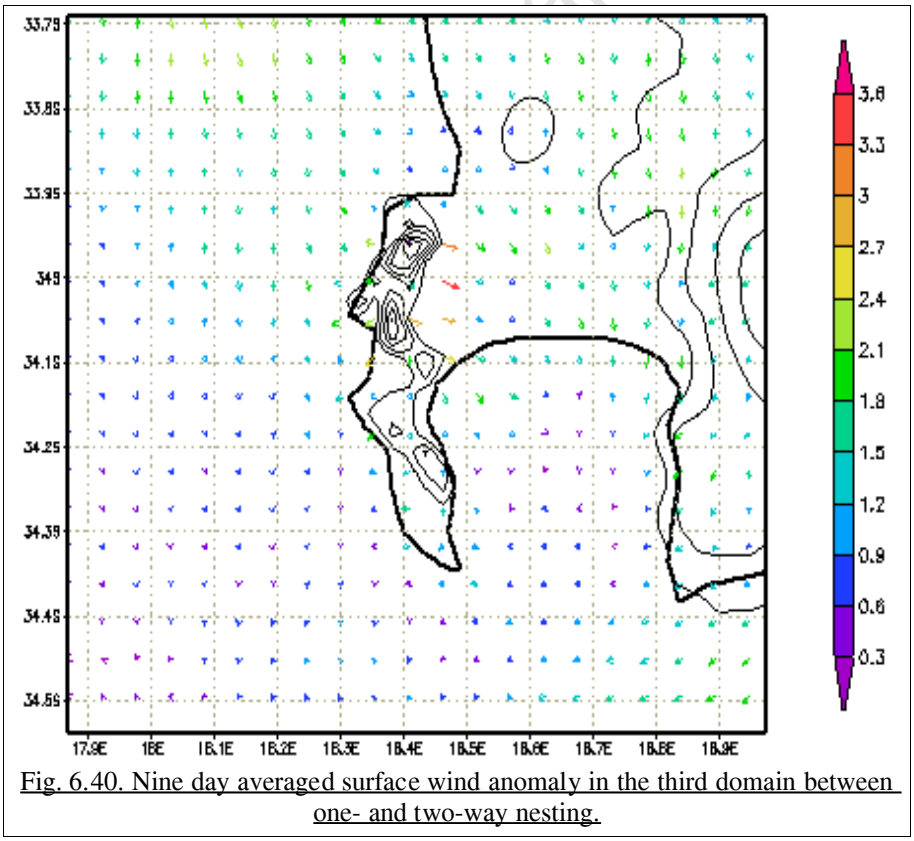

Fig. 6.40. Nine day averaged surface wind anomaly in the third domain between one- and two-way nesting.

At the finest resolution, some micro-scale wind characteristics around the Peninsula in each of the synoptic states described above were captured. At 16h00 on the 25th , both one- and two-way nesting showed surface wind flow was split by the Peninsula during the north-westerly flow on this day (Fig. 6.41). The northern Peninsula deflected surface wind flow to the east around Devil's Peak which then recurved southward and converged with air that flowed over the Peninsula. Wind flows then assumed a northerly flow and followed a trajectory similar to the shape of the eastern Peninsula. On the western seaboard, the north-westerly wind flow was deflected to the south and followed a path through Noordhoek to False Bay where the wind flow converged with the northerly flow on the eastern Peninsula. Also evident (only in the two-way nesting run) was a wave in the lee of the southern Peninsula where flow was more westerly. This orographically generated wave extended upwards to the 800 hPa level and was also evident in the third domain but not the second. Further evidence of split flow was seen during the south-easterly flow on the 29th. At Muizenberg, surface wind flow was forced by the shape of the Peninsula into a more southerly direction along the eastern Peninsula and an easterly direction through Noordhoek (Fig. 6.42).

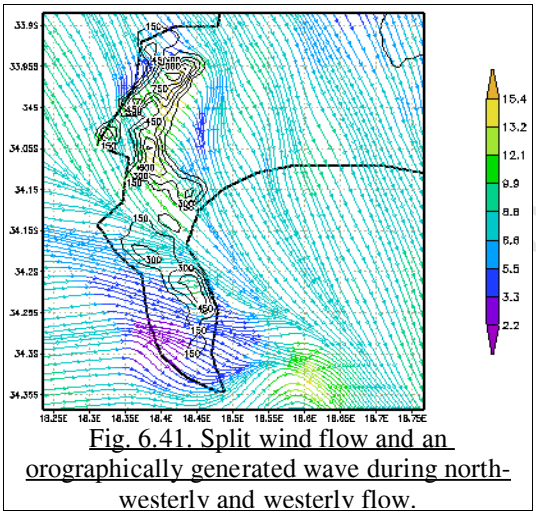

Fig. 6.41. Split wind flow and an orographically generated wave during north-westerly and westerly flow.

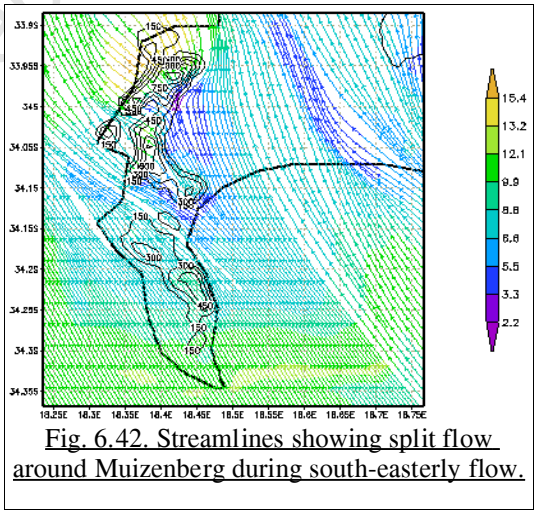

Fig. 6.42. Streamlines showing split flow around Muizenberg during south-easterly flow.

Land and sea breeze circulations became very well defined in this domain. At 08h00 on the 27th streamlines showed a land breeze moving out over False Bay and the Atlantic seaboard (Fig. 6.43). Of particular note were the streamlines that followed the contours of the northern and central Peninsula to Fishoek and then moved westwards over Noordhoek to the Atlantic. Also noteworthy was the small vortex that formed west of Camps Bay in the lee of the Peninsula as winds wrapped around the face of Table Mountain and Lions Head. In Fig. 6.44, at 16h00 the same day, wind flowed eastward through Noordhoek and diverged northward and southward over False Bay and the Cape Flats during the sea breeze.

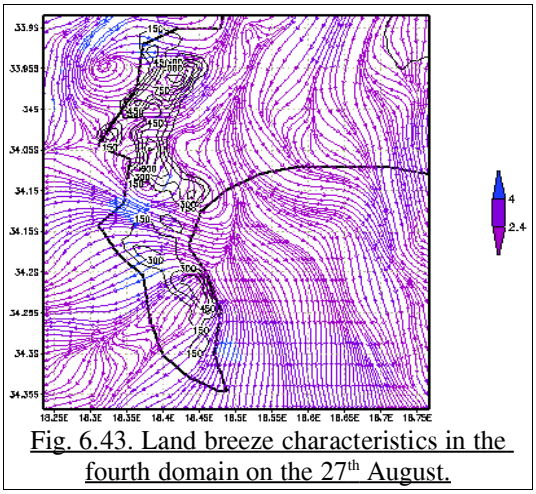

Fig. 6.43. Land breeze characteristics in the fourth domain on the 27th August.

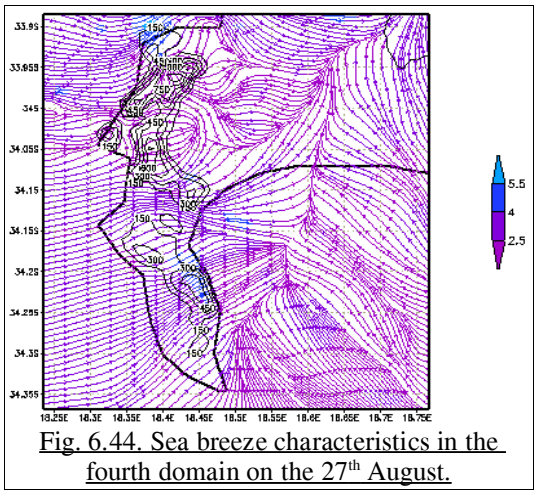

Fig. 6.44. Sea breeze characteristics in the fourth domain on the 27th August.

The differences in wind fields generated by one- and two-way nesting in this domain were generally small except on the eastern and western sides of the northern Peninsula (Fig. 6.45). In these regions, the one-way nested runs produced an average wind field with slower velocities and a more northerly component than the two-way nesting runs which produced wind fields with a more westerly component. In the latter region, one-way nesting produced a wind field with very low velocities. The anomaly maxima here were again realized as a result of northerly and westerly flows associated with the passage of the cold fronts.

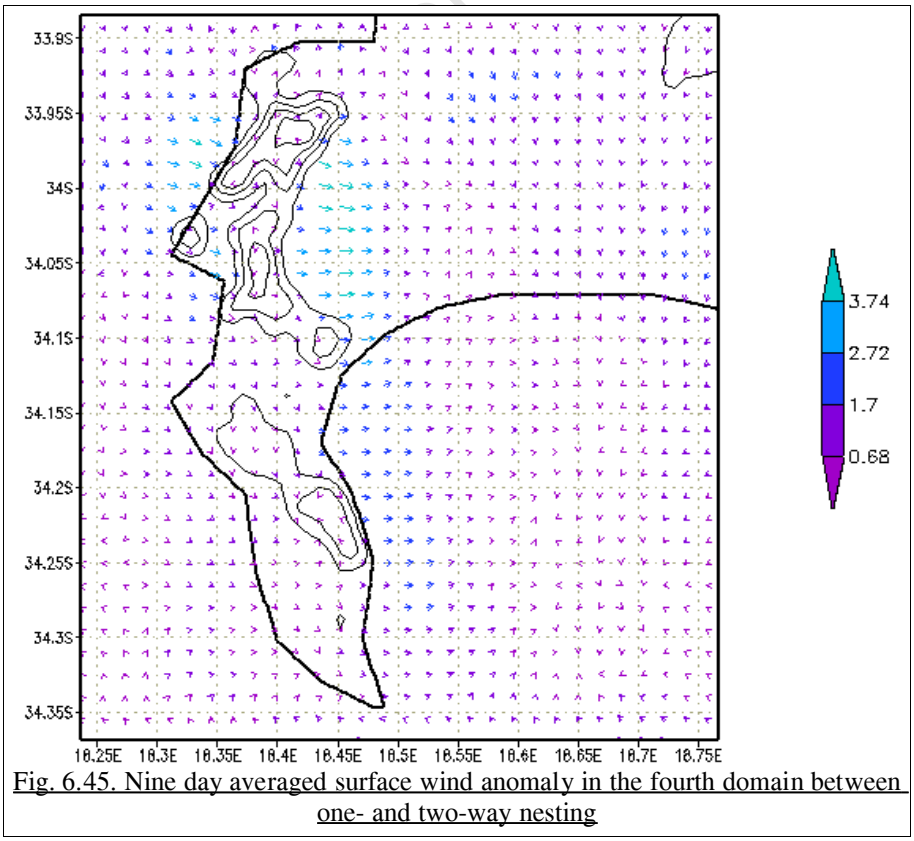

Fig. 6.45. Nine day averaged surface wind anomaly in the fourth domain between one- and two-way nesting

As topographical information in this domain were identical in both techniques, the anomalies were due to lateral boundary conditions obtained from the respective mother domains. The flow of higher resolution data from the mother domains to each subsequent nest in the two-way nesting technique produced more complex wind circulations than the one-way nesting run.

6.6.2 July 2-4

North-westerly winds dominated the surface circulation throughout the three day period. Only the last three time steps of the simulation reported wind directions that were not north-westerly but westerly. Through all domains, the passage of the fronts was not discernible in wind fields at either the surface or upper air as the close proximity of the fronts did not allow much variation in wind direction. At the synoptic scale, velocity maxima (averaged over the three days) were situated over the Hottentots Holland mountain range with minima in the lee of the Hottentots Holland (Fig. 6.46). In the fourth domain, the windward side of the northern Peninsula showed a slowing and split of the wind flow to the south and east by the topography (Fig. 6.47). At this resolution maximum wind velocities were situated over the highest regions of the Peninsula and lowest magnitudes were evident in the lee of the Peninsula.

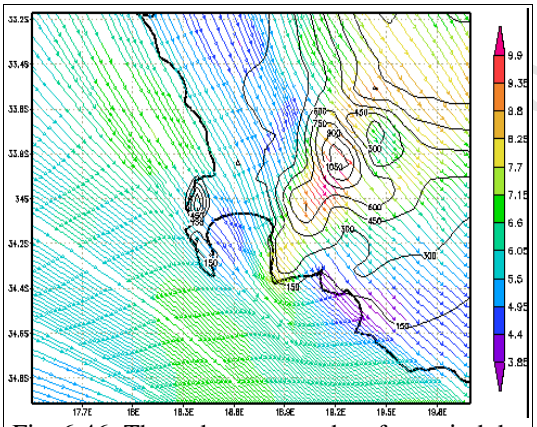

Fig. 6.46. Three day averaged surface wind the second domain for the period 2-4 July 2001.

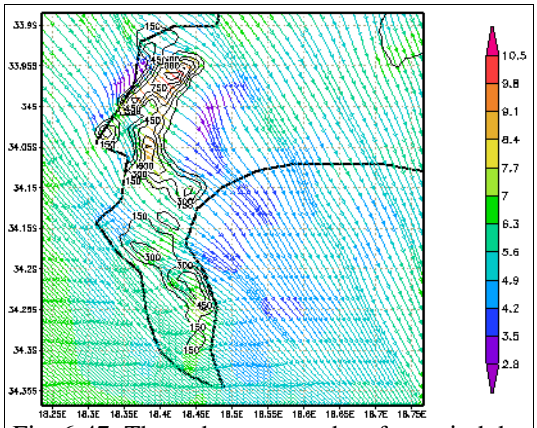

Fig. 6.47. Three day averaged surface wind the fourth domain for the period 2-4 July 2001.

In the anomaly maps, one- and two-way nesting vectors were presented together with the resultant of these two vectors as the homogeneous nature of the wind flow facilitated these additions. The one-way nesting vector is black, the two-way nesting vector maroon and the resultant was coloured with its magnitude. Contour intervals of topography were excluded so as not to obfuscate reading of the anomaly vectors.

In the second domain, maximum anomaly magnitudes were over the southern parts of Hottentots Holland mountains and reached 6 ms^{-1} (Fig. 6.48). Over these regions, averaged two-way nested wind velocities were between 8-9 ms^{-1}, thus the one-way nested values were almost one-and-a-half times greater. In the fourth domain, maximum anomaly values were marginally higher than in the second domain, the highest anomalies situated over the northern Peninsula (where the highest average two-way nesting wind speeds were simulated) and in its immediate lee (Fig. 6.49). Only on the western slopes of the northern Peninsula were averaged two-way nesting velocities higher than one-way nesting values.

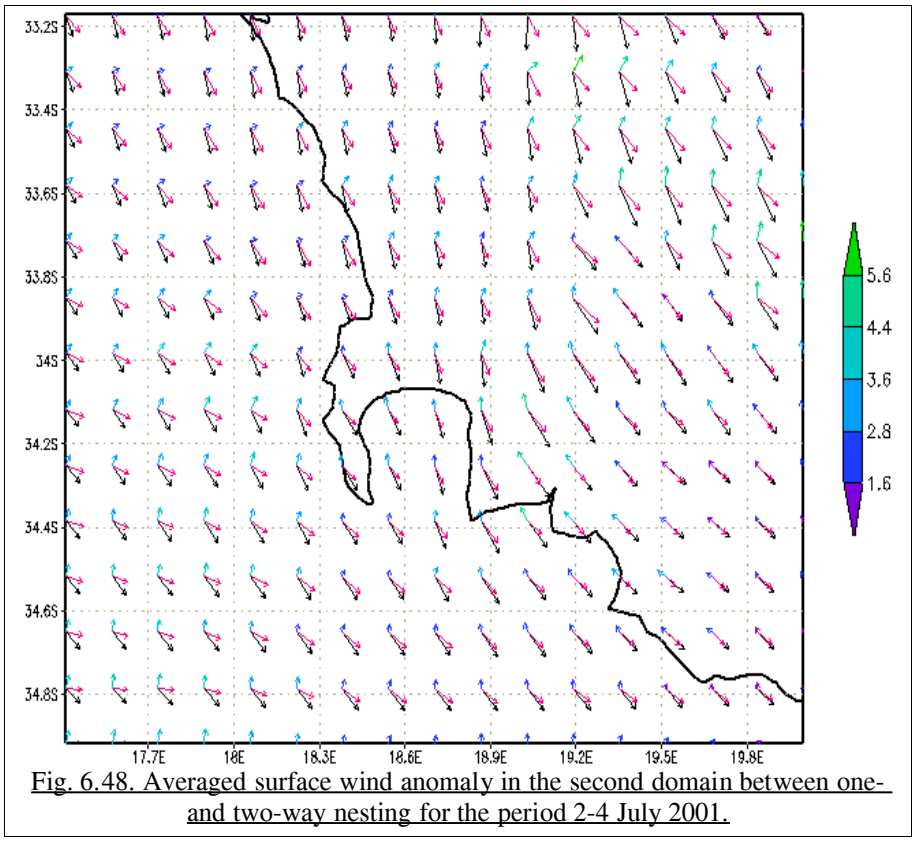

Fig. 6.48. Averaged surface wind anomaly in the second domain between one- and two-way nesting for the period 2-4 July 2001.

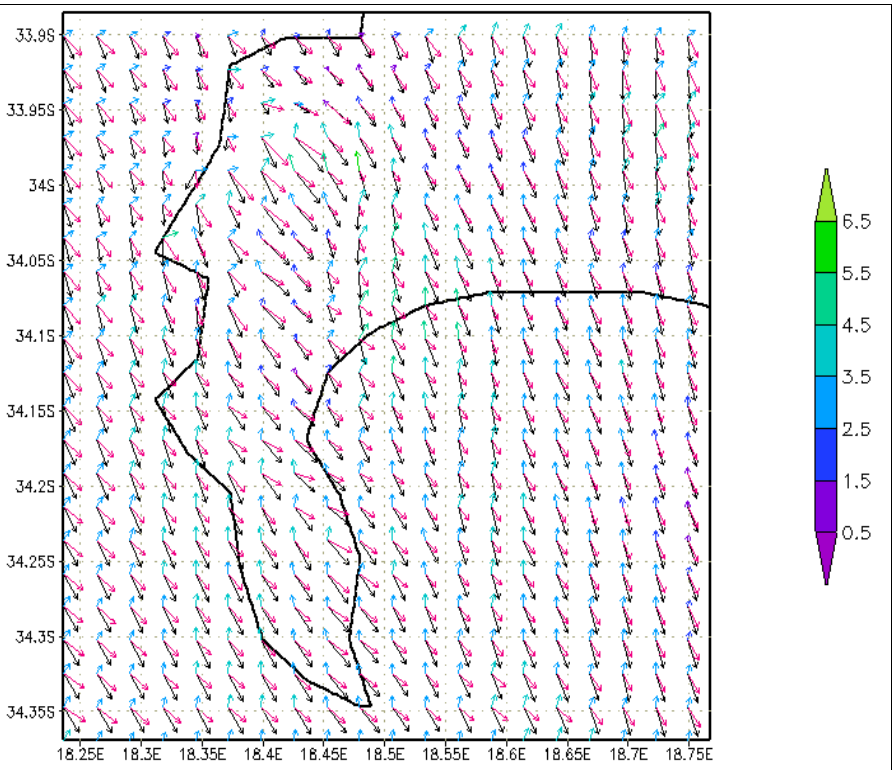

Fig. 6.49. Averaged surface wind anomaly in the fourth domain between one- and two-way nesting for the period 2-4 July 2001.

6.6.3 July 17-19

North-westerlies again dominated the wind flow during this period, however, the passage and intensities of the cold fronts were reflected in the synoptic scale wind circulation. The front of the 18th displayed a wave structure in the upper air as well as at the surface as it approached the south-western coast of South Africa (Fig. 6.50). On the 19th the location of the leading edge of the front was more evident on this day in the region where wind direction changed from north-westerly to westerly (Fig. 6.51). Maximum surface wind velocities were associated with north-westerlies in both cases although wind velocities on the 19th were generally lower.

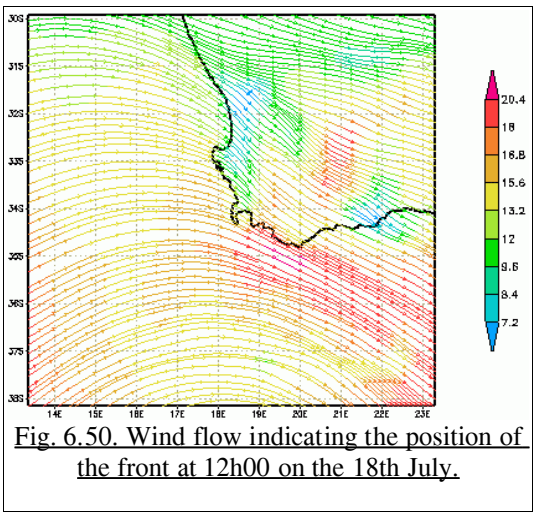

Fig. 6.50. Wind flow indicating the position of the front at 12h00 on the 18th July.

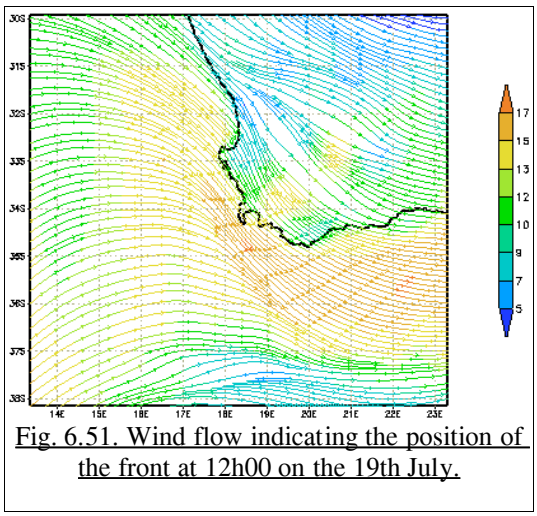

Fig. 6.51. Wind flow indicating the position of the front at 12h00 on the 19th July.

At higher resolutions, topographically altered flow was more apparent during westerly flow than north-westerly flow. During general westerly flow, a northerly flow was set up in the lee of the Peninsula as winds traversed the face of Table Mountain and interacted with flow that traversed the Peninsula (Fig. 6.52). The northerly flow was a shallow feature only evident in the first two vertical levels - above the 900 hPa level flow was again westerly. These flows were typically set up shortly after a transition from northerly to westerly flow. Flows such as these are documented in detail by Schär and Smith (1993a,b) and Baines (1995) who describe shallow stratified flows past an isolated topographical feature.

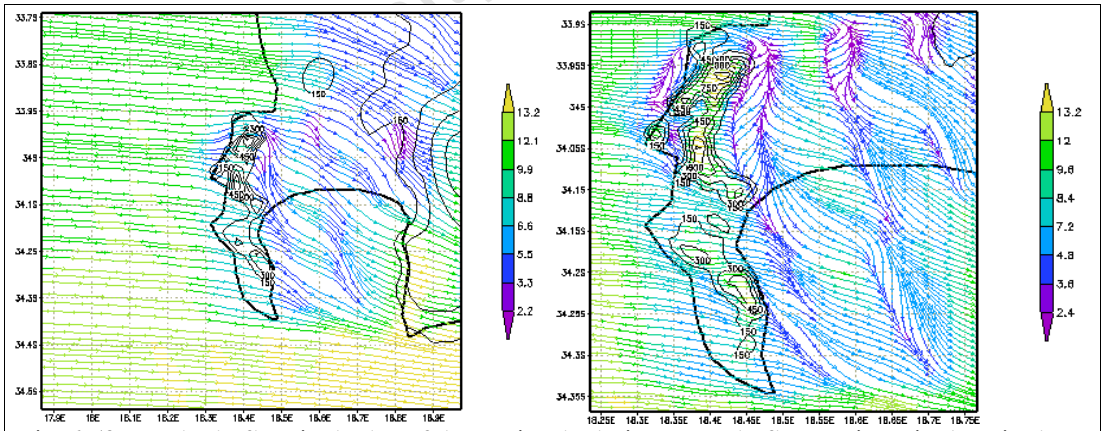

Fig. 6.52. Northerly flow in the lee of the Peninsula during westerly flow regimes in domain three (left) and domain four (right) at midnight on the 19th July.

At the synoptic scale, highest three-day average flows were situated over the Hottentots Holland mountains and over the sea to the south of the region. Lowest surface wind speeds were located over the west coast and in the lee of the Hottentots Holland (Fig 6.53). In the fourth domain,

maximum wind speeds were located over the northern (highest) parts of the Peninsula (Fig. 6.54). A southward deflection of surface wind streams by the northern Peninsula was also evident and lowest wind velocities were associated with this region. This deflection was a surface feature and was not evident above the 900 hPa level. The magnitude of wind maxima in the fourth domain was higher than in the second domain and minima were lower.

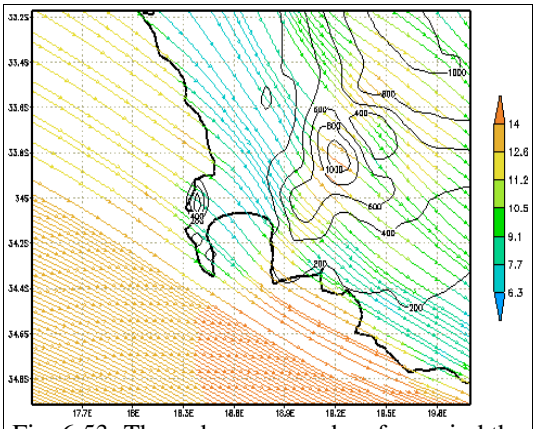

Fig. 6.53. Three day averaged surface wind the second domain for the period 17-19 July 2001.

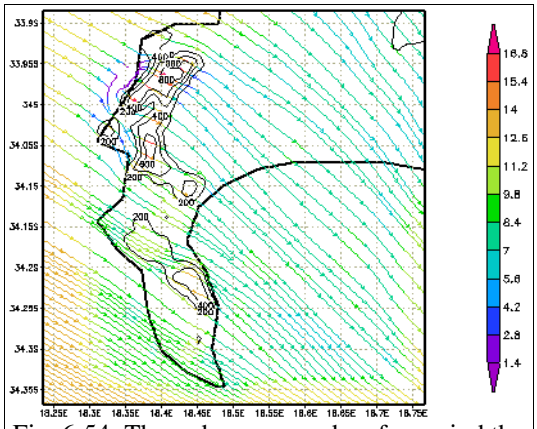

Fig. 6.54. Three day averaged surface wind the fourth domain for the period 17-19July 2001.

Anomalies between the nesting techniques in the second domain were highest over the lower southern region of the Hottentots Holland mountains and the flatter regions of the southern coast (Fig. 6.55). This was as a result of the smoother topography used by the one-way nesting. Anomalies were greatest over land and regions of lower topography and lowest over the sea. At a higher resolution, the fourth domain displayed generally higher anomaly magnitudes (maximum anomalies of 12 ms^{-1}) on the western side of the northern Peninsula (Fig. 6.56). As topographies were identical in this domain, the anomalies were due to differences in the lateral boundary conditions produced by the respective nesting procedures.

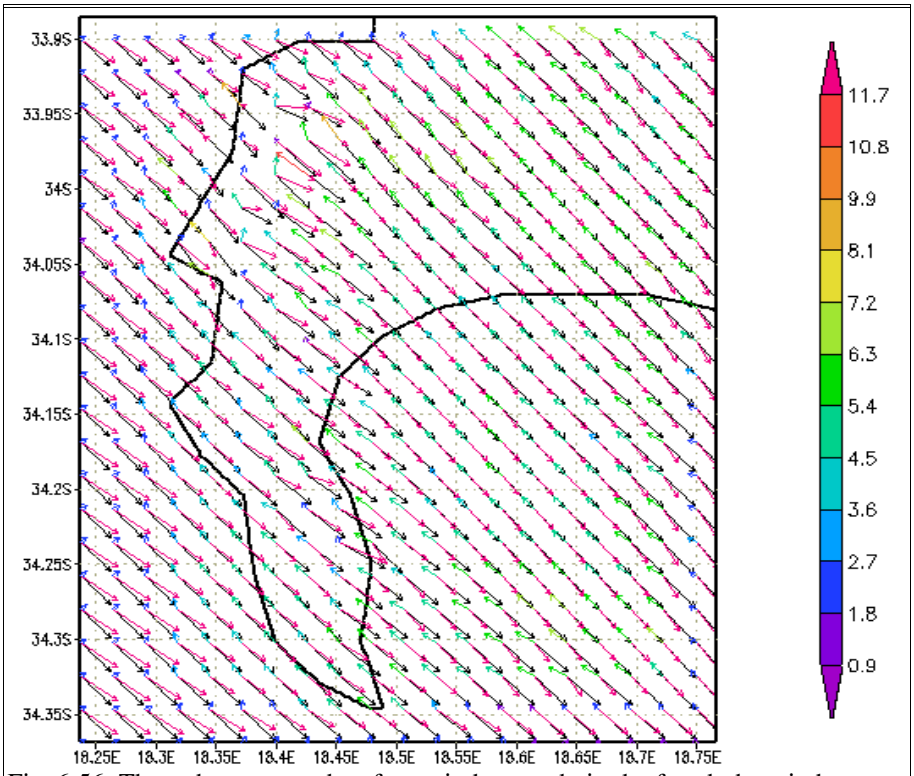

Fig. 6.56. Three day averaged surface wind anomaly in the fourth domain between one- and two-way nesting for the period 17-19 July 2001.

6.6.4 Wind field summary

Expected synoptic-scale wind flows associated with cold fronts and ridging high pressures were evident in the simulated wind streams in the lower resolution domains. As grid resolution increased, meso- and micro-scale surface wind characteristics became more defined as a result of topographic forcing. During strong wind flow regimes, such as north-westerlies and south-easterlies, the topography modified wind flows through deflection and splitting of wind streams and resultant divergence and convergence zones were also captured. Under low wind velocity regimes, well defined land and sea breeze circulations were captured at higher resolutions.

Two-way nesting resolved more complex flows than one-way nesting as a result of both higher resolution topographies over the nested regions as well as enhanced boundary forcing data available for each nest. One-way nesting produced generally stronger wind flows as a result of a smoother, less complex topography. Anomalies were at a maximum when one wind regime dominated the simulation period. When several wind regimes were present, as in the August period, a smoothing of the anomaly values occurred and resulted in smaller anomalies between nesting techniques.

6.7 Summary

The MM5 simulations captured the characteristics of different weather regimes over the region at synoptic, meso- and micro-scale resolutions. At the lowest resolution, variables reflected the synoptic state as well as transitions between states. As the spatial resolution increased from the first domain through the nests, complex, topographically modified features were captured such as lower temperatures over regions of highest topography, split wind flows and wind shadows. At highest resolutions various wind regimes were captured including land and sea breezes that were not evident in coarser domains.

Two-way nesting produced more significant topographical modification of the temperature and wind fields than one-way nesting. Simulations using this nesting technique employed enhanced topographies in the nested regions which in turn generated enhanced lateral boundary forcing data for simulation in successive nests. One-way nesting did not produce the enhanced topography field in the mother domain. Thus different lateral boundary conditions were generated in the mother domain by each nesting technique and were used to force the respective nests. The importance of lateral boundary forcing in the evolution of model output and the propagation of errors through domains, which is principally what occurred here through each technique having a different topography, has been the focus of many studies e.g. Shapiro and O'Brien 1970; Perkey and Kreitzberg 1976; Warner et al. 1997. The differences in the forcing data, having been accumulated through the preceding three domains, resulted in anomalies in the fourth domain despite these having identical topographies.

The two-way nesting scheme captured more complex characteristics of the temperature and wind fields than one-way nesting. Temperature fields produced by the two-way nesting scheme compared more favourably with observed data and more complex topographically modified wind fields were resolved. Although one-way nesting produced warmer than observed temperatures, these were generally limited to a few regions of the Peninsula in the finer nests. This was also true for the wind fields. Thus, both nesting schemes provided satisfactory results over most of the region at the highest resolutions.

Chapter Seven

High Resolution Simulations – Precipitation Results

7.1 Introduction

Simulations were performed at high resolution over the topographically complex South-Western Cape for selected days in July and August 2001 to capture the spatial and temporal characteristics of extreme rainfall over the region. The results of the simulations were then tested against observed and derived precipitation data. The August simulation is presented first to establish the accuracy of the precipitation simulation against station and radar-derived precipitation data. The spatial and temporal distribution of simulated precipitation was examined and in the third and fourth domains compared against observed station data. The differences between one- and two-way nesting were then presented. The simulated data in the third and fourth domains were then compared against radar-derived precipitation data and discussed. Thereafter the results from the two July periods were presented, followed by a discussion of these.

7.2 August 22-29

At the synoptic scale, the passage of the cold fronts on the 23rd and 29th could be seen in the precipitation fields of the first domain, rainfall on the 29th being more widespread (Fig. 7.1a,b). Almost no precipitation was simulated for the passage of the weak front on the 26th at this resolution. Most of the precipitation from the front on the 23rd was simulated between 12h00 and 20h00. The passage of the front on the 29th was preceded by some pre-frontal precipitation at 20h00 on the 28th when the front was situated to the south west of the country. The front made landfall between 00h00 and 04h00 and precipitation persisted until 12h00 (Fig. 7.2). No more precipitation was simulated over the Peninsula by 16h00 and over the Hottentots Holland mountain range by 20h00.

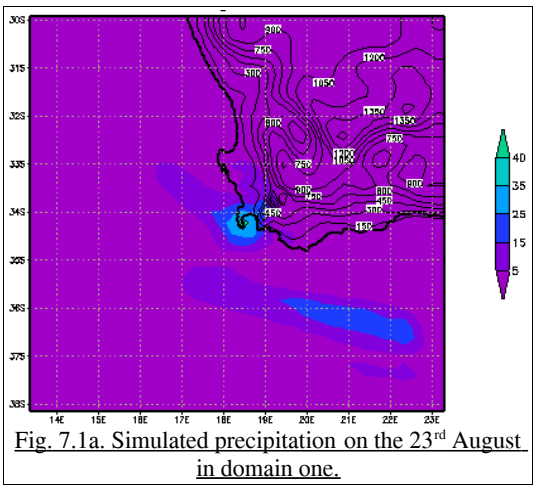

Fig. 7.1a. Simulated precipitation on the 23rd August in domain one.

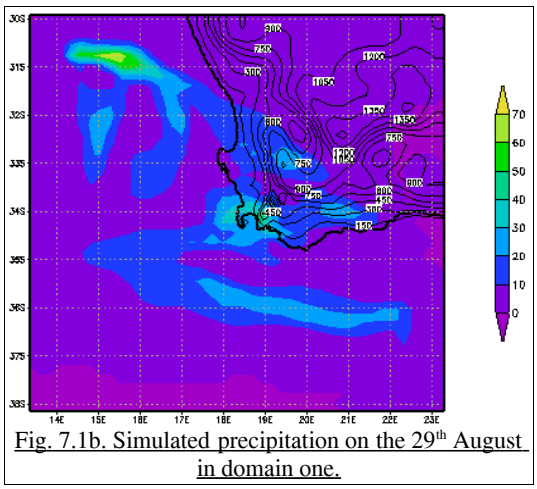

Fig. 7.1b. Simulated precipitation on the 29th August in domain one.

Over the nine day period precipitation maxima occurred over the Peninsula and the Hottentots Holland (Fig. 7.3.). Although almost no topography was apparent for the Peninsula at this resolution, it was in the nested area (where topographies were blended) that highest overall precipitation values were simulated.

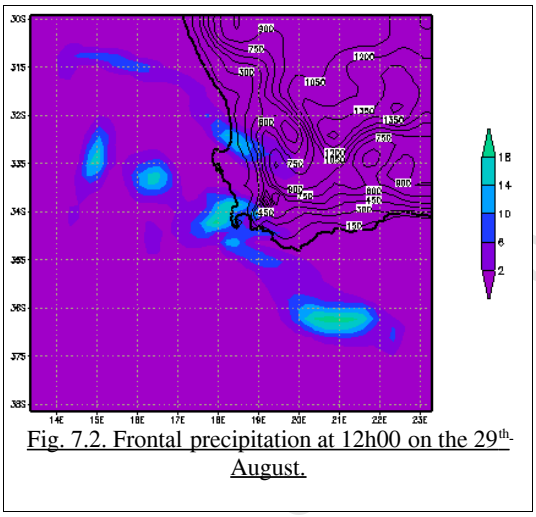

Fig. 7.2. Frontal precipitation at 12h00 on the 29th August.

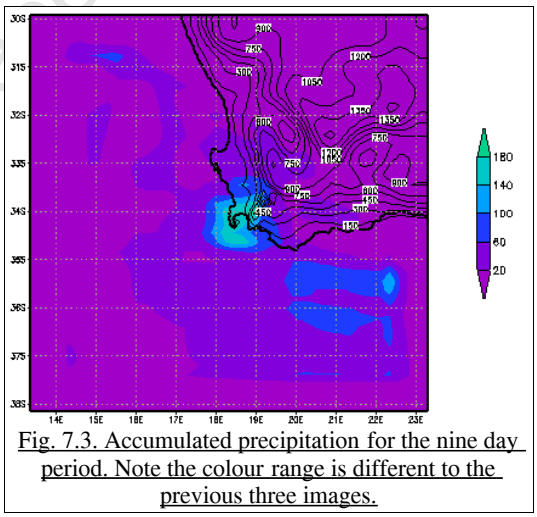

Fig. 7.3. Accumulated precipitation for the nine day period. Note the colour range is different to the previous three images.

The two-way nesting technique simulated more precipitation than the one-way nesting technique (Fig. 7.4). Positive anomalies over the land were strongly evident over the nest area and more weakly so over most of the Western Cape landmass. During specific regimes, such as the cold fronts of the 23rd and 29th, this positive anomaly was also clearly evident, especially over the greater Cape Town region (Fig. 7.5). Here the one-way nesting simulations produced much less precipitation than the two-way nested runs.

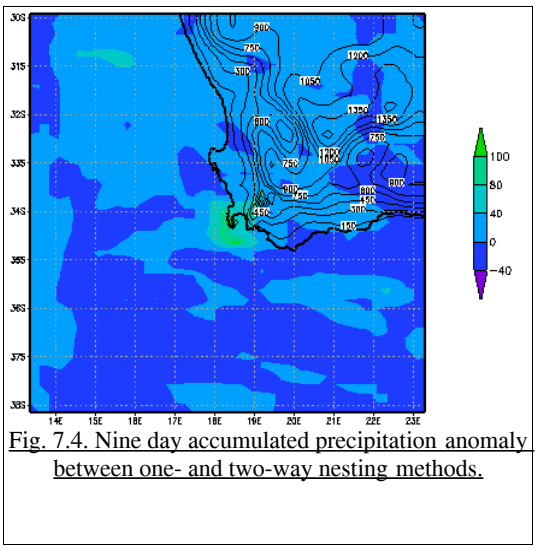

Fig. 7.4. Nine day accumulated precipitation anomaly between one- and two-way nesting methods.

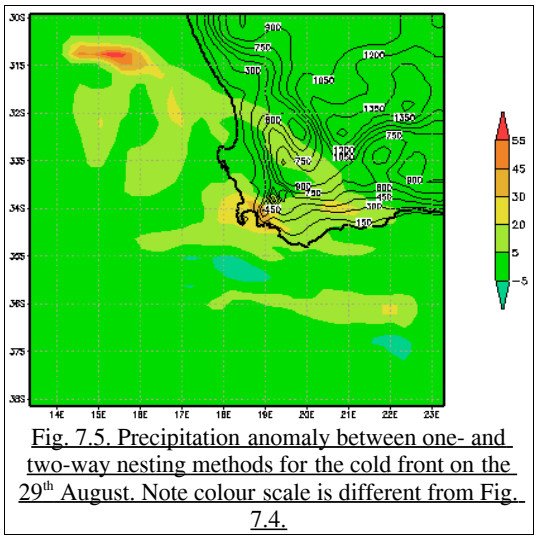

Fig. 7.5. Precipitation anomaly between one- and two-way nesting methods for the cold front on the 29th August. Note colour scale is different from Fig. 7.4.

In the second domain, the effect that the enhanced topography of this domain had on the simulation of precipitation was captured, most notably over the Cape Peninsula and the Hottentots Holland. On the 23rd more precipitation was evident over and in the lee of the higher regions of the Peninsula with precipitation maxima over regions of highest topography (Fig. 7.6a). On the 29th precipitation was more widespread than the weaker front on the 23rd and maxima were again over regions of higher topography (Fig. 7.6b).

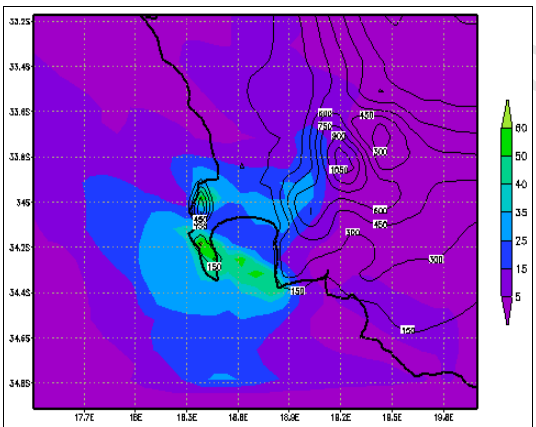

Fig. 7.6a. Simulated precipitation on the 23rd August for the second domain.

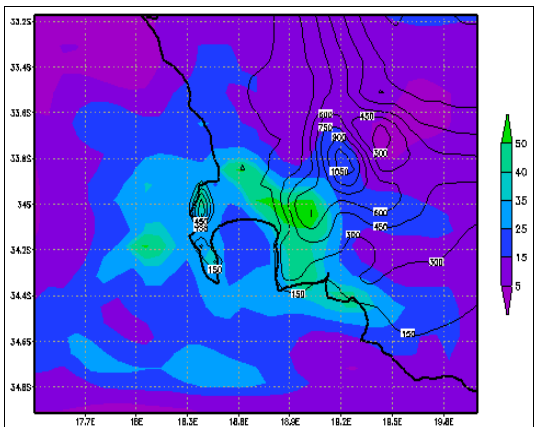

Fig. 7.6b Simulated precipitation on the 29th August for the second domain.

Post-frontal rain was captured over the highest parts of the Peninsula on the 24th, as well as on the slopes of and over the south-western parts of the Hottentots Holland (Fig. 7.7a). The post-frontal precipitation was not evident in the simulation using one-way nesting. With the passage of the weak cold front on the 26th, precipitation was simulated over the Peninsula with a maximum evident over the highest parts of Table Mountain (Fig. 7.7b).

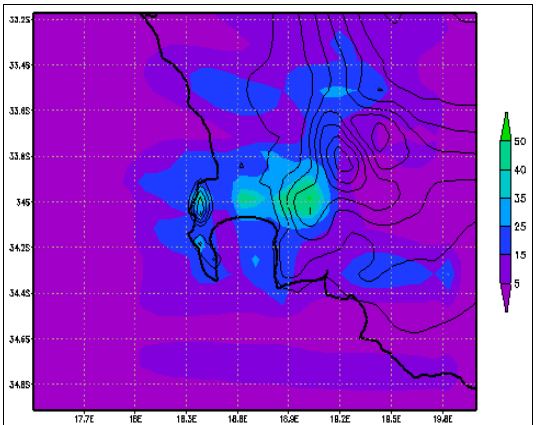

Fig. 7.7a. Simulated post-frontal precipitation on the 24th August for the second domain.

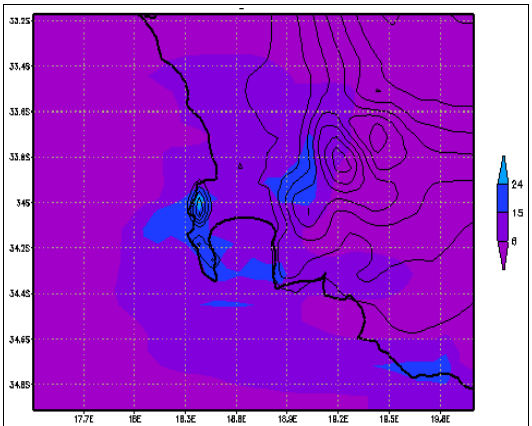

Fig. 7.7b. Precipitation simulated with the passage of the weak cold front on the 26th August for the second domain.

Over the nine days, precipitation maxima were situated over the highest parts of the northern and southern Peninsula and the south-western parts of the Hottentots Holland range (Fig. 7.8). High precipitation values were evident east of the Peninsula over the Cape Flats and the southern regions of False Bay. Large anomalies were evident between nesting techniques in this domain. Over the Peninsula and the Cape Flats the anomalies were positive with maxima over the highest lying regions of the Peninsula (Fig. 7.9). Negative anomalies were apparent off the west coast and north-western regions of the Hottentots Holland.

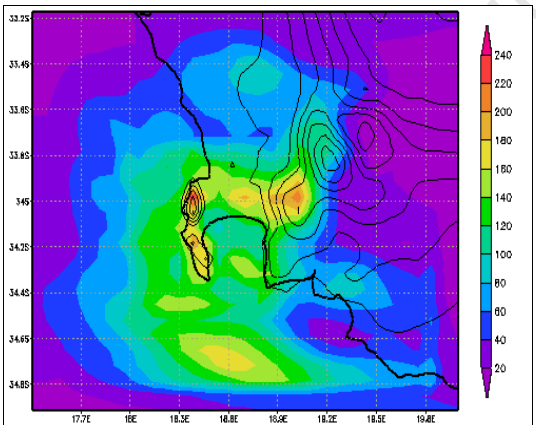

Fig. 7.8. Nine day accumulated precipitation for the second domain.

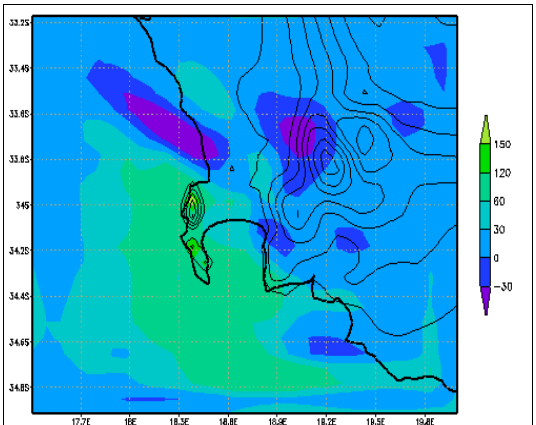

Fig. 7.9. Nine day accumulated precipitation anomaly for the second domain.

The extent of the third domain facilitated the comparison of model results with daily station data as well as radar-derived precipitation data. The 9-day accumulated precipitation for the one- and two-way nested runs were compared first with the station data. Immediately evident was the over-

simulation of precipitation by the two-way nesting procedure at all stations and a more reasonable simulation by the one-way nesting technique (Fig. 7.10a,b).

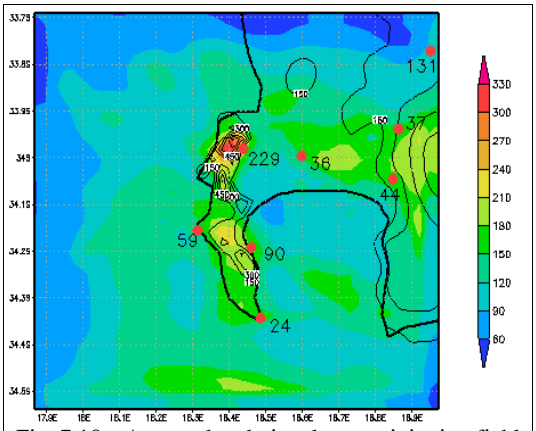

Fig. 7.10a. Accumulated nine day precipitation field for the two-way nested run in the third domain with recorded station data.

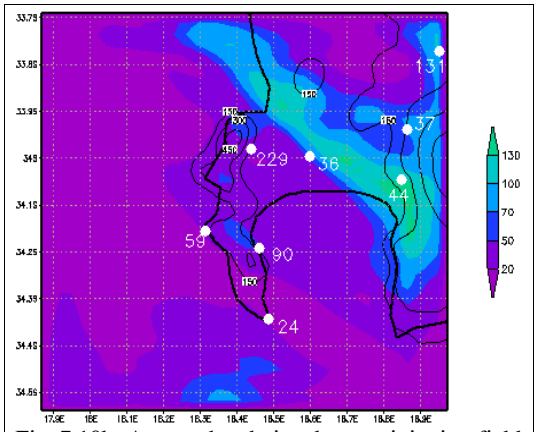

Fig. 7.10b. Accumulated nine day precipitation field for the one-way nested run in the third domain with recorded station data.

The two-way nested simulation produced heavy rainfall over the Cape Flats with a minimum of 90 mm and a maximum of 210 mm throughout the run period. The recorded data at Cape Town International Airport showed the simulated precipitation to exceed observed values by almost three times. Precipitation maxima were simulated over the northern Peninsula with high precipitation values (over 120 mm) over almost the entire region. Observed station data, averaged over the nine days at the eight stations was 81 mm. In contrast, a similarly calculated value for the two-way nesting runs was 165 mm, an excess of more than double. This dramatic over- estimation of precipitation was especially evident during the passage of the cold fronts (Fig. 7.11).

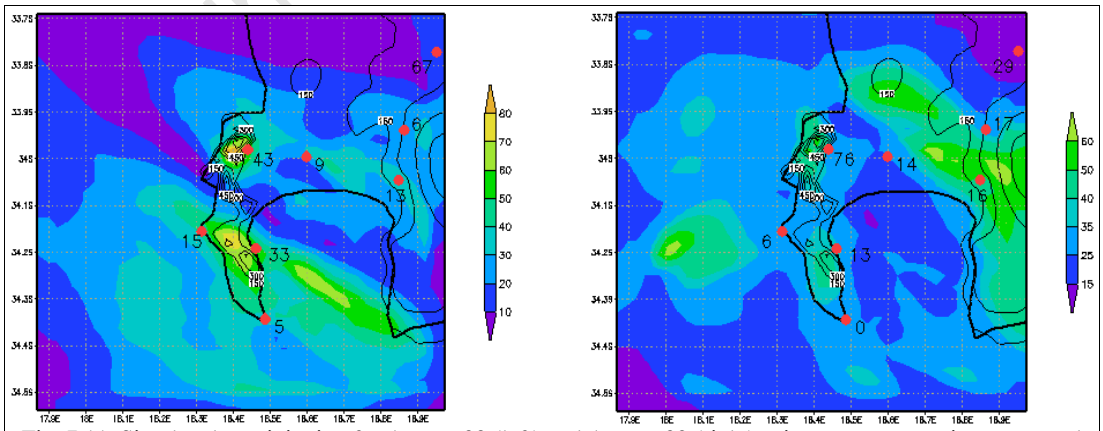

Fig. 7.11. Simulated precipitation for August 23 (left) and August 29 (right) using two-way nesting compared with observed station data.

The one-way nested simulation produced precipitation magnitudes with a much greater degree of accuracy than the two-way nested run. Simulation of the front on the 23rd showed a band of precipitation that stretched from the north-west of the domain to the south-east across the Cape Flats (Fig. 7.12). Precipitation values lower than observed were simulated at stations outside the band of rainfall e.g. Groote Schuur and Simonstown, with higher than observed values at stations inside the band e.g. Strand and the Airport. Simulated precipitation of the front on the 29th was spatially more uniform and there was also closer agreement between the simulated and station data. The nine day average for all eight stations was 68 mm, 13 mm less than the averaged observed record.

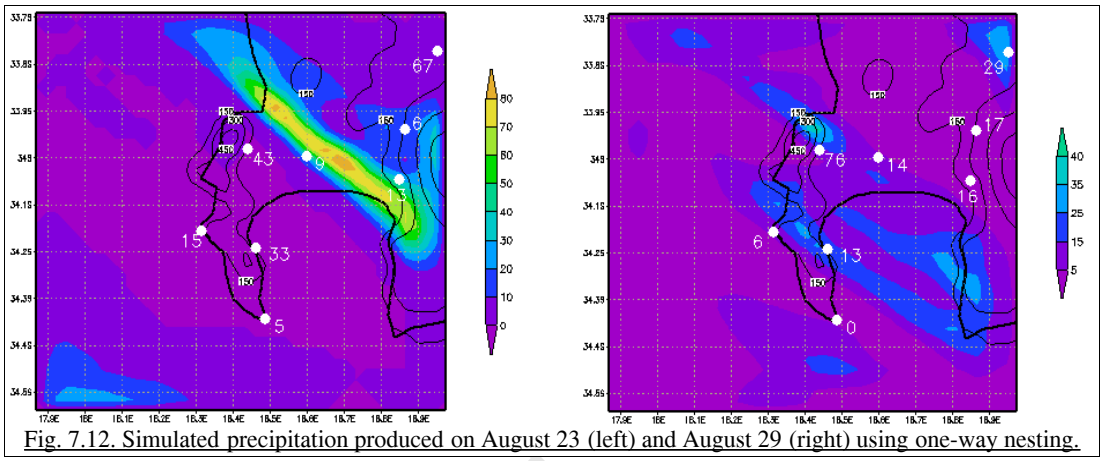

Fig. 7.12. Simulated precipitation produced on August 23 (left) and August 29 (right) using one-way nesting.

The overestimation of precipitation by the two-way nesting technique propagated into the fourth domain. As topographies were identical for both nesting techniques in this nest, the difference between the nesting procedures was due to the forcing data used from the domains above. Over the nine days, the two-way nested simulation produced rainfall values of over 90 mm across almost the entire region with maxima over Table Mountain and the northern Peninsula. The one-way nested runs generally underestimated precipitation, with the exception of the Airport and Cape Point (Fig. 7.13), however, results were more realistic. The anomaly between recorded and modelled precipitation for all stations over the nine day period showed the one-way nested run to underestimate precipitation by almost 250 mm. However, excluding the Groote Schuur station which had a large nine-day difference, this anomaly dropped to an underestimate of 80 mm.

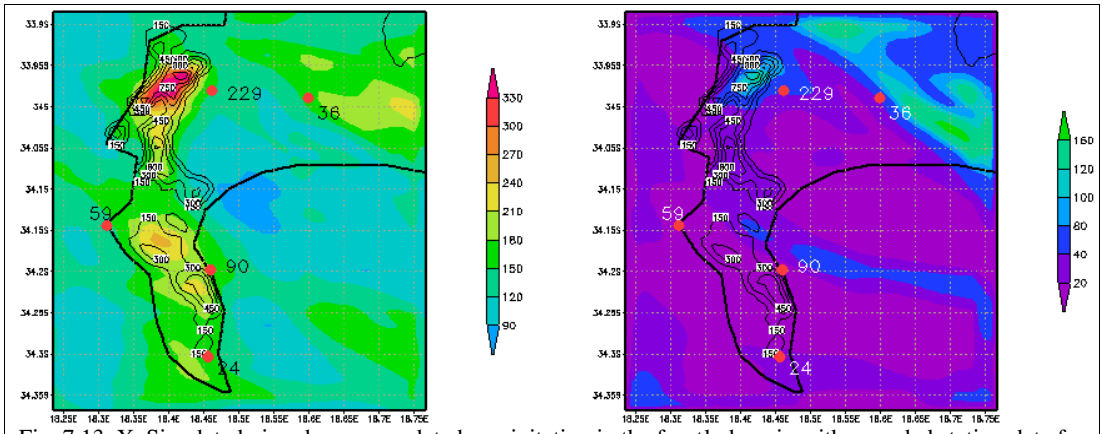

Fig. 7.13. X. Simulated nine-day accumulated precipitation in the fourth domain with recorded station data for two-way (left) and one-way nesting (right).

During the passage of the cold front on the 23rd, the two-way nested run again simulated precipitation well above the observed values (Fig. 7.14). Only at Groote Schuur were values similar to station data whereas at the other stations values were on average three times the observed. The one-way nesting precipitation output was less than the recorded data, except at the Airport, where a tongue of precipitation containing precipitation maxima stretched from Table Bay to the south east of the Cape Flats. The under-simulation of precipitation by the one-way nesting technique at other stations was 63 % of the recorded values.

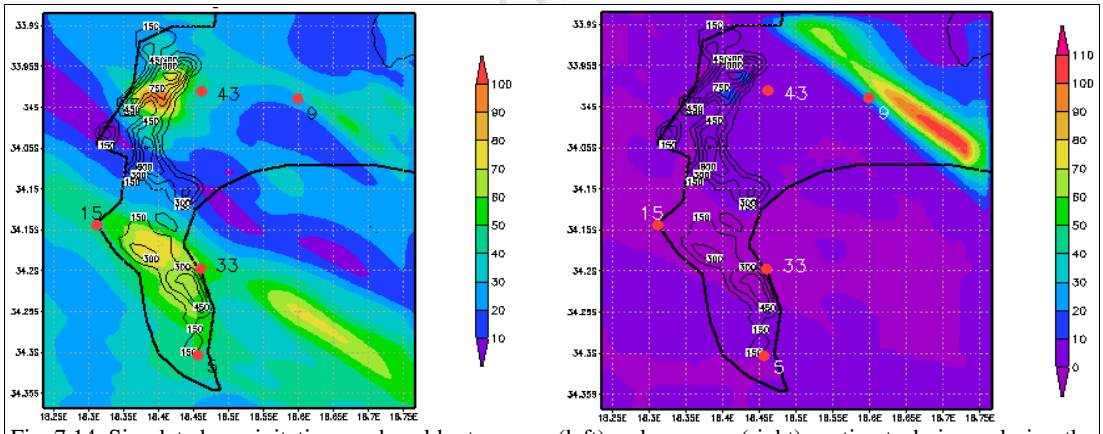

Fig. 7.14. Simulated precipitation produced by two-way (left) and one-way (right) nesting techniques during the front of August 23.

On the 29th, the two-way nesting run simulated 170 % of the 109 mm recorded precipitation at the stations. The one-way nested run simulated a total of 70 mm at the stations, 65 % of the total recorded figure (Fig. 7.15). When the Groote Schuur station was excluded, however, there was good agreement between observed precipitation and the one-way nested run, this having simulated 35 mm of the recorded 33 mm. Spatially, precipitation was simulated in two bands, one over the north of the domain and one across the centre of the domain, both with a north-west to south-east

orientation. Both of these bands had respective precipitation maxima over and in the lee of the Peninsula. The southerly band exhibited a greater spatial extent but higher maxima were simulated in the northerly band.

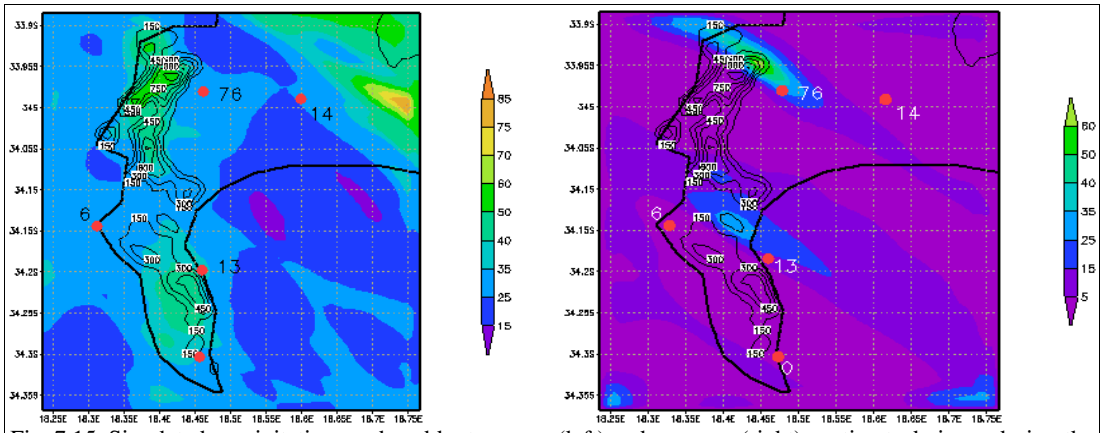

Fig. 7.15. Simulated precipitation produced by two-way (left) and one-way (right) nesting techniques during the front of August 29.

Using the station data, it was possible to roughly discern the spatial and volumetric accuracy of the simulated precipitation. It was also evident from these data that the two-way nesting procedure dramatically overestimated precipitation in the region such that these results were unusable. The one-way nesting procedure simulated lower but more realistic precipitation fields, especially when the heavily orographically modified precipitation data from the Groote Schuur station was excluded. However, station data is restricted by its point source nature and could not provide spatially contiguous information on precipitation volumes and distribution across the entire region. For example, it could not be established using station data if the band of precipitation across the Cape Flats on the 23rd August was a real feature or an incorrect simulation.

In the following section, radar-derived precipitation data is used alongside the station data in an attempt to improve the validation process of simulated precipitation. The radar data were converted into the same format as the model data to facilitate a more robust comparison.

7.3 Verification of simulated precipitation data with radar data

7.3.1 Results

Simulated precipitation data were compared with radar-derived precipitation data in the third and fourth domains to test the temporal and spatial characteristics of the modelled rainfall. The timing, volumes and spatial distributions of the simulated precipitation were tested for the 23rd and the 29th August. Only the one-way nested simulation results were considered as a result of the dramatic overestimation of precipitation by the two-way nesting simulations.

Figure 7.16 compares four-hourly radar data in the left column with simulated rainfall data at a 3 km resolution of the same time slice in the right column. From the radar data, precipitation on the 23rd was seen to occur in the early afternoon and late evening (14h00-22h00). The largest volume of precipitation fell between 16h00-20h00 over the Peninsula and False Bay with regions in the Cape Flats receiving highest volumes between 20h00 and midnight. The simulation did not capture the timing, spatial extent nor volumes of precipitation over this period correctly. Most of the simulated precipitation occurred too early in the day (between 00h00 and 12h00) with almost no rainfall simulated between 16h00 and midnight over the Peninsula and Cape Flats, which was when the majority of actual precipitation took place. The model also failed to capture the precipitation over the Peninsula and in its lee. Although it did capture the spatial extent of the band of precipitation that stretched from Table Bay to the north-east corner of False Bay, the simulated magnitudes were too high.

Radar-derived precipitation

Simulated precipitation

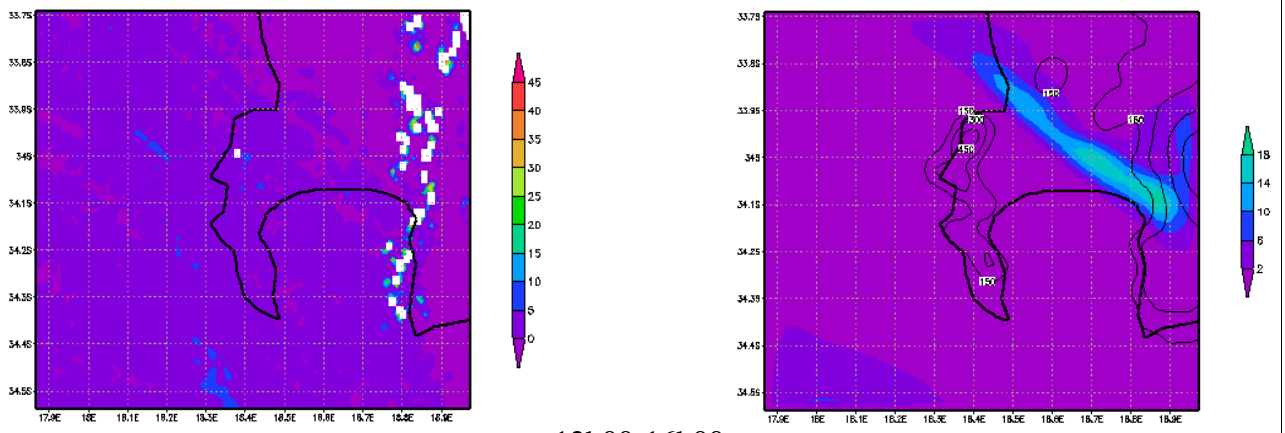

12h00-16h00

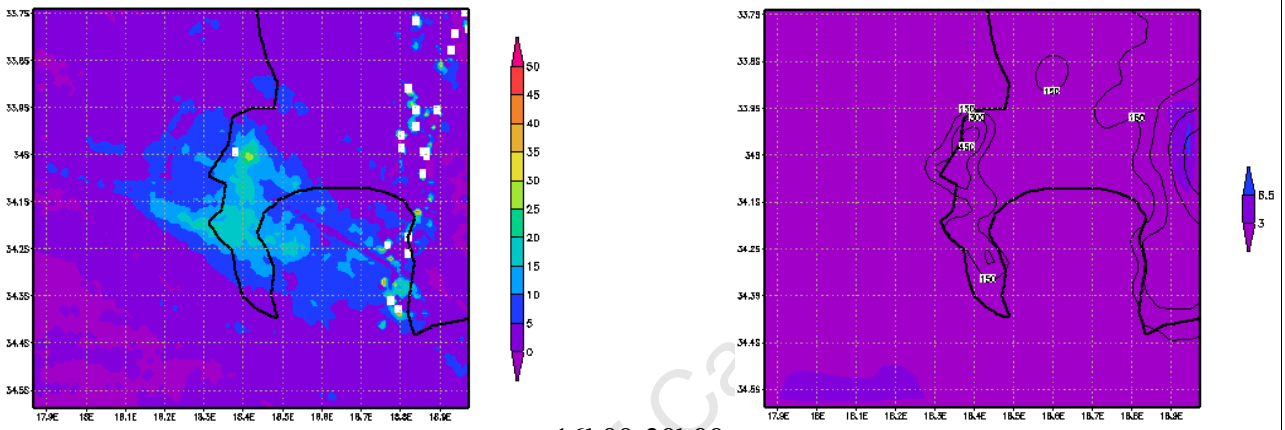

16h00-20h00

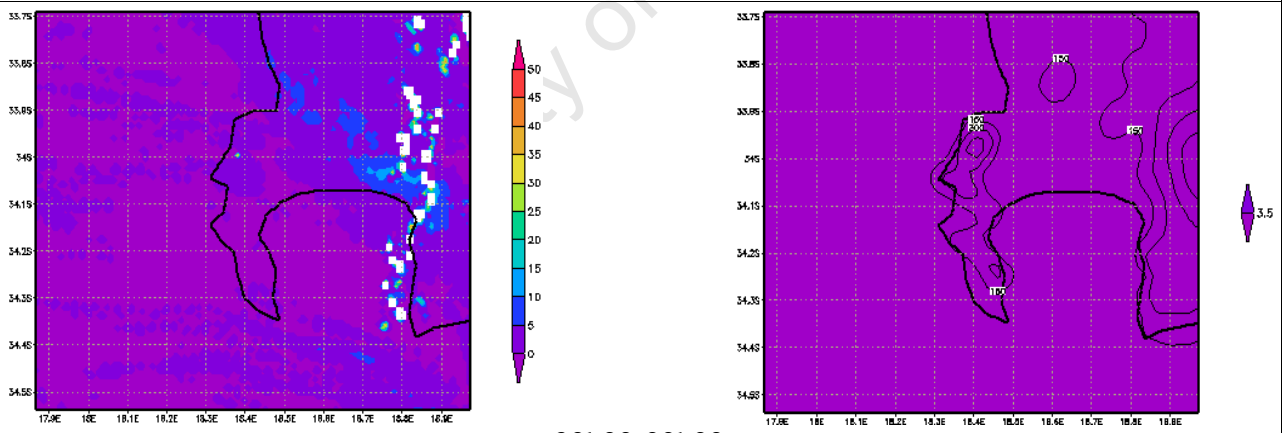

20h00-00h00

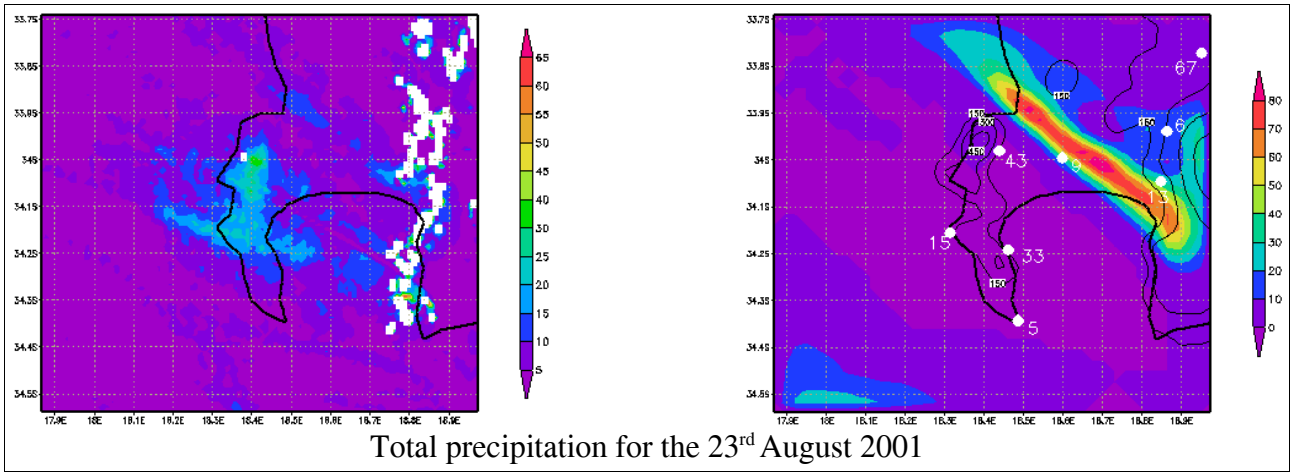

Fig. 7.16. Radar-derived and simulated four-hourly accumulated precipitation for the 23rd August 2001. Values over 50 mm were masked out in the four-hourly radar images and over 80 mm in the total precipitation figure as a result of brightband effects primarily over the Hottentots Holland. Note, the coastal outline is not accurate in the radar images the but offset to the east and west perimeter of the map. The masked out values on the east are over the mountainous regions of the Hottentots Holland and not False Bay. Over the Peninsula this effect less as the region lies in the centre of the map.

Thus the model captured the passage of the cold front on this day, but not the temporal, spatial or volumetric characteristics of the day's precipitation. An inspection of the forcing data revealed higher surface relative humidity (RH) values over the region in the morning than the afternoon. Values of 90 % were seen over the region in the morning with lower values between 70-80 % in the afternoon (Fig. 7.17). The spatial extent of higher RH values also decreased in the afternoon which indicated less moisture in the region at this time. Pressure data also indicated a weakening of the front throughout the day. The forcing wind fields were northerly throughout the day and the temperature data showed a strong diurnal cycle over land with relatively homogeneous values over the ocean. It is unsurprising that given forcing data which indicated stronger frontal conditions in the morning than the afternoon, the model simulated most of the day's precipitation in the morning.

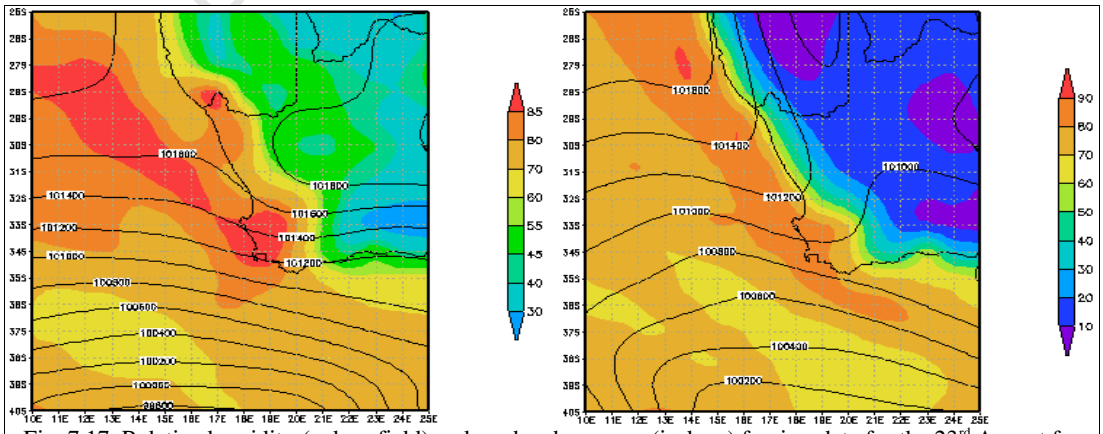

Fig. 7.17. Relative humidity (colour field) and sea level pressure (isobars) forcing data for the 23rd August for 00h00-11h59 (left) and 12h00-23h59 (right).

Simulated precipitation for the 29th August was much improved on the results of the 23rd. Radar showed that rain fell during the early morning to midday (02h00-12h00) with the majority of precipitation falling over the Peninsula and Cape Flats between 04h00-08h00 (Fig. 7.18). Large volumes of precipitation could also be seen over and to the south of False Bay before mid-day. The model simulated precipitation with a north-west south-east orientation throughout the morning, which aligned with the prevailing surface wind direction. The spatial distribution was similar to the radar-derived distribution which showed two distinct bands of precipitation. One band was positioned in the northern part of the domain that stretched from Table Bay to the north-eastern corner of False Bay and a second, more southerly band with heavier precipitation characteristics stretched from the central Peninsula to the south-eastern region of False Bay. The model also captured some of the precipitation upstream of the Peninsula between midnight and 08h00. Precipitation maxima were simulated over the Peninsula and False Bay which was in agreement with the radar data. The model did not capture the lightest band of precipitation situated to the north of the two bands described earlier, which was evident between 04h00 and 08h00 and stretched from north of Table Bay to the south-eastern parts of the Cape Flats nor did it capture precipitation over the central Peninsula as seen in the radar data at this time.

Radar-derived precipitation

Simulated precipitation

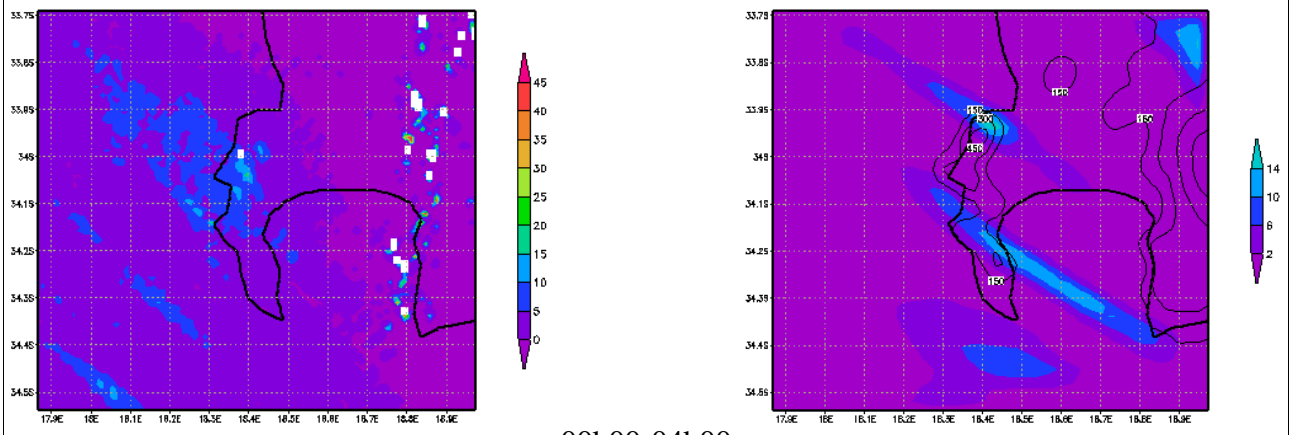

00h00-04h00

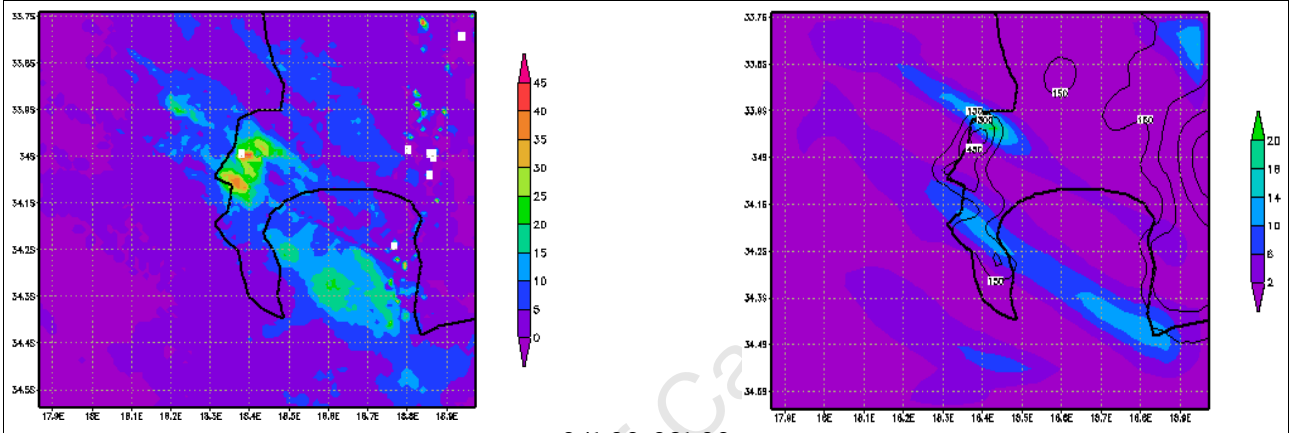

04h00-08h00

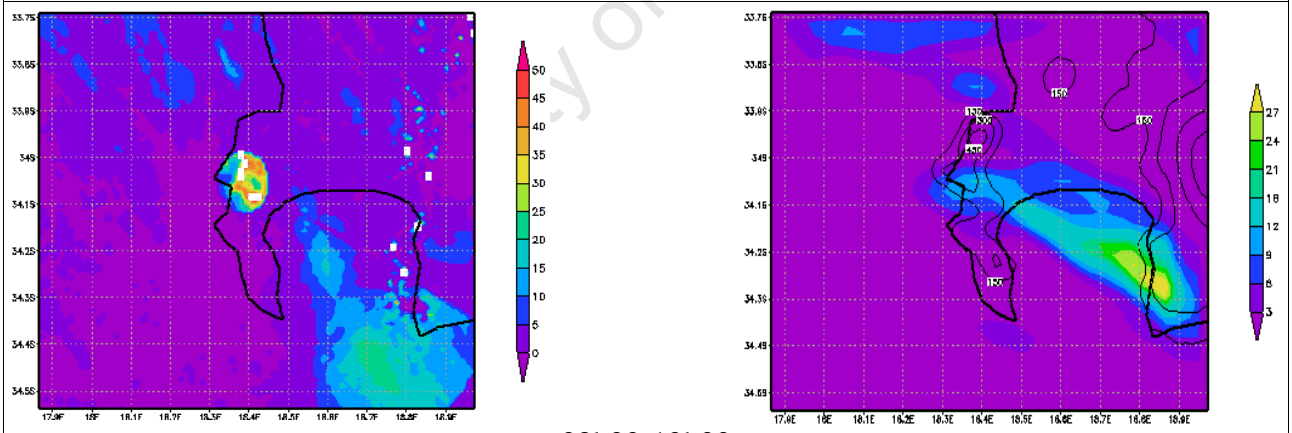

08h00-12h00

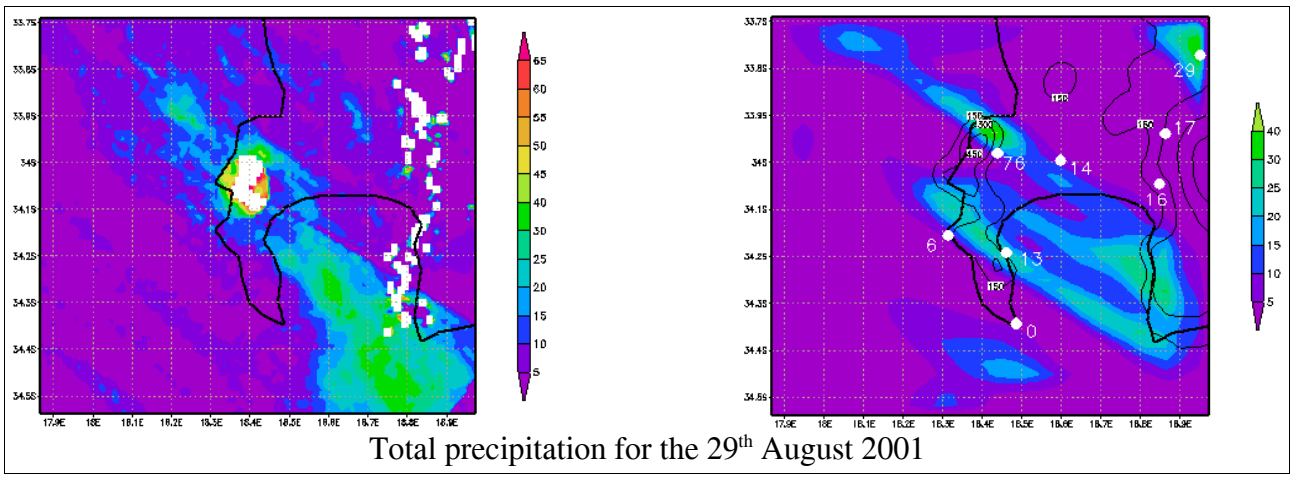

Fig. 7.18. Radar-derived and simulated four-hourly accumulated precipitation in the third domain for the 29th August 2001. Values over 50 mm were masked out in the four-hourly radar images and over 80 mm in the total precipitation figure.

An inspection of the forcing data for the 29th showed a broad band of high surface relative humidity values (90-100 %) to the north-east of Cape Town and of between 80-90 % over Cape Town (Fig. 7.19). Sea level pressure data and the synoptic chart Fig. 4.2 showed the the front to have made landfall in the early morning. During the afternoon the front could be seen to have moved to the east as the south-easterly wind regime began to dominate. Unlike the forcing data of the 23rd, the forcing synoptics on this day were consistent with the passage of a front in the morning and the model captured the associated precipitation.

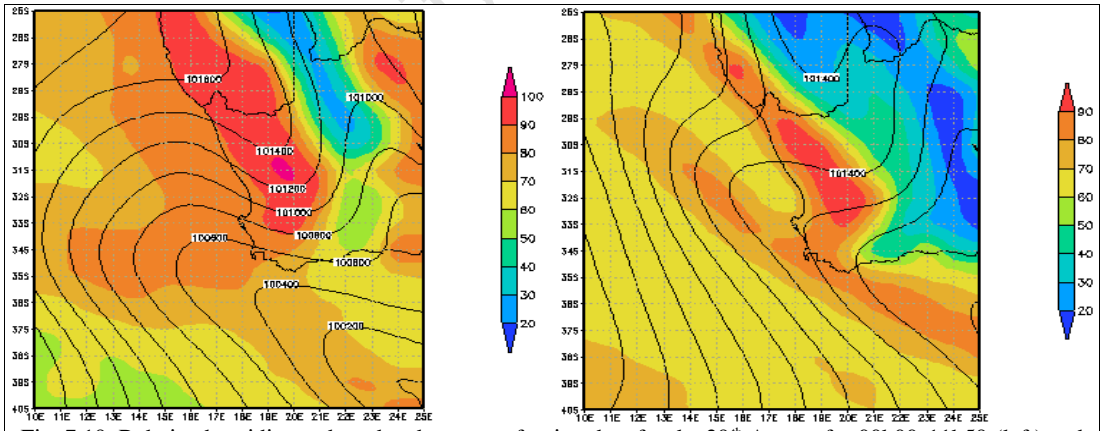

Fig. 7.19. Relative humidity and sea level pressure forcing data for the 29th August for 00h00-11h59 (left) and 12h00-23h59 (right).

Simulated data at the one kilometre resolution were also compared with radar data for the 29th August. The one kilometre resolution simulation improved on precipitation volumes from the third domain where model and radar data overlapped e.g. the northern and central parts of the Peninsula and in their lee as well as the spatial extent of precipitation (Fig. 20). Although the simulated

precipitation over the northern parts of the Peninsula was higher than the radar-derived values, the spatial extent of precipitation generally was improved, including upstream of the Peninsula. The band of precipitation that extended over the Cape Flats was simulated well between midnight and 08h00. It was difficult to compare simulated precipitation over the central Peninsula between 08h00 and 12h00 as a result of the radar data in this region being erroneous, although the spatial extent of precipitation in the lee of this region is similar to that of the radar data. Over the whole morning, only precipitation over the central parts of the northern Peninsula was not captured. Very little precipitation was simulated after mid-day by the model, which was also apparent in the radar data. At this resolution over this domain, the model captured the temporal and spatial characteristics of precipitation for this day very well and improved on results seen in the third domain.

Radar-derived precipitation

Simulated precipitation

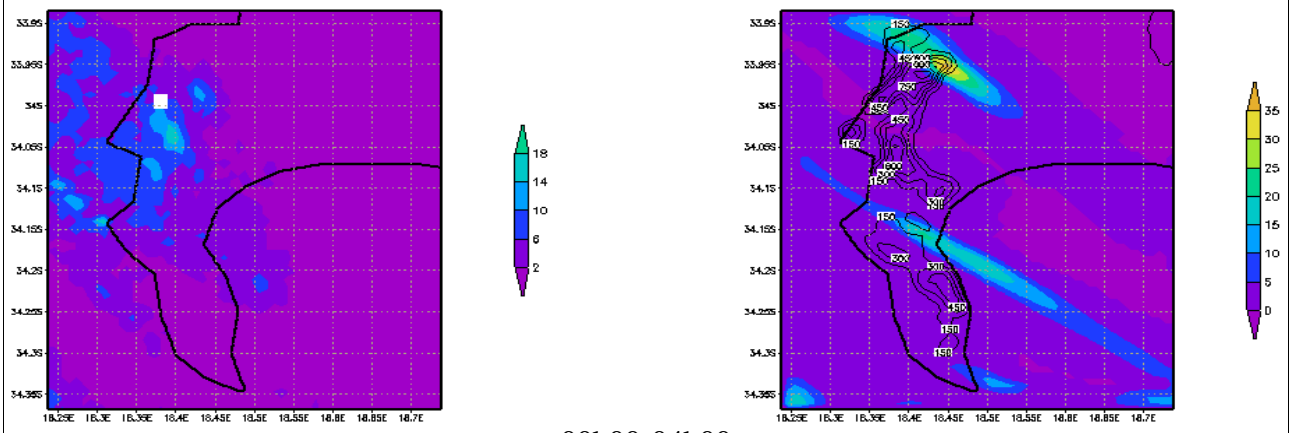

00h00-04h00

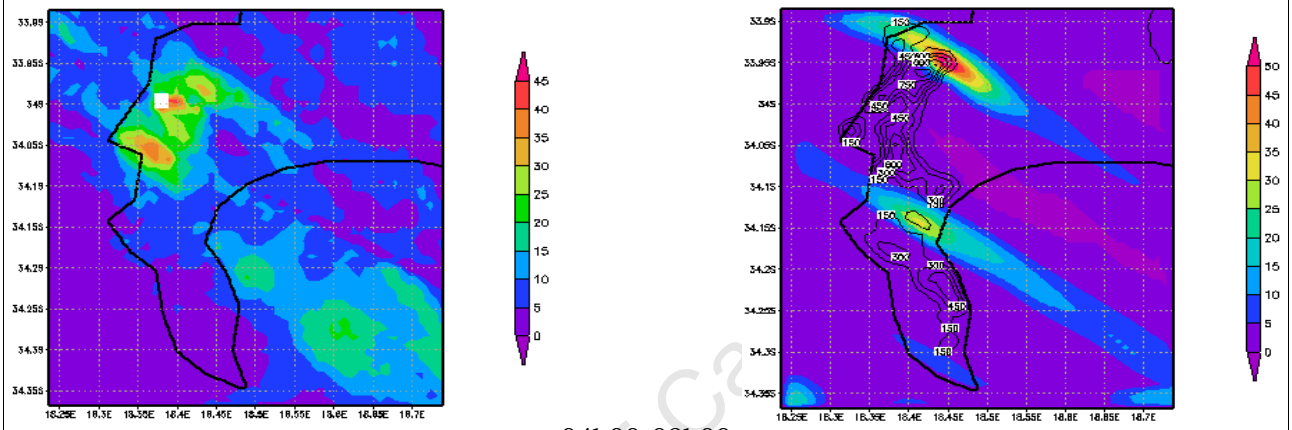

04h00-08h00

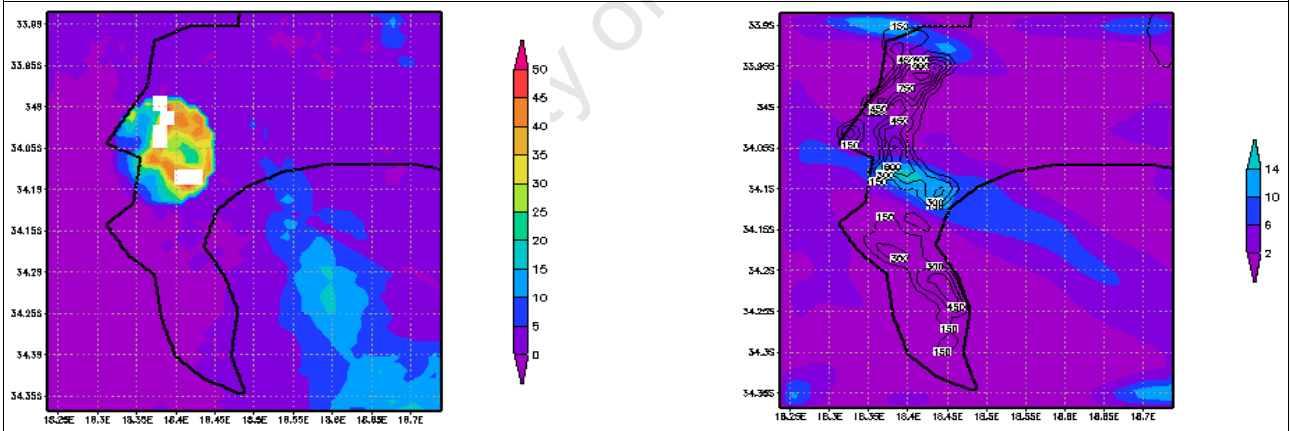

08h00-12h00

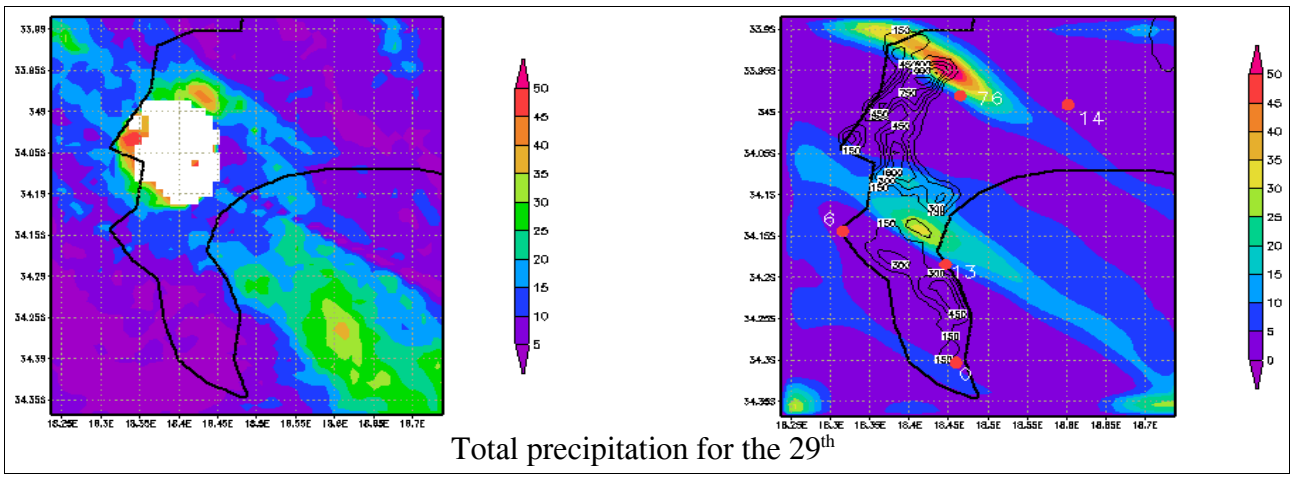

Fig. 7.20. Radar-derived and model simulated four-hourly accumulated precipitation in the fourth domain for the 29th August 2001. Values over 50 mm were masked out in the four-hourly radar images and over 80 mm in the total precipitation figure.

7.3.2 Summary

Discrepancies between simulated and radar-derived precipitation data were not unexpected as a result of the location of the Constantiaberg radar and the fact that precipitation is generally difficult to simulate, especially at a very high resolution in a topographically complex area. However, on the 23rd, the difference in radar-derived and simulated precipitation fields was too great to be ascribed to these factors. Inspection of the forcing data for this day indicated the passage of the front to be on the morning of the 23rd and not the afternoon. Thus the incorrect forcing data led to an incorrect simulation of temporal precipitation characteristics on this day.

On the 29th, however, the model captured the timing, spatial extent and magnitudes of precipitation well when compared with the radar data except over the central Peninsula. Precipitation characteristics upstream of the Peninsula were identified as well as over the Cape Flats and False Bay. The temporal and spatial characteristics of precipitation identified in the third domain were improved on in the fourth such that the spatial distribution of precipitation and precipitation volumes within these distributions were more accurate. This improvement was evident against both radar and station data.

Although there was no radar data available for the July periods, as a result of the good agreement between the observed station data and the radar-derived precipitation data, the station data for these periods were used as a reasonable measure with which to test the accuracy of the simulated precipitation. Only the one-way nesting data are presented for the two July periods as two-way

nesting again over-simulated precipitation as seen in the August data above.

7.4 July 2-4

No precipitation was simulated at all on the 2nd July in any of the domains. An inspection of the forcing data again showed low surface relative humidity values of 70 % and 75 % over the region for the respective half-day time periods (Fig. 7.21). Relative humidity in the vertical column was averaged from the surface to the 850hPa level and produced values between 60-70 % which indicated the lack of moisture in the forcing data was throughout the vertical column. Thus a similar situation existed for this day as existed on the 23rd August where inaccurate forcing data were responsible for the incorrect simulation of precipitation characteristics over the region.

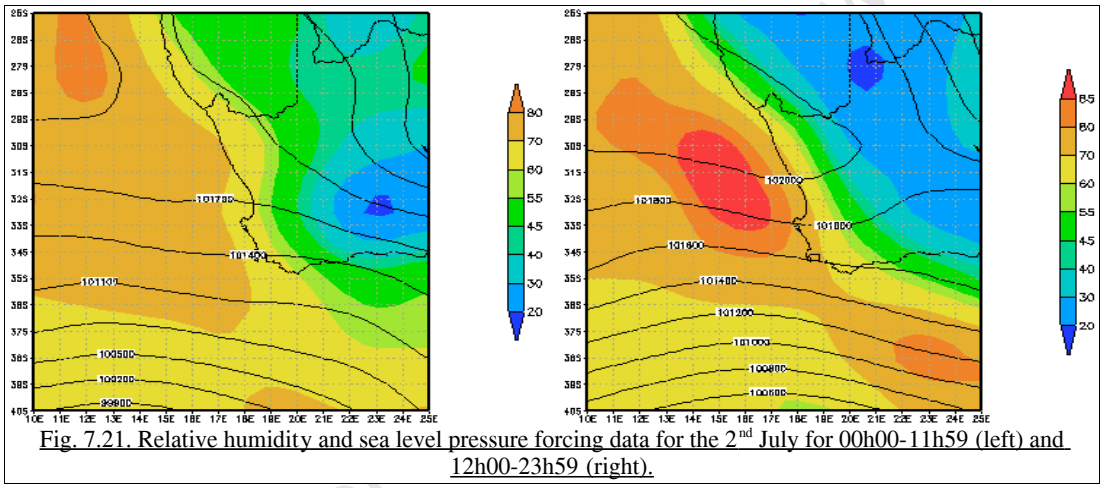

Fig. 7.21. Relative humidity and sea level pressure forcing data for the 2nd July for 00h00-11h59 (left) and 12h00-23h59 (right).

Simulated precipitation on the 3rd and 4th July began on the afternoon of the 3rd and lasted until 20h00 the following day. This was reflected in the forcing data which showed high surface and upper air RH values over this time as well as a slow moving low pressure trough whose influence over the region lasted the two days (Fig. 22).

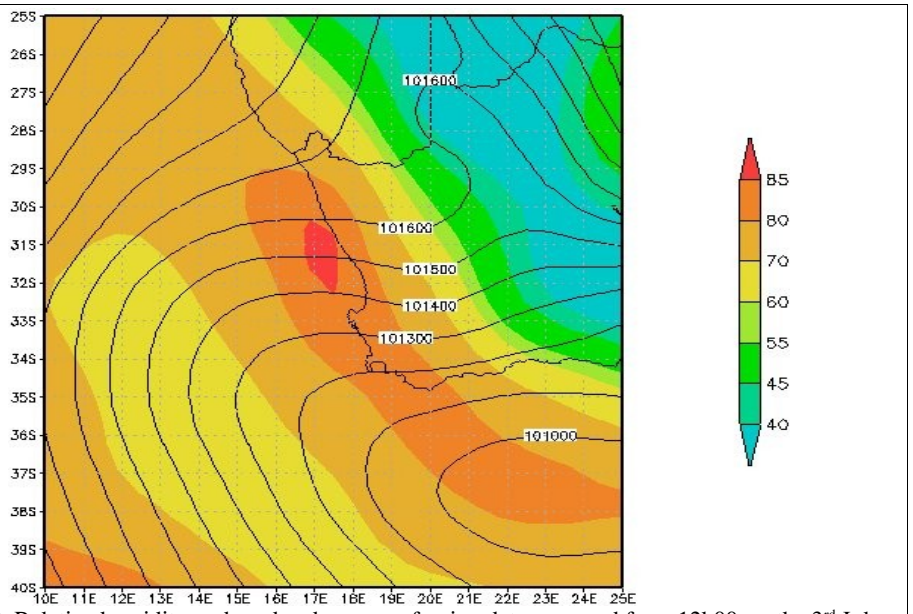

Fig. 7.22. Relative humidity and sea level pressure forcing data averaged from 12h00 on the 3rd July until midnight of the 4th July. Relative humidity values reached 100 % at times over the study region as the low pressure trough propagated through.

Simulated precipitation was widespread across the whole South-Western Cape region (Fig. 7.23). With increased resolution the volumes of precipitation increased and the distribution of precipitation maxima could be seen to be over regions of topography, most significantly over the high regions of the Hottentots Holland range.

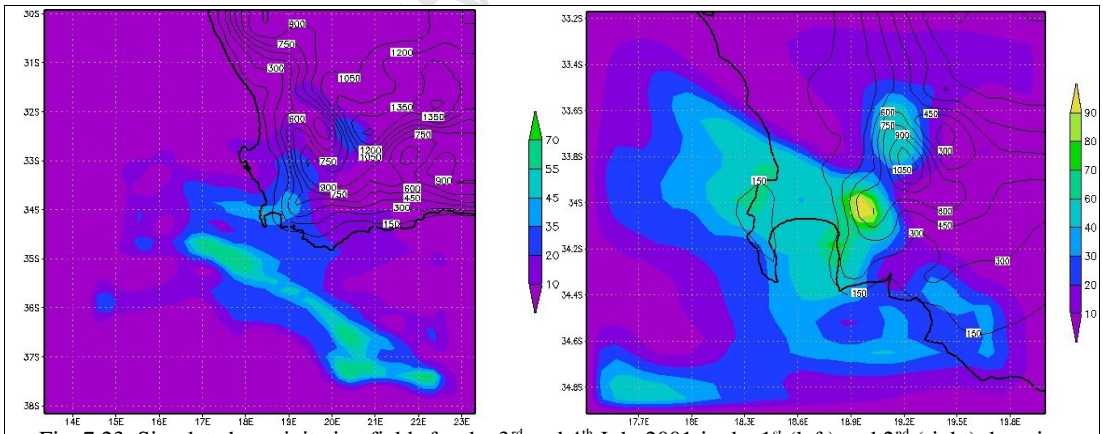

Fig. 7.23. Simulated precipitation fields for the 3rd and 4th July 2001 in the 1st (left) and 2nd (right) domains showing the widespread nature of the rainfall.

The topographical modification of precipitation by the Peninsula on these days became more apparent in the third and fourth domains. Higher precipitation values were located upstream, over and in the lee of the Peninsula with comparatively little rainfall simulated north of approximately 33.9°S. The modification was especially evident as maxima of over 150 mm were simulated over

the highest regions of the northern Peninsula (Fig. 7.24). The distribution of the precipitation, although still generally widespread, also became more defined as tongues of higher rainfall regions were evident in the lee of the Peninsula over the Cape Flats and False Bay.

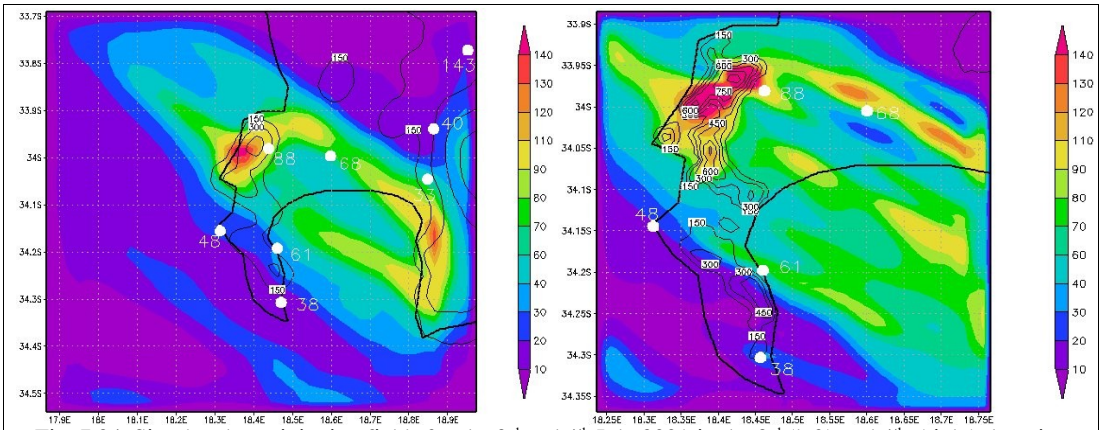

Fig. 7.24. Simulated precipitation fields for the 3rd and 4th July 2001 in the 3rd (left) and 4th (right) domains showing the widespread nature of the rainfall. Note, the colour scale is different to Fig. 7.23 above to accommodate high rainfall values.

In both domains, simulated values at the stations compared favourably with recorded data. Excluding the Paarl station, which was very close to the boundary of the domain, the averaged simulated values at the stations in the third domain was 91 % of the recorded average of 54 mm. In the fourth domain, simulated precipitation at the stations was marginally higher than recorded at 102 % of the recorded 61 mm average. Only at Slangkop was the difference between simulated and recorded values greater than 10 mm.

This three day time period experienced very high precipitation rates and volumes. With the exception of the 2nd July, where incorrect forcing data produced erroneous results, precipitation over this period was very well simulated in both space and time.

7.5 July 17-20

On the 17th, the simulation showed precipitation to start at 04h00. However, very little rainfall was produced when compared with observed data (Fig. 7.25). An analysis of the forcing data again revealed that relative humidity values were comparatively low for this day. Although they were higher in the morning, the sea level pressure data showed the front had not yet reached the coast by this time and only made landfall in the late afternoon (also see the synoptic chart in Fig. 4.2). By

this time RH values had dropped to between 70 – 80 % over the region (Fig. 7.26) and resulted in greatly reduced precipitation volumes being simulated.

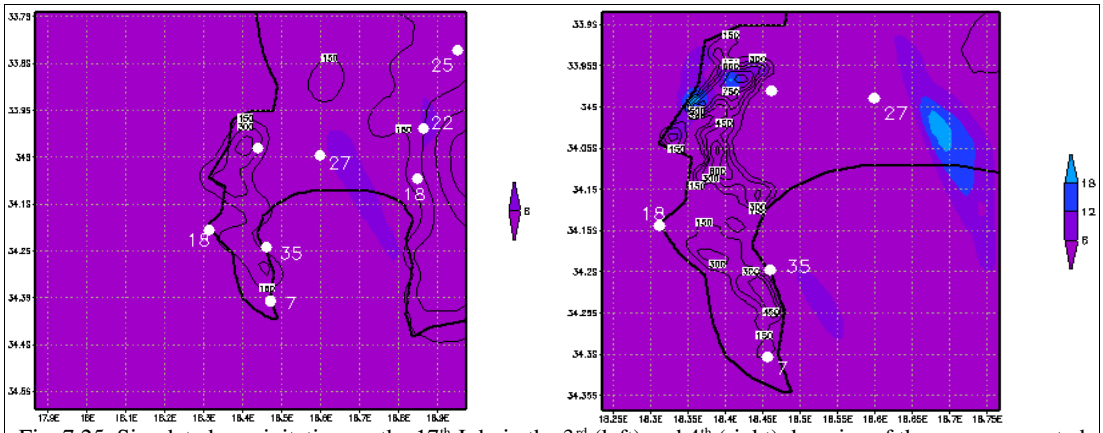

Fig. 7.25. Simulated precipitation on the 17th July in the 3rd (left) and 4th (right) domains of the one-way nested runs. Station data are shown where available.

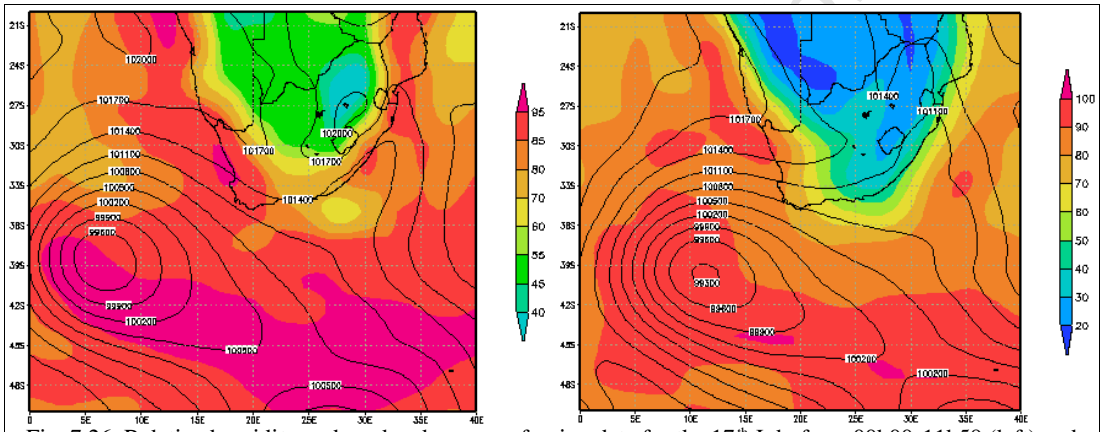

Fig. 7.26. Relative humidity and sea level pressure forcing data for the 17th July from 00h00-11h59 (left) and 12h00-23h59 (right).

On the 18th, the onset of simulated precipitation was at 04h00 and continued until 20h00 that evening. The majority of the rainfall was simulated for a 12 hour period between 04h00 and 16h00. The accumulated rainfall was spatially distributed as a tongue of precipitation stretching from the northern Peninsula across False Bay to Cape Hangklip, which was the distribution seen between 04h00 and 16h00 (Fig. 7.27). This narrow band of precipitation was not evident in the second domain and was resolved only as the resolution was increased. In the fourth domain the spatial characteristics of the precipitation was more distinct, improving on the third domain results in the southern Peninsula when compared to observed data at stations such as Cape Point and Slangkop. Precipitation at Groote Schuur was over simulated at both resolutions. Spatially, simulated data in the fourth domain displayed similar magnitudes to the station data. Unfortunately observed Simonstown data were not available for this day.

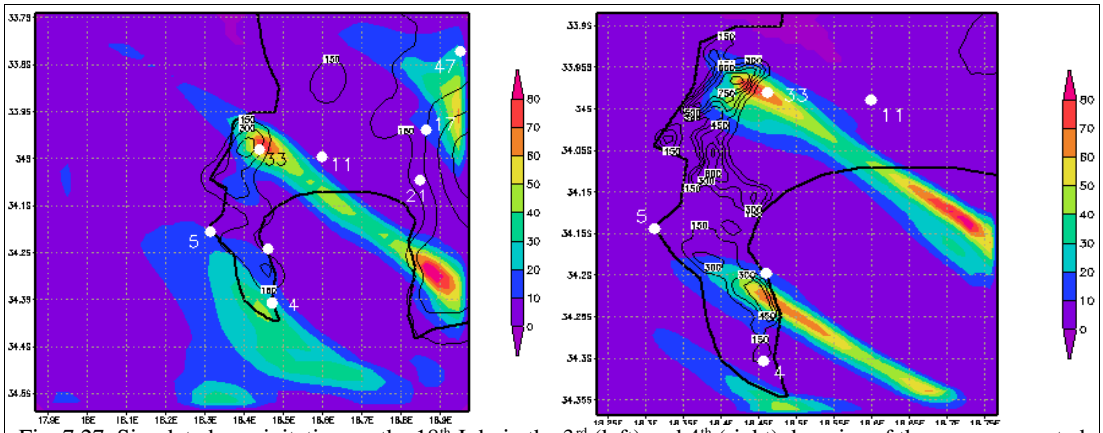

Fig. 7.27. Simulated precipitation on the 18th July in the 3rd (left) and 4th (right) domains of the one-way nested runs. Station data are shown where available.

Forcing data showed the front to make landfall sometime in the late morning/mid-day based on the position of the centre of the low pressure and relative humidity values as well as an inspection of the synoptic chart in Fig. 4.2. Advection of moisture from the south-west of the country could be inferred from the large spatial extent of high relative humidity values here in the morning and the position of a band of RH values (> 90 %) over the study region in the afternoon (Fig. 7.28).

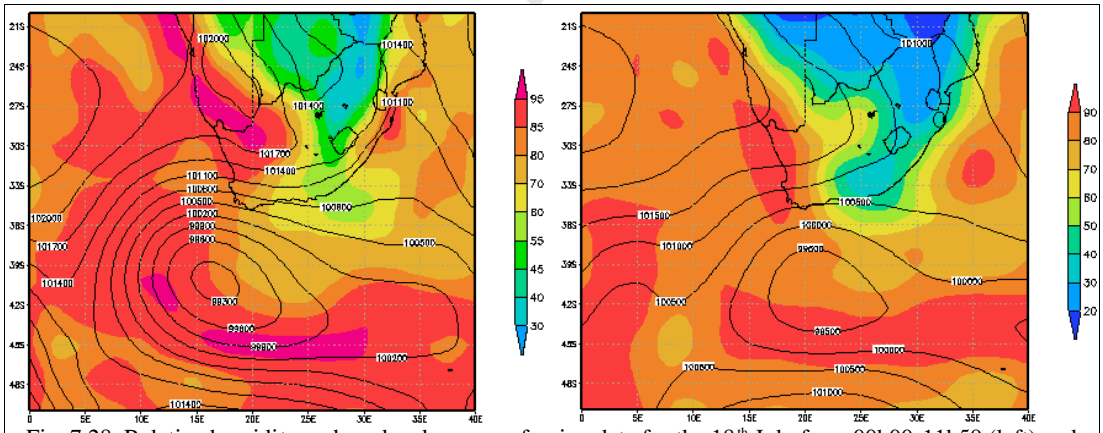

Fig. 7.28. Relative humidity and sea level pressure forcing data for the 18th July from 00h00-11h59 (left) and 12h00-23h59 (right).

The majority of precipitation on the 19th was simulated between 08h00 and 16h00 with lighter rain simulated over the Peninsula between 16h00 and 20h00. Precipitation was simulated over all of the land in the third domain with maxima over the Hottentots Holland and the northern and central parts of the Peninsula (Fig. 7.29). Precipitation was evident over the Cape Flats and a band of values of between 10 mm and 15 mm linked the Peninsula and Hottentots Holland. Data at the Airport, Cape Point, Groote Schuur and Stellenbosch compared favourably with station data however at

Simonstown and Slangkop these were under-simulated by 24 mm and 16 mm respectively. In the fourth domain, the spatial distribution of the precipitation was confined to the central and southern parts of the Peninsula and the lee of this region. The northern Peninsula and central parts of the Cape Flats showed very low precipitation values except at the northern boundary of the domain. Two distinct bands of precipitation were evident, one over and in the lee of the central Peninsula and one over and in the lee of Simonstown. These bands halted at the eastern boundary of the domain and it was not possible to ascertain if they stretched to the Hottentots Holland mountains. In this domain, simulated data did not match any station data in terms of magnitude and spatially only Slangkop and Simonstown were covered. The simulated rainfall values were less than the recorded data at all stations.

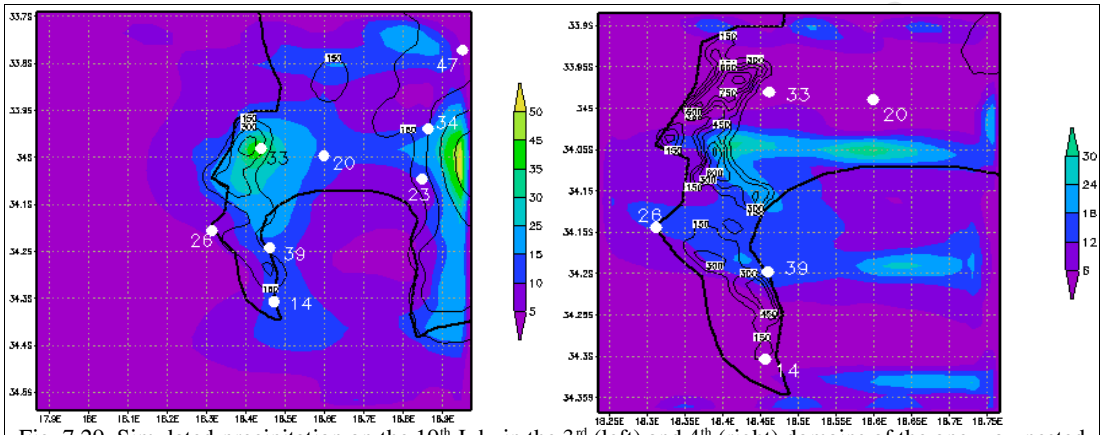

Fig. 7.29. Simulated precipitation on the 19th July in the 3rd (left) and 4th (right) domains of the one-way nested runs. Station data are shown where available.

The spatial orientation of the precipitation on this day was west-east, unlike the general north-west to south-east spatial distribution of most of the other days which simulated precipitation. Sea level pressure fields in the forcing data exhibited a greater zonal component over the region and also were not associated with a closed cyclonic circulation resulting in this distribution (Fig. 7.30). The forcing data also showed a large extent of high RH values in the morning and lower values in the afternoon, which facilitated the temporal precipitation distribution described above.

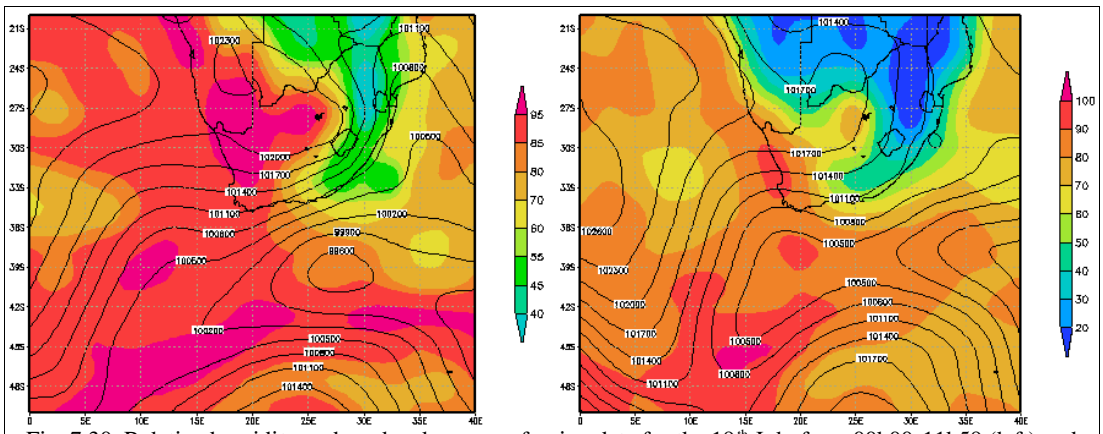

Fig. 7.30. Relative humidity and sea level pressure forcing data for the 19th July from 00h00-11h59 (left) and 12h00-23h59 (right).

The three day accumulated precipitation for the third and fourth domains are shown in Figure 7.31. In the third domain, maxima were over the Hottentots Holland mountains and the northern Peninsula. Over the Peninsula, two distinct spatial regions were simulated, one over the northern and central Peninsula and one over the southern Peninsula. These two distributions were separated by the low lying Noordhoek Valley. A band of precipitation stretched from the northern Peninsula to the the southern regions of the Hottentots Holland and a less prominent band was simulated in the same plane from the southern Peninsula to the south-east boundary of the domain.

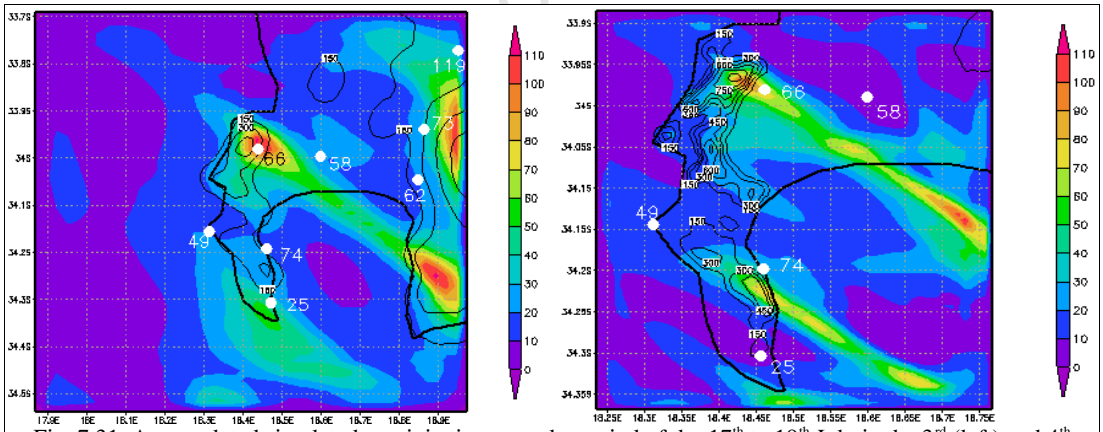

Fig. 7.31. Accumulated simulated precipitation over the period of the 17th to 19th July in the 3rd (left) and 4th (right) domains of the one-way nested runs. Accumulated precipitation station data are shown.

Precipitation values of 20 mm and above were simulated for the central region of the Cape Flats and values of up to 60 mm were simulated just south and south-west of the Airport. These values were similar those recorded at the Airport. Except at Groote Schuur and Cape Point, simulated precipitation values were less than recorded station data. The magnitude of the highest under-simulation was at Simonstown (52 mm) with the other stations having underestimations of between

29 mm and 33 mm. Precipitation was over-simulated at Groote Schuur by 44 mm and at Cape Point by 25 mm. In the fourth domain, the spatial extent of the precipitation was more defined and in the context of the station data, grossly underestimated rainfall. The only station where values were similar was Groote Schuur. However, the discrepancy may be small when one considers the broad distribution of the simulated field and the size of the area. With the exception of Slangkop, the spatial distribution of the simulated rainfall bands were on average within a 5 km radius of each station. Additionally, the simulated precipitation volumes in the rain bands are similar to the closest stations data. For example, the band of simulated rainfall to the south of the Airport lies within 5 km of the Airport and the simulated precipitation volume in this band is similar to the station value. Although the model did not precisely capture the spatial distribution of precipitation fields, the magnitude of simulated precipitation volumes were similar to that of the closest station.

7.6 Summary

The simulations produced spatial and volumetric precipitation distributions that became more defined with increased resolution. Orographic modification of rainfall was evident most especially over and in the lee of the Peninsula. Broad, homogeneous areas of precipitation in low resolution domains were resolved into finer structures at higher resolutions. Higher precipitation volumes and maxima were also simulated in each subsequent nest, these being associated with regions of highest topography.

There was a significant difference in precipitation output between nesting procedures. Two-way nesting over-simulated precipitation in the finer domains by up to three time the observed values. The over-simulation of precipitation by this nesting method resulted from the effect of the enhanced topography on precipitation over the nest region of the mother domain where a positive feedback mechanism between domains was set up. Topography in the mother domain was enhanced in the nest area through the blending process which biased the overlap region towards higher precipitation. The biased results from the mother domain were then used by the nest as forcing data at the lateral boundaries thus setting up a positive feedback mechanism. The over-simulation of precipitation by the two-way nesting methodology excluded these precipitation results from further study.

The one-way nesting technique, although underestimating precipitation generally, rendered results closer to observed station data except the historically wettest stations where the underestimation was large. Precipitation fields compared favourably with radar-derived precipitation data and an

increase in resolution improved the spatial and volumetric characteristics of simulated precipitation. Failure of the model to capture the temporal and volumetric characteristics of precipitation on certain days were attributable to errors in the forcing data with respect to the synoptic timing of the storms as well as low relative humidity values. This highlighted the importance of using accurate forcing data for realistic simulation. However, there was good agreement between the simulated and observed data on the 29th August, 3rd and 4th July and the 19th July, when forcing data were reliable.

At the highest resolution an improvement in the spatial distribution of simulated precipitation was found on the 29th August when radar data were available for comparison. In July, when only station data were available, precipitation volumes compared well with the closest respective station despite the model having not captured the precise distribution of precipitation over these stations.

Therefore, the assessment of the modeling approach provided many useful outcomes. It provided the basis for relating the synoptic modes identified in the empirical approach to the localized expression of weather characteristics. It identified the regional modification of temperature, wind and extreme precipitation fields under various circulation regimes, including those associated with extreme precipitation. Although validation data revealed the simulated results were not precise, the simulations did capture the fine regional expression of the synoptic circulations. The temporal, spatial and volumetric characteristics of the extreme rainfall were evident in the one-way nested runs. The large over-simulation of precipitation by the two-way nested runs suggests that nesting procedures should be tested regionally, especially in regions of complex orography. Failure to do so would likely result in erroneous relationships being reported between synoptic states and their regional expression. Furthermore, regionally specific sensitivity analyses should be performed, especially where convective processes are dominant. Reliable forcing data was shown to be necessary for the realistic simulation of the extreme precipitation fields. The MRF forcing data is the analysis dataset of an operational forecast and is reliant on observations for accuracy. However, in regions like Africa, where observational data are sparse, the likelihood of errors even in the MRF analysis data is relatively high and appropriate care should be taken in the interpretation of simulated results.

Chapter Eight

Summary and conclusions

8.1 Introduction

In many regions of the world, extreme precipitation has become more frequent in occurrence, more intense and the projected changes in the characteristics due to global warming are for these trends to continue. An investigation into the characteristics of regional extreme precipitation, their associated synoptic circulations and changes in these would provide an improved understanding of the linkages between the large scale synoptic forcing and the regional expression of the precipitation field. To this end, local extreme precipitation was examined for changes in the nature of extreme precipitation in the region. Two approaches were then used to further examine these changes. The first explored the historical attributes of extreme precipitation to identify circulations associated with extreme precipitation and changes in these. This approach also facilitated the allocation of days which experienced extreme precipitation to particular synoptic circulations. The second approach tested the ability to produce high resolution simulations that captured topographic enhancement of extreme precipitation using a regional climate model.

8.2 Summary of results

Changes in the nature of extreme precipitation in the Cape Town region were identified through a statistical analysis of three recording stations in the region. Extreme rainfall amounts show a statistically significant decrease at the Cape Town International Airport and a statistically significant increase at Simonstown. These changes are not reflected in a 50 km resolution gridded data set which smoothes out the modification of extreme rainfall by the complex topography.

To further examine these changes, self organizing maps were used to categorize synoptic circulations associated with extreme precipitation into archetypal modes. This established a relationship between synoptic scale circulation and the local scale responses such that key synoptic states associated with extreme precipitation were successfully identified. As the daily data used to describe these relationships could be ascribed to the circulation modes, days likely to be associated

with extreme rainfall in the region could also be identified. Additionally, changes in the frequency of occurrence of these modes could be assessed over a specified time period and demonstrated that synoptic states associated with extreme precipitation over the region had increased. Thus this approach successfully identified synoptic states associated with extreme precipitation, the days associated with these states and provided an historical assessment of these events.

Thereafter, a regional climate model was used to produce high resolution simulations of extreme precipitation in the region. The model results were assessed against observed station and radar data, where the radar data provided spatially continuous data representative of precipitation over the region. At high resolution, the localized spatial and temporal distribution of extreme precipitation was captured as well as the enhancement of these fields by topography. Finer scale processes were also evident in other variables at these resolutions. Two-way nested results were unusable as too much precipitation was simulated. In this scheme the topographies throughout the domains were enhanced which resulted in over-enhanced topographic forcing. These over-enhanced data were then used as lateral boundary forcing data in successive nests and set up a positive feedback mechanism which propagated the error through the domains. However, the one-nesting method produced precipitation results similar to observed values. Therefore, in regional applications of this approach, nesting procedures should always be tested. The modeling approach successfully provided the basis for relating the synoptic modes identified in the first approach to the localized expression of extreme precipitation.

These approaches formed the basis of a methodology to investigate extreme precipitation that may be used in regions of the world where computational resources are limited, especially in Africa. This methodology requires high resolution simulation only of synoptic states historically associated with extreme precipitation. Self organizing maps identify synoptic states associated with extreme precipitation after which days that exhibited these states are simulated at very high resolution using a regional climate model to capture the spatial and temporal nature of extreme precipitation in the region. Simulated precipitation fields are validated against observed data. A summary of the results of this methodology is presented below after which these are discussed in the light of furthering the understanding localized extreme precipitation.

8.3 Identification of extreme precipitation using self organizing maps

Two self organizing maps were generated for analysis. The first identified 20 archetypal circulations based on all winter days from 1979-2000 where winter was defined as 01 April to 30 September. The second identified 12 archetypal synoptic states based only on days in the 23 year time period that were associated with winter 90th percentile rainfall in the South-Western Cape.

The first SOM produced 20 archetypal circulations over which the days in the 23 year time period were very evenly spread, i.e. no one archetype was dominant. These archetypes represented winter synoptic states like the passage of mid-latitude cyclones in the south of the domain, the sub-tropical high pressure system over the interior of the country and the ridging south Atlantic high pressure system. Days that experienced extreme precipitation in the South-Western Cape mapped to archetypes which were associated with the passage of mid-latitude cyclones through the region.

The second SOM used data only from days which experienced extreme precipitation and rendered 12 synoptic archetypes associated with extreme precipitation. These states were all characterized by the passage of a low pressure system to the south of the country, high relative humidity values over the study region and an absence of a contiguous high pressure band over the interior of the country. Of these 12 archetypes, five were associated with the extreme flooding that was experienced in July and August 2001. These circulations were characterized by the passage of frontal systems whose centers were at lower latitudes, had a strong pressure gradient over the region at the surface and in the upper air and very high relative humidity values over the west coast. No one particular circulation archetype was associated with extreme precipitation in the region based on July and August 2001 extreme rainfall days, however, these days were all associated with five states identified by the SOM. Rainfall characteristics of these days ranged from precipitation that fell over a number of days in relatively low daily amounts to very heavy precipitation that fell in less than one day.

An analysis on the winter rainfall data used to train the second SOM as well as the resultant SOM information indicated a non-significant positive trend in the occurrence of extreme rainfall over the 23 year time period. Using the SOM to investigate this more closely indicated a decrease in circulations associated with winter rainfall and a corresponding increase in non-precipitating circulations. Circulations associated with extreme precipitation days only indicated a negative shift in synoptic states associated with weaker low pressure troughs and a positive shift in synoptic

archetypes associated with deep low pressure troughs. This indicated synoptic states associated with extreme precipitation have become more frequent and more intense over time. Thus, although there was an increase in synoptic states not associated with rainfall, circulations associated with extreme precipitation in the region appears to have become more common and the intensity of the storms to have increased. It must be noted that the trends were statistically non-significant and these are only shifts in the circulation modes. However, these observations are in agreement with many other studies that note an increase in the occurrence and intensity of extreme rainfall globally as well as regionally over the South-Western Cape.

Days which the SOM identified as having experienced extreme rainfall included days from the months of July and August 2001 which caused the severe flooding mentioned above. These days were selected for high resolution simulation by a regional climate model whose precipitation output was verified against station and radar data. It was first necessary to establish the reliability of radar data as proxy for rainfall.

8.4 Observational station and radar data

Determining accurate precipitation distributions across mountainous regions is difficult because of the spatial non-uniformity of the precipitation which is heavily influenced by the orography. Station data provided an initial investigation into the characteristics of the temperature and rainfall at different locations in the region during July and August 2001. The physical location of stations displayed much heterogeneity across the region. These ranged from being located at the base of a topographic feature to the central regions of the Cape Flats with elevations of between 8 m and 244 m. All stations reflected the passage of the cold fronts through a drop in temperature as well as the warmer period between fronts.

In terms of precipitation, the passage of fronts was recorded in the rainfall data although on some days not all stations recorded rainfall. Analysis of rainfall in July and August 2001 revealed that it was some of the most extreme rainfall recorded in the 23 year time period. Rainfall in July fell into the 97^{th} percentile and in August the 96^{th} percentile of all rainfall. In terms of the extreme precipitation record, the region received above-average extreme rainfall, especially during the July period.

Although the station data revealed general characteristics of the extreme precipitation experienced in July and August, the sparse nature of the station network provided information at a limited spatial scale and daily temporal scale. Radar data provided spatially continuous information at a very high temporal resolution.

Radar reflectivity data provided information on the broad spatial structure of the precipitation field as well as its temporal attributes. Heterogeneous regions of intense precipitation, embedded in fields of generally lighter rain, were evident across the Peninsula and the Cape Flats as the front passed over the region. The topographic modification of the precipitation field was also evident downstream of the Peninsula. Temporally, the time that extreme precipitation affected certain regions could be ascertained as well as the general residence time of front over the region. The high spatial and temporal resolution reflectivity data added greatly to the information obtained from the station data.

Radar reflectivity data was also related to the actual amount of precipitation received. This relationship was estimated as no study for an optimal relation has been performed for this region. The daily accumulated derived precipitation data slightly underestimated the recorded rainfall at most stations with the exception of the two historically wettest stations (Groote Schuur and Paarl) where the underestimation was large. However, these two stations experience large topographic modification of rainfall and as a result of the location of the radar it was not expected that radar data over these stations would be accurate. Over the spatial continuum, the daily derived rainfall field indicated highest rainfall volumes over the northern and central Peninsula and in its lee and exhibited a general north-west/south-east orientation. The general agreement of radar data with daily station data and the additional spatial and temporal information it provided meant the radar data could be used as a verification tool for the simulated precipitation fields complimentary to the station data.

8.5 High resolution simulations of extreme rainfall

The numerical simulation of extreme at high resolution was shown to be necessary through the spatially heterogeneous changes in the amounts extreme precipitation in the region. Thus the weather associated with a number of days identified by the SOM as having experienced extreme rainfall was simulated at very high resolution (1 km) using the fifth-generation Penn State/NCAR

Mesoscale Model (MM5). The model provides two nesting schemes to attain these high resolutions and both schemes were tested. Three periods were simulated, two of 3 day duration in July and one of 8 day duration in August. The latter period was used to test the model precipitation output against radar data. Unfortunately, radar data were not available for the July periods. Temperature and wind fields were also analyzed.

Simulated temperature fields reflected synoptic scale features such as cold fronts, cold air advection and warming of the region between fronts. As the resolution became finer, temperature fields became more distinct and orographic forcing was evident with coldest temperatures at highest altitudes. In the finest domains there was good agreement between daily maximum recorded temperatures and the two-way nesting simulation temperatures. One-way nesting produced generally higher temperatures than two-way nesting as topography was less well resolved in the former scheme. Highest anomalies between nesting schemes were over regions of topography.

Wind fields associated with the passage of cold fronts (northerlies and north-westerlies), ridging high pressure systems (southerlies) and the transitions between these states were captured in the lower resolution domains. At higher resolutions, topographic forcing of strong laminar flow was evident as flow deflection and split flows with zones of upstream divergence and downstream convergence. Under low wind velocity regimes, the diurnal cycle was captured as well defined land and sea breeze circulations. The two-way nesting scheme resolved more complex wind flows whereas one-way nesting produced generally stronger wind flows, this as a result of the different topography data available to each scheme.

Precipitation was dramatically over-simulated using the two-way nesting technique. In this scheme, the topography in mother domains were enhanced by that of nest domains which resulted in greater topographic forcing in coarser nests than in one-way nesting. The enhanced simulation results were then used as lateral boundary forcing data in successive nests and propagated the error through the domains. One-way nesting results were therefore examined against observed data.

Compared with station data, the one-way nesting simulation generally underestimated precipitation. This underestimation was largest at the three historically wettest stations which experienced a large degree of topographic modification, however, at the other stations the underestimation was small. Spatially and volumetrically, simulated precipitation fields displayed similar characteristics to radar-derived precipitation data when the MRF forcing data was correct. For some days, however,

precipitation was poorly simulated. This was found to be as a result of forcing data that was incorrect temporally with respect to the synoptic timing of the storms and spatially where relatively lower humidity values were present over the region. When the forcing data were consistent with what was observed, the spatial distribution of precipitation, precipitation volumes and the timing of the events were well captured by the simulation. Thus, correct lateral boundary conditions in both the MRF forcing data as well as those produced by the respective nesting process were seen to be of vital importance in the evolution of model output as errors here propagated through the domains.

8.6 Discussion

Local extreme precipitation characteristics were examined using statistical and numerical approaches. Using the statistical approach, a non-uniform change in the amounts of extreme rainfall received at locations in the region was found. The Airport showed a significant decrease and Simonstown a significant increase whereas Paarl showed no significant change. The atmospheric states associated with extreme precipitation were also identified and their characteristics described. Historical changes in the frequency and intensity of synoptic states associated with regional extreme rainfall could also be explored. The changes observed here were an increased occurrence of synoptic states associated with extreme rainfall and a decrease in synoptic circulations associated with general rainfall. This added to the current knowledge base in providing a description of the synoptic states associated with extreme precipitation as well as their change in occurrence over time. Furthermore, this approach facilitated the successful identification of days which experienced extreme precipitation. Thus the potential exists, in a weather forecasting context, for the forecasting only of days whose synoptic characteristics are similar to those of synoptic archetypes associated with localized extreme precipitation. This would have great benefit many in regions of the world where current computational capacity restricts the generation of qualitative forecasts.

The spatially heterogeneous changes in extreme precipitation indicated that results from a particular location should not be taken in isolation. Thus no broad statement concerning extreme rainfall in the region should be made, as has been done in the literature. Extreme rainfall is as much a function of local topographic modification of the precipitation field as it is of climatological synoptic forcings. The numerical modeling provided a means to investigate the nature of extreme rainfall at high resolutions which do not smooth out and generalize a result over a large area. Through these types of simulations, the nature of topographic forcings was included and the effect on the precipitation

field examined. In doing so, the regional expression of the synoptic forcing was demonstrated. The numerical approach successfully simulated temperature, wind and extreme precipitation fields at high resolutions and identified the regional modification of these fields through the effects of topography. Given reliable forcing data at the lateral boundaries, the regional model successfully generated fine scale structures in the high resolution circulation field absent at coarser resolutions The reasonably successful high resolution simulation of these events provides valuable information to understanding the local expression of extreme precipitation. However, this is not a black box suitable for regions with different weather features. There is a necessity for sensitivity testing of model parameterizations in the region it would be implemented to construct the region-appropriate optimal set of these. Then given a reasonable simulation of extreme at high resolutions, the relationship between synoptic forcing and the local expression of extreme precipitation may potentially provide information to relevant authorities and a better preparedness of communities most vulnerable to these events.

Reliable observational data is necessary for the assessment of the regional climate model. Station and radar-derived data were successfully used to validate the high resolution precipitation fields in the study region. However, no data was available for the validation of wind fields which serves to highlight the problem of observational data sparsity in the African context. In the introductory chapter, it was shown that Africa has the worst climate observational capacity globally. This poses an important problem to the verification of simulated regional processes. Satellite derived data address the problem in some measure, however, the temporal resolution is not fine enough to capture extreme events that have lifetimes of the order of a few hours and the spatial resolution cannot capture the fine scale structure of the circulation fields. Therefore, the application of these approaches is likely limited to regions that have reliable observational data with which simulated regional circulations can be validated.

This approach also has application to future climate projections. A self organizing map, trained on historical data, can be used to assess changes in the occurrence of archetypal synoptic states from general circulation model projections. Given that the relationship between the synoptic forcing and regional climate remains constant (see their discussion of stationarity in Hewitson and Crane (2006)), changes in the frequency and intensity of future synoptic states would provide information on future regional changes in the characteristics of extreme precipitation. It would be possible to identify the frequency of the occurrence of synoptic states associated with regional extreme precipitation in the future. It is recognized that predictor variables in one region of Africa, e.g. Cape

Town may not be appropriate for another, e.g. the tropics. The SOM technique may be adapted to use variables in the training process that provide the most useful information concerning extreme rainfall for that region. Using the numerical approach, further information would be provided through the understanding of high resolution attributes of extreme precipitation fields in the future. Given changes in the intensity of these events, this would aid in assessing the impact these changes would have on a region's population, infrastructure and economy.

8.7 Caveats

As with any research, there are invariably limitations in the methodologies through which the results should be assessed. These limitations provide sources of uncertainty in the respective methodologies and are identified below.

The SOM produced synoptic archetypes to which extreme precipitation days were mapped. Within the data space of the SOM, the Euclidean distance from each respective archetypal circulation of the daily mappings varied. Days closer to the node had circulations which more closely resembled the archetypal circulation than days located furthest from the node. Thus, the potential for a false positive identification of extreme precipitation exits in synoptic states that map furthest from the node. In an operational forecast context, therefore, days identified as having synoptic states associated with extreme precipitation but have large Euclidean distances from synoptic archetypes should be checked against other forecast data. Only once the likelihood of extreme precipitation can be confirmed need high resolution simulation be considered. However, should this not be possible, the high resolution simulation may itself be used to check the likelihood of extreme precipitation. If the simulation indicates extreme rainfall, further caveats notwithstanding, appropriate measures may be taken.

As alluded to above, the regional coverage of the observational station network, although forming the basis of the validation process, was spatially and temporally sparse. Very limited information could be inferred for regions where no stations were present. A further result of this was that the relationship between radar reflectivity and rainfall rate (Z-R) could not be accurately determined. An accurate volumetric analysis would require the placement of a a very high resolution station network with which to calibrate the radar data, which is not likely in the near future because of the high cost of such an exercise. However, through an informed estimation of the Z-R relationship, the

radar data greatly improved on the information available from the station network and provided a valuable dataset against which to test the simulated precipitation fields.

The high resolution simulation of weather in topographically complex regions has many potential error sources. These may be due to limitations in the understanding of physical processes and their parameterizations, necessary simplifications of the numerical algorithms, inaccurate initial conditions and the ingestion of forcing data at the lateral boundaries. In weather forecasting models, the major source of uncertainty lies with the lateral boundary conditions. Warner et al. (1997) showed the importance of having correct ingestion of the forcing data at the lateral boundaries. Pan et al. (2001) demonstrated that the ability of RCMs to simulate the regional climate depended strongly on the realism of the large-scale circulation provided at the lateral boundaries and the ingestion thereof. Denis et al. (2002) listed additional sources of uncertainty such as the parameterization of physical process in the atmosphere and nesting procedures.

In the simulations presented here, the nesting procedure and lateral boundary conditions had a dramatic effect on the simulation of precipitation. Two-way nesting greatly exaggerated rainfall production and inaccurate initial conditions resulted in the non-simulation of precipitation. However, when the large scale forcing data were correct, one-way nested runs produced results similar to observed values. These positive results should also be seen in a context where no sensitivity studies over the region exist. It is therefore suggested that sensitivity studies be performed for the region (as well as other regions where this methodology might be implemented) as these would inform the optimal choice of parameterizations and domain boundary locations and likely improve on the results. Nonetheless, the ability of nested domains to generate meaningful fine-scale structures that were absent in coarser domains was clear.

A final caveat lies in the implementation of the methodology in an African context. Although this methodology is relatively inexpensive computationally, it does require access to computing resources capable of running very high resolutions periodically. In addition, selection of extreme precipitation days for the SOM training procedure and the regional configuration of the model requires reliable observational data, the state of which has been shown to be worse than that of any other continent. However, the selection of extreme precipitation days may be done at the station scale. Although this would not be ideal, the synoptic forcing would be reflected in the rainfall characteristics obtainable from even a single station. The high resolution simulations may also be run at a 3 km resolution and not all the way down to 1 km. Finer information was available at this

resolution than in the coarser nests in which precipitation distributions and magnitudes were accurately captured. At this resolution, the computational cost of the simulation is reduced by more than half that of a 1 km resolution and may be more accessible in an African context.

Although there are caveats and limitations, these can be accounted for through an informed configuration of the methodology for a particular region in both the SOM predictor variables and the model parameterizations. Furthermore, the development of technical expertise and the provision of even limited resources makes this methodology very accessible to agencies currently not able to provide good forecasts of extreme precipitation.

8.8 Conclusions

In an attempt to advance the understanding of regional extreme precipitation, especially in an African context where the capacity climate science is poor, change in the characteristics of extreme precipitation were investigated in the Cape Town region. Then a methodology was presented to identify and simulate extreme precipitation at very high resolutions. To this end, the four hypotheses as described in the Preface were tested with the following results:

(i) There are positive and negative trends in the intensity of extreme rainfall at different locations within the relatively small region of greater Cape Town. A single station result cannot be used as representative for the entire region.

(ii) Self organizing maps successfully identified synoptic states associated with extreme precipitation and correctly mapped days which experienced extreme precipitation to these states.

(iii) Radar-derived precipitation data could be used as a reliable proxy for actual precipitation in the test region and was used in the validation of simulated precipitation results.

(iv) The MM5, run at resolutions of up to 1 km, reasonably simulated the spatial, temporal and volumetric characteristics of extreme precipitation as well as other weather characteristics.

Having satisfied these hypotheses, caveats and further testing notwithstanding, the additional information provided by approaches potentially provide a means for the forecast of extreme precipitation in many nations currently lacking the capacity to do so. It would require a high

resolution forecast only when synoptic states associated with extreme rainfall were evident in an operational forecast. The development and region-specific refinement of this methodology would help address the multiple challenges faced in Africa needed to understand climate and weather variability over the continent.

References

Alexander, W. J. R., 1993: Flood warning systems. *S. Afr. Waterbull.*, **19**, 8-10.

Allen, M. R., and W. J. Ingram, 2002: Constraints on future changes in climate and the hydrological cycle. *Nature*, **419**, 224–232.29, 139-154.

Ambroise, C., G. Seze, F. Badran, and S. Thiria, 2000: Hierarchical clustering of self-organizing maps for cloud classification. *Neurocomputing,* **30**, 47-52.

Andres, M., C. Tomas, and F. De Pablo, 2000. Spatial patterns of the daily non-convective rainfall in Castillay Leon (Spain). *Int. J. Climatol.*, **20**, 1207-1224.

Anthes, R. A., and T. T. Warner, 1978: Development of hydrodynamical models suitable for air pollution and other mesometeorological studies. *Mon. Wea. Rev.*, **106**, 1045 -1048.

Anthes, R. A., E. Hsie, and Y. Kuo, 1987: Description of the Penn State/NCAR Mesoscale Model Version 4 (MM4). *NCAR Tech. Note,* NCAR/TN-282+STR, 66 pp.

Arakawa, A., and V. R. Lamb., 1977: Computational Design of the Basic Dynamical Processes of the UCLA General Circulation Model. In: *General Circulation Models of the Atmosphere.* J. Chang, (Ed.), Academic Press, San Francisco, 173-265.

Austin, P. M., 1987: Relation between measured radar reflectivity and surface rainfall. *Mon. Wea. Rev.*, **115**, 1053 -1070.

Badran, F., and S. Thiria, 1991: Wind ambiguity removal by the use of neural network techniques. *J. Geophys. Res.*, **92**, 20512-20529.

Baines, P. G., 1995: *Topographic effects in stratified flows.* Cambridge University Press, 482 pp.

Bankert, R. L., 1994: Cloud classification of AVHRR imagery in maritime regions using a probabilistic neural network. *J. Appl. Meteor.*, **33**, 909-918.

Battan, L. J., 1973: *Radar Observations of the Atmosphere*. University of Chicago Press, 324 pp.

Bernadet, L. R., L. D. Grasso, J. E. Nachamkin, C. A. Finley, and W. R. Cotton, 2000: Simulating convective events using a high-resolution mesoscale model. *J. Geophys. Res*., **105**, 14963-14982.

Blackadar, A. K., 1979: High resolution models of the planetary boundary layer. In: *Advances in Environmental Science and Engineering.* J. Pfafflin and E. Ziegler, (Eds.), Vol. 1, Gordon and Breach, 50-85.

Boraine, A., (Ed.) 2004: *State of the cities report, 2004*. South African Cities Network, Johannesburg, 204 pp.

Breed, D., R. Bruintjes, T. Jensen, V. Salazar, A. Al Mangoosh, and A. Al Mandoos, 2003: Design and overview of the feasibility study for rainfall enhancement in the United Arab Emirates. *Presented at the eighth WMO Scientific Conference on Weather Modification*. World Meteorological Organization, Casablanca, Morocco.

Brown, M.J., J.D. Locatelli, M.T. Stoelinga, and P.V. Hobbs, 1999: Numerical modeling of precipitation cores on cold fronts. *J. Atmos. Sci*., **56**, 1175-1196.

Browning, K. A., and N. M. Roberts, 1996: Variation of frontal and precipitation structure along a cold front. *Quart. J. Roy. Meteor. Soc.*, **122**, 1845-1872.

Calheiros, R. V., and I. Zawadedski, 1987: Reflectivity-rain-rate relationships for radar hydrology in Brazil. *J. Clim. Appl. Meteorol*., **26**, 118-132.

Cavazos, T., 1999: Large-scale circulation anomalies conducive to extreme precipitation events and derivation of daily rainfall in northeastern Mexico and southeastern Texas. *J. Clim.,* **12**, 1506-1523.

Cavazos, T., 2000: Using self-organizing maps to investigate extreme climate events: An application to wintertime precipitation in the Balkans. *J. Clim.*, **13**, 1718-1732.

Cavazos, T., and B. C. Hewitson, 2005: Performance of NCEP–NCAR reanalysis variables in statistical downscaling of daily precipitation. Clim. Res. **28**, 95-107.

Cecil, D. J., E. J. Zisper, and S. W. Nesbitt, 2002: Reflectivity, ice scattering, and lightning characteristics of hurricane eyewalls and rainbands. Part I: Quantitative description. *Mon. Wea. Rev.,* **130**, 769-784.

Cecil, D. J., and E. J. Zisper, 2002: Reflectivity, ice scattering, and lightning characteristics of hurricane eyewalls and rainbands. Part II: Intercomparison of observations. *Mon. Wea. Rev.,* **130**, 785-801.

Chaing, C., C. H. Bishop, G. S. Lai, and W. -K., Tao, 1997: Numerical simulations of an observed narrow cold-frontal rainband. *Mon. Wea. Rev.,* **125**, 1027-1045.

Chen, F., and J. Dudhia, 2001a: Coupling an advanced land-surface hydrology model with the Penn State-NCAR MM5 modeling system. Part 1: Model implementation and sensitivity. *Mon. Wea. Rev.,* **129**, 569-585.

Chen, F., and J. Dudhia, 2001b: Coupling an advanced land-surface hydrology model with the Penn State-NCAR MM5 modeling system. Part 2: Preliminary model validation. *Mon. Wea. Rev.,* **129**, 587-604.

Chen Y. -L. and J. Feng, 2001: Numerical simulations of air flow and cloud distributions over the windward side of the island of Hawaii. Part II: The effects of Trade winds inversion. *Mon. Wea. Rev.,* **129**, 1117-1134.

Chen, L., and J. Gasteiger, 1997: Knowledge discovery in reaction databases: landscaping organic reactions by a self organizing map. *J. Am. Chem. Soc.,* **119**, 4033-4042.

Chien, F. -C., C. Mass, and Y. -H. Kuo, 1997: Interaction of a warm season frontal system with the coastal mountains of the United States. Part I: Prefrontal onshore push, coastal ridging, and alongshore southerlies. *Mon. Wea. Rev.,* **125**, 1705-1729.

Chien, F. -C., and C. Mass, 1997: Interaction of a warm season frontal system with the coastal mountains of the United States. Part II: Evolution of a Puget Sound convergence zone. *Mon. Wea. Rev.,* **125**, 1730-1752.

Chien, F.-C., C. F. Mass, and P. J. Neiman, 2001: An observational and numerical study of an intense land-falling front along the northwest coast of the U.S. during COAST IOP2. *Mon. Wea. Rev*., **129**, 934-955.

Christensen, .J.H., B. Machenhauer, R. G. Jones, C. Schar, P. M. Ruti, M. Castro and G. Visconti, 1997: Validation of present-day regional climate simulations over Europe: LAM simulation with observed boundary conditions. *Clim. Dyn.,* **13**, 489-506.

Christensen, .J. H., O. B. Christensen, B. Machenhauer, and M. Bozet, 1998: Very high resolution regional climate simulations over Scandinavia, present climate. *J. Clim.*, **12**, 3204-3229.

Clothiaux, E. E., and C. M. Bachmann, 1994. Neural networks and their applications. In: *Neural Nets: Applications in geography*. Hewitson, B., C., and R. G. Crane, (Eds.), Kluwer Academic Publishers, Dordrecht, The Netherlands, 35-50.

Cocke, S., and T. E. LaRow, 2000: Seasonal predictions using a regional spectral model embedded within a coupled ocean-atmosphere model. *Mon. Wea. Rev.,* **128**, 689-708.

Colle, B. A., and C. F. Mass, 1998: Windstorms along the western side of the Washington Cascade Mountains. Part I: A high-resolution observational and modeling study of the 12 February 1995 event. *Mon. Wea. Rev.*, **126**, 28-52.

Colle, B. A., K. J. Westrick, and C. F. Mass, 1999A: Evaluation of MM5 and Eta-10 precipitation forecasts over the Pacific Northwest during the cool season. *Wea. Forecasting*, **14**, 137-154.

Colle, B. A., C. F. Mass, and B. F. Smull, 1999b. An observational and numerical study of a cold front interacting with the Olympic Mountains during COAST IOP5. *Mon. Wea. Rev.,* **127**, 1310-1334.

Colle, B. A., and C. F. Mass, 2000a: The 5-9 February 1996 flooding event over the Pacific Northwest: Sensitivity studies and evaluation of the MM5 precipitation forecasts. *Mon. Wea. Rev.,* **128**, 593-617.

Colle, B. A., and C. F. Mass, 2000b: High-resolution observations and numerical simulations of easterly gap flow through the Strait of Juan de Fuca on 9-10 December 1995. *Mon. Wea. Rev.,* **128**, 2398-2422.

Courant, R., K. O. Friedrichs, and H. Lewy, 1928: Ueber die partiellen Differenzgleichungen der mathematische Physik. *Mathematische Annalen,* **100**, 32–74. Translated into English as:
Courant, R., K. O. Friedrichs, and H. Lewy, 1967: On the partial difference equations of mathematical physics. *IBM J. Res. Develop.*, **11**, 215–234.

Crimp, S. J. and S. J. Mason, 1999: The extreme precipitation event of 11–16 February 1996 over South Africa. *Meteorol. Atmos. Phys.,* **70**, 29-42.

Cubash, U., G. A. Meehl, G. J. Boer, R. J. Stouffer, M. Dix, A. Noda, C. A. Senior, S. Raper, and K. S. Yap, 2001: Projections of future climate change. In: *Climate Change 2001: The Scientific Basis. Contribution of Working Group I to the Third Assessment Report of the Intergovernmental Panel on Climate Change* [Houghton, J.T., et al. (Eds.)]. Cambridge University Press, Cambridge, United Kingdom and New York, NY, USA, pp. 525–582.

Davidson, N. E., K. Kurihara, T. Kato, G. mills, and K. Puri, 1998: Dynamics and prediction of a mesoscale extreme rain event in the Baiu Front over Kyushu, Japan. *Mon. Wea. Rev.,* **126**, 1608-1629.

Denis B., R. Laprise, D. Caya, and J. Cote, 2002: Downscaling ability of one-way nested regional climate models: the big brother experiment. *Clim. Dyn.*, **18**, 627-646.

Dickinson, R. E., R. M. Errico, F. Giorgi, and G. T. Bates, 1989: A regional climate model for the western United States. *Clim. Change,* **15**, 383-422.

Dixon M., and G. Wiener 1993: TITAN: Thunderstorm identification, tracking, analysis and

nowcasting - a radar-based methodology. *J. Atmos. Oceanic Tech.*, **10**, 785-797.

Doyle, J 1995: Coupled ocean wave-atmosphere mesoscale model simulations of cyclogenesis. *Tellus A,* **47**, 766-778.

Dudhia, J., 1989: Numerical study of convection observed during the Winter Monsoon Experiment using a mesoscale two-dimensional model. *J. Atmos. Sci.* **46**, 3077-3107.

Dudhia, J., 1993: A nonhydrostatic version of the Penn State/NCAR Mesoscale Model: Validation tests and simulations of an Atlantic cyclone and cold front. *Mon. Wea. Rev.*, **121**, 1493-1513.

Dudhia, J., and J. F. Bresch, 2002: A global version of the PSU-NCAR mesoscale model. *Mon. Wea. Rev.,* **130**, 2989-3007

du Plessis, L. A., 2002. A review of effective flood forecasting, warning and response system for application in South Africa. *Water SA*, **28**, 129-137.

Durman, C. F., J. M. Gregory, D. C. Hassel, R. G. Jones, and J. M. Murphy, 2001: The comparison of extreme European daily precipitation simulated by a global an a regional climate model for present and future climates. *Quart. J. Roy. Meteor. Soc.,* **127**, 1005-1016.

Easterling, D. R., J. L. Evans, P. Ya. Groisman, T. R. Karl, K. E. Kunkel, and P. Ambenje, 2000: Observed variability and trends in extreme climate events: A brief review. *Bull. Amer. Meteor. Soc.*, **81**, 417-425.

Eckert, P., D. Cattini, and J. Ambühl, 1996. Classification of ensemble forecasts by means of an artificial neural network. *Meteorol. Appl*. **3**, 169-178.

Edwards, M., 1997. Heavy rain and floods in South Africa during January February 1996: Synoptic review. *Proceedings of the Fifth International Conference of Southern Hemisphere Meteorology and Oceanography.* Boston: American Meteorological Society, pp. 9-10.

Ehrendofer, M., 1987. A regionalization of Austria's precipitation climate using principal

component analysis. *J. Climatol.*, **7**, 71-89.

Estie, K. E. 1981. The Laingsburg flood disaster of January 1981. *South African Weather Bureau Newsletter,* **383**, 19-32.

Faccani, C., R. Ferretti, and G. Visconti, 2003: High-resolution forecasting over complex orography: Sensitivity to the assimilation of conventional data. *Mon. Wea. Rev.,* **131**, 136-154.

Fast, J. D., R. P. Addis, and B. L. O'steen, 1995: Advanced atmospheric modeling for emergency response. *J. Appl. Meteor.*, **34**, 626-649.

Fausett, L., 1994: *Fundamentals of neural networks: Architectures, algorithms and applications.* Prentice-Hall Inc., New Jersey, 461 pp.

Feng, J., and Y. -L. Chen, 2001: Numerical simulations of air flow and cloud distributions over the windward side of the island of Hawaii. Part I: Nocturnal flow regime. *Mon. Wea. Rev.,* **129**, 1135-1147.

Fraser, A., 2006: Southern Cape floods and landslides cost six lives and cripple parts of the economy. *Civil Engineering*, **14(9)**, 2-3.

Frich, P., L. V. Alexander, P. Della-Marta, B. Gleason, M. Haylock, A. M. G. Klein Tank, and T. Peterson, 2002: Observed coherent changes in climatic extremes during the second half of the twentieth century. *Climate Res.*, **19**, 193–212.

Fyfe, J, C., 2003. Extratropical southern hemisphere cyclones: harbingers of climate change? *J. Clim.,* **16**, 2802-2805.

Gachon, P., R. Laprise, P. Zwack, and F. Saucier, 2003:The role of forcing interactions in the development of a polar low simulated by the Canadian Regional Climate Model. *Tellus A,* **55**, 61-87.

Gardner, M. W., and S. R. Dorling, 1998: Artificial neural networks (the multilayer perception) – a

review of applications in the atmospheric sciences. *Atmospheric Environment*, **32**, 2627-2636.

Garreaud, R. D., and J. Rutlland, 2003: Coastal lows along the subtropical west coast of South America: numerical simulation of a typical case. *Mon. Wea. Rev.,* **131**, 891-908.

Gillett, N. P., T. D. Kell, and P. D. Jones, 2006: Regional climate impacts of the Southern Annular Mode. *Geophys. Res. Lett.* **33**, L23704.

Giorgi, F. L. 1990: On the simulation of regional climate using a limited area model nested in a general circulation model. *J. Clim.,* **3**, 941-963.

Giorgi, F. L., and L. O. Mearns, 1991: Approaches to the simulation of regional climate change. A review. *Rev. Geophys.*, **29**, 191-216.

Giorgi, F., L. O. Mearns, C. Shields, and L. McDanial, 1998: Regional nested model simulations of present-day and 2xCO_2 climate over the Central Plains of the U. S. *Clim. Change,* **40**, 457-493.

Giorgi, F., X. Bi, and J. Pal, 2004. Mean, interannual variability and trends in a regional climate change experiment over Europe. II: climate change scenarios (2071–2100). *Clim. Dyn*., **23**, 839-858.

Giorgi, F., and L. O. Mearns, 1999: Regional climate modeling revisited. *J. Geophys. Res.,* **104**, 6335-6352.

Gohm, A., G. Zangl, and G. J. Mayr, 2004: South Foehn in the Wipp Valley on 24 October 1999 (MAP IOP 10): Verification of high-resolution numerical simulations with observations. *Mon. Wea. Rev.*, **132**, 78-102.

Gould, K., C. K. Mueller and J. W. Wilson, 1993: Rules for short-term forecast of thunderstorm initiation and evolution: procedures and automation. *Preprints, 13th Conference on Weather Analysis and Forecasting including Symposium on Flash Floods*, Vienna, VA.

Grell, G. A., 1993: Prognostic evaluation of assumptions used by cumulus parameterizations. *Mon.*

Wea. Rev., **121**, 764-787.

Grell, G. A., J. Dudhia, and D. R. Stauffer, 1994: A description of the fifth-generation Penn State/NCAR Mesoscale Model (MM5). *NCAR Tech. Note,* NCAR/TN-398+STR, 138 pp.

Grell, G. A., J. Dudhia, and D. R. Stauffer, 1995: A description of the fifth-generation Penn State/NCAR mesoscale model (MM5). *NCAR Tech. Note,* NCAR/TN-3981STR, 122 pp.

Groisman, P and Coauthors, 1999: Changes in the probability of heavy precipitation: Important indicators of climatic change. *Climatic Change*, **42**, 243-283.

Groisman, P, R. W. Knight, and T. R. Karl, 2001: Heavy precipitation and high streamflow in the contiguous United States: Trends in the twentieth century. *Bull. Amer. Meteor. Soc*., **82**, 219-246.

Groisman, P, R. W. Knight, D. R. Easterling, T. R. Karl, G. C. Hegerl and V. N. Razuvaev, 2005: Trends in intense precipitation in the climate record. *J. Climate*, **18**, 1326-1350.

Gutowski, W. J., 2001: Self organizing maps: Proposed RMIP analysis. Regional Model Intercomparison Project. Science team meeting, Kobe, Japan, 11-13 December, 2001.

Guo, Z., D. H. Bromwich, and J. J. Cassano, 2003: Evaluation of Polar MM5 simulations of Antarctic atmospheric circulation. *Mon. Wea. Rev.,* **131**, 384-441.

Haddad Z. S. and D. Rosenfeld, 1997: Optimality of empirical Z-R relations. *Q. J. R. Meteorol. Soc.,* **123**, 1283-1293.

Hanna, S. R. and R. Yang, 2001: Evaluations of Mesoscale Models. Simulations of Near-Surface Winds, Temperature Gradients, and Mixing Depths. *J. Appl. Meteor.*, **40**, 1095-1104.

Harrison, M. S. J., 1984. A generalized classification of South African summer rain-bearing synoptic systems. *J. Climatol.*, **4**, 547-560.

Henderson-Sellers, A., and K. McGuffie, 1987: *A Climate Modeling Primer*. John Wiley and Sons,

Suffolk, 217, 217 pp.

Henry, S. G., 1995: Evaluation of automated, short-term, thunderstorm forecast rules. Preprints, Sixth Conference on Aviation Weather Systems, Dallas, TX.

Hewitson, B. C., and R. G. Crane, 1992: Large scale atmospheric controls on local precipitation in tropical Mexico. *Geophys. Res. Lett.*, **19**, 1835-1838.

Hewitson, B. C., and R. G. Crane (eds), 1994: *Neural nets: Applications in Geography.* Kluwer Academic Publishers, Dordrecht, The Netherlands, 194 pp.

Hewitson, B.C. and R.G. Crane, 1996: Climate downscaling techniques and applications. *Clim. Res.*, **7**: 85-95.

Hewitson, B. C., and R. G. Crane, 2002: Self organizing maps: Applications to synoptic climatology. *Clim. Res*. **22**, 13-26.

Hewitson, B. C., and R. G. Crane, 2005: Gridded area-averaged daily precipitation via conditional interpolation. *J. Clim,*, **18**, 41-57.

Hewitson, B. C., and R. G. Crane, 2006: .Consensus between GCM climate change projections with empirical downscaling. *Int. J. Climatol.,* **26**: 1315-1337.

Hisashi, K., H. Hiromaru, K. Nishizawa, and F. Giorgi, 1999: Performance of the NCAR RegCM in the simulation of June and January climates over eastern Asia and the high-resolution effect of the model. *J. Geophys. Res.*, **104**, 6455-6476.

Hobbs, P. V., 1978: Organization and structure of clouds and precipitation on the mesoscale and microscale in cyclonic storms. *Rev. Geophys. Space Phys.*, **16**, 741–755.

Hobbs, P. V., and K. R. Biswas, 1979: The cellular structure of narrow cold-frontal rainbands. *Quart. J. Roy. Meteor. Soc*., **105**, 723–727.

Hope, P. K., 2006: Projected future changes in synoptic systems influencing southwest Western Australia. *Clim. Dyn.,* **26**, 765-780.

Hope, P. K., W. Drosdowsky, and N. Nicholls, 2006: Shifts in the synoptic systems influencing southwest Western Australia. *Clim. Dyn.,* **26**, 751-764.

Horel, J. D., and C. V. Gibson, 1994: Analysis and simulation of a winter storm over Utah. *Wea. Forecasting*, **9**, 479-494.

Hostetler, S. W., F. Giorgi, G. T. Bates, and P. J. Bartlein, 1994: Lake-atmosphere feedbacks associated with paleolakes Bonneville and Lahontan. *Science,* **263**, 665-668.

Hostetler, S. W., P. J. Bartlein, P. U. Clarke, E. E. Small, and A. M. Soloman, 2000: Simulated influence of Lake Agassiz on the climate of central North America 11,000 years ago. *Nature,* **405**, 334-337.

Hudson, D. A., 1998: *Antarctic sea-ice extent, Southern Hemisphere circulation and South African rainfall.* Unpublished Ph.D. thesis, University of Cape Town, Cape Town, 308 pp.

Huffman, G. J., R. F. Alder, P. Arkin, A. Chang, R. Ferraro, A. Gruber, J. Janowiak, A. McNab, B. Rulof and U. Schneider, 1997: The global precipitation climatology project (GPCP) combined precipitation dataset. *Bull. Amer. Meteor. Soc.*, **78**, 5-20.

IFRCRCS, 1997: *World Disasters Report 1997.* Oxford University Press, 173 pp.

Intergovernmental Panel on Climate Change (IPCC). 1996: *Climate change 1995 – The science of climate change: Contribution of working group 1 to the second assessment report of the Intergovernmental Panel on Climate Change.* Houghton J. T., L. G. Meira Filho, B. A. Callander, N. Harris, A. Kattenberg and K. Maskell (Eds), Cambridge University Press, Cambridge, 572 pp.

Intergovernmental Panel on Climate Change (IPCC) 2001: *Climate change 2001. The scientific basis. Contribution of working group I to the third assessment report of the Intergovernmental*

Panel on Climate Change. Houghton, J. T., Y. Ding, D. J. Griggs, M. Noguer, P.J. van der Linden, X. Dai, K. Maskell & C. A. Johnson (Eds), Cambridge University Press, Cambridge, 881 pp.

Iwashima, T., and R. Yamamoto, 1993: A statistical analysis of the extreme events: Long-term trend of heavy daily precipitation. *J. Meteor. Soc. Japan*, **71**, 637-640.

Jakobs, H.J., H. Feldmann, H. Hass, and M. Memmesheimer, 1995: The use of nested models for air pollution studies: An application of the EURAD model to a SANA episode. *J. Applied Met.*, **34**, 1301-1319.

James, P. K., and K. A. Browning, 1979: Mesoscale structure of line convection at surface cold fronts. *Quart. J. Roy. Meteor. Soc.*, **105**, 371-382.

Jones, R.G., J.M. Murphy and M. Noguer, 1995: Simulation of climate change over Europe using a nested regional climate model. Part I: Assessment of control climate including sensitivity to location of lateral boundaries. *Quart. J. Roy. Met. Soc.*, **121**, 1413-1449.

Jones, R. G., J. M. Murphy, N. Noguer, and A. B. Keen, 1997: Simulation of climate change over Europe using a nested regional-climate model. II: Comparison of driving and regional model responses to a doubling of carbon dioxide. *Quart. J. Roy. Meteor. Soc.*, **123**, 265-292.

Jones, R., B. Kirtman, R. Laprise, H. von Storch, and W. Werner, 2002: Atmospheric regional climate models (RCMs): a multipurpose tool? *Report of the Joint WGNE/WGCM* ad hoc *Panel on Regional Climate Modeling*, 19 pp.

Joutsiniemi, S. L., S. Kaski, and T. A. Larsen, 1995: Self-organizing map in recognition of topographic patterns of EEG spectra. *IEEE Trans. Biomed. Eng.*, **42**, 1062-1068.

Kain, J. S., and J. M. Fritsch, 1993: Convective parameterization for mesoscale models: The Kain-Fritsch scheme. In: *The representation of cumulus convection in numerical models.* K. A. Emmanuel and D. J. Raymonds, (Eds.), Amer. Meteor. Soc., 246 pp.

Kalnay, E., M. Kanamitsu, R. Kistler, W. Collins, D. Deaven, L. Gandin, M. Iredell, S. Saha, G. White, J. Woolen, Y. Zhu, A. Leetmaa, R. Reynolds, M. Chilliah, W. Ebusuzaki, W. Higgins, J. Janowaik, K. C. Mo, C. Ropelewski, J. Wang, R. Jenne, and D. Joseph, 1996. The NCEP/NCAR 40-year reanalysis project. *Bull. Amer. Meteor. Soc*, **77**, 437-471.

Karl, T. R., and R. W. Knight, 1998: Secular trends of precipitation amount, frequency, and intensity in the USA. *Bull. Amer. Meteor. Soc.*, **79**, 231–241.

Katz, R. W., 1999: Extreme value theory for precipitation: Sensitivity analysis for climate change. *Adv. Water Resour.*, **23**, 133-139.

Kim, J., 2005: A projection of the effects of the climate change induced by increased CO_2 on extreme hydrologic events in the western U.S. *Climatic Change*, **68**, 153-168.

Kistler, R., E. Kalnay, W. Collins, S. Saha, G. White, J. Woolen, M. Chelliah, W. Ebusuzaki, M. Kanamitsu, V. Kousky, H. van den Dool, R. Jenne, and M. Fiorino, 2001. The NCEP/NCAR 50-year reanalysis: monthly means CD-ROM and documentation. *Bull. Amer. Meteor. Soc*, **82**, 247-267.

Klein Tank A. M. G., and G. P. Koennen, 2003: Trends in indices of daily temperature and precipitation extremes in Europe, 1946–99. *J. Clim.,* **16,** 3665-3680

Kohonen, T., J. Hynninen, J. Kangas, and J. Laaksonen, 1997. SOM_PAC: The Self Organizing Map Program Package. Technical Report A31, Helsinki University of Technology, Laboratory of Computer and Information Science, Finland.

Kohonen, T., 1995. *Self-organizing maps*. Springer, Berlin, 362 pp.

Kohonen, T., 1997. *Self-organizing maps*. Springer-Verlag, Berlin, 426 pp.

Krichak, S. O., and P. Alpert, 2000: November 2 1994: Severe storm in the southeastern Mediterranean. *Atmospheric Research,* **53**, 45-62.

Kuligowski, R. J., and A. P. Barros, 1999: High-resolution short-term quantitative precipitation forecasting in mountainous regions using a nested model. *J. Geophys. Res.,* **104**, 31553-31564.

Kundzewicz, Z. W., M. Radziejewski1 and I. Pinskwar, 2006: Precipitation extremes in the changing climate of Europe. *Clim. Res*. **31**, 51-58.

Kushner, P. J., I. M. Held, and T. L. Delworth, 2001: Southern Hemisphere atmospheric circulation response to global warming. *J. Clim.,* **14,** 2238-2249.

Lambert, S. J., 1995: The effect of enhanced greenhouse gas warming on winter cyclone frequencies and strengths. *J. Clim.,* **8**, 1447-1452.

Laprise, R., D. Caya, M. Giguere, G. Bergeron, H. Cote, J. P. Blanchet, G. J. Boer, and N. A. McFarlan, 1998: Climate and climate change in Western Canada as simulated by the Canadian Regional Climate Model. *Atmos.-Ocean,* **36**, 119-167.

Li J., R. A. Maddox, X. Gao, S. Sorooshian, and K. Hsu, 2003: A numerical investigation of storm structure and evolution during the July 1999 Las Vegas flash flood. *Mon. Wea. Rev.,* **131**, 2038-2059.

Lin, E.-P., and I. Simmonds, 2002: Explosive cyclone development in the Southern Hemisphere and a comparison with Northern Hemisphere events. *Mon. Wea. Rev.,* **130**, 2188-2209.

Liu, Y., D. -L. Zhang, and M. K. Yau, 1997: A multiscale numerical study of Hurricane Andrew (1992). Part 1: Explicit simulation and verification. *Mon. Wea. Rev.,* **125**, 3073-3094.

Liu, Y., D. -L. Zhang, and M. K. Yau, 1999: A multiscale numerical study of Hurricane Andrew (1992). Part 1: Kinematics and inner-core structures. *Mon. Wea. Rev.,* **127**, 2597-2616.

Locatelli, J. D., J. E. Martin, and P. V. Hobbs, 1995: Development and propagation of precipitation cores on cold fronts. *Atmos. Res*., **38**, 177–206.

Lüthi, D., A. Cress, H.C. Davies, C. Frei and C. Schär, 1996: Interannual variability and regional climate simulations. *Theor. Appl. Clim.*, **53**, 185-209.

Lynch, A. H, M. F. Gluck, W. L. Chapman, D. A. Bailey, and J. E. Walsh, 1997: Remote sensing and climate modeling of the St. Lawerence Is. Polynya. *Tellus A*, **49**, 277-297.

Machenhauer, B, M. Wildelband, M. Botzet, R. G. Jones, and M. Deque, 1996: Validation of present-day regional climate simulations over Europe: Nested LAM and variable resolution global model simulations with observed or mixed-layer ocean boundary conditions. Max -Planck Institute Report No. 191, Max-Planck-Institut fur Meteorologie, Hamburg, Germany.

Machenhauer, B., M. Wildelband, M. Botzet, J. H. Christensen, M. Deque, R. G. Jones, P. M. Ruti, and G. Visconti, 1998: Validation and analysis of regional present-day climate and climate-change simulations over Europe. Max -Planck Institute Report No. 275, Max -Planck-Institut fur Meteorologie, Hamburg, Germany.

Main, J., 1997: *Seasonality of circulation in southern Africa using the Kohonen self organizing map*. Unpublished M.Sc. thesis, University of Cape Town, Cape Town, 84 pp.

Manning, K. W., and P. L. Haagenson, 1992: Data ingest and objective analysis for the PSU/NCAR modeling system: Programs DATAGRID and RAWINS. *NCAR Tech. Note*, NCAR/TN-376+IA, 209 pp.

Marshall, J. S., R. C. Lagille and W. Mc K. Palmer, 1947: Measurement of rainfall by radar. *J. Meteor.*, **4**, 186-192.

Marshall, J. S., and W. Mc K. Palmer, 1948: The distribution of raindrops with size. *J. Meteor.*, **5**, 165-166.

Marzban, C., and G. J. Stumpf, 1996: A neural network for tornado prediction based on Doppler radar derived attributes. *J. Appl. Meteor.*, **35**, 617-626.

Mass, C. F., and Y.-H. Kuo, 1998: Regional real-time numerical weather prediction: Current status and future potential. *Bull. Amer. Meteor. Soc.*, **79**, 253-263.

Mass, C. F., D. Ovens, K. Westrick, and B.A. Colle, 2002: Does increasing horizontal resolution produce more skillful forecasts? The results of two years of real-time numerical weather prediction over the Pacific Northwest. *Bull. Amer. Meteor. Soc.*, **83**, 407-430.

Mason, S. J., and A., M., Joubert, 1997: Simulated changes in extreme rainfall over southern Africa. *Int. J. Climatol*., **17**, 291-301.

Mason, S. J., P. R. Waylen, G. M. Mimmack, B. Rajaratnam, and J. M. Harrison, 1999: Changes in extreme rainfall events in South Africa. *Clim. Change*, **41**, 249-257.

McGregor, J. L., and K. Walsh, 1994: Climate change simulation of Tasmanian precipitation using multiple nesting. *J. Geophys. Res.,* **99**, 20889-20905.

Meehl, G. A. 1992: Global coupled models: atmosphere, ocean, sea ice. In Trentberth, K. E. (editor) *Climate System Modeling*. Cambridge University Press, London, 788 pp.

Meehl, G. A., F. Zwiers, J. Evans, T. Knutson, L. Mearns, and P. Whetton, 2000: Trends in extreme weather and climate events: Issues related to modeling extremes in projections of future climate change. *Bull. Amer. Meteor. Soc*., **81**, 427-436.

Navone H. D., and H. A. Ceccatto, 1994: Predicting Indian monsoon rainfall: A neural network approach. *Clim. Dyn.*, **10**, 305-312.

New, M., B. Hewitson, D. Stephenson, A. Tsiga, A. Kruger, A. Manhique, B. Gomez, C. Coelho, D. N. Masisi, E. Kululunga, E. Mbambalala, F. Adesina, H. Saleh, J. Kanyanga, J. Adosi, L. Bulane, L. Fortunata, and R. Lajoie, 2006: Evidence of trends in daily climate extremes over southern and west Africa. *J. Geophys. Res*., **111**, D14102.

Noguer, M., R. G. Jones, and J. Murphy, 1998: Sources of systematic errors in the climatology of a nested regional climate model over Europe. *Clim. Dyn.,* **14**, 691-712.

Openshaw, S., 1994. Neuroclassification of spatial data. In*: Neural Nets: Applications in geography*. Hewitson, B., C., and R. G. Crane, (Eds.), Kluwer Academic Publishers, Dordrecht,

The Netherlands, 53-70.

Osborn, T. J., and M. Hulme (2002): Evidence for trends in heavy rainfall events over the UK. *Philos. Trans. R. Soc., Ser. A*, **360**, 1313-1325.

Osborn, T. J., M. Hulme, P. D. Jones, and T. A. Basnett, 2000: Observed trends in the daily intensity of United Kingdom precipitation. *Int. J. Climatol*., **20**, 347-364.

Palakal, M. J., U. Murthy, S. K. Chittajallu, and D. Wong, 1995: Tonotopic representation of auditory responses using self organizing maps. *Math. Comput. Model.,* **22,** 7-21.

Pan, Z., J.H. Christensen, R.W. Arritt, W. J. Gutowski, Jr., E.S. Takle, and F. Otenio, 2001: Evaluation of uncertainties in regional climate change simulations. *J. Geophys. Res*., **106**, 17735-17752.

Patterson, D. W. 1996: *Artificial neural networks: Theory and application*. Simon and Schuster, Singapore, 477 pp.

Perkey, D. J., and C. W. Kreitzberg, 1976: A time-dependent lateral boundary scheme for limited area primitive equation models. *Mon. Wea. Rev.*, **104**, 744-755.

Petroliagis, T., R. Buizza, A. Lanzinger and T.N. Palmer, 1996: Extreme rainfall prediction using the European center for medium-range weather forecasts ensemble prediction system. *J. Geophys. Res*., **101**, 26227-26236.

Phillips, N. A. 1956: The general circulation of the atmosphere: A numerical experiment. *Quarterly Journal of the Royal Meteorological Society,* **82**, 123-164.

Pielke, R. A., Jr., and M. W. Downton, 2000: Precipitation and damaging floods: Trends in the United States, 1932–97. *J. Climate*, **13**, 3625-3637.

Pielke, R. A., R. L. Wlako, L. Steyaert, P. L. Vidale, G. E. Liston, and W. A. Lyons, 1999: The influence of anthropogenic landscape changes on weather in south Florida. *Mon. Wea. Rev.,* **127**,

1663-1673.

Pixoto, J. P., and A. H. Oort, 1992: *Physics of Climate.* American Institute of Physics, New York, 520 pp.

Ravallion, S., and M. Chen, 2004: How have the world's poorest fared since the early 1980s? *The World Bank Research Observer*, **19(2)**, 141–169.

Rayleigh, L., 1871. On the scattering of light by small particles. *Phil. Mag.,* **41**, 447-452.

Reason, C. J. C., 2002: The wet winter of 2001 over the southwestern Cape, South Africa: potential large scale influences. *S. A. J. Sci.,* **98**, 307-310.

Reason, C. J. C., D. Jagadheesha, and M. Tadross, 2003: A model investigation of the inter-annual winter rainfall variability over the southwestern South Africa and associated ocean-atmosphere interaction. *S. A. J. Sci.,* **99**, 75-80.

Reisner, J., R. M. Rasmussen, and R. T. Bruintjies, 1998: Explicit forecasting of supercooled liquid water in winter storms using the MM5 mesoscale model. *Quart. J. Roy. Meteor. Soc.*, **124**, 1071-1108.

Reusch, D. B., R. B. Alley and B. C. Hewitson, 2005. Relative performance of self-organizing maps and principal component analysis in pattern extraction from synthetic climatological data. *Polar Geography*, **29**, 227-251.

Rinehart, R.E., 1991: *RADAR for Meteorologists*. Grand Forks, North Dakota, 334 pp.

Roebber, P. J., and J. R. Gyakum, 2003: Orographic influences on the mesoscale structure of the 1998 ice storm. *Mon. Wea. Rev.,* **131**, 27-50.

Rogers, R. F., J. M. Fritsch, and W. C. Lambert 2000: A simple technique for using radar data in the dynamic initialization of a mesoscale model. *Mon. Wea. Rev.,* **128**, 2560-2574.

Rosenfeld, D., and C. W. Ulbrich, 2003: Cloud microphysical properties, processes, and rainfall estimation opportunities. Radar and atmospheric science: A collection of essays in honor of David Atlas. *Meteor. Monogr.*, **52**, 237-258.

Roy, S. S., and R. C. Balling, 2004: Trends in extreme daily rainfall indices in India. *Int. J. Climatol*., **24**, 457-466.

Pradier, S., M. Chong, and F. Roux, 2003: Radar Observations and numerical modeling of a precipitating line during MAP IOP 5. *Mon. Wea. Rev.,* **130**, 2533-2553.

Sammon, J. W., 1969. A nonlinear mapping for data structure analysis. *IEEE Transaction on Computers*, **C18**, 401-409.

Schär, C., and R. B. Smith, 1993a: Shallow-water flow past isolated topography. Part I: Vorticity production and wake formation. *J. Atmos. Sci.*, **50**, 1373-1400.

Schär, C. and R. B. Smith, 1993b: Shallow-water flow past isolated topography. Part II: Transition to vortex shedding. *J. Atmos. Sci*., **50**, 1401-1412.

Serafin, R. J., and J. W. Wilson, 2000: Operational weather radar in the United States: Progress and opportunity. *Bull. Amer. Meteor. Soc.*, **81**, 501-518.

Semenov, V. A., and L. Bengtsson, 2002: Secular trends in daily precipitation characteristics: Greenhouse gas simulation with a coupled AOGCM. *Climate Dyn.*, **19**, 123-140.

Shapiro, M. A., and J. J. O'Brien, 1970: Boundary conditions for fine-mesh limited-area forecasts. *J. Appl. Meteor.,* **9**, 345-349.

Sharda, R., and D. Delen, 2006. Predicting box-office success of motion pictures with neural networks. *Expert systems with applications,* **30**, 243-254.

Sistla, G., W. Hao, J. -Y. Ku, G. Kallos, K. Zhang, H. Mao, and S. T. Rao, 2001: An operational evaluation of two regional-scale air quality modeling systems over the United States. *Bull. Amer.*

Meteor. Soc., **82**, 945-964.

Smagorinsky, J., 1963: General circulation experiments with the primitive equations. 1. The basic experiment. *Mon. Wea. Rev.,* **91**, 99-164.

Smallcomb, C., 2001: Using an operational MM5 in the fire weather forecast process for west Texas and southeastern New Mexico. Preprints, *11th PSU/NCAR Mesoscale Model User s Workshop*, Boulder, CO, PSU/NCAR, 32-35.

Spencer, P. L., and D. J Stensrud, 1998: Simulating flash flood events: Importance of subgrid representation of convection. *Mon. Wea. Rev.,* **126**, 2884-2912.

Stauffer, D.R., N.L. Seaman, T.T. Warner and A.M. Lario, 1993: Application of an atmospheric simulation model to diagnose air-pollution transport in the Grand Canyon region of Arizona. *Chemical Engineering Communications*, **121**, 9-26.

Steiner, M., J. A. Smith, and R. Uijlenhoet, 2004. A microphysical interpretation of radar reflectivity-rain rate relationships. *Journal of the Atmospheric Sciences*, **61**, 1114-1131.

Stout, G. E., and E. A. Mueller, 1968: Survey of relationships between rainfall rate and radar reflectivity in the measurement of precipitation. *J. Appl. Meteor*., **7**, 465-474.

Suppiah, R., and K. Hennessy, 1998: Trends in seasonal rainfall, heavy rain-days, and number of dry days in Australia 1910– 1990. *Int. J. Climatol*., **18**, 1141-1155.

Takle, E. S., W. J. Gutowski, R. A. Arritt, Z. Pan, C. J. Anderson, R. R. da Silva, D. Caya, S.-C. Chen, J. H. Christensen, S.-Y. Hong, H.-M. H. Juang, J. Katzfey, W. M. Lapenta, R. Laprise, P. Lopez, J. McGregor and J. O. Roads, 1999: Project to Intercompare Regional Climate Simulations (PIRCS): Description and initial results. *J. Geophys. Res*., **104**, 19,443-19,461.

Taljaard, J. J., 1985: Cut-off lows in the South African region. South African Weather Bureau Tech. Paper No. 14, 153 pp.

Tarassenko, L., 1998: *A guide to neural computing applications*. John Wiley and Sons Inc., New York, 139 pp.

Tarhule, S., and M. Woo, 1998: Changes in rainfall characteristics in northern Nigeria. *Int. J. Climatol*., **18**, 1261-1272.

Tebaldi C., K. Hayhoe, J. M. Arblaster, and G. A. Meehl, 2006: Going to the extremes: An intercomparison of model-simulated historical and future changes in extreme events. *Climatic Change*, **79**, 185-211.

Tennant, W. J., 2002: *Event characteristics of intra-seasonal climate circulations.* Unpublished Ph.D. thesis, University of Cape Town, Cape Town, 185 pp.

Tennant, W. J., 2004: Considerations when using pre-1979 NCEP/NCAR reanalyses in the southern hemisphere. *Geophys. Res. Lett.*, **31**, L11112.

Toracinta, E. R., D. J. Cecil, E. J. Zisper, and S. W. Nesbitt, 2002: Radar, passive microwave, and lightning characteristics of precipitating systems in the tropics. *Mon. Wea. Rev.,* **130**, 802-824.

Trenberth, K. E. 1996: Coupled Climate System Modeling. In Giambelluca, T. W. and A. Henderson-Sellers (editors), 1996: *Climate Change, Developing Southern Hemisphere Perspectives.* John Wiley and Sons, West Sussex, England, 475 pp.

Tyson, P. D., and R. A. Preston-Whyte, 2000. *The weather and climate of Southern Africa.* Oxford University Press, Cape Town, South Africa, 396 pp.

Van Heerden, J., and P. C. L. Steyn, 1999. Weather radar measurement of rainfall for hydrological and other purposes. *South African Water Research Commission Report, No. 693/1/99,* 106 pp.

Van Heerden, J., and Taljaard, J. J., 1998: Africa and surrounding waters. In Karoly, D. J., and D. G. Vincent (editors), 1998: Meteorology of the Southern Hemisphere. *Meteorological Monographs*, **49**, 141-174.

Von Storch, H., M. Costa-Cabral, C. Hagner, F. Feser, J. Pacyna, E. Pacyna and s. Kolb, 2003: Four decades of gasoline lead emissions and control policies in Europe: A retrospective assessment, *Sci. Total Environ*. **311**, 151–176.

Wang, Y. 2001: An explicit simulation of tropical cyclones with a triply nested movable mesh primitive equation model: TCM3. Part 1: Model description and experiment. *Mon. Wea. Rev.,* **129**, 1370-1394.

Warner, T. T., Y.-H. Kuo, J. D. Doyle, J. Dudhia, D. R. Stauffer, and N. L. Seaman, 1992: Nonhydrostatic, mesobeta-scale real-data simulations with the Penn State University/National Center for Atmospheric Research mesoscale model. *Meteor. Atmos. Phys.*, **49**, 209-227.

Warner, T. T., R. A. Peterson, and R. E. Treadon, 1997: A tutorial on lateral boundary conditions as a basic and potentially serious limitation to regional numerical weather prediction. *Bull. Amer. Meteor. Soc.*, **78**, 2599-2617.

Warner, T. T., and H. -M. Hsu, 2000: Nested model simulation of moist convection: The impact of coarse grid parameterized convection on fine-grid resolved resolved convection. *Mon. Wea. Rev.,* **128**, 2211-2231.

Washington, R., M. Harrison, D. Conway, E. Black, A. Challinor, D. Grimes, R. Jones, A. Morse, and M. Todd, 2004: African climate report. A report commissioned by the UK Government to review African climate science, policy and options for action. DFID/DEFRA, 45 pp.

Washing, R., M. Harrison, D. Conway, E. Black, A. Challinor, D. Grimes, R. Jones, A. Morse, G. Kay, and M. Todd, 2006: African climate change: taking the shorter route. *Bull. Amer. Meteor. Soc.*, **87**, 1355-1366.

Wei, H., W. J. Gutowski, C. J. Vorosmarty, and B. M. Fekete, 2003: Calibration and validation of a regional climate model for Pan-Arctic hydrologic simulation. *J. Clim*., **15**, 3222-3236.

Wen, L., W. Yu, C. A. Lin, M. Beland, R. Benoit, and Y. Delage, 2000: The role of land surface schemes in short-range, high spatial resolution forecasts. *Mon. Wea. Rev.,* 128, 3605-3617.

White, B. G., J. Feagle, W. J. Steenburgh, J. D. Horel, R. T. Swanson, L. K. Cook, D. J. Onton, and J. G. Miles, 1999: Short-term forecast validation of six models. *Wea. Forecasting,* **14**, 84-108.

Wilson, J. W., and C. K. Mueller, 1993: Nowcast of thunderstorm initiation and evolution. *Wea. Forecasting,* **8**, 113-131.

Xiu, A., and J. E. Pleim, 2000: Development of a land surface model part I: Application in a mesoscale meteorology model. *J. Appl. Meteor.*, **40**, 192-209.

Yarnel, B. 1993. *Synoptic climatology in environmental analysis: A primer.* Belhaven Press, London, 195 pp.

Zhang, D., and R. A. Anthes, 1982: A high-resolution model of the planetary boundary layer - Sensitivity tests and comparisons with SESAME-79 data. *J. Appl. Meteor.*, **21**, 1594-1609.

Zhang, D. -L., E. Raveda, and J. Gyakum, 1999a: A family of frontal cyclones over the western Atlantic ocean. Part I: A 60-h simulation. *Mon. Wea. Rev.,* **127**, 1725-1744.

Zhang, D.-L., E. N. Radeva and J. Gyakum, 1999b: A family of frontal cyclones over the western Atlantic ocean. Part II: Parameter studies. *Mon. Wea. Rev.,* **127**, 1745-1760.

Zhang, D.-L., Y. Liu and M.K. Yau, 2000: A multiscale numerical study of Hurricane Andrew (1992). Part III: Dynamically-induced vertical motion. *Mon. Wea. Rev.,* **128**, 3772-3788.

Zhang, D.-L., Y. Liu and M.K. Yau, 2001: A multiscale numerical study of Hurricane Andrew (1992). Part IV: Unbalanced dynamics. *Mon. Wea. Rev.,* **129**, 92-107.

Zhang, D.-L., Y. Liu and M.K. Yau, 2002: A multiscale numerical study of Hurricane Andrew (1992). Part V: Inner-core thermodynamics. *Mon. Wea. Rev.,* **130**, 2745-2763.

Zhang, Q. -H., K. -H. Lau, Y. -H. Kuo, and S. -J Chen, 2003: A Numerical Study of a Mesoscale

Convective System over the Taiwan Strait. *Mon. Wea. Rev.,* **131**, 1150-1170.

Zhang, X., W. D. Hogg, and E. Mekis, 2001: Spatial and temporal characteristics of heavy precipitation events in Canada. *J. Climate*, **14**, 1923-1936.

Zhai, P. M., A. Sun, F. Ren, X. Liu, B. Gao, and Q. Zhang, 1999: Changes of climate extremes in China. *Climate Change*, **42**, 203-218.

Zhong, S., and J. Fast, 2003: An evaluation of the MM5, RAMS, and Meso-Eta models at subkilometer resolution using VTMX Field Campaign data in the Salt Lake Valley. *Mon. Wea. Rev.,* **131**, 1301-1322.

Zwiers, F. W., and V. V. Kharin, 1998: Changes in the extremes of the climate simulated by CCC GCM2 under CO2 doubling. *J. Climate*, **11**, 2200-2222.

Zwiers, F. W., and X. Zhang, 2003: Toward regional-scale climate change detection. *J. Clim.*, **16**, 793-797.